Mechanical properties of *MC* multimetallic carbides in steel

THÈSE N^{O} 8615 (2018)

PRÉSENTÉE LE 17 AOÛT 2018

À LA FACULTÉ DES SCIENCES ET TECHNIQUES DE L'INGÉNIEUR
LABORATOIRE DE MÉTALLURGIE MÉCANIQUE
PROGRAMME DOCTORAL EN SCIENCE ET GÉNIE DES MATÉRIAUX

ÉCOLE POLYTECHNIQUE FÉDÉRALE DE LAUSANNE

POUR L'OBTENTION DU GRADE DE DOCTEUR ÈS SCIENCES

PAR

Lionel MICHELET

acceptée sur proposition du jury:

Prof. K. Scrivener, présidente du jury
Prof. A. Mortensen, directeur de thèse
Prof. M. Legros, rapporteur
Prof. J. Chevalier, rapporteur
Prof. H. Van Swygenhoven, rapporteuse

ÉCOLE POLYTECHNIQUE
FÉDÉRALE DE LAUSANNE
Suisse
2018

The current version of this thesis has been corrected with respect to the manuscript that was submitted and approved in June 2018.

Modifications made to the original version of the thesis:

Page 7	Résumé	Change in the last paragraph
Page 9	Abstract	Change in the last paragraph
Page 135	Table 3.13	Changes in rows 8, 9 & 12 (text and picture)
Page 140	Hardness	Addition of a final paragraph
Page 141	Chapter 4.1.1	Paragraph 3 of the chapter has been rewritten
Page 141	Chapter 4.1.1	Changes for the Hysitron Berkovic diamond tip and for the silicon carbide reference
Page 141	Chapter 4.1.2	Chapter 4.1.2 has been rewritten
Page 143	Chapter 4.2.1	Chapter 4.2.1 has been rewritten
Page 143	Table 4.1	Table 4.1 has been changed with the new values
Page 144	Table 4.2	Table 4.2 has been changed with the new values
Page 144	Figure 4.2	Figure 4.2 has been redrawn with the new values
Page 145	Table 4.3	Table 4.3 has been changed with the new values
Page 145	Figure 4.3	Figure 4.3 has been redrawn with the new values
Page 145	Table 4.4	Table 4.4 has been changed with the new values
Page 145	Table 4.5	Table 4.5 has been changed with the new values
Page 145	Table 4.6	Table 4.6 has been changed with the new values
Page 146	Figure 4.4	Figure 4.4 has been redrawn with the new values
Page 146	Figure 4.5	Figure 4.5 has been redrawn with the new values

Page 147	Figure 4.6	Figure 4.6 has been redrawn with the new values
Page 147	Table 4.7	Table 4.7 has been changed with the new values
Page 148	Chapter 4.3	Paragraph 2 has been rewritten
Page 148	Table 4.8	Table 4.8 has been added
Page 149	Chater 4.3.1	Chapter 4.3.1 has been rewritten
Page 150	Chapter 4.3.2	Chapter 4.3.2 has been rewritten
Page 153	Chapter 4.3.3	Chapter 4.3.3 has been rewritten
Page 153	Chapter 4.3.4	Chapter 4.3.4 has been rewritten
Page 205	Table 6.4	Table 6.4 has been changed (Hardness and fracture toughness) according to the new values
Page 206	Figure 6.9	Figure 6.9 has been redrawn with recalculated fracture toughness
Page 207	Figure 6.10	Figure 6.10 has been redrawn with recalculated fracture toughness
Page 208	Figure 6.11	Figure 6.11 has been redrawn with recalculated fracture toughness
Page 209	Figure 6.12	Figure 6.12 has been redrawn with recalculated fracture toughness
Page 210	Figure 6.13	Figure 6.13 has been redrawn with recalculated fracture toughness
Page 219	Figure 6.19	Figure 6.19 has been redrawn with recalculated fracture toughness
Page 221	Figure 6.20	Figure 6.20 has been redrawn with recalculated fracture toughnesses
Page 226	Chapter 7.1	All paragraphs from and including the fourth paragraph in chapter 7.1 have been rewritten
Page 226	Table 7.1	Table 7.1 has been changed with the new hardness values
Page 228	Chapter 7.2	Bullets n°6, 9, 10 & 11 have been changed

REMERCIEMENTS

Quomodo fabula, sic vita : non quam diu, sed quam bene acta sit, refert

Lucius Annaeus Seneca, Lettre à Lucilius LXXVII

᾽Ανδρα μοι ἔννεπε, Μουσα, πολύτροπον, ὃς μάλα πολλὰ
πλάγχθη, ἐπεὶ Τροιης ἱερὸν πτολίεθρον ἔπερσε·

Homère, Odyssée, Chant I

Cette thèse synthétise plus de cinq années de travail de recherche, et tout ceci n'aurait pas été possible sans le précieux soutien de toutes les personnes que je tenais à remercier ici.

Je remercie le Conseil Européen de la Recherche (ERC) pour avoir financé ce projet (FP/2007-2013 – ERC Advanced Grant Agreement N°291085)

Tous mes remerciements à mon jury de thèse : Prof. Karen Scrivener, Prof. Helena Van Swygenhoven, Prof. Marc Legros et Prof. Jérôme Chevalier pour leur temps, leurs remarques pertinentes ainsi que pour les discussions très intéressantes sur le travail présenté dans ce manuscrit. Je remercie également très sincèrement le professeur Michel Rappaz qui m'a suivi non seulement tout au long de cette thèse, mais aussi durant toutes mes années d'études à l'EPFL.

Je remercie chaleureusement l'EPFL, l'EDMX, le CIME (en particulier Marco et Fabienne pour leur aide précieuse) ainsi que toute l'équipe de l'ATMX, dont l'excellent travail m'a permis d'arriver à ce résultat aujourd'hui.

Un merci particulier au Dr Léa Deillon qui a mis en évidence une erreur dans l'interprétation des mesures de dureté, ce qui a permis de produire cette version corrigée.

J'ai eu la chance de passer cinq magnifiques années au sein du LMM, et j'adresse un très profond merci à tous ses membres que j'ai eu l'occasion de côtoyer. Un merci particulier au "staff" du laboratoire, Fabienne, Raph, Cyril et Ludger, toujours à disposition en cas de problème ou pour une franche discussion scientifique.

Durant ce grand projet, j'ai eu l'occasion de travailler avec une équipe formidable, et je remercie ici le fameux "ERC-team", Martin, Vaclav, Goran, Marta et Léa. Sans leur aide, je ne serai pas parvenu à produire les pages qui vont suivre. Une dédicace toute particulière à mes deux correctrices préférées et attitrées : Marta et Léa.

Au sein du LMM, j'ai eu l'occasion de rencontrer des collègues, mais plus que tout de véritables amis. Je remercie du fond du cœur Maïté (et Alex), Gio (et Vys), Léa et Hamed pour tous ces bons moments, les traditionnelles discussions débiles du café et les activités que nous avons vécues. J'espère sincèrement que cette amitié perdurera une fois que nous aurons tous (bientôt) quitté l'EPFL. Et surtout, Gio, n'oublie pas que "Oui, tu as raison !".

Un grand merci à ma famille qui m'a toujours supporté dans mes études comme pour tout le reste. Merci pour tout !

Last but not least, le plus grand des mercis revient bien évidemment à Mélina pour son formidable soutien et surtout sa patience dans cette longue épopée. Je t'aime !

RÉSUMÉ

DESCRIPTION DES CORRECTIONS APPORTÉES À CETTE VERSION DE LA THÈSE:
Le résumé a été modifié pour tenir compte de la nouvelle conclusion apportée à cette thèse.

Les carbures sont des matériaux utilisés dans de nombreuses applications où d'excellentes propriétés mécaniques, telles que dureté, résistance à la déformation et ténacité, sont requises. L'industrie des matériaux d'usinage est un exemple où les carbures ont une importance considérable.

Que ce soit dans les aciers outils ou pour la fabrication de cermets, les alliages les plus performants sont composés de carbures ternaires, contenant deux éléments métalliques en plus du carbone, et présents en renforts dans la matrice métallique. De tels carbures constituent des renforts conférant de meilleures propriétés en comparaison avec des carbures binaires. Toutefois, les connaissances de ces carbures ternaires en tant que tels restent très insuffisantes, et seules les propriétés des alliages ont été caractérisées. La principale raison à ce manque est la petite taille de ces particules, de l'ordre du micron, qui complique la mesure des propriétés mécaniques.

Cette thèse a pour but de combler ces lacunes au moyen d'essais micromécaniques capables de mesurer les propriétés locales des particules prises individuellement. Ceci est possible grâce aux récents développements de la nanoindentation et des faisceaux d'ions. Les challenges sont donc de produire des carbures sous forme de particules dans une matrice de fer, en contrôlant leur composition, de tester mécaniquement et individuellement ces particules, et de proposer une explication à l'évolution des propriétés avec la composition, dans le but de trouver un carbure optimal en termes de propriétés mécaniques.

Le principal challenge vient non seulement de la faible dimension des particules (< 40 μm), mais aussi de la matrice qui les entoure, plus complaisante, et qui fausse les mesures des propriétés élastiques. Les techniques de nanoindentation standards ne peuvent pas mesurer précisément les propriétés élastiques de ces combinaisons particules-matrices, et de nouvelles méthodes ont été développées dans le but de résoudre ce problème.

Les particules de carbures ont été produites *in situ* en fondant de la fonte et des chips d'éléments d'alliage dans un four à arc, tout en variant les compositions. Trois propriétés mécaniques ont été ensuite mesurées : le module d'élasticité, la dureté et la ténacité, en indentant la surface polie des carbures, ou par flexion et rupture d'une poutre pré-entaillée. Ce trio de propriétés est essentiel pour caractériser correctement un matériau, à plus forte raison pour une utilisation ultérieure dans l'usinage.

Les carbures binaires nous ont servi de référence, et nous avons pu caractériser cinq systèmes ternaires, à savoir (Ti,W)C, (Ti,V)C, (Ti,Ta)C, (Ti,Nb)C et (Ta,V)C. Le ratio des éléments métalliques a été varié dans le but de couvrir toute la gamme de compositions. Pour ces carbures ternaires, nous avons mesuré des modules ainsi que des duretés supérieures d'environ 15-20% par rapport aux valeurs des carbures binaires correspondants. Une comparaison de ces résultats à la théorie développée par Jhi et al. et reposant sur la densité d'électrons de valence met en évidence que cette théorie seule ne permet pas d'interpréter tous les résultats obtenus ici et que d'autres paramètres sont tout autant importants pour déterminer la dureté et le module élastique de ces carbures.

Mots-clés : Composites à matrice métallique, Carbures, Aciers, Module élastique, Dureté, Ténacité, Essais Micromécaniques, Nanoindentation, Concentration d'Électrons de Valence.

ABSTRACT

DESCRIPTION OF CORRECTIONS BROUGHT TO THE SUBMITTED THESIS VERSION:
The abstract has been corrected in order to account for the modified conclusion of the thesis.

Carbides constitute a class of materials used for many applications, especially where excellent mechanical properties, such as stiffness, hardness and fracture toughness, are required. The machining industry is a typical example where carbide are crucial materials.

Whether it be in tool steels or in cermets, the most performant machining alloys are actually composed of ternary carbides, i.e. contain two different metallic elements in addition to carbon, present as a reinforcement in a metallic matrix. Ternary carbides constitute better reinforcements providing enhanced mechanical properties in comparison with binary carbides; however, our knowledge of ternary carbides *per se* is still insufficient, and only the properties of the alloys have been characterized. The main reason explaining such a lack of data is the relative small size of these particles, in the micro-range, which complicate the measurement of their mechanical properties.

This thesis aims to contribute towards filling this gap by means of micromechanical methods able to measure locally the main properties of individual microscopic carbide particles. This is now possible thanks to the recent developments of experimental techniques such as nanoindentation and Focused Ion Beam. The challenges of this thesis are then to be able to (i) produce carbides particles embedded in iron with tailored compositions, (ii) test mechanically individual particles and (iii) explain the evolution of the properties with changes in composition, in order to find an optimal composition characterized by enhanced mechanical properties.

The main challenges come from the small dimension of the particles (< 40 μm) and the fact that such particles are embedded in a steel matrix, more compliant than the particles, which can then bias the measurement of elastic properties. Standard nanoindentation techniques cannot measure accurately the mechanical properties of such matrix/particle combinations and new methods have been developed in this thesis in order to overcome this problem.

Carbide particles have been grown in situ by arc-melting cast iron with transition metal high purity chips, in order to properly tune the composition. Three mechanical properties have been measured: elastic modulus, hardness and fracture toughness, by indenting a polished surface, or by bending up to fracture notched micro-cantilever beams. This trio of properties is essential in order to characterize properly a material in view of an application in machining industry.

By using binary carbide compositions as references, we have characterized five ternary carbide systems, namely (Ti,W)C, (Ti,V)C, (Ti,Ta)C, (Ti,Nb)C and (Ta,V)C, as well as the quaternary

(Ti,Ta,V)C system. The ratio of the metallic elements has been varied in order to cover the entire range of compositions. For the ternary systems, we found compositions that exhibited both a higher hardness and modulus than the two corresponding binary carbides, enhancing the properties by ~15-20%. Comparing results of this study with the Valence Electron Concentration (VEC) based theoretical predictions of Jhi et al shows poor agreement, leading to conclude that other parameters than the VEC are equally important in governing the elastic modulus and hardness of carbides explored in this work.

Keywords: Metal Matrix Composites, Carbides, Steel, Elastic modulus, Hardness, Fracture toughness, Micro-mechanical tests, Nanoindentation, Valence Electron Concentration.

CONTENT

LIST OF FIGURES

Chapter 1

Chapter 2

Chapter 3

Chapter 4

Chapter 5

Chapter 6

Chapter 7

Appendix B

Appendix C

Appendix D

LIST OF TABLES

Chapter 1

Chapter 2

Chapter 3

Chapter 4

Chapter 5

Chapter 6

Chapter 7

Appendix A

CHAPTER 1:

INTRODUCTION

1.1 Motivation and background

The micromechanical behavior of two-phase metallic alloys and metal matrix composites (MMC) represents one of the most promising and prolific research field of modern metallurgy. The number of related publications in various scientific journals attests this fact: during the last 20 years, more than 10'000 scientific articles have been published in this specific field[i].

Micromechanics aims to link the global macroscopic mechanical properties of a material, including notably alloys and composites, with its microstructure and the values of local properties of individual phases and interfaces within the material; those are, *in fine*, the main parameters by which one can design the best material for a given application. It is well known that macroscopic properties are governed by the material microstructure: the specific structure at the micro-scale is a key feature in determining properties as different as elastic modulus, hardness, or fracture toughness.

There is a myriad of possible combinations to form metallic-based alloys or composites, and there are no fewer different microstructures. They can however be grouped into two main categories: homogeneous solid solutions and heterogeneous microstructures containing second phases. The latter category encompasses alloys forming intermetallic particles and MMCs, where the second phase consists of a prefabricated phase generally called the reinforcement. The nucleation of fine-scale (submicron) intermetallic precipitates is a well-known hardening mechanism, since the discovery of Alfred Wilm[1], which allows to strongly increase mechanical properties such as hardness or yield strength; Al_2Cu and Mg_2Si precipitates constitute examples of intermetallics formed in aluminium alloys. In steels, the presence of cementite, a metallic carbide with the chemical formula Fe_3C, allows to increase the mechanical properties over those of pure iron. If intermetallics can positively influence the strength, they also often contribute to reduce the ductility and the fracture toughness of the phase in which they are embedded. For other systems,

[i] Source: www.sciencedirect.com; Keywords: micromechanics, metals; Years: 1999-2018; Results: 11'725 (15.11.2017)

intermetallic precipitates can have a global negative effect over the alloy properties; Au_5Al_2 and $AuAl_2$ are intermetallic particles that are formed at the interface when gold is welded to aluminium; these intermetallics make gold mechanically weak (less strong and less ductile), and at the same time also decrease significantly the alloy interfacial electrical conductivity[2].

Despite the importance of understanding the influence of a given reinforcement on the properties of an alloy, very little is actually known about the intrinsic properties of those reinforcements, despite their intensive use in the metallurgical industry; for example, cementite is not very well characterized from the standpoint of its intrinsic mechanical behavior[3]. Local second phase properties matter, however. A previous study led in our laboratory demonstrated that both the shape and the quality of the reinforcement may have a significant impact over mechanical properties of alumina reinforced aluminium composites, such as their ultimate tensile strength (UTS) and fracture toughness[4]. By infiltrating an aluminium matrix with two different alumina reinforcements, namely inexpensive comminuted (angular) or alternatively high-quality vapor-grown (polygonal) particles, an increase of both the UTS and the fracture toughness was found for the alloys containing polygonal alumina particles (Fig. 1.1).

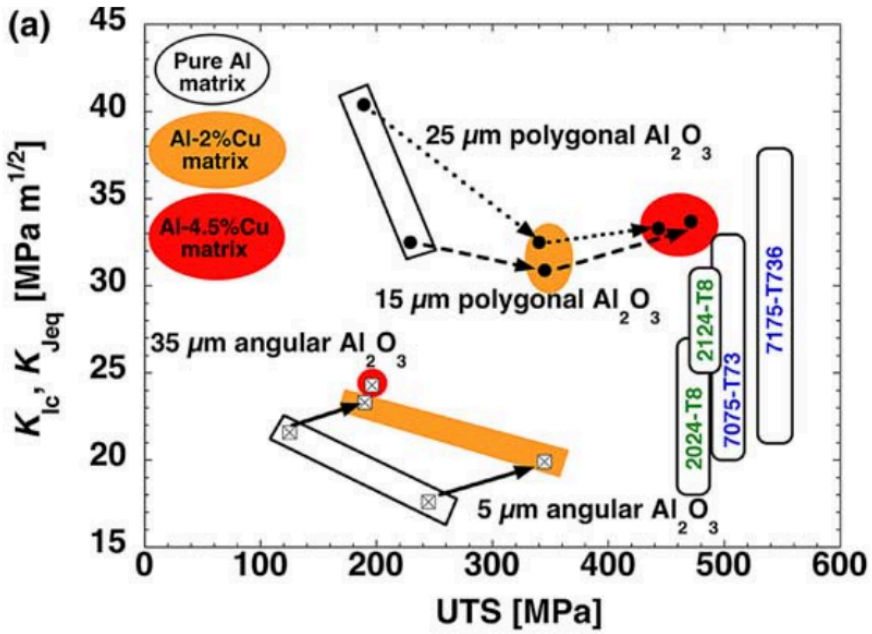

Fig. 1.1 – Tensile strength/toughness for various Al/alumina composites and comparison with common aerospace Al alloys; reproduced from Ref [4].

Among the investigated composites in Fig. 1.1, four parameters were varied: the composition of the aluminium matrix (pure Al, Al-2 wt% Cu and Al-4.5 wt% Cu), together with the alumina particle size, quality and morphology/shape. The comminuted particles contain many cracks, as a consequence of their production method, whereas the vapor-grown particles are much more expensive but of better quality with a cleaner surface and less defects. The two kinds of Al_2O_3 particles are depicted in Fig. 1.2.

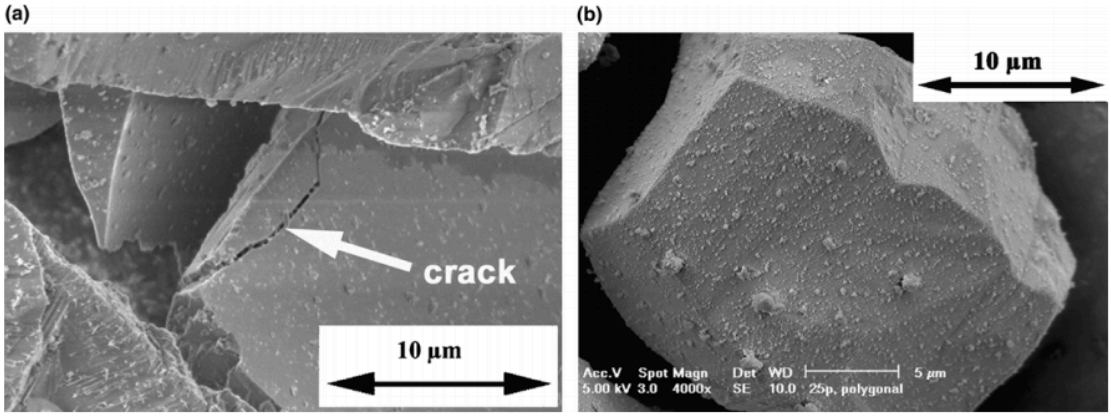

Fig. 1.2 – a) Angular comminuted 35 µm alumina particles; b) vapor-grown polygonal 25 µm alumina particles; reproduced from Ref [4].

If we compare composites according to the quality of their reinforcements, all other things being equal, a better particle quality results in a global increase of the composite material toughness (K_{IC} is almost doubled for a pure Al matrix), while the strength increases as well. If we had to simulate the behaviour of those two composites with a standard micromechanical model, we would be limited by the lack of input parameters characterizing the difference in quality between the two types of particles (instead, when one seeks to access such local phase properties, those are generally back-calculated, using micromechanical models, from the measured composite properties).

A similar situation can happen in alloys containing second phases formed *in situ* instead of prefabricated particles: if it is possible to change those particles with alterations in the material processing parameters, so as to change either their morphology or their composition, would it then be possible to enhance the properties of the alloy? That question is of primary importance, because, in case of a positive answer, this would represent a further step towards the amelioration of metallic alloys. To answer it, we must however no longer consider reinforcements as a second phase, but rather as a bulk material. We have then to determine the relevant properties as a function of the state of the particle, i.e. its morphology, its composition, etc. Second phases are often the first cause of fracture in multiphase metallic materials. Improving the quality of the reinforcement, by reducing for example the proportion or size of internal of interfacial cracks, or by tuning their chemical composition to improve their stiffness or toughness, is an approach that is still seldom used to produce better alloys or MMCs. The main goal of this thesis is to contribute to this approach.

Because of their industrial importance, especially in tool steels and in cermets, we focus our study on MC carbides, where one metallic atom is present for each carbon atom; examples of MC carbides are TiC, VC, TaC, NbC and WC. Regarding the matrix, we embed such carbides particles in steel matrices. This choice is due to the fact that steel constitutes, in terms of mass, by far the most commonly used metal in industry, with more than 1'600 million tons produced in 2015[ii] and, due to the natural presence of carbon in steel, carbides constitute the most common reinforcements. Carbide particles are furthermore also extensively used in cermets, another important family of metal-ceramic composites, where very hard prefabricated ceramic particles are embedded within a hard metallic matrix that serves to bind the particles together and toughen the material. Moreover, carbides are, *per se*, very interesting ceramics, because of their very high mechanical properties, and also because most metals can form a stable chemical compound with carbon. Since most MC carbides share the same NaCl-type crystalline structure (except WC, which exhibits a simple hexagonal structure), they are totally or partially soluble with each other: this

[ii] Source: www.worldsteel.org; 2015: 1'621 millions of tons

interesting feature allows to form ternary, quaternary or higher order reinforcements, by partial substitution of the metallic atoms with another metallic element.

Taking advantage of this feature, this thesis aims at investigating and optimizing mechanical properties of MC carbides by varying their chemical composition, embracing ternary and finally quaternary MC carbides, the carbides being all precipitated and embedded in steel.

1.1.1 MC carbides

Strength and hardness are the most important features explaining why transition metal MC carbides are extensively used in engineering applications. Their very high melting point make them suitable for high-temperature structural applications, since they retain a large part of their strength and hardness while gaining in ductility. Their principal limitation comes from their brittleness at room temperature, this being a consequence of the ease of crack nucleation and propagation within these low-toughness phases. Their toughness depends on the ease of dislocation motion within the carbides, and therefore on factors such as Peierls stress and the rate of diffusion of carbon and metal atoms. Diffusion prevails at high temperatures, whereas the Peierls stress is more important at lower temperatures. Below 800°C, all the transition carbides break in a brittle fashion: the stress required to move dislocations is so high that fracture is promoted. At more elevated temperatures, there is a ductile-brittle transition, which translates a shift in the comparative values of the yield strength σ_y and the fracture strength σ_f as a function of temperature.

A summary of the mechanical properties of dense monocrystalline MC carbides at room temperature is given in Table 1.1 (more details are given about the mechanical properties of carbides in the next chapter). As seen, those vary significantly with composition.

Table 1.1 – Mechanical properties of selected monocrystalline carbides.

	E [GPa]	H [GPa]	K_{IC} [MPa·m$^{0.5}$]
TiC	451[5]	28-35[5]	1.6-3.0[6]
VC	430[7]	27-31[7]	1.3-1.9[8]
TaC	472[9]	17-29[7]	3.6-3.8[10]
NbC	537[5]	18-24[11,12]	7.7[13]
WC	696[5]	21-26[11,14]	7.5-8.9[15]

Carbides, beyond their use as reinforcements in steels and cermets, find nowadays application in several branches of industry.

Hard carbides are suitable for application as a coating: it is of great industrial interest to be able to form a very hard thin film on a given surface, to improve its hardness and wear resistance. Drills or razor blades are a good example, with a core made of a tough and strong material (typically steel), while the cutting properties are restricted to the surface. As toughness and hardness are inverse properties, coating the surface with ultra-hard titanium carbide (or nitride) is an easy and inexpensive solution to overcome the problem. Aside from mechanical properties, coatings can

modify other properties, such as electric and thermal conduction, reflectivity or corrosion resistance. Chemical vapor deposition (CVD), physical vapor deposition (PVD) and thermal spraying are the major processes for coating tool steels with hard carbonitrides.

In the automotive and aerospace industries, various carbides and nitrides are used for structures where high temperatures and/or corrosive environments are involved. Silicon nitride rotors are produced for turbochargers in the automotive industry; aircraft gas turbines operate in an erosive and corrosive environment and are hence protected by a coating of zirconia or a mixture of tungsten, chromium and titanium carbide[16]. Carbon fibers are also in certain applications coated via CVD by silicon or hafnium carbide, to provide protection against oxidation above 500°C[17]. Ball bearings are often coated with TiC or silicon nitride, in order to increase the hardness and provide a smoother surface, and then a lower coefficient of friction[18].

Nowadays, carbides are also used for nuclear applications. Boron carbide is an excellent neutron absorber used to control the neutron flux in nuclear reactors. The ability of refractory carbides to sustain strong thermal shocks also makes them suitable as coating in nuclear fusion devices: as examples, TiC is used on graphite neutron beam armor and B_4C is applied for wall protection.

1.1.2 Tool Steels

Depending on the carbon concentration, as well as on the presence of alloying elements, steels can be grouped into several categories. Main ones are carbon steels, alloy steels, stainless steels and tool steels. Carbon steels contain mainly iron and carbon, with only minor quantities of alloying elements; according to their carbon content, they can be subdivided into low carbon (C wt% < 0.3), medium carbon ($0.3 \leq$ C wt% ≤ 0.6), and high carbon steels (C wt% > 0.6). Alloy steels contain more alloying elements (generally between 4 and 8 wt%), such as Mn, Mo, Ni or Cr that allow an interesting increase of their properties in comparison with carbon steels. Alloying elements can be carbide-forming, as is the case of Mn, Cr, Mo, W, V, Ti and Nb, or not carbide-forming (Si, Al, Cu, Ni, Co). In tool steels, the amount of such carbide-forming elements is increased above 10 wt%, leading to a carbide volume fraction in the range 10-20 vol%, thus making them ideal materials for cutting or drilling tools.

The first alloyed tool steel was produced by Robert Mushet in 1868, by incorporating tungsten (between 4 and 12 wt%) into a high-carbon steel (1.5 – 2.5 wt% of C)[19]. Nowadays, the most common alloying elements for standard tool steels are manganese, chromium, vanadium, tungsten, molybdenum, nickel and titanium.

According to their use, processing and composition, tool steels can be classified in 8 groups as shown in Table 1.2.

Table 1.2 – Classification of tool steels[20].

	Group	Symbol	Main alloying elements (AE)	Carbon and alloying elements content (wt%)
1	Water-hardening tool steels	W	Mn, Si, Mo, V	C: 0.6 - 1.4 AE: 0.25 - 0.50
2	Shock-resisting tool steels	S	Ni, Si, Mo	C: 0.45 - 0.55 AE: 1.5 - 4.5

3	Oil-hardening cold-work tool steels	O	Mn, Cr, W, Si, V	C: 0.9 - 1.2 AE: 1.6 - 2.5
4	Air-hardening, medium-alloy cold-worked tool steels	A	Cr, Mn, Mo, V	C: 0.5 - 2.25 AE: 4.0 - 12.0
5	High-carbon, high-chromium cold-work tool steels	D	Cr, Mn, V	C: 1.5 - 2.35 AE: 12.0 - 17.0
6	Hot-work tool steels	H	Cr, W, Mo	C: 0.35 - 0.5 AE: 6.0 - 24.0
7	Tungsten high-speed tool steels	T	Cr, W, V, Ti, Ta	C: 0.75 - 1.5 AE: 23.0 - 38.0
8	Molybdenum high-speed tool steels	M	Cr, Mo, W, V, Ti	C: 0.8 - 1.3 AE: 14.5 - 27.0

W-grade steels are essentially high carbon steels; they are the most commonly used tool steels because of their low cost. A water quench is needed to achieve a maximum hardness and they cannot be used over 150°C, since they begin to soften above that temperature. Additions of manganese, silicon and molybdenum significantly increase fracture toughness, while vanadium is added to limit grain growth during heat treatment. The shock-resisting group, S-grade tool steels, is characterized by a low carbon content ($0.45 \leq C\ wt\% \leq 0.55$) and a comparatively low amount of alloying elements (< 4.5 wt%) in order to maximize fracture toughness.

O-grade steels are oil quenched and then tempered; they are characterized by a medium amount of carbon ($0.9 \leq C\ wt\% \leq 1.2$) and a low amount of alloying elements (< 2.5 wt%). A-grade steels contain a high chromium content (~5 wt%) and are characterized by a good balance of wear resistance and toughness. D-grade steels contain between 10 and 13 wt% of chromium that forms, in this case, carbides rather than participate to the corrosion protection offered by a surface layer of chromium oxide. H-grade tool steels can contain either chromium (~5 wt%), tungsten (9-18 wt%) or molybdenum (~5 wt%) as their main alloying element. Their carbon content is however low (< 0.5 wt%) in order to avoid the extensive formation of carbides.

T/M-grade steels contain W (14-20 wt%) or Mo (5-10 wt%) with more than 0.75 wt% of carbon, in order to create a higher volume fraction of carbide. The presence of tungsten or molybdenum carbides increases strongly both the hardness and the stiffness of these steels.

Regarding the microstructure of a standard tool steel in the hardened state, it consists of a matrix of martensite containing a dispersion of carbides, or iron and/or alloying elements (Fig. 1.3).

Carbides in steel can form either during hot working, if the alloying elements are strongly carbide-forming, or can precipitate from martensite during tempering. In most tool steels, carbides are formed during solidification if the alloy is initially cast, or sometimes by reaction sintering if the material is produced by powder metallurgy using blended elemental powders. Later on, the morphology and the composition of those precipitates can be modified by hot forming or heat treatment of the alloy. A high carbon content obviously increases the volume fraction of carbides and produces a steel harder and more resistant to wear but of lowered toughness. Depending on the final application, examples being tools for forming, shearing, cutting or molding, the required properties vary and a more specialized tool steel can be produced by tailoring its composition and processing. As an example, a cutting tool requires both high hardness and wear resistance, sometimes at high temperature, whereas toughness is the crucial parameter for shock-resistant tools used in hammers.

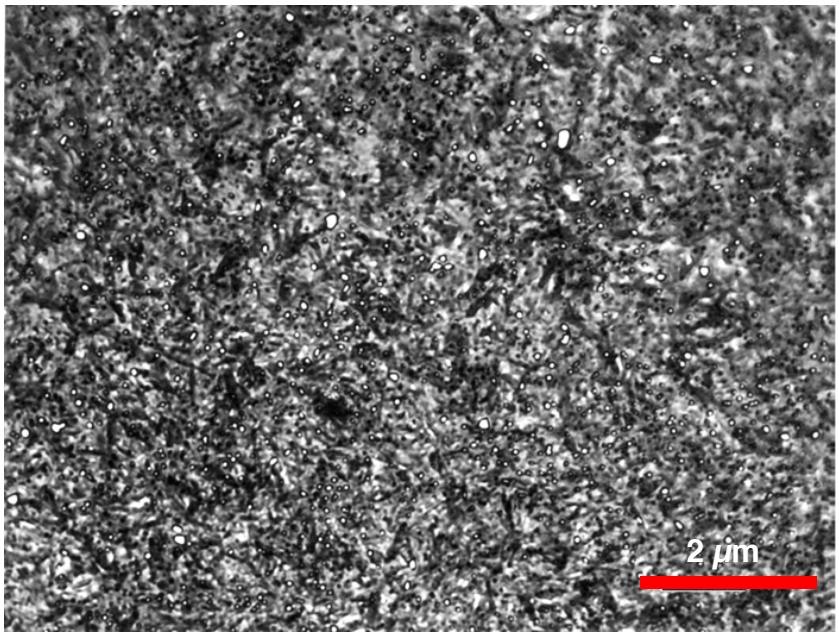

Fig. 1.3 – W-tool steel microstructure (1.05 C wt%), austenized at 800°C and brine quenched. The microstructure is composed of plate martensite with un-dissolved cementite (white particles). Specimen etched with Nital. Figure reproduced from George Vander Voort[iii].

Carbide-forming elements alloyed in steels can result in different kinds of reinforcements, such as MC, M_3C or M_6C carbides, giving rise to a wide range of properties. Typically, MC carbides exhibit the best properties in terms of hardness, while M_3C carbides, such as cementite, are weaker and M_6C carbides show intermediate properties. It is then possible to tune steel properties by combining different types of carbides, the choice depending on the final application. As an example, Fig. 1.4 represents the hardness of some carbides present in tool steels, compared with typical matrices hardness.

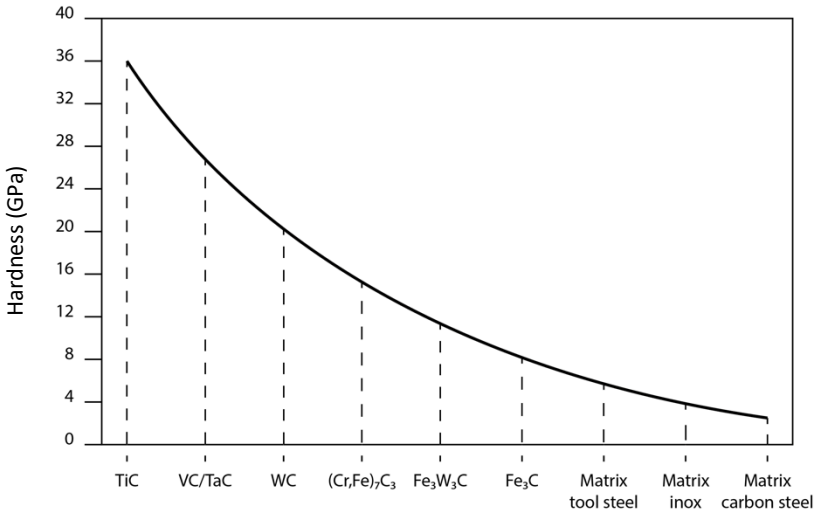

Fig. 1.4 – Hardness of the different carbides types in tool steels, and comparison with matrices hardness; figure reproduced from Ref [21].

[iii] George Vander Voort, Revealing the Microstructure of Tool Steels, March 15, 2012

1.1.3 Cermets

Besides their use as reinforcements in tool steel, carbides are also found in cermets. Cermets can be considered as a category of MMC characterized by a metallic matrix usually of cobalt, molybdenum or nickel, and containing reinforcements made of various carbides, borides and/or oxides. The typical volume fraction of reinforcements ranges from 30 to 90 vol%, and an example of a cermet microstructure is given in Fig. 1. 5.

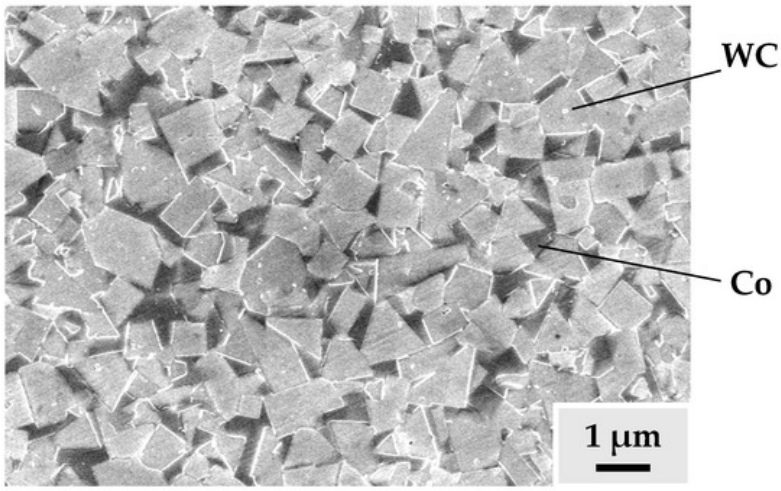

Fig. 1. 5 – WC-Co cermet microstructure (13 Co wt%), The average WC grain size is ~0.45 μm; figure reproduced from Ref [22].

Such phase combinations give rise to materials exhibiting both the extreme strength and hardness typical of ceramics and a toughness that is higher than what is typical for ceramics, nearer that of metals. Cermet properties depend on the properties of the individual phases, the size and the distribution of those phases, and the interfacial energy between the matrix and the carbide particles. The most common cermet is WC-Co, meaning that WC particles are embedded in a cobalt matrix. In terms of cutting performance, the WC-Co cermets are comparable to high-speed T/M tool steels. WC-Co cermets are usually obtained by liquid-phase sintering of a mixed powder of carbide and cobalt. The hardness increases with the amount of WC particles and by decreasing the particle size; the toughness follows the opposite trend. WC-Co can be alloyed with other MC carbides: TiC has the highest hardness among binary MC transition carbides at room temperature and is thus often used in combination with WC, making ternary WC-TiC-Co cermets the most common material for metal cutting purposes nowadays. TiC can also be replaced by TaC, which is harder above 500°C, where high-temperature and thermal shock resistances are requested. Both TiC and TaC improve the wear resistance in cutting applications. Due to the high cost of TaC, it is nowadays often replaced by NbC without changing significantly the cermet properties[23].

When WC is fully replaced by TiC or TiCN, another family of cermets can be developed, characterized by superior wear resistance and cutting performance, but inferior toughness compared with WC-Co cermets. Many efforts have also been devoted to substituting the Co binder, which is expensive, with Ni or an alloy of nickel and chromium; however, because of their

insufficient strength at high temperatures, so far, those substitute metals did not reach industrial application.

Illustrative cermet, tool steel and carbide coating applications are presented in Fig. 1.6:

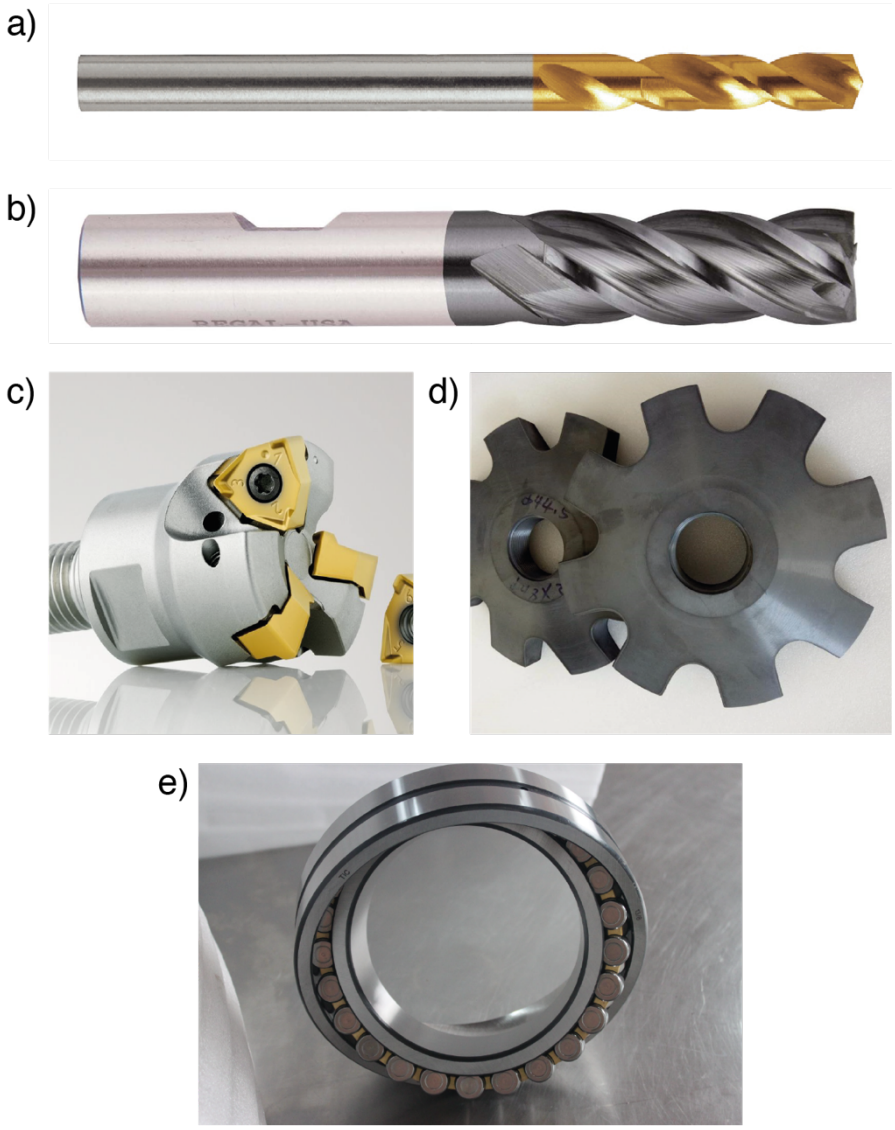

Fig. 1.6 – Practical carbide applications: a) High-speed tool steel drill with a TiCN coating (in gold)[iv]; b) WC-Co cermet end mills[v]; c) Metal cutter for a CNC machine, the three tungsten carbide inserts are coated with TiN (in gold)[vi]; d) Si_3N_4 ceramic rotor[vii]; e) TiC coated ball bearing[viii].

[iv] Image reproduced from: http://www.suttontools.com/products/panel-drills-single-ended-tin-coated-d127/

[v] Image reproduced from: https://www.regalcuttingtools.com/products/end-mills/high-speed-steel-end-mills/four-and-more-flute-hss-end-mills/four-and-more-flut-6

[vi] Image reproduced from: https://www.secotools.com/#article/83057?language=fr

[vii] Image reproduced from: https://www.alibaba.com/product-detail/ceramic-Silicon-Nitride-degassing-rotor-impeller_60682992372.html?spm=a2700.7724857.main07.18.3b5b61c9GJUyPD&s=p

[viii] Image reproduced from: http://www.tic-techs.com/products/

1.2 Problem addressed and objectives of the thesis

We have outlined in what precedes the industrial importance and relatively wide range of carbides used to reinforce engineering structural materials; that constitutes an excellent reason to measure their intrinsic properties and seek ways to improve them.

The binary Fe-C system forms a rather complex system, and the addition of other carbide-forming elements contributes to increase significantly that complexity. The *in situ* formation of MC carbides in a steel matrix constitutes then the first challenge of this thesis, especially for ternary and higher order carbides, where more than one metallic element is present. We must then not only produce the carbide, but also be able to tune its composition. Note that, because of their high thermodynamical stability and their low solubility in liquid iron, the modification of the microstructure by thermal treatment, following carbide formation, can be very complicated and can require very high temperatures. Moreover, some elements, e.g. Fe or impurities present in Fe, tend to diffuse within most of the carbide to form a higher order carbide, contributing generally to reduce their mechanical properties.

The second challenge this thesis faces is related to the measurement of local mechanical properties of small MC carbide particles. In fact, the small size of such particles (2-40 μm) limits the possibilities available to test them mechanically, requiring high precision in the positioning and the measurement procedures. Thanks to the evolution of measurement techniques at the micro-scale, based on nanoindentation, it is nowadays possible to test very small volumes of material. Moreover, by coupling nanoindentation with focused ion beam technology (FIB), it is now possible to machine very small specimens and thus scale down, to the micron-scale, tests traditionally performed on a much larger scale. Furthermore, other phenomena can influence the sample response such as electrostatic forces or surface adhesion, both of which gain importance over gravity as the scale of objects decreases. Precision also becomes a more difficult issue, regarding the milling and the loading part: the sample cannot be seen by naked eyes, therefore electronical or optical microscopes are required to shape and characterize the structures tested. Microscale testing thus constitutes a second interesting challenge this thesis aims to tackle.

Finally, *in situ* grown carbides are characterized by an irregular shape, most often that of dendrites or variously shaped, often angular, particles, depending on the composition, the processing and the heat treatment cycle of the steel sample. This irregular morphology constitutes the third difficulty of the thesis. An easy solution for getting around the problem consists in testing mirror-polished particles still embedded in the matrix. This solution however adds an indirect complication: because the steel matrix is much more compliant than the carbide particle, indenting the particle inevitably leads to a non-negligible deformation of the surrounding matrix. We could assimilate this situation to an equivalent system formed by two springs in series, with the first one, stiffer, simulating the particle, and the second spring representing the matrix. When the system is loaded, the more compliant spring is necessarily deformed, such that the particle stiffness is always underestimated. This extra-compliance furthermore varies, being dependent on particle shape and the applied load and cannot be ignored for all the measurements involving elastic properties. A new measurement method was therefore developed in order to measure the elastic modulus of these tiny and irregular carbide particles. In order to measure hardness and fracture toughness, on the other hand, we used already developed methodologies, by adapting them to our particles.

Data interpretation is finally based on atomic bonding considerations, namely of density of metal-carbon or metal-metal bonds and density of occupied states (DOS), based on contributions in the literature. This approach allows us to understand some of the measured trends in the evolution of elastic modulus or hardness as a function of composition for ternary and higher order systems.

The objectives of the thesis can be subdivided into three distinct parts:

1. Development of a processing route able to generate ternary and quaternary carbides embedded in steel and characterized by tailored composition, homogeneity and proper size;
2. Development of micromechanical testing methodologies by which the elastic modulus, the hardness and the fracture toughness of hard carbides reinforcing iron alloys can be directly measured;
3. Determination of optimal compositions and interpretation of the measured properties including atomic bonding considerations.

After this first introductive chapter, a literature review is presented in Chapter 2. The thermodynamics of carbide formation in liquid iron are firstly presented, followed by a brief review of binary carbide properties, with a focus on the five that we investigated in this work: TiC, WC, VC, TaC and NbC. We then present the state of the art regarding ternary carbide systems, with an emphasis on the change in mechanical properties along with the composition. In a second part, we expose the bases of contact mechanics, as well as the bases of nanoindentation. We describe the different methods developed to measure elastic modulus, hardness and fracture toughness. Finally, we present several pertinent micro-mechanical tests that have been developed to measure the fracture toughness at the microscale.

Chapter 3 describes the processing of binary, ternary and quaternary carbides in steel. Details on the method used to create the various sample are presented, as well as all the obtained microstructures, with the identification of the different phases.

Chapter 4 presents the methods and results for the hardness measurements. At the end of the chapter, the method accuracy is discussed, followed by an interpretation of the hardness evolution for ternary and quaternary compositions.

Chapter 5 and Chapter 6 have a similar structure but are dedicated respectively to elastic modulus and fracture toughness measurements.

Finally, a conclusion is the subject of Chapter 7.

1.3 Thesis framework and funding

This thesis was part of the ERC Advanced Grant Agreement N° 291085 awarded to Prof. Andreas Mortensen, director of the Laboratory of Mechanical Metallurgy (LMM), at EPFL, under the European Union's Seventh Framework Programme. This ERC project was carried out between May 2012 and April 2017; funding for the continuation work on this thesis past April 2017 was provided by basic laboratory funds from EPFL. Global objectives of the ERC project were to develop micromechanical tests and use them to determine the mechanical properties of hard second phases in alloys and MMC. Three PhD theses were produced within this project:

1. A thesis focused on silicon in Al-Si alloys, by M.G. Mueller;
2. A thesis on alumina reinforcements in MMC, by V. Pejchal;
3. The present thesis, focused on carbides in steel.

Three post-doctoral researchers who contributed full-time to the project helped me significantly in my work: Dr. G. Zagar with testing and simulation, Dr. M. Fornabaio with specimen processing and analyses and Dr. L. Deillon with thermodynamics. Other members of the LMM have also variously contributed to the project: R. Charvet and C. Dénéreaz for many technical aspects of my work; A. Rossoll and A. Singh (who also worked full-time on the ERC project) as scientific collaborators at the beginning of the ERC project.

CHAPTER 2:

LITERATURE REVIEW

The purpose of this chapter is to lay the groundwork for understanding and interpreting the results and their discussion, exposed in subsequent chapters, and also to present the state of the art in relevant scientific topics related to this thesis.

We start with an overview of MC carbides generally, including their thermodynamics, their crystal structure and their chemical bonding; we focus afterwards on the mechanical properties of the five binary MC carbides explored here, namely TiC, VC, TaC, NbC and WC.

In a second section of this survey, we discuss ternary carbides, addressing relevant phase diagrams, their general properties, and the known causes of the variation of mechanical properties – typically hardness – with composition.

The third part of this chapter is dedicated to mechanical testing at a small scale. We start by summarizing the basis of contact mechanics and we continue with a review of the different nanoindentation techniques that have been developed to measure the elastic modulus, the hardness and the toughness of materials at the microscale, from the Oliver and Pharr method to more recent techniques. Finally, we discuss different micromechanical tests, in particular the chevron-notched cantilever beam method, that have been developed to measure specific mechanical properties in samples a few micrometers wide.

2.1 Thermodynamics of the Fe-C system

Since steel constitutes the matrix in which *in situ* created carbides of this work are embedded, we review now briefly the Fe-C system, by focusing on its liquid phase, where carbides formation takes place.

By definition, steel is a binary alloy of iron and carbon, whose composition lies between 0.02 and 2.00 wt% (in practice 1.5% is seldom exceeded) carbon (Fig. 2.1). The presence of carbon atoms, which are significantly smaller than the iron atoms and therefore occupy interstitial sites in the Fe

crystal lattice, is the first reason for the rise of mechanical properties of steel in comparison with pure iron: carbon in solid solution interacts strongly with dislocations. One part of the carbon forms a compound with iron: a M_3C carbide called "cementite" generally forms, whereas the other part remains within the iron lattice by filling the octahedral interstices, thus distorting the crystalline lattice. Below 0.02 wt% of carbon, cementite does not form, while when the limit of 2.00 wt% is reached, the solidification process passes through a eutectic transformation and a more brittle alloy is formed directly from the liquid phase: this is (by definition) cast iron, containing either the more stable form of carbon, namely graphite (grey cast iron) or cementite (white cast iron).

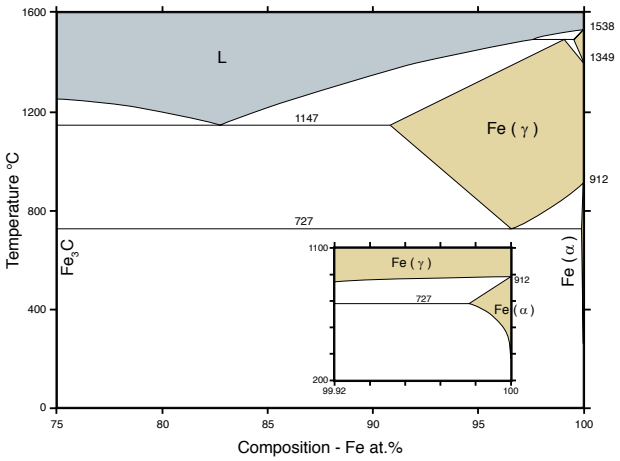

Fig. 2.1 – C-Fe partial phase diagram; insert: Fe(α) single-phase domain near the eutectoid temperature.

Reactions that lead to the formation of stable MC carbides are governed by the behavior of the carbon atoms. As they are significantly smaller than those of iron and most of the alloying atoms (except boron), their diffusion is then faster, also in the liquid phase. Chipman[24] wrote in 1972 a review of the complex thermodynamics that govern phase transformations in the Fe-C system: the behavior of the carbon atoms within the different phases appears to be a key parameter in explaining the reactions that take place during cooling, especially carbide formation. The chemical potential, or the activity, of the alloying elements govern their solubility in iron and the driving force for the formation of carbides.

The chemical potential μ, defined as the rate of change of the free energy for a thermodynamic system with respect to the change in the number of atoms of the species, is often quantified using the chemical activity a_i, which expresses the difference between the chemical potential of a species in the considered (real) state (μ_i) and that in a standard state, of chemical potential (μ_i^θ) for the same species:

$$\mu_i = \mu_i^\theta + RT \ln a_i \qquad \text{Eq. 2.1}$$

where R is the gas constant and T the absolute temperature. When the activity is equal to unity, the element is in its standard state, and $\mu_i = \mu_i^\theta$. In a thermodynamic solution, the activity measures the effective concentration of a species in a mixture, assumed to be equal to unity for pure substances as these are generally chosen as the relevant standard state. The carbon activity,

measured relative to graphitic carbon as the standard state (i.e. $a_c = 1$ at saturation), in the austenite and in the liquid phase has been calculated by Ban-ya et al.[25] (Fig. 2.2).

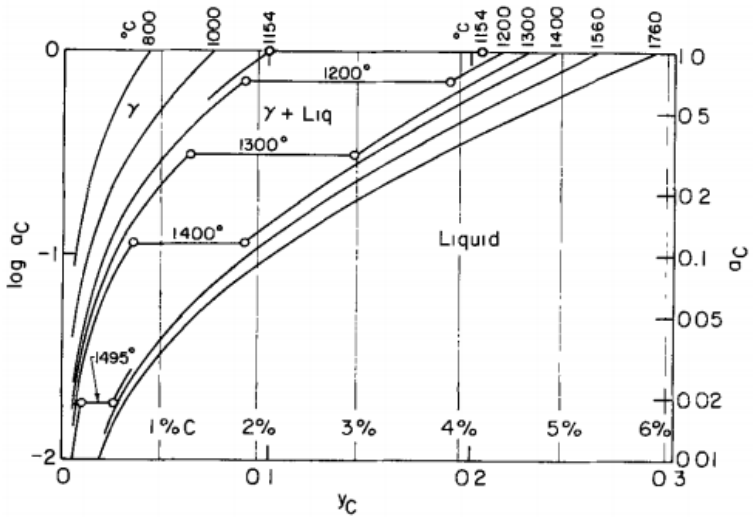

Fig. 2.2 – Activity of carbon in austenite and liquid iron; reproduced from Ref [24]; y_C is the atomic ratio n_C/n_{Fe}.

We may observe that the carbon concentration at which the carbon activity is equal to unity in liquid iron (at which, in other words, phase separation between the liquid and graphite begins) increases with increasing temperature[26-30](Fig 2.3). Temperatures involved in the processing of steels, on the order of 2500°C, are higher than the melting point of iron (1538°C). At these temperatures, the activity of carbon in usual alloys is generally well below unity.

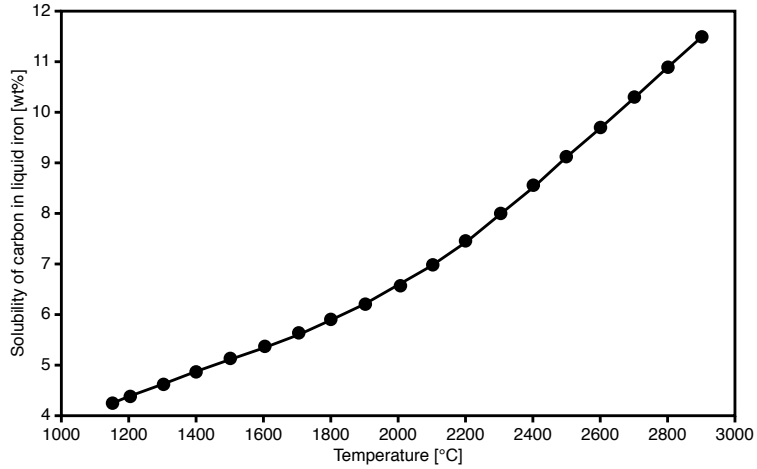

Fig. 2.3 – Solubility of carbon in iron, curve reconstructed from data in Refs [26, 27, 28, 29 and 30].

This rise in solubility is a definite advantage for the design of steel alloys because more dissolved carbon is then available for carbide formation if processing starts at elevated temperatures, well above the melting point of iron.

Cementite, Fe_3C, is the most frequent natural iron carbide, but it is metastable with respect to graphite at all temperatures[31]. The simplest chemical reaction for its formation is:

$3\,Fe(\gamma) + C\ (graph) \rightarrow Fe_3C$. Scheil[32] and Smith[33] have measured separately the standard free energy associated with that reaction (Fig. 2.4).

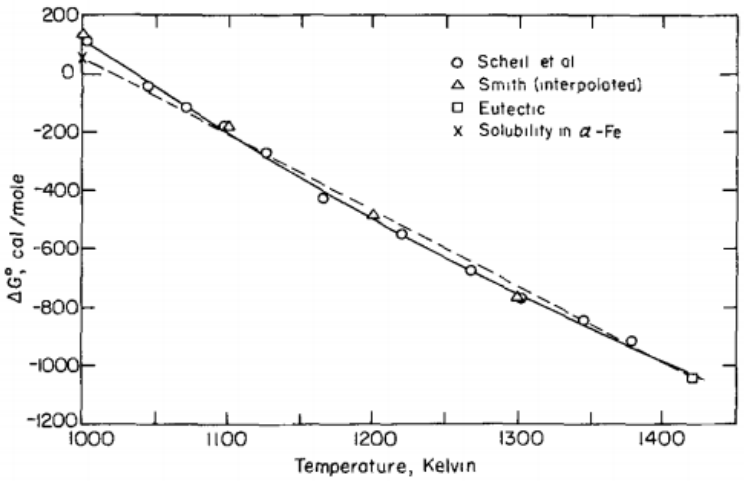

Fig. 2.4 – Gibbs free energy associated with the formation of cementite[32,33] ; figure reproduced from Ref [24].

The driving force for the reaction increases with temperature, as outlined in Fig. 2.4 by the decrease in Gibbs free energy $\Delta G°$. The absolute value of the energy associated with the formation of cementite remains, however, small in comparison with the energies involved in the formation of other transition metal carbides.

The reaction synthesis of carbides in liquid iron is governed by the solubility of carbon and that of foreign metallic atoms in the melt, by interface kinetics, as well as by nucleation and growth processes[34]. Nucleation occurs when a critical supersaturation is reached, which depends on carbide and liquid composition, carbon and metals activities, temperature and interfacial energies.

The starting melt is generally considered to be a homogeneous solution of iron and other metals atoms. Where carbide nuclei form and grow, two diffusion fluxes, of carbon and metal, control the growth process if interface kinetics are sufficiently rapid. The diffusion coefficients of carbon, D_C^l, and of the metal, D_M^l, in liquid iron therefore influence the final microstructure. Resulting microstructures of a slowly cooled steel containing carbide-forming elements consists in a dispersion of carbides, the shape of which is often dendritic and can be faceted or rounded, within a matrix of steel, the structure of which can, in turn, itself be quite complex.

2.2 Binary MC carbides

Carbides constitute a category of ceramics that has been extensively investigated because they combine several attractive properties. Carbides are indeed among the best materials in terms of elevated hardness and elastic modulus. From the perspective of electrical properties, most carbides are conductive ceramics and superconductors; on top of that, their crystal structure – particularly that of MC carbides – is simple, which makes them attractive materials in attempting to understand the relationship between properties and microstructure. Among the many possible carbides, MC

compositions exhibit the highest hardness and stiffness values, are thermodynamically stable at room temperature and exist over a wide range of compositions, since many metal atoms can be substituted for others in such crystals, with the implication that MC carbides can be ternary or quaternary alloy phases, of composition $(M_xM'_yM''_{(1-x-y)})C$. A large number of investigations have been carried out during the second half of the 20th century on those materials, generally based on thermodynamics considerations, or on mechanical tests at the macroscale.

Given the rapid current pace of evolution of numerical simulation methods, a new trend in carbide research consists in simulating their properties, using DFT-based methods. While "classical" binary carbides are still often investigated, in ternary or higher order systems, a new category of complex carbides, called Nowotny carbides, has emerged to offer new research opportunities. Within Nowotny compounds, the metallic atoms are no longer arranged in a compact crystal lattice, but occupy the vertices of an octahedron, whose center is occupied by an atom of carbon. Nowotny carbides have the general chemical formulation $(M'_xM''_y)C$[35,36]. This includes carbides with the formula $M'_3M''_2C$, in which octahedrons are linked by their vertices (e.g. Nb_3Al_2C, V_3Ga_2C, Mo_3Al_2C, etc.). Nowotny carbides can also adopt a perovskite structure $M'_3M''C$ where the octahedra form a simple cubic structure (e.g. Sc_3AlC, Fe_3InC, Pt_3HgC, etc.). Carbides of formula $M'_2M''C$ are structured in such a way that the octahedra share an edge (Cr_2AlC, Mo_2BC, Hf_2SnC, etc.); finally, if the octahedra share a complete face, they have the formula $M'_3M''_3C$ (W_3Co_3C) or $M'_4M''_2C$ (W_4Co_2C). The large number of Nowotny carbides – more than 600 different compositions have already been identified – exhibit different properties: few can be classified as refractory and fewer are characterized by mechanical properties similar to those of MC carbides. Many exhibit very interesting and promising electronical properties but are mechanically weak and totally unsuitable for any structural application. This thesis therefore focuses on more traditional carbides, having a MC composition and a much simpler crystal structure.

We will first discuss the thermodynamics of phase in which the particles are formed, and then will focus on MC carbides, from near 0K temperatures – at which they are considered in DFT simulations – to finite and high temperature, where their formation takes place. We will then give an overview of the crystal structures encountered in the most common carbides, with a focus on the B1-NaCl structure and the simple hexagonal structure of WC, as these constitute the structures of the five binary carbides we study here. Finally, we will discuss atomic orbital-based considerations for structures where the carbide contains a transition metal, as bonding then involves a complex d-orbital hybridization. Linked with symmetry of the cubic MC crystal structure, those considerations constitute the basis for the interpretation of the measured mechanical properties using results of DFT simulation.

2.2.1 Thermodynamics of MC carbide formation

The properties of carbides give hints about their thermodynamical characteristics. Their frequently extreme melting points, for example, reaching up to almost 4000°C for TaC and HfC, are indications of very strong chemical bonding between atoms, and also of a high chemical stability.

Almost all metals of the Periodic Table can form a stable chemical binary compound with carbon (Fig. 2.5).

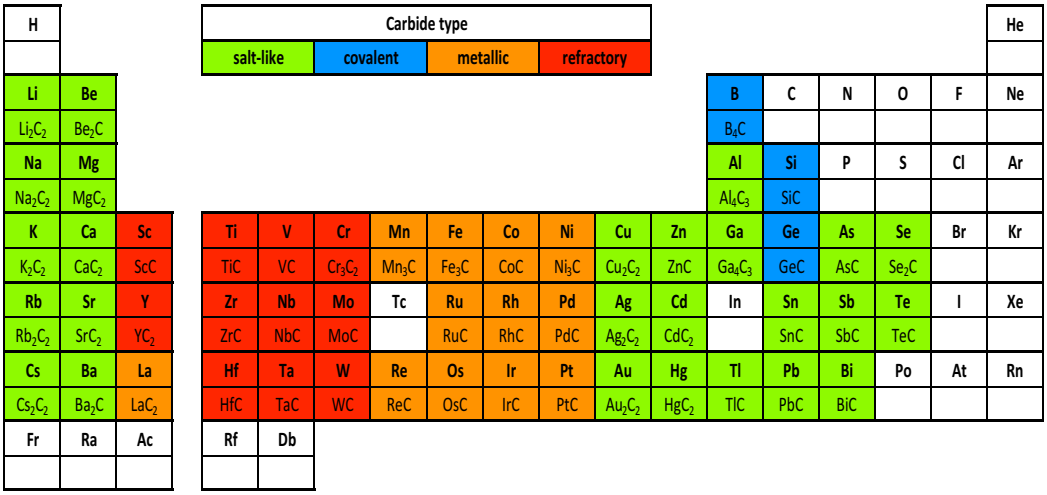

Fig. 2.5 – Overview of binary carbides.

Among this multitude of carbides, we can distinguish four categories:

1. Covalent carbides
2. Salt-like carbides
3. Interstitial carbides
4. Intermediate carbides

Covalent carbides are formed when the difference in electronegativity $\Delta\chi$ between carbon and metal is small: the nature of their chemical bond is therefore mostly covalent; these carbides show excellent mechanical properties. Only three binary covalent carbides exist: SiC, B_4C and GeC. When $\Delta\chi$ is large, salt-like carbides are formed: these are ionic species that can be hydrolyzed, making them unsuitable for nearly any structural application, since in contact with water they produce either methane, or acetylene. Calcium carbide is a typical example, which was in fact used as a source of acetylene for underground applications.

Interstitial and intermediate carbides are formed with the elements of the first eight groups of the d-block of the Periodic Table; these are often named metallic carbides. $\Delta\chi$ values are intermediate in comparison with values for covalent or salt-like carbides, resulting in a mixed covalent-polar bond. Depending on the atomic size ratio, these carbides can be classified as interstitial or intermediate.

Intermediate carbides, such as Fe_3C and chromium carbides, have lower mechanical properties in comparison with interstitial or covalent carbides. Nevertheless, they are important in the steel industry.

The formation of a stable carbide depends mainly on $\Delta\chi$, on the ratio of the atomic radii and on the nature of the chemical bond that holds the atoms together. Carbon is an electronegative atom, with χ = 2.55, which is higher than for all carbide-forming metallic elements (Appendix A). The second factor controlling the formation of carbides is the ratio of the atomic radii (Table 2.1). With some approximations, we can consider a sp^3 hybridization or CN = 6 for p- and d- blocks

respectively, in order to describe the electron position, giving rise to the values of atomic radii reported in Table 2.1.

Table 2.1 – Ratio of atomic radii (p-block: sp^3; d-block: CN=6)[7].

	Atomic radius [pm]	r_C/r [-]	
C	78.0		
Si	117.0	0.666	covalent
Cr	126.7	0.615	intermediate
Fe	126.0	0.619	intermediate
Ti	146.7	0.531	interstitial
V	133.8	0.582	interstitial
W	139.4	0.559	interstitial
Ta	146.2	0.534	Interstitial
Nb	145.1	0.538	interstitial

The last parameter we have to take into consideration in order to explain the formation and structure of carbides is the nature of the bond between the carbon and metal atoms, which obviously depends on the two first parameters. Generally, the bond involves a complex combination of ionic, covalent and metallic bonding. The covalent bond is the principal type; the ionic part of the bond is due to the electronegativity difference and tends to make the bond asymmetric; the metallic contribution is a direct consequence of the crystalline arrangement of the metallic atoms in the carbide.

Regarding these three parameters, thermodynamics give us a powerful tool to understand the formation of carbides, as well as their evolution in a given environment, and have been widely studied during the last 50 years[37,38,39,40,41,42,43].

We can write a general carbide formation reaction as:

$$\frac{x}{y}M + C \leftrightarrow \frac{1}{y}M_xC_y$$

Eq. 2.2

where M and C represent respectively the metal and carbon, and x and y are the stoichiometric parameters. This reaction is associated with a change in Gibbs free energy ΔG_T°:

$$\Delta G_T^\circ = \Delta H_T^\circ - T\Delta S_T^\circ$$

Eq. 2.3

The enthalpy variation ΔH_T° is associated with the change in bond energy, as new chemical bonds are created during the reaction. The entropy variation ΔS_T° measures the increase of the system disorder. At constant pressure, both enthalpy and entropy are functions of the heat capacity c_p:

$$\Delta G_T^\circ = \left(\Delta H_{298}^\circ + \int_{298}^{T} c_p(T)dT \right) - T\left(\Delta S_{298}^\circ + \int_{298}^{T} \frac{c_p(T)}{T} dT \right)$$

Eq. 2.4

where ΔH_{298}° and ΔS_{298}° are respectively the change of enthalpy and the change of entropy at room temperature. The heat capacity is a parameter easily accessible to measurement and has been used extensively to calculate the free energy of many chemical reactions. Formation reactions of the most important carbides, with their associated free energies, are given in Appendix A and are summarized in Fig. 2.6 in the form of an Ellingham-type diagram.

The energies associated with the formation of interstitial cubic carbides, i.e. TiC, VC, TaC and NbC, are higher in absolute value than the energies required for the formation of intermediate or covalent carbides (SiC, Cr_xC, Fe_3C, etc.). At elevated temperatures, the M_2C carbides are however always more stable than their MC counterpart.

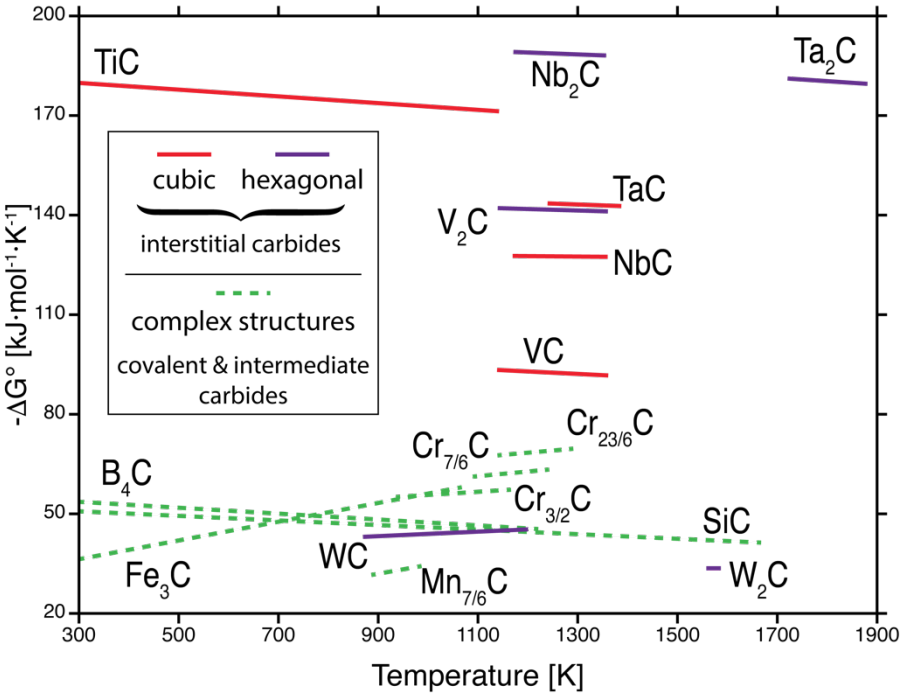

Fig. 2.6 – Ellingham representation of the change in Gibbs free energy associated with carbide formation; figure drawn from data in Ref [44].

A deeper thermodynamic analysis requires knowledge of the heat capacity at low temperatures, the changes in enthalpy ΔH_{298}° and entropy ΔS_{298}° at ambient temperatures, as well as the temperature dependence of $c_p(T)$.

Values of c_p close to 0K are necessary to interpret calculated electronic structures as well as the atomic bonding of materials. The heat capacity of an ideal material can be divided into two parts at very low temperatures: an electronic and a vibrational contribution (Einstein-Debye model).

$$c_p = c_{el} + c_{latt} = \frac{\pi^2 N k^2}{2E_F} T + \frac{12\pi^4 N k}{5T_D^3} T^3 = \gamma T + \alpha T^3$$

Eq. 2.5

where c_{el} is the electronic contribution to the heat capacity and c_{latt} the vibrational specific heat. The electronic term is directly proportional to the temperature T, while the lattice term is proportional to T^3. Both proportionality coefficients, γ and α, can be expressed as functions of the number of atoms N, Fermi energy E_F, Debye temperature T_D and Boltzmann constant k. Real materials deviate from the Einstein-Debye model and their heat capacity is better represented by a higher-order polynomial. Most of the carbides are furthermore superconductors, with a relatively high critical temperature T_c; it is then more difficult to obtain reliable data at 0K, because of the ensuing discontinuity of c_p at T_c. Pessal et al.[45] proposed an extrapolation procedure widely used to determine γ, α and β (Appendix A):

$$c_p(T) = \gamma T + \alpha T^3 + \beta T^5$$

Eq. 2.6

The triplet (γ, α, β) is calculated from a set of three equations:

$$\begin{aligned} c_p(T_n)_{measured} &= \gamma T_n + \alpha T_n^3 + \beta T_n^5 \\ \left(\frac{dc_p(T_n)}{dT}\right)_{measured} &= \gamma + 3\alpha T_n^2 + 5\beta T_n^4 \\ \left(\int_0^{T_n} \frac{c_p}{T} dT\right)_{measured} &= \gamma T_n + \frac{1}{3}\alpha T_n^3 + \frac{1}{5}\beta T_n^5 \end{aligned}$$

Eq. 2.7

where T_n is a temperature above T_c. The Debye temperature T_D, defined as the temperature at which the highest vibrational frequency mode is excited, is also directly proportional to the average sound velocity and thus depends on elastic constants. Toth et al.[46] measured the evolution of T_D for TaC and NbC as a function of the carbon/metal atomic ratio and found a rise for rich carbon compositions (Fig. 2.7). That increase is correlated with the increment in bond strength between metal and carbon atoms, which stiffens the lattice, decreasing the atomic vibration and then raising T_D.

The next important thermodynamic parameters are the changes in enthalpy and entropy from 0K to room temperature. These are given in Eq. 2.8. Storms[40] deduced the variation of enthalpy and entropy from 0K up to room temperature (Appendix A) by integration of the heat capacity:

$$H^{\circ}_{298} = H^{\circ}_{0K} + \int_0^{298} c_p dT \Rightarrow \Delta H^{\circ}_{298} = \int_0^{298} c_p dT$$
$$S^{\circ}_{298} = S^{\circ}_{0K} + \int_0^{298} \frac{c_p}{T} dT \Rightarrow \Delta S^{\circ}_{298} = \int_0^{298} \frac{c_p}{T} dT$$

Eq. 2.8

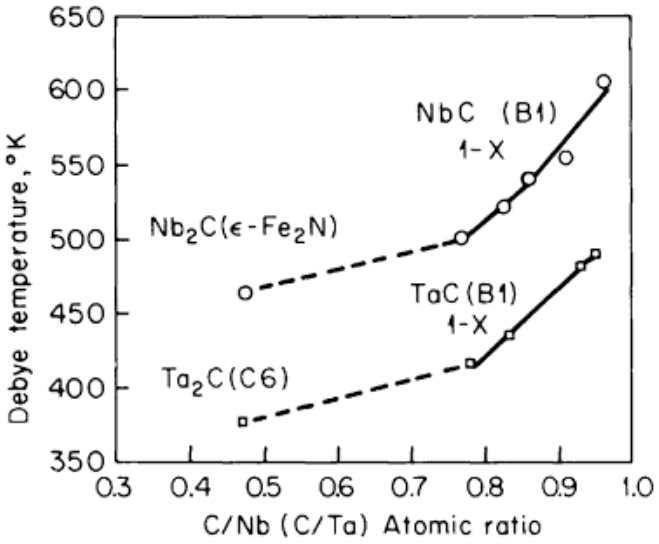

Fig. 2.7 – Evolution of T_D with C/M ratio for Nb and Ta carbides; reproduced from Ref [46].

Storms also evaluated the standard heat of formation corresponding to Eq. 2.2 at 298K (Table 2.2) and observed a decrease in $-\Delta H^{\circ}_f$ with the group number, as well as a strong C/M ratio dependence (Fig. 2.8). The compound's band structure is involved in the interpretation of ΔH°_f variations with the increase of the group number, as antibonding levels are filled for higher groups[47]. For that reason, Group IV carbides have stronger bonds and exhibit very interesting properties; however, only TiC has important industrial applications, because zirconium and especially hafnium are far more expensive metals.

High temperature thermodynamic data pertinent to carbide formation have been compiled by many authors (Storms[40], Kelley[42], Chang[39], Barin[48], etc.). These are provided in Appendix A for the five investigated binary systems.

Table 2.2 – Standard heat of formation at 298K[40].

	$-\Delta H_f^\circ$ [kJ·mol^{-1}]	Group
TiC	185.22	
ZrC	197.40	IV
HfC	210.33	
VC	102.90	
NbC	141.12	V
TaC	143.22	
WC	40.61	VI

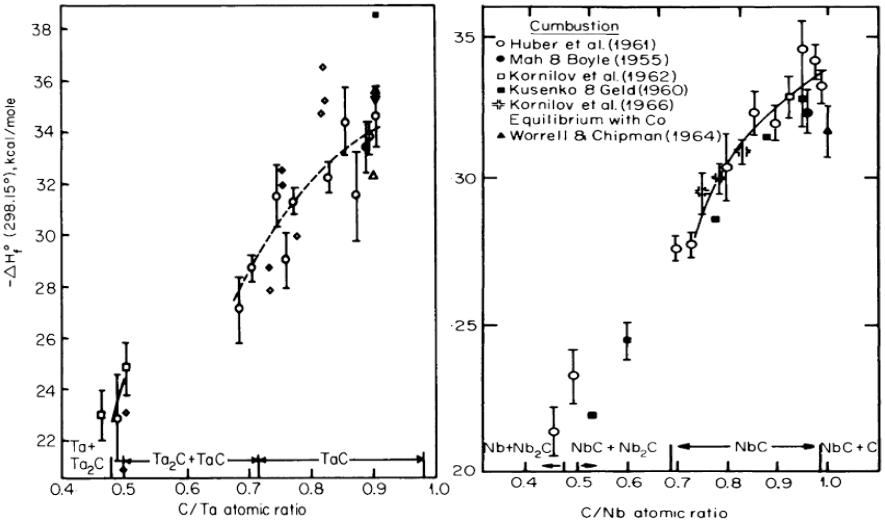

Fig. 2.8 – Variation of $-\Delta H_f^\circ$ with the C/M ratio in the C-Ta (left) and C-Nb (right) systems; reproduced from Ref [40].

2.2.2 Crystal structure

The theoretical structure of crystals is strongly linked to thermodynamic data, as both are governed by the physics of bonding, the atoms seeking to be packed such as to minimize the global energy of the structure. In the case of metal carbides, the crystal structure can evolve from a fcc structure (TiC) to a much more complex icosahedron-based structure (B_4C). The crystal structure of carbides depends strongly on the parameters discussed in the previous section: the atomic radius, the electronegativity and the nature of the chemical bonds.

Although carbon atoms are small, tetrahedral sites are not large enough to accommodate them, and only the octahedral sites in the fcc and hcp structures, or the trigonal prisms in the hexagonal simple lattice, can contain an atom of carbon. If all the octahedral sites are occupied, we have the B1 NaCl-type structure; apart from WC, which exhibits a simple hexagonal structure (Fig. 2.9), all

the MC interstitial carbides adopt a B1 structure. With half of the octahedral sites occupied in a hcp structure, the L_3' structure is formed, which is often observed in M_2C carbides (Fig. 2.10).

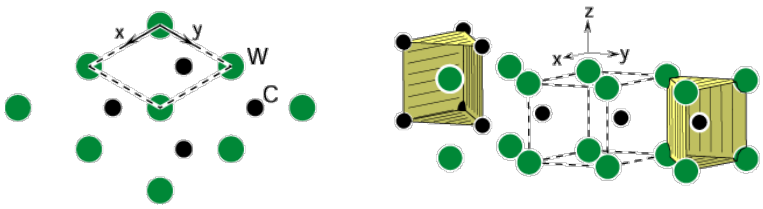

Fig. 2.9 – Crystal structure of WC (hexagonal simple)[ix].

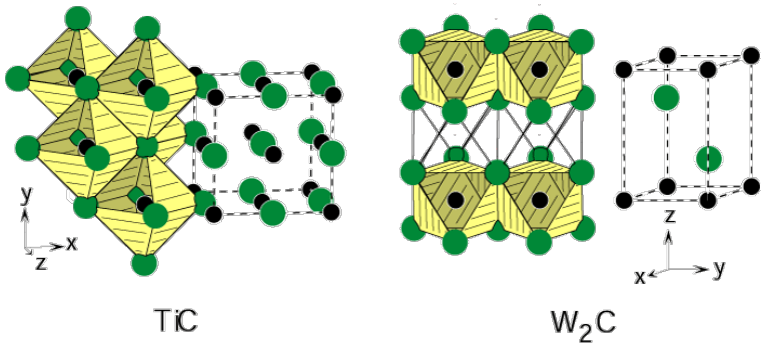

Fig. 2.10 – Crystal structure of TiC (B1) and W_2C (L_3')[x].

Hägg[49] published an empirical rule to predict the structure of metallic carbides: if $r_C/r_M < 0.59$, the interstitial spaces are large enough to accommodate the carbon atoms and the structure is then simple. Otherwise, the distortion of the lattice becomes too large and the strength of the metallic bond cannot ensure the cohesion of the crystal: a more complex, less compact, structure is then formed. By analyzing Hägg's rule, we find that $r < 0.59$ for all the transition elements of the fourth first columns of the d-block, except Cr. Their structure follows the rule, and they exhibit either the B1, or the L_3' structure.

Because $r_C/r_{Cr} = 0.615 > 0.59$, chromium carbides have a different and more complex crystal structure, as well as a different stoichiometry: Cr_3C_2, Cr_7C_3 and $Cr_{23}C_6$ (Fig. 2.11).

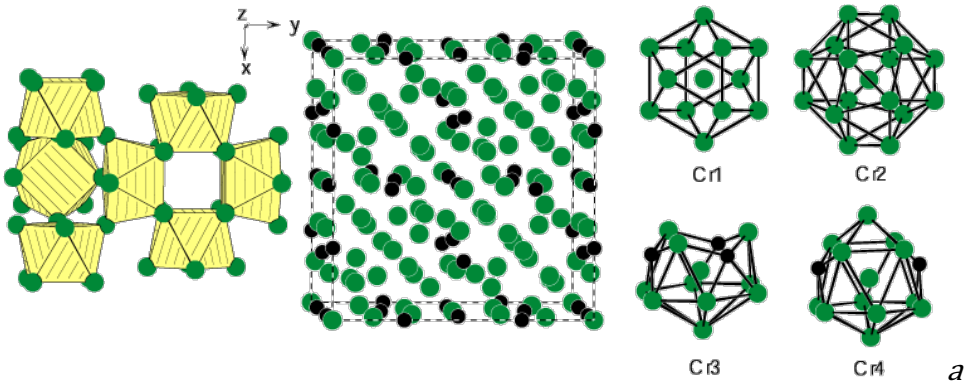

[ix] Reproduced from www.hardmaterials.de/html/_crystal_structures.html

[x] Reproduced from www.hardmaterials.de/html/_crystal_structures.html

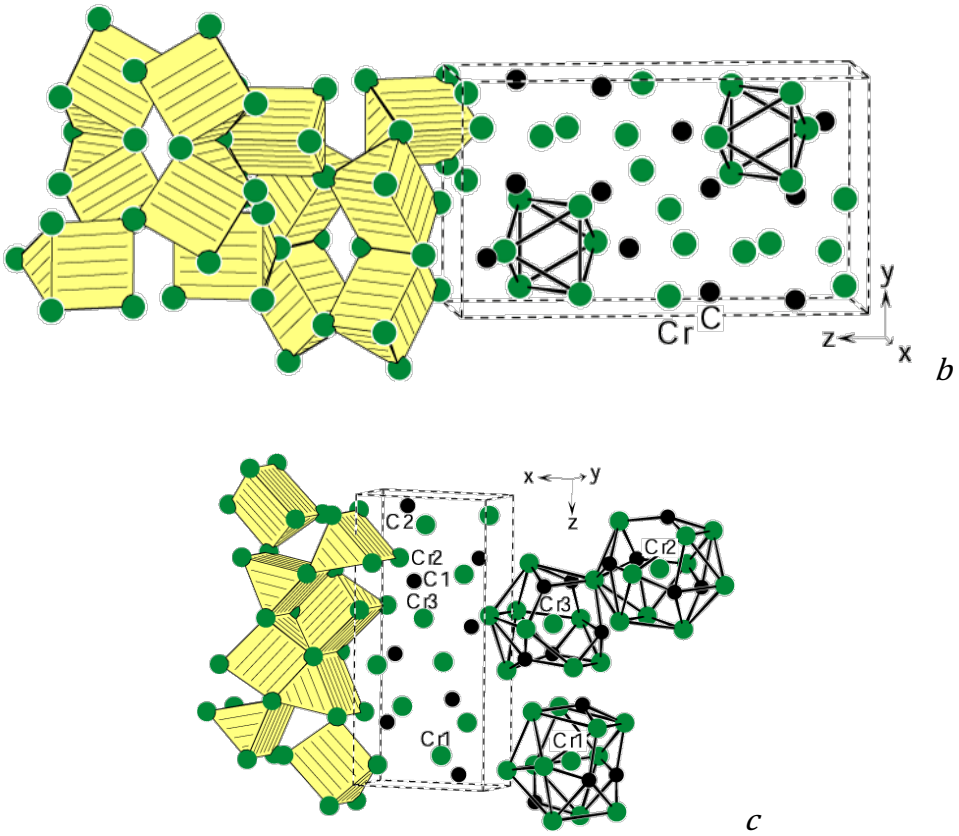

Fig. 2.11 – Crystal structure of a) $Cr_{23}C_6$; b) Cr_7C_3; c) Cr_3C_2[xi].

2.2.3 Atomic bonding

As outlined in the previous sections, bonding in interstitial carbides involves contributions of covalent, metallic and ionic bonds to the cohesive energy; the covalent and metallic parts constitute the most important contribution, the ionic part of the bond having limited effects on bond strength. Some properties of the carbides, such as their good electrical conductivity, suggest that there is also a strong influence of the metallic crystal lattice, because values of those properties suggest the presence of a large number of free electrons. This is characteristic of the metallic bond, where the electrons are delocalized within a lattice of arranged metallic ions.

Conversely, some properties, such as the lack of plasticity and ensuing brittleness of carbides, are mostly governed by the covalent nature of the bonds, as this prevents the formation of dislocations, and in turn of slip-driven plastic deformation. Rundle[50] first observed that most of the interstitial carbides have a B1 structure, with carbon occupying the octahedral interstices of the lattice, thus increasing the distances between two metallic atoms and suggesting that M-C bonds are more important than M-M bonds. Ern and Switendick[51] proposed a more elaborate model that predicts electron transfer from the d-band of the metal to the p-band of the carbon.

The carbon atom counts 6 electrons, with an electronic configurations $1s^2 2s^2 2p^2$. The transition elements are characterized by a partially empty d-orbital. The electronic structure of groups IV, V and VI are:

[xi] Reproduced from www.hardmaterials.de/html/_crystal_structures.html

Ti: [Ar] $4s^2 3d^2$	V: [Ar] $4s^2 3d^3$	Cr: [Ar] $4s^1 3d^5$
Zr: [Kr] $5s^2 4d^2$	Nb: [Kr] $5s^1 4d^2$	Mo: [Kr] $5s^1 4d^5$
Hf: [Xe] $6s^2 5d^2$	Ta: [Xe] $6s^2 5d^3$	W: [Xe] $6s^2 5d^4$

The electronic structures of Cr, Nb and Mo show anomalies with respect to the Aufbau principle, which dictates the order of filling, because the highest s-orbital is only half-full, whereas the d-orbital counts an extra electron. The explanation of these anomalies is given by pairing energies: there is a cost in energy to pair electrons in the lower s-orbital, because of electronic repulsion. Depending on the energy difference between the s and the d-orbital, it could be more stable to place one of the two electrons in the d-orbital than to keep the pair in the s-orbital.

Since d-orbitals are associated with the orbital quantum number $L = 2$, there are five possible values for the magnetic quantum number m_L, giving rise to as many sub-orbitals. The shape of these sub-orbitals in the ground state is more complex than for lower orbital quantum numbers; in particular, these sub-orbitals are multi-directional (Fig. 2.12). Each sub-orbital exhibits two nodal planes (there is only one for p sub-orbitals and zero for s-orbitals). Four of the five sub-orbitals consist of 4 coplanar lobes, intersected by two perpendicular nodal planes. These orbitals are geometrically equivalent. The fifth sub-orbital is mathematically equivalent to the others, despite its different electron distribution; that shape is a normalized linear combination of the $d_{z^2-y^2}$ and the $d_{z^2-x^2}$ functions. As more shells are filled, the size of the orbital increases, but the shape of the sub-orbitals remains identical.

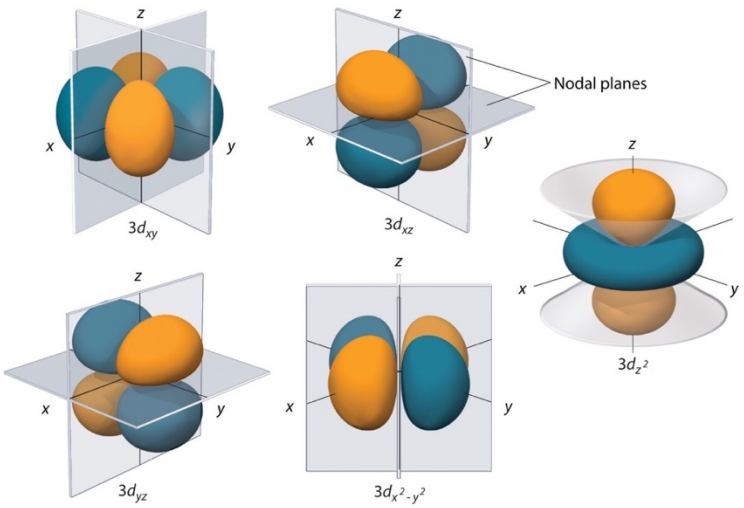

Fig. 2.12 – Shape of the five d sub-orbitals[xii].

Each sub-orbital exhibits two nodal planes (there is only one nodal plane for p sub-orbitals and none for s-orbitals). Four of the five sub-orbitals consist of 4 coplanar lobes, intersected by two mutually perpendicular nodal planes. These orbitals are geometrically equivalent. The fifth sub-orbital is mathematically equivalent to the others, despite its different electron distribution; the

[xii] Reproduced from www.chem.libretexts.org

shape of which is governed by a normalized linear combination of the $d_{z^2-y^2}$ and the $d_{z^2-x^2}$ functions. As more shells are filled, the size of the orbital increases, but the shape of the sub-orbitals remains identical.

As is the case for s and p orbitals, d-orbitals can hybridize. Combining two d-electrons with three p-electrons and one s-electron a set of six equivalent sp^3d^2 hybrid orbitals is obtained (Fig. 2.13). These hybrids are oriented along the three principal directions and form therefore an octahedron, which is indeed the most commonly observed elementary structure among the interstitial MC carbides.

Since the bond between the carbon atom and the metallic atom is mainly covalent and polar, two theories can be taken into consideration to model the bond: crystal field theory (CFT), to describe the ionic contribution of the bond, and molecular orbital theory (MOT), which provides a covalent bonding model.

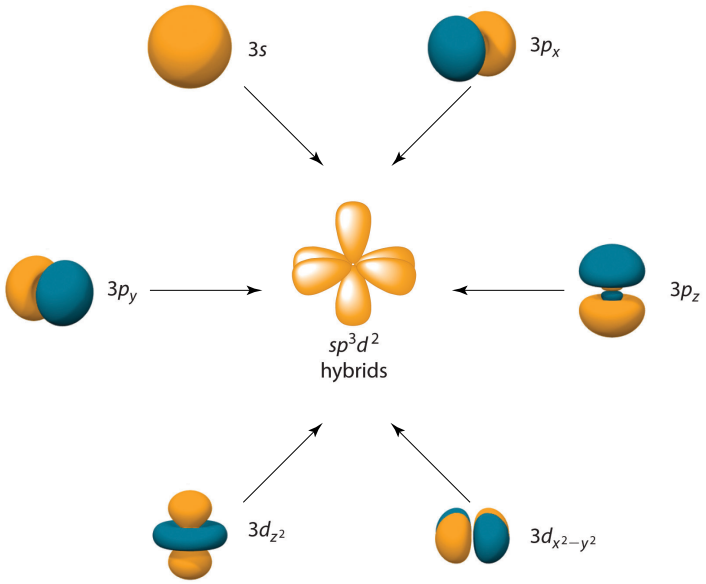

Fig. 2.13 – sp^3d^2 hybridization[xiii].

CFT represents metallic atoms as a central positive charge surrounded by negative point charges representing carbon atoms. Since the attraction between two opposite charges corresponds to a purely ionic bond, in this theory the strength of a bond derives from electrostatic forces and, in the ground state, all five d sub-orbitals of the cation are degenerated. In the presence of an electric field, created by six negative charges forming an octahedron around the cation, the electrons of the metal atom interact repulsively, and their energy rises. Because the $d_{x^2-y^2}$ and d_{z^2} sub-orbitals point directly to the anions, whereas the three other sub-orbitals point at 45° to the anions, their energy levels are split (Fig. 2.14). $d_{x^2-y^2}$ and d_{z^2} are called e_g orbitals, and d_{xy}, d_{xz} and d_{yz} t_{2g} orbitals. The energy gap between the two, Δ_o, is called the crystal field splitting parameter (CFSP).

[xiii] Reproduced from www.chem.libretexts.org

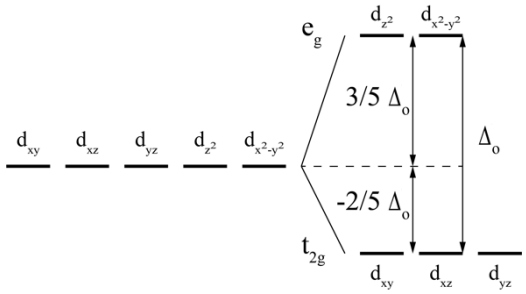

Fig. 2.14 – Octahedral crystal field splitting, with Δ_o splitting parameter; reproduced from Ref [52].

Once the structure of the crystal is known, one must determine which sub-orbital will be occupied by the electrons. For an octahedral configuration, e_g energy is higher than t_{2g}. Depending on the number of d-electrons and on the difference between the pairing energy, E_P, and the CFSP, they can occupy a low-spin, or a high-spin configuration.

For 1, 2 or 3 electrons, the only possibilities are the t_{2g} sub-orbitals, and there is no high-spin configuration; for 8, 9 or 10 electrons, the only possibilities left are the e_g half-empty sub-orbitals and there is no low-spin configuration. For 4, 5, 6 or 7 electrons, both high- and low-spin configurations are possible: if it costs less energy to pair two electrons in the same sub-orbital than to promote one of the two to a higher-energy sub-orbital, the configuration will be low-spin; if not, we have a high-spin configuration.

The five binary carbides that we have investigated, TiC, WC, VC, TaC and NbC, count between 4 and 6 valence electrons, and can then occupy either a low-spin or a high-spin configuration. As we will discuss later, this possibility is one of the reasons explaining the variation of properties with the carbide composition.

Alternatively, the covalent-polar bond can be treated as being purely covalent: we consider now the bond between the carbon atom and the metallic atom as a dative covalent bond, i.e. the metallic atom in a sp^3d^2 hybridization donates one electron to each of the six carbon atoms. The total number of sub-orbitals involved in an octahedral configuration is then fifteen: 9 coming from the metal outer-shell (1s + 3p + 5d), and 6 coming from the six carbon atoms. Twelve of those form the covalent bonds and are split in 6 bonding and 6 antibonding states; the remaining 3 sub-orbitals, corresponding to the t_{2g} group, are non-bonding (Fig. 2.15).

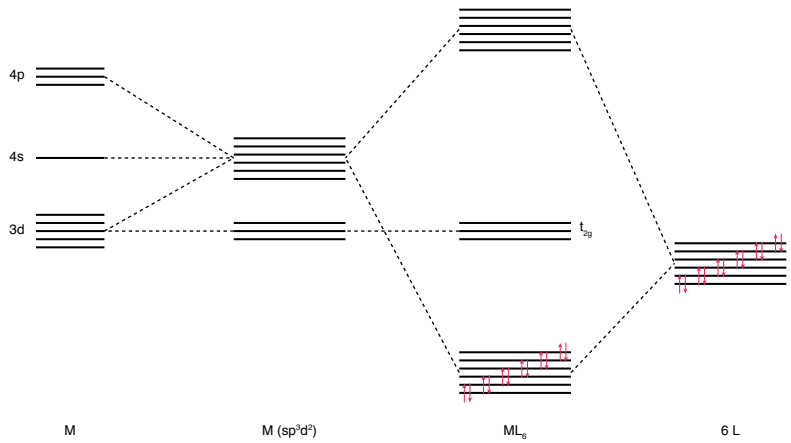

Fig. 2.15 – Covalent dative bonding in an octahedral configuration in the ground state; the six covalent bonds are represented by the magenta arrows, each pair being one bond.

More precisely, we must consider each of the available metal valence sub-orbitals and determine what combinations of the carbon sub-orbitals can overlap with them; overlapping of orbitals is a requirement to form a bond. The s-orbital, given its spherical symmetry, overlaps with all the six carbon sub-orbitals to give a bonding configuration called a_{1g}. The situation for the three p sub-orbitals is more complex, as they are asymmetric: each sub-orbital p_x, p_y and p_z overlaps with a carbon sub-orbital situated in their respective direction, forming three bonding configurations called t_{1u}. For the d sub-orbitals, we need to consider separately the e_g and t_{2g} group. The two e_g sub-orbitals overlap with the carbon, while they are pointing directly at the six anions. For the three t_{2g} sub-orbitals, it is impossible to find a bonding combination: the net result is always a zero overlap, which is why they are considered as non-bonding. For each bonding situation, an antibonding counterpart exists, which is formed by reversing the signs of the ligand orbitals. That situation is represented in Fig. 2.16.

There is a correlation between both theories: the three t_{2g} non-bonding sub-orbitals and the two low-energy anti-bonding e_g set are identical for the two theories; crystal field theory does not consider the a_{1g} and t_{1u} groups. The energy that separates the t_{2g} non-bonding set from the e_g bonding set in molecular orbital theory is equivalent to Δ_o in the CFT. For a strong M-C bond, the energies of the bonding levels tend to decrease, while the energies of the anti-bonding counterparts increase, leading to a large energy difference between the highest anti-bonding level and the lowest bonding level; since the energy of the non-bonding level remains constant, Δ_o increases with the strength of the bond. In contrast, weaker bonding results in closer bands, and *in fine* a smaller gap between the t_{2g} and e_g sets together with a smaller Δ_o.

Δ_o constitutes therefore a very useful measurable parameter. It depends strongly on the period of the metal: when the size of the orbitals increases with the first quantum number n, the splitting parameter increases by a factor comprised between 1.2 and 1.5 for each new shell[52].

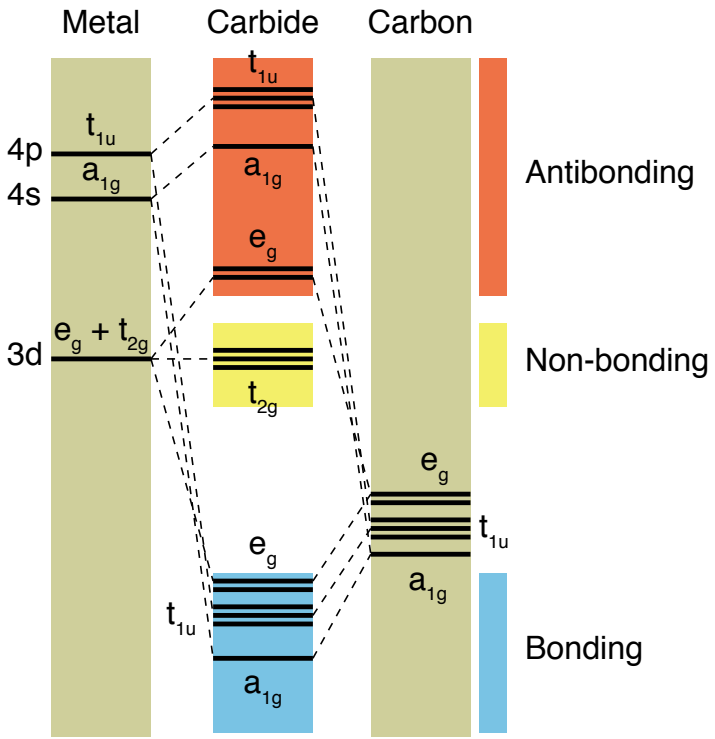

Fig. 2.16 – Complex bonding in an octahedral configuration.

Electronic considerations have been used by several scientists to explain the elastic properties of carbides. Kang[53] studied the YC, ZrC, NbC and RhC 5th-shell carbides via electronic band structure calculations. Density of states (DOS) theory confirmed the presence of both covalent M-C and metallic M-M bonds. The number of valence electrons induces changes in the bonding structure and influences therefore the elastic properties of the carbides. Values of bulk modulus and lattice parameter of the 5th-shell transition metal carbides have been measured by Korir[54] and are given in Table 2.3. The bulk modulus increases and goes through a maximum for NbC: as the interatomic distances become shorter, the modulus first increases due to a stronger covalent bond. The modulus then decreases when antibonding states are filled. Kang calculated the DOS for these four carbides (Fig. 2.17).

Table 2.3 – Bulk modulus and lattice parameter of the 5th-shell transition metal carbides[54].

	d^k	B [GPa]	a_0 [Å]
YC	d^1	124.3	5.09
ZrC	d^2	220.1	4.71
NbC	d^3	300.2	4.49
RhC	d^6	280.6	4.36

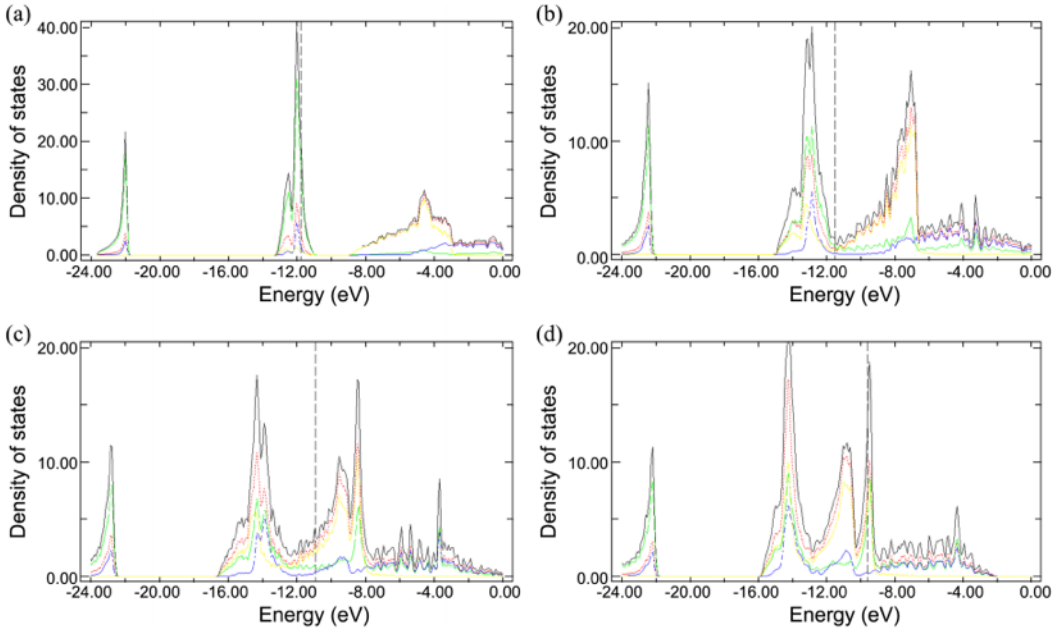

Fig. 2.17 – DOS of 5th-shell transition carbides; a) YC; b) ZrC; c) NbC; d) RhC – total DOS (black line) – metal (red line) – carbon (green line) – e_g (blue line) – t_{2g} (yellow line) – Fermi level (dashed line); reproduced from Ref [53].

The four DOS show similarities: the density is never zero at the Fermi level, confirming the metallic character of the carbides. The states are grouped into three well separated regions: a lower valence band (LVB), an upper valence band (UVB) and a conduction band. The LVB is dominated by the C-2s orbitals; the partially filled UVB is composed of C-2p and M-4d orbitals: the peaks

correspond to the M-C bonding states and their anti-bonding equivalent, above the Fermi level, form the conduction band. The strong overlap between C-2p and M-4d orbitals confirm the strong covalent character of the bond. When moving along the period from YC to NbC, the number of valence electrons increases and the 4d orbitals are shifted toward lower energies: the overlap with C-2p is better and bonding becomes stronger, explaining the rise in bulk modulus. The e_g bonding states are progressively filled until the set is full; when more electrons are added, they must occupy a non-bonding t_{2g} sub-orbital. When replacing Nb with Rh, the extra electrons occupy the Rh-4d-C-2p anti-bonding states, decreasing the total overlap and then reducing the bulk modulus as the number of bonds decreases.

Atomic considerations have also been used to describe the very high hardness of binary carbides. For ceramics, the Peierls stress required to move dislocations is high; the stresses leading to plastic deformation are then directly related to the shear modulus G, and then to the c_{44} elastic constant for a cubic material. Jhi et al.[55] investigated the modifications of the band structure of TiC when a shear strain is applied to the crystal (Fig 2.18). Important changes occur for states derived from C-2p orbitals and e_g d-orbitals: the energy of the fourth band, which is directly related to directional σ M-C bonds between those two sets of orbitals, increases near the *K*-point of the first Brillouin zone, suggesting that electrons occupying that band have a stronger resistance to shear. The first Brillouin zone is a primitive cell in reciprocal space; for a fcc lattice, the primitive cell is represented by a truncated octahedron, with the *K*-point corresponding to the middle of an edge joining two hexagonal faces (Fig. 2.19). At the opposite, the fifth band, composed of directional M-M π bonds, is equally affected by shear strain, but its energy decreases with increasing shear. The second and third bands, which involve t_{2g} π p-d bonds, are quite insensitive to shear strain, except near the Γ-point, corresponding to the centre of the Brillouin zone, where their energy decreases with increasing shear.

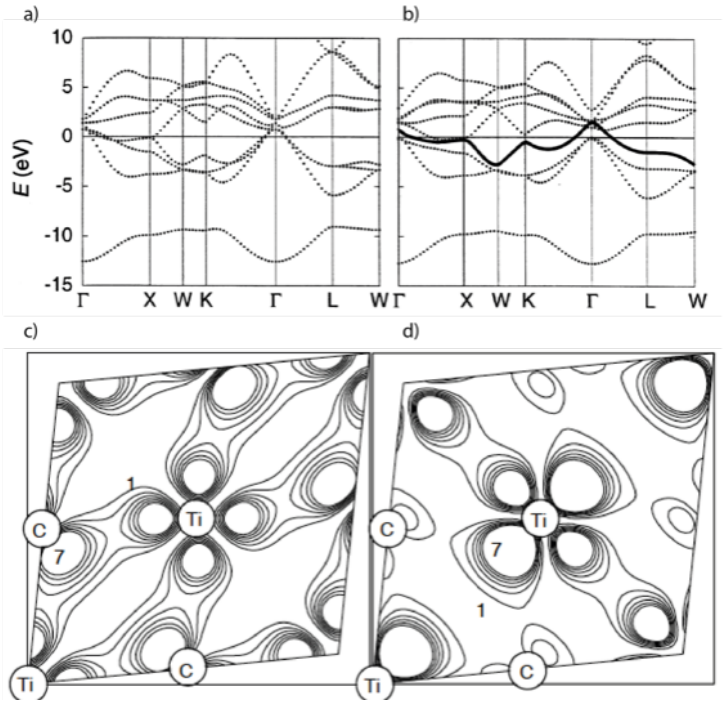

Fig. 2.18 – a) band structure of TiC; b) band structure of TiC under shear strain (ε_{xy} = 0.1), with the fourth band highlighted (in bold); c) charge density of TiC near the K-point of the Brillouin zone, under shear strain, fourth band on the (001) plane; d) as in (c) but for the fifth band; reproduced from Ref [55].

As highlighted in Fig. 2.18 c,d, electrons of the fourth band give a positive contribution to the shear modulus, as shear tends to elongate M-C bonds; fifth-band electrons, on the contrary, give a negative contribution, as shear tends to shorten M-M bonds. As M-C bonds prevail in MC carbides, they are extremely resistant to shear and also to plastic deformation.

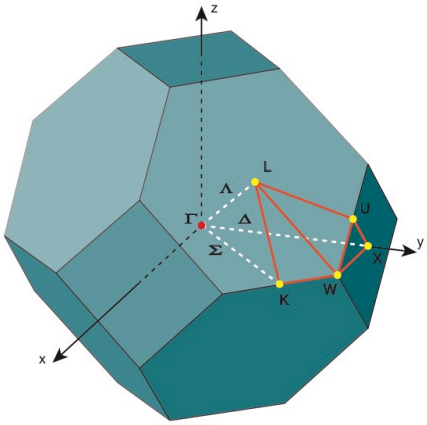

Fig. 2.19 – First Brillouin zone of the fcc lattice in reciprocal space. *Γ*, *K*, *L*, *U*, *W* and *X* correspond to high-symmetry points; Λ, Δ and Σ to high-symmetry lines.

Besides hardness and bulk modulus, other properties can be at least partially explained based on electronic arguments. The very high melting point is due to the large splitting of bonding and antibonding bands around the Fermi level and is coherent with the high strength of carbides. The decrease in thermodynamic stability coincides with the filling of antibonding states. The brittleness at room temperature can be linked with the presence of highly directional covalent M-M and M-C bonds. Finally, the crystal structure, first explained from atomic size considerations, is coherent with sp^3d^2 hybridizations.

2.2.4 Mechanical properties of MC carbides

Carbides are known to have a high elastic modulus, their Young's modulus being generally above 400 GPa. The elastic behavior of carbides is strongly influenced by temperature, porosity, and composition. The C/M ratio is an important parameter, since binary MC carbides can exist over a given range of composition.

The temperature dependence has been experimentally established to follow the empirical relationship[56]:

$$E(T) = E_0 - BT\,exp(-T_0/T)$$

Eq. 2.9

with E_0 the modulus at room temperature and B and T_0 empirical constants depending on the material. Variations of E with porosity P, which is often present in bulk carbides, have been

investigated by Speck and Miccioli[57], who proposed a linear empirical relationship, as a function of the modulus at full density $E_{P=0}$ and a material dependent constant k:

$$E(P) = E_{P=0}(1 - k \cdot P)$$

Eq. 2.10

Other correlations exist for this function, however. Most of the time, elastic constants values reported in literature show large variations, which come from the presence of uncharacterized porosity within the sample, anisotropy, or carbon-to-metal atomic ratio. Table 2.4 illustrates the variation of reported values for Young's modulus E for some selected carbides, according to a commonly used source of materials information: www.matweb.com.

Table 2.4 – Range of elastic modulus measured vales for selected carbides.

	E [GPa]
TiC	448-451
VC	268-430
NbC	330-537
TaC	241-720
WC	669-696

More recently, calculations have been performed based on atomistic simulations such as density functional theory (DFT), that allows, by determining the electronic structure of a compound in variously deformed states, to calculate its elastic constants. The method used to calculate the elastic constants and the interatomic potentials can still lead to large differences; for example, a compilation of values from different publications gives a range of 401-466 GPa[58,59] for the elastic modulus of TiC.

Carbides exhibit a surprisingly high ductility at elevated temperature, at which they are able to plastically deform. The slip systems consist, as is usual, of close-packed planes and close-packed directions. For cubic carbides, the closest-packed planes are $\{111\}$ and the closest-packed directions are $\langle 1\bar{1}0 \rangle$[60]. This slip system corresponds to that commonly found in fcc metals, coherently with the fact that the atoms of carbon are small and located in interstitial sites. Ductility is made possible because carbides deforming along $\{111\}\langle 1\bar{1}0 \rangle$ have five independent slip systems[61].

The critical resolved shear stress necessary to cause slip has been studied for binary carbides as a function of temperature, and for TiC as a function of composition as well (Fig. 2.20 & Fig. 2.21). The rise in critical shear stress with respect to the C/Ti atomic ratio is in agreement with the increase in the number of Ti-C bonds and the corresponding decrease in vacancy concentration, since the critical shear stress is directly related to the number of bonds that must be broken in order to move a dislocation.

The brittleness of carbides at room temperature is a consequence of the ease of crack nucleation and propagation, which depends on the ease of dislocation motion, and therefore on factors controlling it such as the Peierls stress and the rate of diffusion of carbon and metal atoms.

Diffusion prevails at high temperature, whereas the Peierls stress is more important at lower temperatures. For TiC, it has been calculated that diffusion phenomena take over above 1150°C[60].

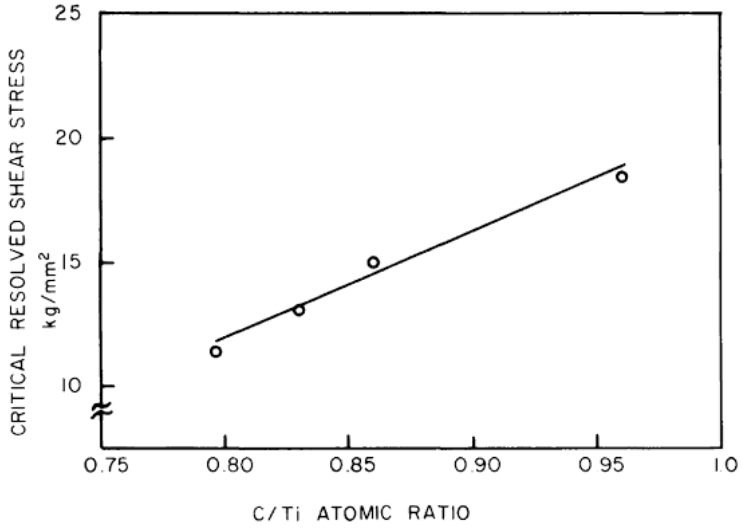

Fig. 2.20 – Effect of composition on the critical shear stress in TiC; reproduced from Ref [62].

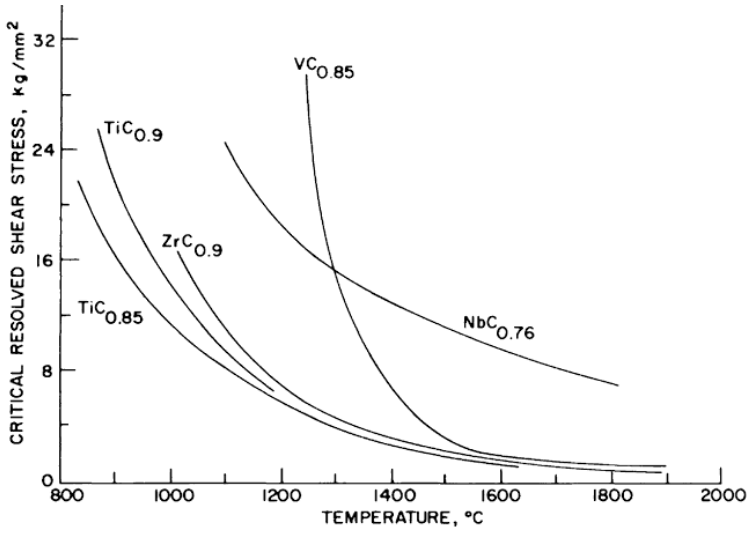

Fig. 2.21 – Effect of temperature on the critical shear stress in various carbides; reproduced from Refs [63,64].

The fracture strength is also strongly dependent on the C/M ratio, as the number of bonds that must be broken during fracture increases with the carbon content.

Carbides are extremely hard materials: their hardness depends on temperature, C/M atomic ratio and porosity. The hardness behavior as a function of the C/M ratio is erratic and varies from one carbide to another one (Fig. 2.22). For instance, the hardness of TiC_{1-x} increases sharply with increasing C/M ratio, whereas the hardness of TaC_{1-x} reaches a maximum at a point situated out of stoichiometry[65,66].

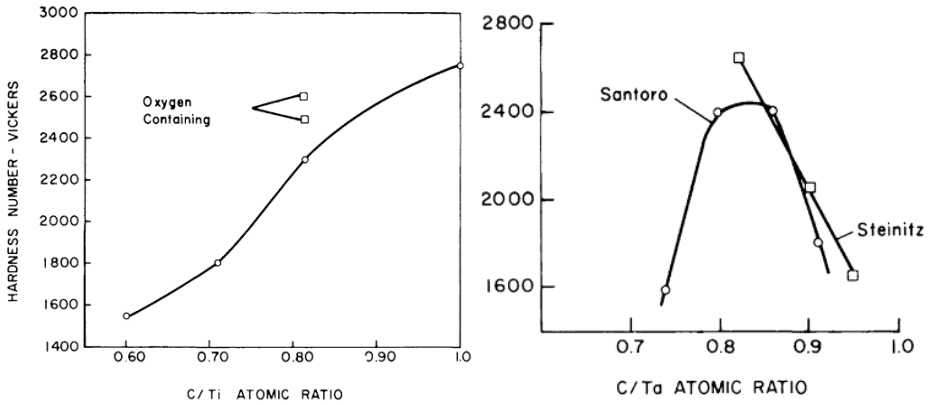

Fig. 2.22 – Effect of C/M ratio on TiC and TaC hardness; reproduced from Refs [60,65].

2.2.5 Phase diagrams & mechanical properties of binary carbides

Among MC carbides, five have been selected for our study: TiC, VC, TaC, NbC and WC; they not only exhibit very good mechanical properties, but they are also among the most used in terms of industrial applications. We review now briefly these five binary systems, with an emphasis on their phase diagrams and mechanical properties.

The phase diagrams present several similarities; Fig. 2.23 presents the five binary diagrams.

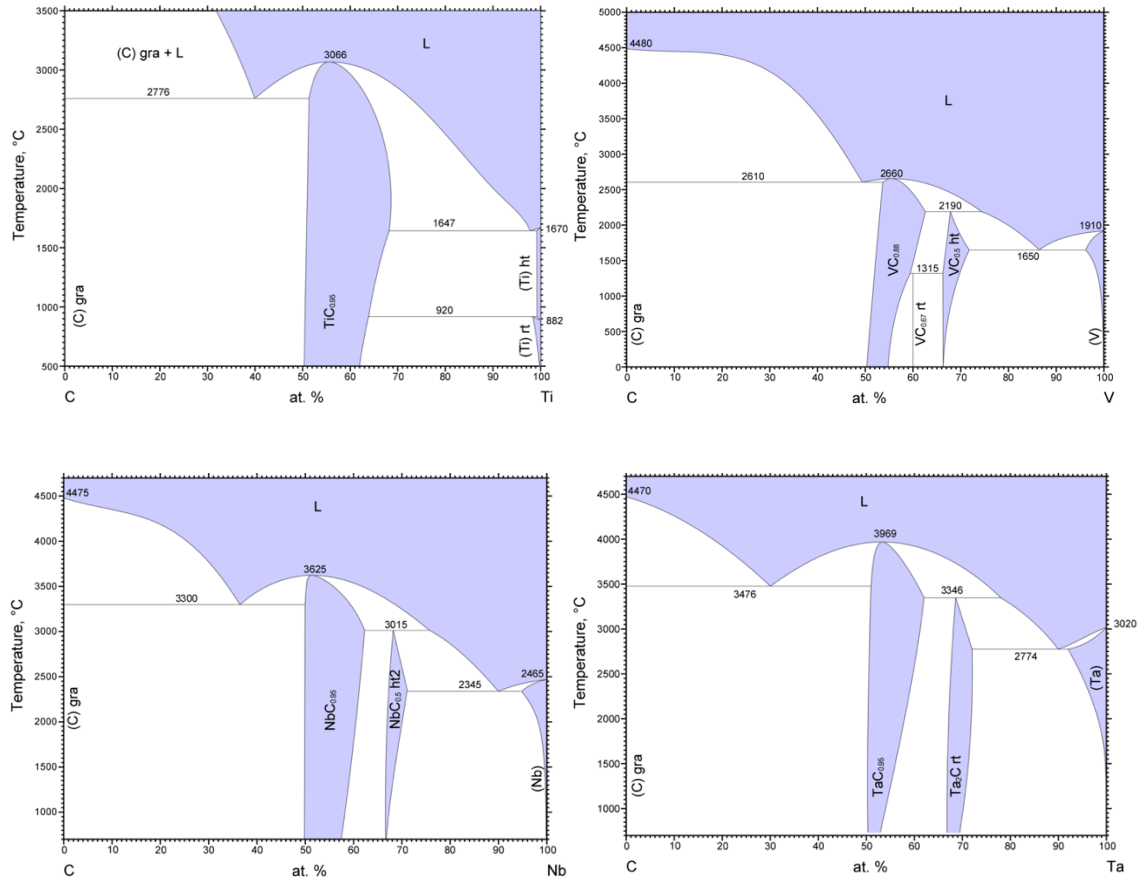

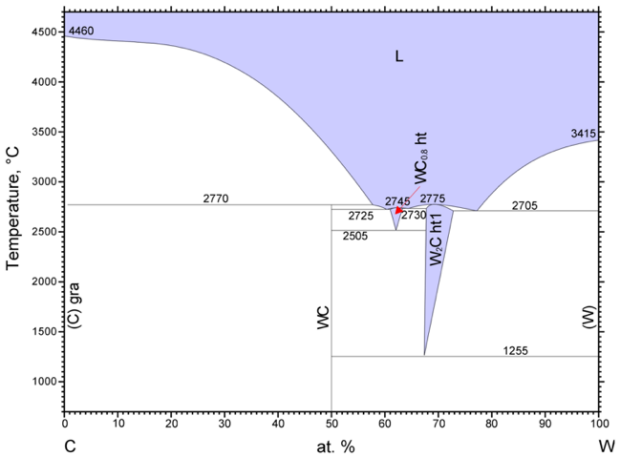

Fig. 2.23 – Binary phase diagrams for the binary C-Ti, C-V, C-Nb, C-Ta and C-W[xiv].

According to the group of the metal atom, TiC is part of Group IV (with ZrC and HfC), VC, NbC and TaC are the three carbides forming the Group V, and WC is part of Group VI.

Except WC which is stoichiometric, all the other MC and M_2C carbides of this work exhibit a range of possible compositions. The absence of a M_2C phase is a characteristic of Group IV, and therefore TiC is the only carbide of the C-Ti system. TiC_x has a homogeneity range between $x = 0.47$ and $x = 0.99$. The melting point of TiC is very high, 3066°C.

The phase diagrams of the systems of Group V are more complex with the presence of a M_2C phase. The C-V system is characterized by a melting point of VC at 2658°C while V_2C decomposes by a peritectic reaction at 2193°C. V_2C is stable at room temperature, with a stoichiometric composition. A third stoichiometric V_3C_2 phase is predicted by the phase diagram. The C-Nb and C-Ta systems are similar to C-V in terms of phases (without the M_3C_2 phase). The melting point of NbC is 3625°C, and Nb_2C decomposes at 3015°C. TaC has one of the highest melting points: 3969°C; it keeps its mechanical properties at higher temperatures than TiC, and it is therefore mainly used in addition to other carbides for high-temperature service.

The C-W phase diagram exhibit three carbide compounds: WC, W_2C and $WC_{0.8}$. The WC phase is stoichiometric and is the only stable phase at room temperature. It has a simple hexagonal structure and is formed via a peritectic reaction at 2770°C. The L_3' W_2C phase, formed from the liquid, exists until 1255°C, where it decomposes into WC + W. It has a melting point of 2775°C. Finally, $WC_{0.8}$ is a high-temperature phase, with a salt-like-cubic structure; it is directly formed from the liquid at 2745°C and decomposes into WC + W at 1255°C.

The crystal structure and lattice parameters of the MC and M_2C phases are given in Table 2.5:

Table 2.5 – Crystal structure and lattice parameter for MC and M_2C carbides of the C-Ti, C-V, C-Ta, C-Nb and C-W binary systems[5].

	TiC	VC	V_2C	NbC	Nb_2C	TaC	Ta_2C	WC	W_2C
Structure	fcc	fcc	hcp	fcc	hcp	fcc	hcp	hex	hcp
a_0 [Å]	4.32	4.16	2.90	4.47	3.12	4.45	2.87	2.90	3.00
c_0 [Å]	-	-	4.58	-	4.96	-	4.57	2.80	4.75

[xiv] Reproduced from www.asminternational.org/phase-diagrams

As outlined when discussing general carbide properties, it is common to find references exhibiting a large range of reported values. In order to understand where these differences come from, it is important to discuss now in more detail the methods used to predict or measure such properties (DFT, mechanical waves, indentation, etc.), the test conditions (variation of composition, of temperature, etc.), as well as the characteristics of samples (sintered, single-crystal, etc.).

Mechanical measurements of the TiC elastic modulus E range from 400[59] for $TiC_{0.84}$ to 460[67] GPa for $TiC_{0.99}$. DFT simulations give an even wider range, namely 342-517[68] GPa. Within these ranges, we selected the value of E_{TiC} = 451[5] GPa as reference value, as it has been mechanically measured on (bulk) single crystal carbide, with a carbon/metal ratio close to unity; therefore, it represents the value as close as possible to our system. The hardness has been measured too, giving values from 25[69] to 35[70] GPa, depending on the composition; and simulated to give values from 19[14] to 32[71] GPa. Maerky et al.[6] measured the hardness anisotropy by indenting bulk TiC single crystals with different orientations (Fig. 2.24-a,b) and we chose their results obtained with Vickers and Berkovich indenters, H_{TiC} = 25.5 – 34 GPa, as our reference values. The same authors investigated the TiC fracture toughness, including its anisotropy; their values for K_C range from 1.7 to 4.0 MPa·m$^{0.5}$ and are also dependent on the crack propagation direction in TiC (Fig. 2.24 c-e).

The elastic modulus of VC has been measured, to give values from 255 to 466[72] GPa depending mainly on stoichiometry and porosity. It has been simulated with different DFT models, to give values in the range 420-685[68] GPa. We use the value of E_{VC} = 430[5] GPa as our reference, because it was mechanically measured on a sample with a V/C ratio close to unity without porosity. Another indentation-based measurement by Wu et al.[73] gave a modulus of 436 GPa and thus confirmed the previous value. The hardness of VC ranges from 19[11] to 33[73] GPa, being the lowest values measured on porous samples, we consider as proper range H_{VC} = 27[5]-33 GPa. The fracture toughness K_C has been measured between 1.3 and 1.9 MPa·m$^{0.5}$ by Govila et al.[8].

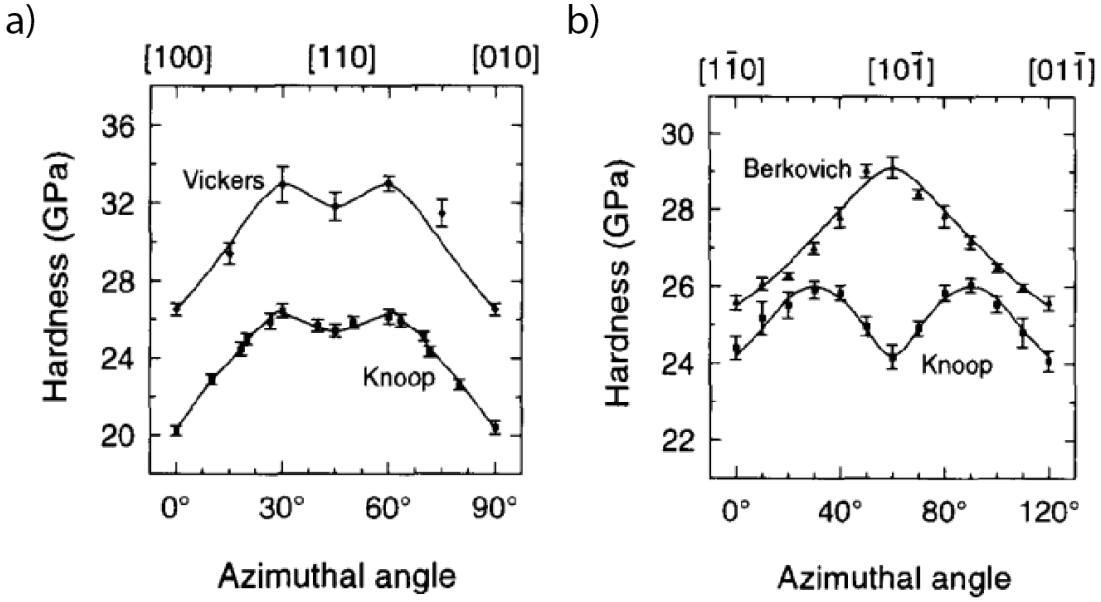

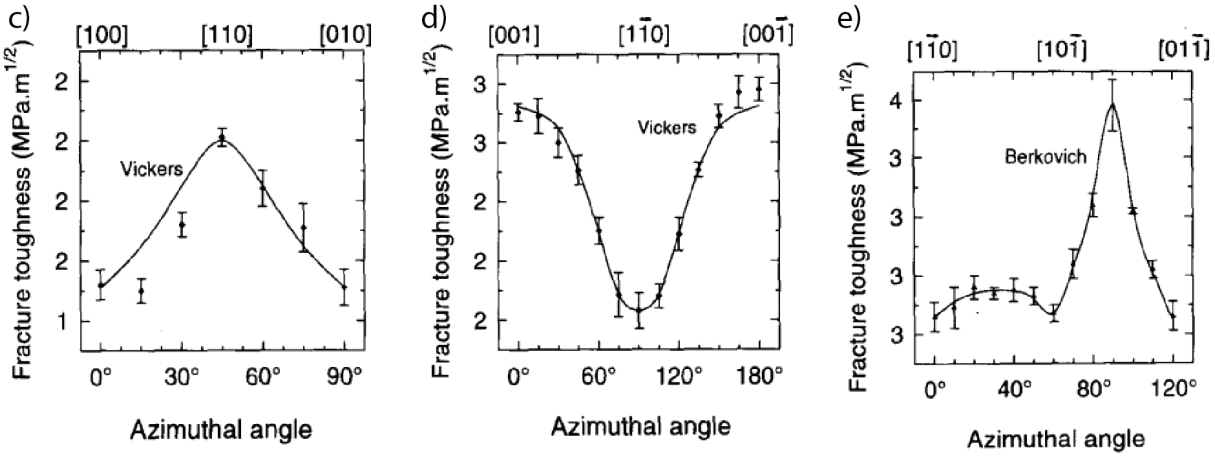

Fig. 2.24 – TiC hardness and fracture toughness anisotropy; a) and b) hardness, indentations on (001) and (111) planes respectively; c), d) and e) toughness, indentations on (001), (110) and (111) planes respectively. For all graphs, the azimuthal angle represents the rotation angle from the indenter axis to the vertical; reproduced from Ref [12]. Vickers and Berkovich indenters are chosen for symmetry reasons.

NbC elastic modulus values vary from 360 to 604[68] GPa, with simulated and measured results merged; as a reference, we use E_{NbC} = 537[5] GPa, from work where a NbC bulk single crystal sample was measured by a sound wave technique. The hardness measurements and simulations vary from 19.5[69] to 29.4[12] GPa, but once again, low hardness values correspond to porous samples. Therefore, the range H_{NbC} = 27.5[12]-29.4 is selected as our reference. Indentation fracture toughness has been measured by Kim et al.[13] giving values between 7.0 and 8.6 MPa·m$^{0.5}$.

Among the five binary carbides presented, TaC exhibits the widest range of values concerning its mechanical properties. TaC is indeed very sensitive to changes in stoichiometry, as well as porosity. Due to its extreme melting point, sintering processes are less efficient than for other carbides. The range obtained by compiling several mechanical measurements of E starts at 303[72] GPa and increases up to 549[10] GPa. Simulated values vary from 380[74] to 550[75] GPa. We choose the reference value E_{TaC} = 472[9] GPa, measured by sound wave propagation on a dense sample made of hot pressed TaC powder. Several other publications, based on mechanical tests, confirm that measurement[76,77]. Hardness measurements range from 14[10] to 26[77] GPa, but values below 21[69] GPa correspond to porous samples. Our hardness reference range of TaC is then H_{TaC} = 21-26 GPa. The fracture toughness K_C has been measured by Nino et al.[10] and found to vary from 3.5 to 4.5 MPa·m$^{0.5}$.

The mechanical properties of WC exhibit a smaller range of values compared to B1 carbides, mainly because of its fixed stoichiometry. The main reason for the variation is then the hexagonal crystal structure and ensuing anisotropy. The elastic modulus has been measured and simulated with values from 623[78] to 722[79] GPa. We choose E_{WC} = 696[5] GPa as a reference value, because it has been mechanically measured (sound waves) on WC bulk single crystal samples. Hardness measurements and simulations range from 19[80] to 30[81] GPa; in that case, we used only mechanical measurements (H_{WC} = 19-24[82] GPa) as our reference values, because the DFT calculations have never been confirmed experimentally and seem to be overestimated. K_C fracture toughness varies from 7.5 to 8.9[15] MPa·m$^{0.5}$.

Table 2.6 summarize the relevant mechanical properties of TiC, VC, TaC, NbC and WC, chosen as our reference values.

Table 2.6 – Reference mechanical properties chosen for the TiC, VC, TaC, NbC and WC binary carbides. Reference for the Poisson's ratio ν : [5]; M is called the indentation modulus.

		TiC	VC	NbC	TaC	WC
E	[GPa]	451	430	537	472	696
ν	[-]	0.19	0.22	0.21	0.24	0.18
H	[GPa]	25.5-34	27-33	27.5-29.4	21-26	19-24
K_C	[MPa·m$^{0.5}$]	1.7-4.0	1.3-1.9	7.0-8.6	3.5-4.5	7.5-8.9

2.3 Ternary Carbides

As discussed in the Introduction Chapter, TiC, VC, TaC, NbC and WC can be used alone; however, most of the time binary carbides are combined together to form higher-order carbides. An interesting property of carbides resides in their large mutual solubility: most of the binary systems can form a homogeneous ternary phase with other MC carbides. Thereby, it is possible to produce ternary or quaternary carbides exhibiting improved properties.

Thermodynamic considerations are first presented, with regard to the solubility of the transition elements carbide and the isothermal sections of ternary phase diagrams. We then present the few studies that have been done on the mechanical properties of ternary carbide system. Finally, we introduce the two mechanisms affecting the mechanical properties: the valence electron concentration and the precipitation of second phases in ternary carbides.

2.3.1 Ternary phase diagrams of transition carbides

Ternary carbides are based on the high solubility between MC carbides: it is possible to form a new ternary (M,M')C homogeneous phase which conserves the MC crystal structure, i.e. the M' atoms substitute atoms of the element M, while the crystal remains homogeneous. The properties of such new phases are interesting, because they generally do not follow a linear relationship between the properties of MC and M'C binary carbides and can exhibit sometimes a maximum at intermediate compositions.

The large solubility among most of the transition carbides originates from the fact they are comparable in terms of properties, atomic bonding and crystal structure, as illustrated in Table 2.7. Green boxes in Table 2.7 represent total solubility of the secondary element M' in the MC carbide, while orange signifies partial solubility and red very limited solubility. Chromium, molybdenum and tungsten carbides are exceptions, mostly because they have more complex crystal structures.

Table 2.7 – Intersolubility of transition carbides.

Secondary element \ Principal Element	Ti	V	Cr	Zr	Nb	Mo	Hf	Ta	W
Ti									
V									
Cr									*
Zr									
Nb									
Mo									**
Hf									
Ta									
W			*			**			

* W_2C extremely soluble in Cr_3C_7

** W_2C totally soluble in Mo_2C

Different solubilities are illustrated in Fig. 2.25.

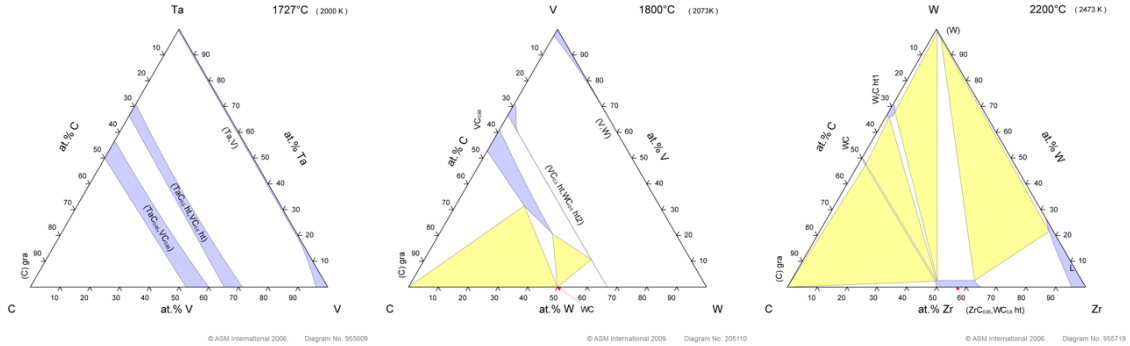

Fig. 2.25 – a) Ta-V-C system (full MC & M_2C solubility); b) V-W-C system (partial solubility of W in VC); c) Zr-W-C system, (almost no solubility)[xv].

Because a complete description of all the ternary systems would be too wide, this section will be devoted only to systems of present interest, namely Ti-W-C, Ti-V-C, Ti-Ta-C, Ti-Nb-C and Ta-V-C. A complete ternary phase diagram is often difficult to visualize, and is also often not available,

[xv] Reproduced from www.asminternational.org/phase-diagrams

such that we prefer the use of isothermal sections. Six sections of the Ti-W-C system are presented in Fig. 2.26.

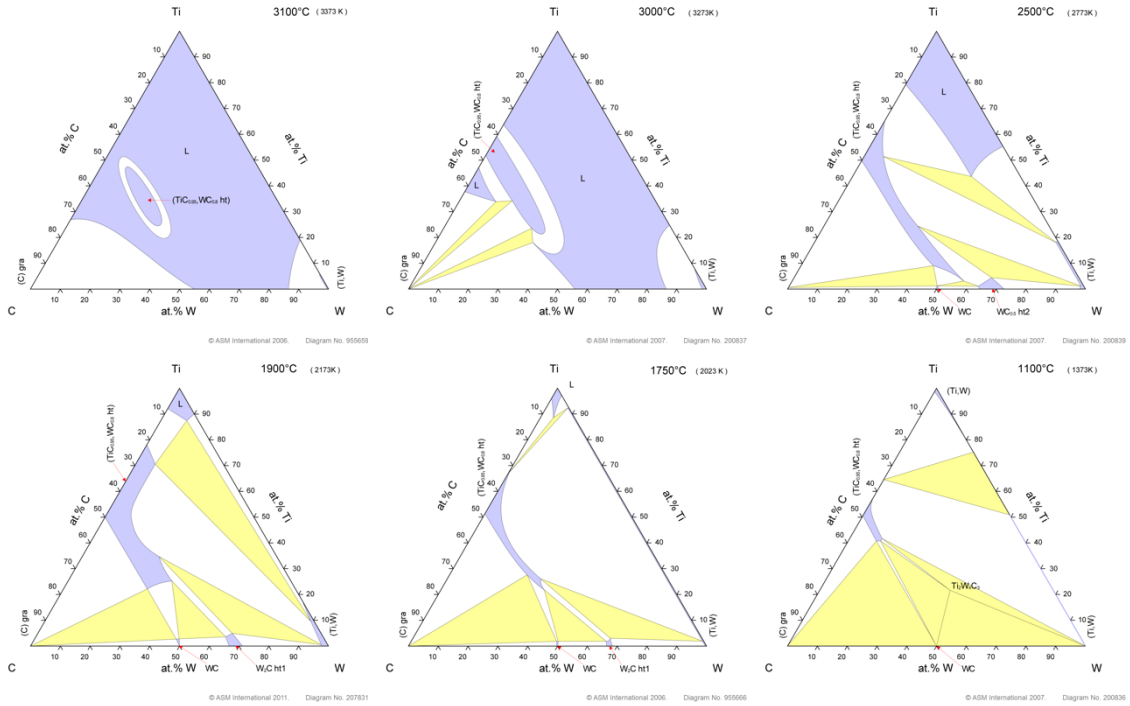

Fig. 2.26 – Isothermal sections of the Ti-W-C ternary system from 3100°C down to 1100°C[xvi].

At elevated temperatures, the liquid phase dominates; binary WC and TiC are both liquid, and only tungsten, carbon and some compositions of the ternary (Ti,W)C carbide remain solid. When the temperature decreases to 3000°C, the solid domain of the ternary carbide extends up to TiC, but W-rich compositions are still liquid. At 2500°C, tungsten carbide is solid; the solubility of W in TiC is almost total, and TiC decomposes only for W-rich compositions, into WC and a W-poorer (Ti,W)C compound. From 2500 to 1900°C, the solubility of W in TiC decreases significantly until ~50 at%; at that temperature, only the titanium remains liquid. The situation at 1750°C is relatively similar, except that the area of the single-phase (Ti,W)C is drastically reduced. At 1100°C, finally, the W_2C phase disappears and the solubility of W in TiC drops.

Rudy has investigated most of the ternary systems, including those of great interest for us, Ti-W-C, Ti-V-C, Ti-Ta-C and Ti-Nb-C, from a thermodynamic point of view in 1969 and a deeper discussion can be found in that compendium[83]. Tungsten carbide, as one of the most used material for the machining of high-performance steels, is often alloyed with titanium, in order to form the ternary (Ti,W)C. Although TiC and WC have different crystal structures at room temperature (TiC being cubic and WC hexagonal simple), they still exhibit partial solubility (Fig. 2.26), being WC soluble within titanium carbide up to ~50 at% at 1750°C. The single-phase (Ti,W)C area gets smaller as the temperature decreases. At 2500°C however, the solubility of W in TiC is almost total.

Rudy studied more specifically this system[84] and found that there is a total mutual miscibility of both carbides above 2530°C, because at that temperature, WC adopts a stable cubic phase. Metcalfe[85] measured a surprising variation in the lattice parameter for a cubic ternary carbide: he

[xvi] Reproduced from www.asminternational.org/phase-diagrams

observed a plateau up to ~ 50 at%, followed by a decrease of the lattice parameter (Fig. 2.27) by increasing the W exchange.

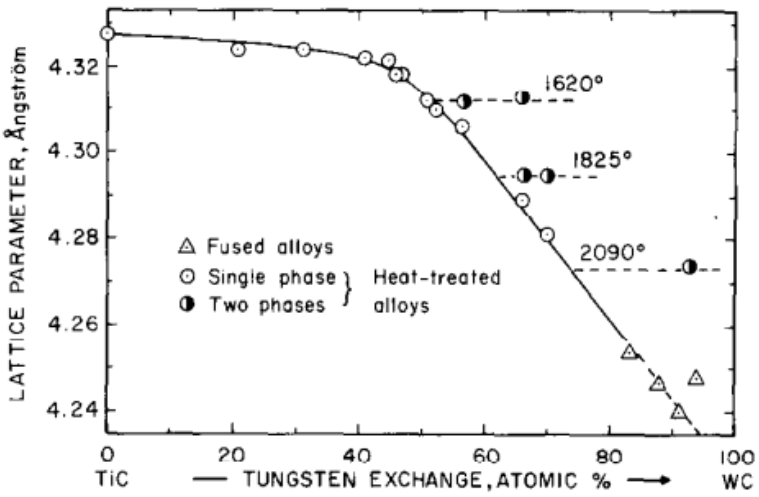

Fig. 2.27 – Evolution of the lattice parameter of (Ti,W)C with the tungsten content; reproduced from Ref [85]

With regard to processing, Jiang, Fei and Han[86] synthesized (TiWC)-Fe composites, the particles being formed *in situ* by arc-melting. More in detail, they mixed and compacted titanium, tungsten, graphite and iron powders and melted the specimens within an electric arc furnace; the result was a dispersion of spheroidal ternary and close-to-stoichiometric carbide particles in a steel matrix. A microstructure of their sample is presented in Fig. 2.28.

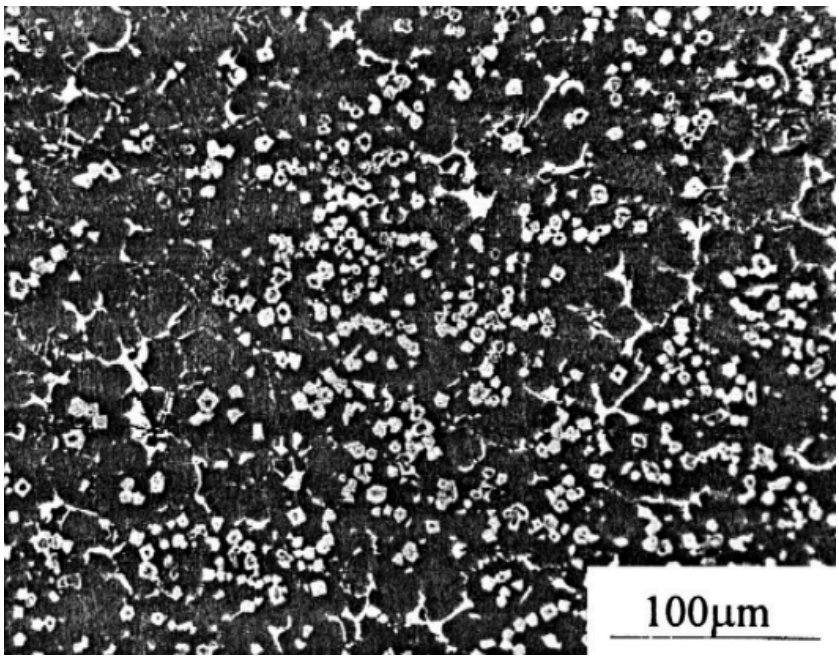

Fig. 2.28 – Fe-Ti-W-C composite microstructure; reproduced from Ref [86]. The carbides (in white) are spheroidal and uniformly distributed in the Fe-matrix.

A thermodynamic description of the Ti-V-C system has also been done by Zhang et al.[87], and Bandyopadhyay et al.[88] based on simulation, founding a good correlation with the measured phase diagram exposed by Rudy.

Ono and Moriyama[89] investigated phase relationships within the Ti-Nb-C system; the samples were produced from niobium oxide, metallic niobium and titanium powders, and graphite. NbC and Nb_2C were prepared by carbothermic reduction of Nb_2O_5 at 2000°C; the Ti-Nb-C carbide was then sintered, confirming a continuous solid solution for this system. The microstructure of Ti-Nb-C compounds was investigated by Wei et al.[90]; the samples were prepared by melting powders of Nb, Ti and graphite in an arc-melter. In a matrix of Nb, both Nb_2C and the ternary (Ti,Nb)C carbides are formed, depending on the composition. An illustration of a Nb-21Ti-4C microstructure is provided in Fig 2.29.

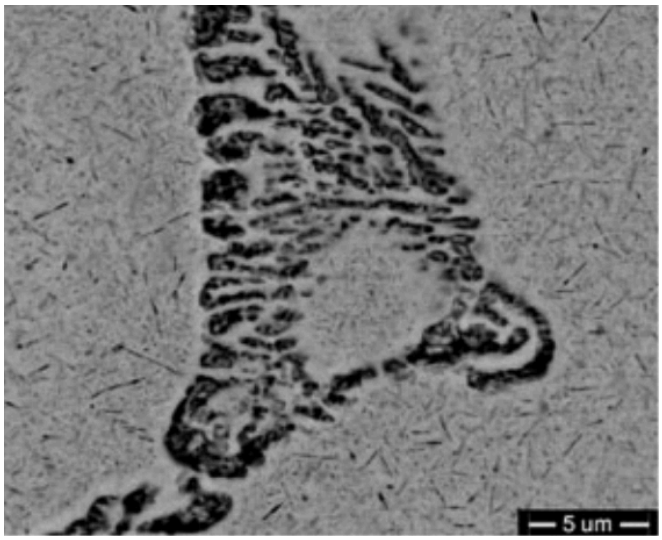

Fig. 2.29 – Nb-21Ti-4C microstructure, heat treated[90,86]. The ternary carbides (in black) are spheroidal and uniformly distributed in the Fe-matrix.

To our knowledge, very little work has been published about the Ta-V-C system; it is not present in Rudy's compendium. Tret'yachenko et al.[91] published, however, a study of the phase equilibria in this specific system.

2.3.2 Mechanical properties of ternary carbides

The mechanical properties of sintered polycrystalline (Ti,W)C have been measured by Jung and Kang[92]; the samples were produced by reducing a mix of carbon, titanium and tungsten oxide, followed by sintering at 1510°C. Vickers hardness values varying between 19.2 and 20.5 GPa were found, with a maximum for the $Ti_{60}W_{40}C$ composition. Fracture toughness values varied between 6.4 and 7.7 $MPa \cdot m^{0.5}$, as a function of tungsten content (for a maximum of 50 at% W).

Tret'yachenko and Eremenko[93] performed a first study on the crystal structures of the Ti-V-C ternary system in 1966. Both binary TiC-VC and TiC-V_2C sections of the ternary diagram were investigated, through microhardness measurements. They measured a decrease in hardness with

the increase of VC content, from 3450 to 2580 HV, and a decrease from 3450 to 2250 HV for V-richer compositions.

Ternary (Ti,Ta)C carbides of various compositions have been produced via SHS (self-propagating high-temperature synthesis) by Levashov et al.[94] and then characterized in a second paper[95]. The measured hardness of precipitated (Ti,Ta)C carbides ranges from 14.2 to 18.0 GPa, depending on the porosity (from 10 to 19%) and composition.

Cermets based on titanium and tantalum carbonitride in a Co matrix have been produced via a mechanically induced self-sustaining reaction (MSR) by Chicardi et al.[96]. They studied the effect of Ta content on the oxidation resistance of the cermet and found an interesting improvement[97]: the weight gain per unit area after 48h, (measuring the oxidation), is divided by a factor 7 when replacing 20% of Ti atoms by Ta. The effect of TaC addition to a titanium carbonitride cermet has been investigated by Wu et al.[98], to find an increase in strength, but a reduction in hardness and toughness, as more TaC is added (up to 7 wt%).

Jiao et al.[99] measured the mechanical properties of Ti-Nb-C alloys. The Vickers hardness of the alloy was measured, without focusing on the properties of the carbide second phases: the hardness increases with the titanium content, up to 20 at% (Ti-richer compositions have not been investigated), as well as the yield strength, both at room temperature and at 1200°C.

By way of conclusion, we see that relatively little is known about ternary carbides, especially considering their mechanical properties. Most of the few studies to date are based on thermodynamic considerations, and the even fewer mechanical measurements that have been done, concern polycrystalline sintered particles or multi-phase metal matrix composites. Consequently, we cannot use those values as references for our monocrystalline, *in situ* formed, ternary carbide particles, and the only relatively reliable comparative values remain the measurements performed on binary compositions.

2.3.3 Valence electron concentration

By definition, the valence electron concentration (VEC) is the number of valence electrons (VE) per unit cell of the crystal lattice. Both B1 cubic and hexagonal simple structures count one metal atom and one carbon atom per cell. As carbon has four valence electrons in its hybridized sp^3 state, and each transition metal atom counts from 4 to 6 VE, TiC is characterized by 8 VE, VC, NbC and TaC by 9, while WC has 10 VE.

The VEC is a parameter that can be easily tuned by forming a ternary or quaternary carbide and thus by changing its composition, the VEC being directly proportional to the concentration of the different transition metals, following Eq. 2.11:

$$VEC([M_xM'_{1-x}]C) = x \cdot VEC(M) + (1-x) \cdot VEC(M') + 4$$

Eq. 2.11

Some authors use a slightly different definition, where the number of VE per cell is normalized by the number of atoms per cell. As a result, their VEC is then divided by a factor two; we choose to use the former definition, as it is the most common.

H. Holleck[100] reviewed the hardness of several ternary carbides and carbonitrides as shown in Fig. 2.30:

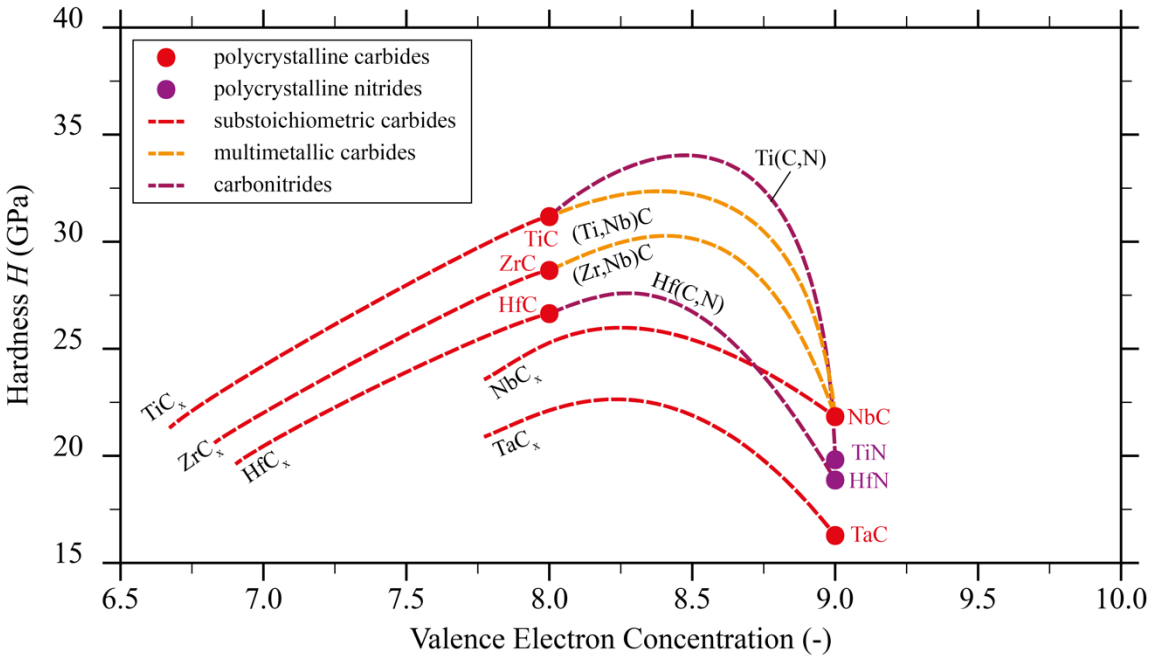

Fig. 2.30 – Evolution of the hardness of ternary carbides and carbonitrides with valence electron concentration; reproduced from Ref [100].

The valence electron concentration used for the horizontal scale in Fig. 2.30 is linked at the same time with atomic bonding and with the composition of the ternary carbide. The most important result of that graph is the systematic maximum that is exhibited by each ternary system; the hardness at the maxima is always higher than the hardnesses of both the MC and the M'C carbides.

As emphasized in Fig. 2.30, mechanical properties can be strongly influenced by a change in composition and hence in VEC. Hardness is one of the mechanical properties that is the most affected: the resistance to plastic deformation increases when the atomic bonds get shorter, when the iconicity of the bonding is reduced, or when the density of bonds is increased. Among those three possibilities, the last is the easiest to control and increasing the VEC is one way to increase the density of atomic bonds[11].

Jhi[55] illustrated that behavior with the variation of the c_{44} elastic constant in (cubic) ternary titanium carbonitride and explained it with the directionality of the e_g d-sub-orbitals. Substituting atoms of metal is not the only way to change the VEC of carbides; one can also replace carbon atoms (4 VE) by nitrogen (5 VE). In both cases, e_g sub-orbitals are progressively filled when the VEC increases; Jhi calculated that they became saturated when VEC ≈ 8.4. From there on, other d sub-orbitals, t_{2g}, with different directionalities, begin to fill, and shearing along directions defining c_{44} then promotes M-M bonds, which decrease the hardness. In Fig. 2.31 we can observe the change in overlap between (C,N)/p and M/d-e_g orbitals when shear strain is applied (Fig. 2.31-a,b), together with the change in overlap between two M/d- t_{2g} orbitals (Fig. 2.31-c,d). Increasing the VEC changes the density of such bonds, increasing the density of M-C bonds when VEC ≤ 8.4 and M-M when VEC > 8.4.

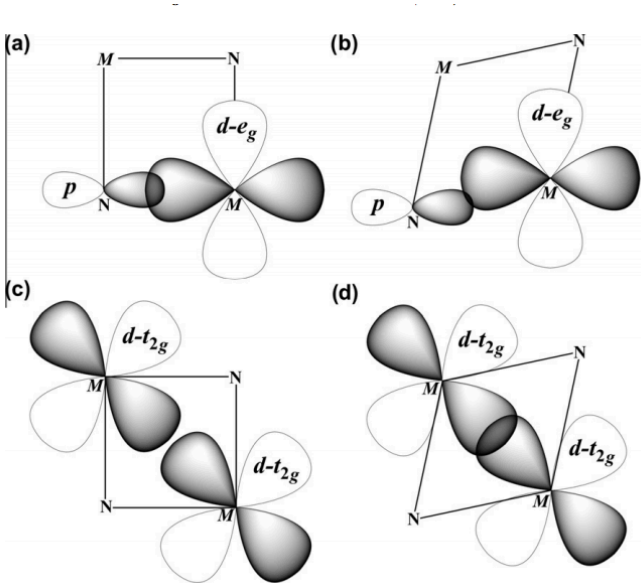

Fig. 2.31 – Shearing of e_g and t_{2g} bonds in a carbonitride; reproduced from Ref [101].

The bulk modulus B measures the resistance of a material to isostatic pressure. Under that kind of stress, the strain differs from pure shear strain, and the directional covalent bonds are then subjected to other types of alteration. TiN, for example, has a higher bulk modulus than TiC, because it counts more electrons per volume[102]: B increases as carbon atoms are replaced by nitrogen atoms. The additional electrons first occupy the e_g sub-orbitals and provide a strong contribution to the bulk modulus; when those orbitals are full, similarly to what is seen with the hardness, the additional electrons start to fill the t_{2g} sub-orbitals, which, in that case, do not add a negative contribution to B, but rather a "less strong" positive effect. We have thus a bulk modulus increasing strongly as x decreases from 1.00 and less strongly when x comes close to 0 (Fig. 2.32). For some systems, it has been found that the deviation from linearity is small and that B can for practical purposes be considered as a linear function of composition, or of the VEC[103,104].

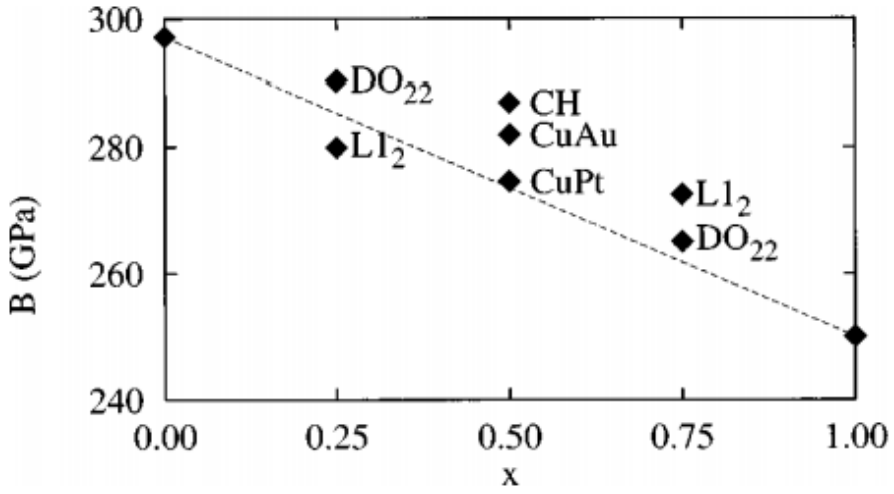

Fig. 2.32 – Calculated values of bulk modulus of TiC_xN_{1-x}. Five different supercell configurations have been considered: $L1_0$(CuAu), CH, $L1_1$ (CuPt), DO_{22} and $L1_2$. The dashed line is an interpolation between the bulk modulus of TiN and TiC; reproduced from Ref [102].

Ivashchenko et al.[105] performed *ab initio* calculations for several compositions of titanium carbonitride. They predicted a linear evolution of the lattice parameter as a function of the nitrogen content and confirmed the results of Jhi regarding the maximum of the c_{44} elastic constant for a VEC of ~8.4.

2.3.4 Phase separation in ternary carbides

Phase separation, exemplified by precipitation hardening, which is a well-known strengthening mechanism in metal alloys, can also be effective in hard carbides.

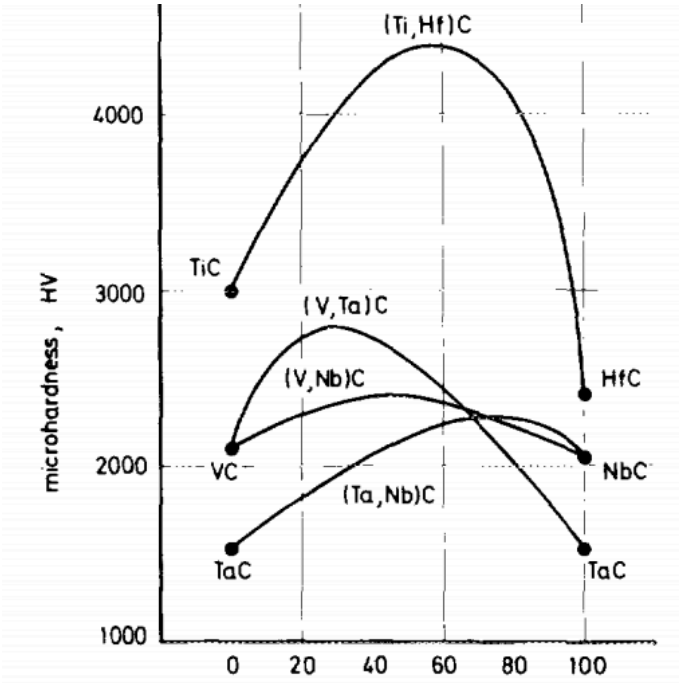

Fig. 2.33 – Evolution of hardness of several ternary carbides with composition (in at%) by the mechanism of second phase precipitation by spinodal decomposition; reproduced from Ref [100].

As illustrated in Fig. 2.33, phase separation can have a rather strong effect on the strength of various ternary carbides compositions. An interesting feature of many MC-M'C systems in this respect is that they exhibit a spinodal decomposition at low temperatures when their phase diagram presents a miscibility gap within a single solid phase region[106] (e.g. TiC-ZrC in Fig. 2.34): the mixed ternary composition separates into two new ternary phases with different compositions. That behavior leads to the formation of two very fine-scale separated phases, and this can increase the mechanical properties of the carbide.

Ma et al.[107] investigated the behavior of the (Ti,Zr)C system: they aged samples of different compositions for 500 hours at 1300°C, a temperature high enough for diffusion to be operational, yet low enough to enter the temperature range for phase separation. The result was a lamellar structure of alternating Zr-rich and Ti-rich carbides. When the aging temperature was increased to 1800°C, after 10 hours precipitation along the grain boundaries of both Zr-rich and Ti-rich domains was observed. The decomposition rates are clearly influenced by the temperature: at lower

temperature, decomposition is not limited to the interfaces, whereas at high temperature, phase separation is confined at the grain boundaries (Fig. 2.35).

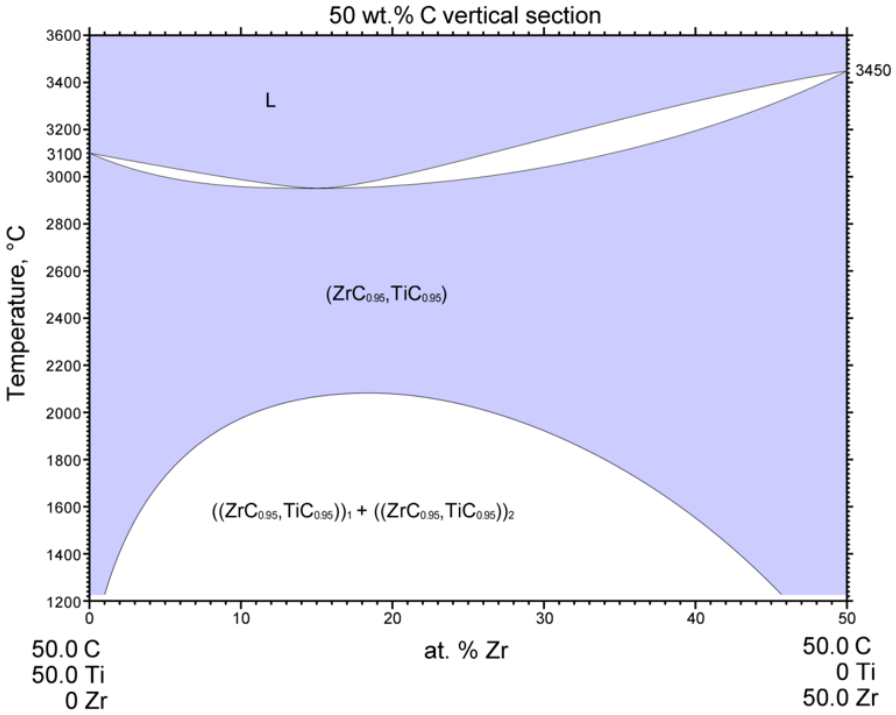

Fig. 2.34 – Pseudo-binary TiC-ZrC phase diagram[xvii].

The mechanism of phase decomposition in these experiments was identified as discontinuous precipitation[109]. Li et al.[108] reported the evolution of hardness and of the fracture toughness of a TiC-ZrC solid solution prepared by spark plasma sintering, as a function of the aging time (Fig. 2.36) and observed both an increase of the hardness and of the fracture toughness. On single crystal particles, Ma et al. reported a hardness over 40 GPa[107].

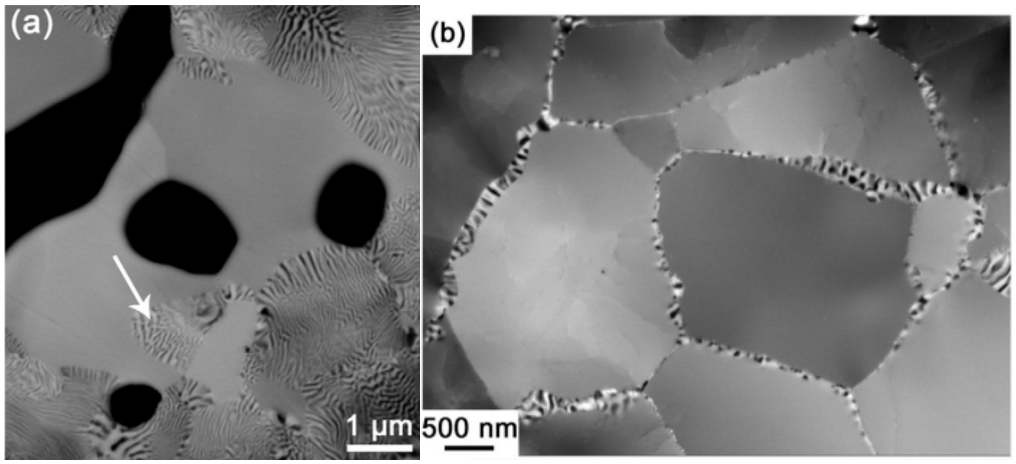

Fig. 2.35 – a) Low temperature decomposition of (Ti,Zr)C; b) high temperature decomposition; reproduced from Refs [107,109].

[xvii] Reproduced from www.asminternational.org/phase-diagrams

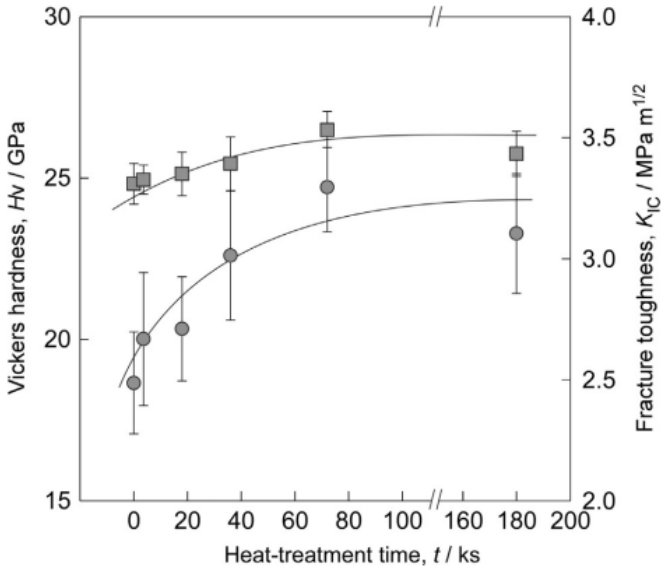

Fig. 2.36 – Effect of aging time on hardness (●) and fracture toughness (■) for TiC-ZrC composite; figure reproduced from Ref [108].

2.4 Mechanical Testing at Microscopic Scales

We now turn to the various nanoindentation-based methods, as well as small-scale mechanical tests, that have been used to measure mechanical properties at micron-scale. We place particular emphasis on the adequacy of these various tests in the context of this work, meaning toward measuring the mechanical properties on steel-surrounded carbide particles of this work.

2.4.1 Contact Mechanics

Hertz was the first scientist to study the deformation of materials when they are in contact with each other: in 1882, he solved the contact problem of two elastic materials with curved surfaces[110,111]. Hertz assigned a given shape to the surfaces of contact (Fig. 2.37), exploring shapes that satisfy the following boundary conditions:

- Stresses and strains must satisfy the equations of elasticity; stresses tend to zero far away from the contact surface;

- The contact is assumed to be frictionless;
- Along the contact surface, normal pressures are equal and opposite for the two bodies; the normal pressure is zero elsewhere;
- Perfect contact is assumed, i.e. the distance between surfaces is zero inside the circle of contact;
- The integral of the pressure distribution gives the force acting between the two bodies

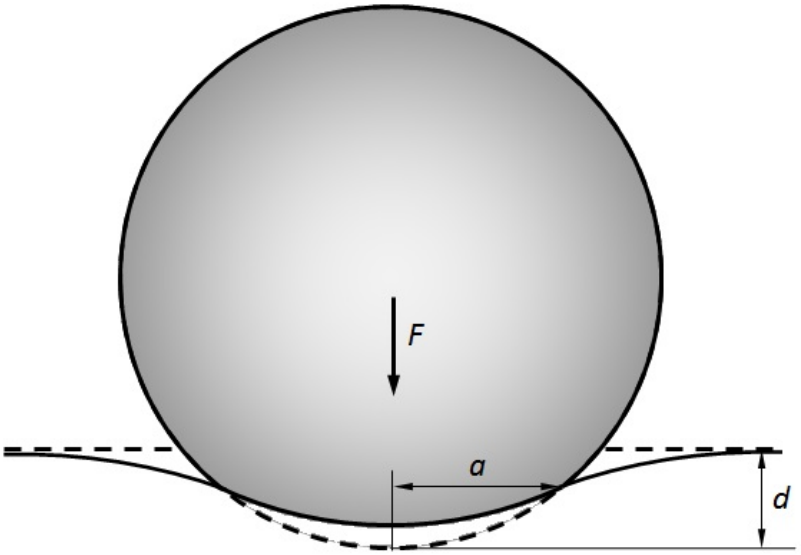

Fig. 2.37 – Contact radius a of a sphere; d represents the distance between the initial surface and the maximal penetration of the non-deformed sphere, under a force F. By convention, the load is always positive. Reproduced from Ref [122].

With the profile of the contacting surfaces represented by a quadratic function, Hertz found that an ellipsoidal radial distribution of the normal pressure $\sigma_z(r)$ is a solution to those specific boundary conditions. When the contact surface is a circle, this gives:

$$\frac{\sigma_z(r)}{p_m} = -\frac{3}{2}\sqrt{1-\frac{r^2}{a^2}}$$

Eq. 2.12

where p_m is the mean pressure over the contacting surfaces and a the radius of the contact circle. That equation, called the Hertz equation, is valid for $r \leq a$. Huber[112] then calculated, based on Hertz's theory, the stress field caused by the indentation of a sphere on a flat surface. That important stress field was subsequently re-evaluated by Fuchs[113], Huber and Fuchs[114], and Morton and Close[115]. Sneddon[116] extended the theory to other tip geometries, including axi-symmetric tips.

The initial condition in indentation is described by a point contact, which was studied by Boussinesq[117]. Its solution can be extended to give the stress for any pressure distribution if one applies the principle of superposition of linear elasticity. Any contact configuration, e.g.

indentations with various indenter geometries, can thus be interpreted as a distribution of point loads along the tested sample surface.

The stresses within a given material in a point contact situation were calculated by Timoshenko and Goodier[118], based on Boussinesq's results, in cylindrical coordinates:

$$\sigma_r(r,z) = \frac{P}{2\pi}\left[(1-2\nu)\left[\frac{1}{r^2} - \frac{z}{r^2\sqrt{r^2+z^2}}\right] - \frac{3r^2 z}{(r^2+z^2)^{\frac{5}{2}}}\right]$$

$$\sigma_\theta(r,z) = \frac{P}{2\pi}(1-2\nu)\left[-\frac{1}{r^2} + \frac{z}{r^2\sqrt{r^2+z^2}} + \frac{z}{(r^2+z^2)^{\frac{3}{2}}}\right]$$

$$\sigma_z(r,z) = -\frac{3P}{2\pi}\frac{z^3}{(r^2+z^2)^{\frac{5}{2}}}$$

$$\tau_{rz}(r,z) = -\frac{3P}{2\pi}\frac{rz^2}{(r^2+z^2)^{\frac{5}{2}}}$$

Eq. 2.13

where P is the applied load, σ_r the radial stress, σ_θ the tangential stress, σ_z the normal stress and τ_{rz} the shear stress in a radial plane. By convention, r and z are positive quantities. The corresponding strains can be calculated by using Hooke's law.

Knowing the pressure distribution of a point contact, it is then possible to calculate the ensuing surface deflection by a superposition of those arising from individual point contacts:

$$u_z = \frac{1-\nu^2}{\pi E}\iint_S p(r,\theta)\,dr\,d\theta$$

Eq. 2.14

From the displacement, it is in turn possible to compute the strains and the stresses from Hooke's law. Describing an indentation requires defining the stresses and deflections of points along the surface and within the material as a function of the indenter geometry.

Spherical indenter

For a spherical indenter, the pressure distribution is directly given by the Hertz equation (Eq. 2.12). The normal stress reaches a maximum at $r = 0$, and is zero along the edge of the contact circle, where $r = a$. The local surface displacement with respect to the original free surface is:

$$u_{z,sph} = \frac{1-\nu^2}{E}\frac{3}{2}p_m\frac{\pi}{4a}(2a^2 - r^2)$$

Eq. 2.15

We can observe that $u_{z,sph}(r = a) = \frac{1}{2}u_{z,sph}(r = 0)$

The radial stress distribution and the related displacement at the surface and inside the contact circle have been calculated by Johnson[119]:

$$\frac{\sigma_r}{p_m} = \frac{1-2\nu}{2}\frac{a^2}{r^2}\left[1 - \left(1 - \frac{r^2}{a^2}\right)^{\frac{3}{2}}\right] - \frac{3}{2}\sqrt{1 - \frac{r^2}{a^2}}$$

$$u_r = -\frac{(1-2\nu)(1+\nu)}{3E}\frac{a^2}{r}\frac{3}{2}p_m\left[1 - \left(1 - \frac{r^2}{a^2}\right)^{\frac{3}{2}}\right]$$

Eq. 2.16

The peak radial stress is found at $r = a$. The stresses within the material for a spherical indenter have also been calculated[114,120] and are given in Appendix B.

Hertz[110,111] found that the radius a of the contact circle is related to the load, the indenter radius R and the mechanical properties of the material (E_r) by the following relation:

$$a^3 = \frac{3}{4}\frac{PR}{E_r}$$

Eq. 2.17

the reduced modulus E_r being a combined function of the modulus of the indenter (subscript i) and that of the specimen (subscript m):

$$\frac{1}{E_r} = \frac{1-\nu_i^2}{E_i} + \frac{1-\nu_m^2}{E_m}$$

Eq. 2.18

When $P = 0$, i.e. the indenter just touches the surface, the distance $h(r)$ between the indenter of radius R (with $R >> h$) and the surface is given by:

$$h(r) = \frac{r^2}{2R}$$

Eq. 2.19

When load is applied, the total displacement $\delta(r) - h(r)$ is the sum of the indenter displacement $u_{z,i}$ and that of the material surface $u_{z,m}$:

$$\delta(r) - h(r) = u_{z,i} + u_{z,m}$$

Eq. 2.20

Using the pressure distribution along a spherical indenter (Eq. 2.15), we can write $\delta(r) - h(r)$ as:

$$\begin{aligned}\delta(r) - h(r) = \delta(r) - \frac{r^2}{2R} &= \frac{1-\nu_i^2}{E_i}\frac{3\pi p_m}{8a}(2a^2 - r^2) + \frac{1-\nu_m^2}{E_m}\frac{3\pi p_m}{8a}(2a^2 - r^2) \\ &= \frac{1}{E_r}\frac{3\pi p_m}{8a}(2a^2 - r^2)\end{aligned}$$

Eq. 2.21

Setting $r = 0$, $p_m = P/\pi a^2$, and using Eq. 2.17 we get:

$$\delta^3 = \left(\frac{3}{4E_r}\right)^2 \frac{P^2}{R}$$

Eq. 2.22

For a spherical indenter, we then reach the conclusion that P is proportional to $\delta^{3/2}$.

Conical Indenter

For a conical indenter, the pressure distribution is given by:

$$\frac{\sigma_z(r)}{p_m} = -\cosh^{-1}\frac{a}{r}$$

Eq. 2.23

The associated displacement beneath the indenter ($r \leq a$) is:

$$u_z = \left(\frac{\pi}{2} - \frac{r}{a}\right) a \cot\phi$$

Eq. 2.24

with ϕ the semi-angle of the cone. The complete stress field for a conical indenter is given in Appendix B.

The radius of the contact circle is related to the applied load via[121]:

$$a^2 = \frac{2}{\pi}\frac{P\,tan\,\phi}{E_r}$$

Eq. 2.25

At $r = 0$ and using Eq. 2.24, we have then:

$$P = \frac{2}{\pi}E_r \cdot tan\,\phi \cdot u_{z,r=0}^2$$

Eq. 2.26

For a conical indenter, P is thus proportional to the square of the displacement (as can be surmised given the fact that, in this configuration, the problem remains geometrically self-similar).

A similar development for a flat punch indenter is given in Appendix B. It leads to conclude that load and displacement are proportional to one another (as can be surmised given the fact that, in this configuration, there is no evolution of the contact surface with load).

Fig. 2.38 summarizes local values of the normalized contact pressure distribution, the surface deflection and the surface radial stresses for spherical, conical and flat punch indenters, as a function of r/a.

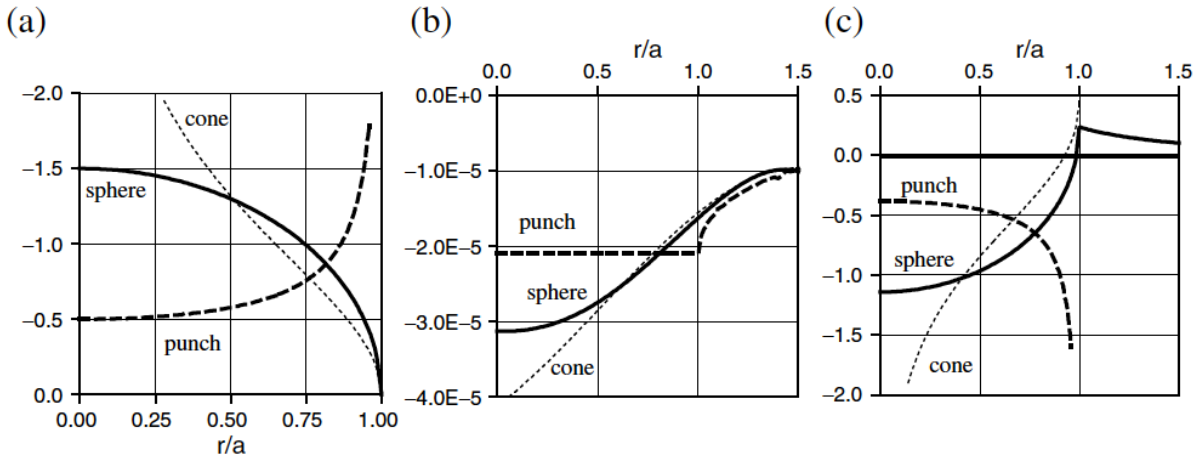

Fig. 2.38 – a) Normalized contact pressure distribution; b) Deflection of the surface; c) Magnitude of normalized surface radial stress; figure reproduced from Ref [122].

2.4.2 Nanoindentation

Nanoindentation is a standard method that is extensively used to measure mechanical properties at the micro-scale. It is based on the penetration of a rigid indenter into a material, the test measuring the load-displacement curve. Three kinds of indenters are used in practice: spheres, cones and flat punches (Fig. 2.39 a-c); note that pyramidal geometries such as Vickers, Berkovich

or cube corner tips are cones, which are often assimilated to axi-symmetric conical indenters (Fig. 2.39 d-f). The semi-angles ϕ of those pyramidal indenters are given in Table 2.8.

Table 2.8 – Semi-angles for Vickers, Berkovich and cube corner pyramidal indenters.

	Semi-angle ϕ	Symmetry
Vickers	68°	4
Berkovich	65.3°	3
Cube corner	35.3°	3

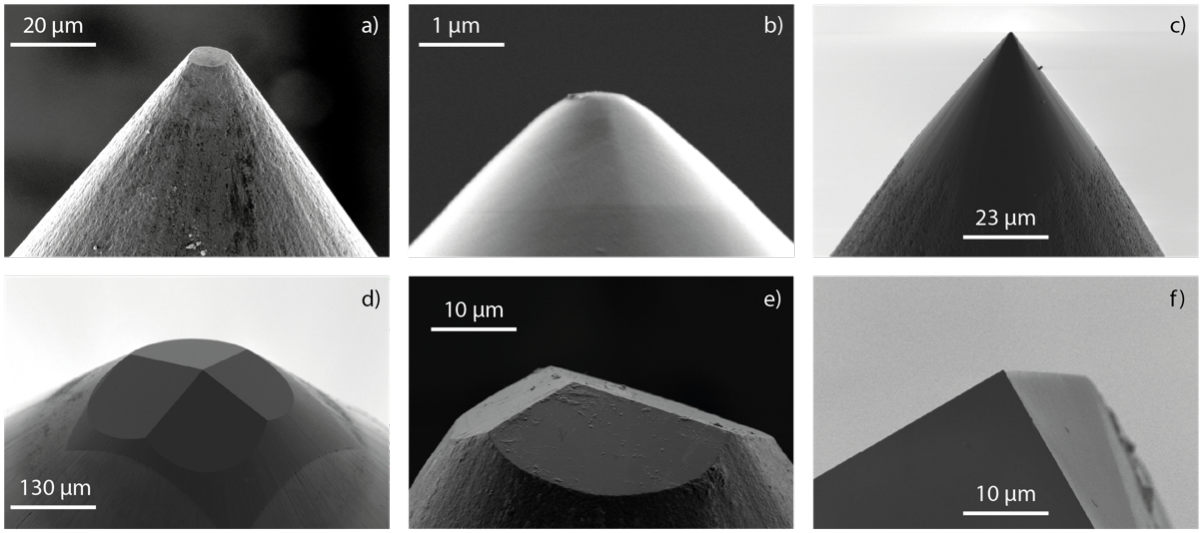

Fig. 2.39 – Typical indenter geometries: a) flat punch; b) sphere; c) cone; d) Vickers; e) Berkovich; f) cube corner

Oliver and Pharr have developed a now very often used methodology[123], which starts by assuming that all the information is contained in the unloading part of the indent. The key underlying observation (or at times assumption) is such unloading is purely elastic, contrary to the loading path, where nearly all materials exhibit a certain amount of irreversible deformation such as plasticity. More recent techniques or data interpretation schemes have been developed since, for example to measure other mechanical properties. Most recent apparatuses have sensors able to measure loads as small as a few µN, or a setup able to heat the specimen and then perform high-temperature indentations. A.C. Fischer-Cripps published several reviews of standard nanoindentation techniques[124,125]. We present now eight different methods that have been developed to measure the elastic modulus of bulk materials and thin films. Pros and cons are summarized in Table 2.9, as well as the main adequate use of each.

Table 2.9 – Pros and cons of E indentation-based measurement methods.

Method	Equation	Pros	Cons	Principal use
Oliver & Pharr	Eq. 2.28	Simple method Adapted to automatization	Not adapted for thin films on hard substrates	Most situations
Doerner & Nix	Eq. 2.37	Adapted to thin films	Empirical relation Depends on the material	Thin films on W and Si
King, Nix and Saha	Eq. 2.38	Adapted to thin films	Thickness of the film must be precisely known	Thin films
Spherical indentation	Eq. 2.39	Simple method	Not adapted for thin films on hard substrates	Most situations
Lee et al.	Eq. 2.40	Take into account of sink-in or pile-up	FE modelling required	Valid for most materials
Cheng et al.	Eq. 2.42	No calibration of the tip required	Only for conical indenters	Adapted for work-hardening materials
Oliver	Eq. 2.43	Less affected by deviation from ideal indenter	Not valid for pile-up Conical indenter only	Most situations
Malzbender and De With	Eq. 2.44	Less affected by deviation from ideal indenter shape Valid in the presence of pile-up or sink-in	Conical indenter only	Most situations

2.4.2.1 The Oliver & Pharr Method

As mentioned, the Oliver & Pharr method (OPM)[123] is based on an analysis of the unloading part of the indentation curve. If the loading section is a combination of elastic and plastic deformations, the unloading part is (assumed to be) exclusively elastic and can thus be used to determine the elastic modulus.

When indentation is performed up to a peak load P_{max}, the material will be deformed, and the tip of the indenter will penetrate to a depth h_{max}. If the material is elasto-plastic, when the load is progressively removed, the imprint will be resorbed by elastic recovery up to (remaining indentation) a certain depth, h_f. Fig. 2.40 displays a classical load-displacement curve.

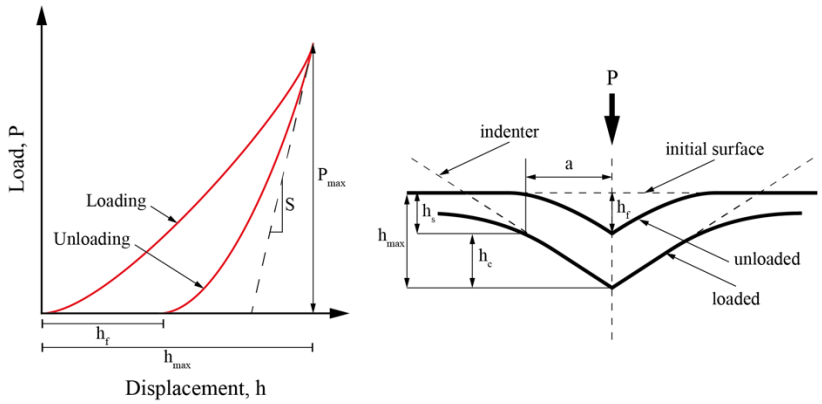

Fig. 2.40 – Nanoindentation load-unload curve and penetration; reproduced from Ref [123].

The analysis that is used to determine the elastic modulus accounts for the particular curvature of the unloading curve, which is usually approximated by a power law:

$$P(h) = \alpha\left(h - h_f\right)^m$$

Eq. 2.27

where α and m are fitting constants. Parameter m depends on the tip geometry, as seen above: $m = 1$ for flat cylinders, $m = 1.5$ for spheres and paraboloids of revolution, and $m = 2$ for cones. Oliver and Pharr have tested several materials with a Berkovich indenter and the fitted values for m show, however, values in the range $1.2 \leq m \leq 1.6$ (the OPM assumes that the behavior of the Berkovich indenter can be modeled by a circular conical indenter with an angle ϕ = 65.3°).

The model introduces a parameter called the contact length h_c (Fig. 2.40-b), corresponding to the vertical distance along which contact is made with the tip. In reality, the profile of the permanent mark is never perfect, because of the sink-in phenomenon, and thus $h_c \neq h_{max}$.

The reduced modulus E_r is calculated from the unloading curve as:

$$E_r = \frac{\sqrt{2}}{\pi}\frac{S}{\sqrt{A}}$$

Eq. 2.28

where S is the slope of the unloading curve at P_{max} and A is the contact area. The value of S is calculated from the power law fit, by differentiating the equation and evaluating the derivative at the point of peak load and called contact stiffness.

To determine the contact area, the OPM assumes that the indenter can be described by an area function $f(h)$ that depends on the distance from its tip. A is then defined from the relation $A = f(h_c)$. The deflection of the surface at the contact perimeter $h_s = h_{max} - h_c$ is given by Sneddon's law for a conical indenter:

$$h_s = \frac{\pi - 2}{\pi}(h - h_f)$$

Eq. 2.29

and the force-displacement relationship for a conical indenter is then

$$(h - h_f) = 2\frac{P}{S}$$

Eq. 2.30

Moreover, Oliver and Pharr defined a parameter, ε, as the proportionality constant between P_{max}/S and h_s. For a conical indenter, ε = 0.72; for a flat punch and a paraboloid of revolution, the values are respectively ε = 1.0 and ε = 0.75. depending on ε, h_c can thus have a range of possible values (Fig. 2.41).

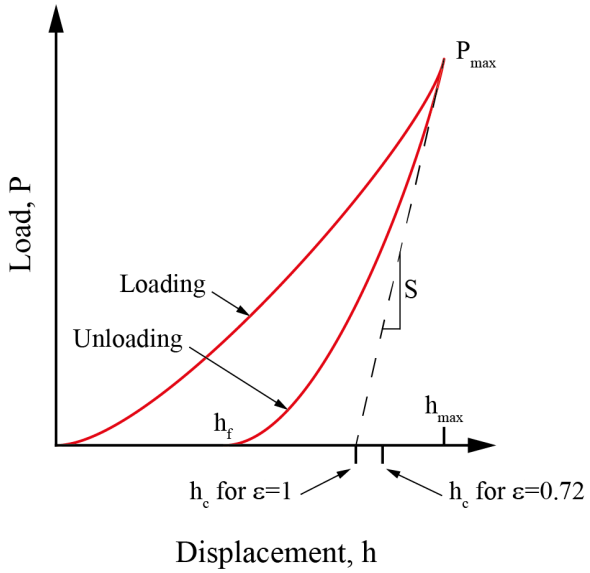

Fig. 2.41 – Range of possible h_c displacement as a function of ε ; reproduced from Ref [123].

Given the values of the fitting parameter m measured for different materials, the indenter geometry that provides the best description of the unloading curve is the paraboloid of revolution.

Another important consideration in the OPM is the determination of the load frame compliance. Knowing this compliance is essential because the measured displacement is the sum of the indent and the load frame deformations. It is particularly important for materials that have a high modulus, for which the load frame movement can be a significant fraction of the total displacement. The overall compliance is modelled as two springs in series:

$$C_{tot} = C_{frame} + C_{specimen} = C_{frame} + \frac{1}{S} = C_{frame} + \frac{\sqrt{\pi}}{2E_r}\frac{1}{\sqrt{A}}$$

Eq. 2.31

The OPM measures C_{frame} by plotting C versus $A^{-½}$. The most accurate values of C_{frame} are obtained when $1/S$ is small, i.e., for large indentations. Usually, a pure aluminium reference sample is used to measure C_{frame}, because of its low hardness.

In 2004[126], Oliver and Pharr published a second paper, adding refinements and limitations to the method. They defined the new concept of "effective indenter shape" (EIS) to understand why the equations derived for indentation of a flat elastic half-space remain valid for a half space whose surface has been distorted by the formation of an indent. The EIS is a cylindrical function $z = u(r)$ that describes a shape that produces the same normal surface displacement on a flat surface as that which a conical indenter would produce on the indent. $u(r)$ is the distance between the indenter and the original surface, and r is the radial distance from the center of the tip. Finite element analysis has shown that the z function can be approximated by a power law relation:

$$z = Br^n$$

Eq. 2.32

with n varying from 2 to 6 depending on the material properties. Using Sneddon's equation for indentation of a half space by an indenter described by a power law EIS, it was concluded that:

$$P = \frac{2E_r}{\left(\sqrt{\pi}B\right)^{\frac{1}{n}}}\frac{n}{n+1}\left[\frac{\Gamma\left(\frac{n+1}{2}\right)}{\Gamma\left(\frac{n}{2}+1\right)}\right]^{\frac{1}{n}} h^{1+\frac{1}{n}}$$

Eq. 2.33

where Γ represents the gamma function. If we compare the exponent of h, we obtain $m = 1 + 1/n$, meaning $1.2 \leq \mathrm{m} \leq 1.5$, which agrees with experimental observations.

Oliver and Pharr also derived a general expression for ε, using the EIS:

$$\varepsilon = m\left[1 - \frac{2\Gamma\left(\frac{m}{2(m-1)}\right)}{\sqrt{\pi}\Gamma\left(\frac{1}{2(m-1)}\right)}(m-1)\right]$$

Eq. 2.34

making it possible to determine h_c for any axially symmetric indenter by determining the fitting parameter m.

The OPM does not account for pile-up around the imprint. When this is present, the contact area increases, and the modulus is overestimated. This inability to deal with pile-up is a consequence of using an elastic analysis. Oliver and Pharr showed that the amount of pile-up or sink-in depends on the ratio h_f/h_{max} and on the rate of work-hardening of the material. Pile-up is important for h_f/h_{max} close to unity with little work-hardening.

Oliver and Pharr also added a new correction factor β. This parameter is used to correct the deviation from axisymmetric geometry for the indenter. Finite element analysis provided an expression for β:

$$\beta = \pi \frac{\left[\frac{\pi}{4} + 0.1548 \cdot cot\phi \cdot \frac{1-2\nu_i}{4(1-\nu_i)}\right]}{\left[\frac{\pi}{2} - 0.8312 \cdot cot\phi \cdot \frac{1-2\nu_i}{4(1-\nu_i)}\right]^2}$$

Eq. 2.35

The authors also provided an improved calibration procedure for measuring the load frame compliance. This new method relies on the P/S^2 ratio and on the hardness of the material H:

$$\frac{P}{S^2} = \frac{\pi}{4\beta^2}\frac{H}{E^2}$$

Eq. 2.36

This ratio is independent of the contact area and is not altered by the presence of pile-up or sink-in behavior. The basic idea for the load frame compliance measurement is that P/S^2 should be constant if the hardness and the modulus are also constant. The proper compliance is then found by changing C_{frame} until P/S^2 becomes constant when plotted versus the penetration depth.

2.4.2.2 Elastic modulus measurement

Even if the Oliver and Pharr method is still the most frequently used method nowadays in the interpretation of nanoindentation data, it has some limitations that make it unsuitable in certain situations, as for instance measurements of the elastic modulus of carbide reinforcements in a steel matrix or of thin films. Other methods, or corrections to the OPM, have been then developed to address such situations.

The measurement of the modulus of a material making a thin film is more complex because, in that case, the indenter deforms not only the film, but also the underlying substrate: the measured modulus is then a composite modulus, which is furthermore a function of the indentation depth. Doerner and Nix[127] suggested an empirical equation to take into account the effect of the substrate:

$$\frac{1}{E} = \frac{1}{E_f} + \left(\frac{1}{E_s} - \frac{1}{E_f}\right) e^{-\left(\frac{t}{h}\right)}$$

Eq. 2.37

where indices f and s denote respectively the film and the substrate, and t is the film thickness.

King[128] provided another empirical model for a flat punch, which was subsequently improved by Saha and Nix for conical indenters[129]:

$$\frac{1}{E_r} = \frac{1-\nu_i^2}{E_i} + \frac{1-\nu_f^2}{E_f}\left(1 - e^{-\alpha\frac{t-h}{\sqrt{A}}}\right) + \frac{1-\nu_s^2}{E_s} e^{-\alpha\frac{t-h}{\sqrt{A}}}$$

Eq. 2.38

Vlassak[130] proposed an approach similar to the OPM but based on Yu's solution[131] for the elastic contact of an indenter on a layered half space instead of Sneddon's equation for a homogeneous semi-infinite half-space.

The OPM is not the only nanoindentation-based method that can be used to measure the elastic modulus of bulk materials, and several other models have been developed during the last 20 years.

Indentations performed with a spherical tip follow Hertz's contact analysis. The load is then linked to the displacement by a simple relationship:

$$P \propto E_r \sqrt{R}\, h_c^{\frac{3}{2}}$$

Eq. 2.39

Herbert et al.[132] showed that Hertz's analysis was successful in measuring the elastic modulus if the geometry of the indenter is truly spherical and the displacements are small in comparison to the radius of the tip.

Lee et al. [133] provided a more accurate method based on FE modelling, to take into account pile-up and sink-in phenomena. As a result, they introduced a correction factor κ into the elastic modulus equation:

$$E = \frac{1-\nu^2}{\frac{d_{max}}{\kappa S} - \frac{1-\nu_i^2}{E_i}}$$

Eq. 2.40

where the maximum contact diameter d_{max} is taken at the maximal displacement h_{max}, with material pile-up or sink-in considered.

Another interesting approach uses the work of indentation. Cheng et al.[134] demonstrated that the ratio of the energies developed during the loading and the unloading parts of the indentation are a function of multiple parameters, such as the elastic modulus and the angle of the indenter. If the unloading curve is purely elastic (i.e., if no reverse plasticity occurs) and the loading curve is elastoplastic, then the reduced modulus E_r influences the shape of both curves. The authors established a linear relationship between the ratio H/E_r and the ratio of the energies[135]:

$$\frac{H}{E_r} = \gamma \frac{W_{unloading}}{W_{loading}}$$

Eq. 2.41

This equation is valid for indenters with an angle between 60° and 80° (Ni et al.[136] extended the method for spherical indenters) and do not require a calibration of the indenter. The reduced modulus can then be easily calculated as:

$$E_r = \gamma \frac{\pi}{4} S^2 \frac{W_{unloading}}{W_{loading}} \frac{1}{P_{max}}$$

Eq. 2.42

Oliver[137] proposed a method based on the evaluation of the loading S_L and unloading S_U slopes:

$$\frac{S_U}{S_L} = \frac{E_r}{H\sqrt{\pi C}} + \frac{\varepsilon}{2}$$
$$E_r = \sqrt{\frac{\pi}{C}} \frac{1}{2P_{max}\beta} \left(\frac{S_U^2 S_L}{2S_U - \varepsilon S_L} \right)^2$$

Eq. 2.43

where C is equal to 24.5 for a Berkovich indenter, β and ε are the same parameters than for the OPM.

Malzbender and De With[138] proposed a similar relationship that described by Oliver, but taking pile-up or sink-in into account:

$$\frac{S_U}{S_L} = \frac{\pi \tan \alpha}{\beta} \frac{H}{E_r} \frac{h_c}{h_t}$$
$$E_r = \frac{S_U^2 S_L}{2 \cdot f(n) \cdot S_U - \varepsilon S_L} \frac{1}{2P\beta \tan \alpha}$$

Eq. 2.44

where $f(n)$ is a correction function that accounts for pile-up or sink-in.

Leggoe[139] studied the indentation of particles embedded in a soft matrix and quantified the interaction of the stress field with the surrounding matrix by performing FE simulations of a second indentation of the surrounding matrix, the particle acting thus as a pseudo cylindrical flat punch. Assuming that the matrix deformation is purely elastic, its deformation is then subtracted from the total deformation to deduce the elastic modulus of the particle from the test signal. This approach gave promising results if the matrix is sufficiently stiff such that the elastic matrix deformation is small; however, it requires FE simulation of each indent.

2.4.2.3 Hardness measurement

Hardness is a measurement of the capability of a given material to resist permanent deformation during compression under a hard surface. Usually, a sharp (general diamond) indenter is pressed against the material surface with a load large enough to generate plastic deformation.

As indentation can quickly produce a permanent imprint, it is a convenient method to measure the hardness. A load is applied via a spherical or pyramidal indenter and the pressure distribution beneath the surface, more precisely the mean contact pressure p_m, is used to determine the hardness knowing the permanent deformation induced by the indentation. With an ideally plastic material (which does not work harden), p_m remains constant with an increase of the indenter load and is directly proportional to the material's yield, producing a direct relationship between H and Y, c being the proportionality constant:

$$H = c \cdot Y$$

Eq. 2.45

If we compare an indentation test with a standard uniaxial compression test, the mean contact pressure required to initiate yield is higher in the former case. Indeed, plastic flow is driven by the shear component of the stress field and the stress field of an indentation is characterized by an important hydrostatic part, due to constraint exerted by the stressed material in the surrounding bulk. The c factor in Eq. 2.45 is then called the "constraint factor" and depends upon the indented material and the indenter. For a material showing a large ratio E/Y (e.g., metals), c is in theory close to 3; for low values of E/Y (e.g., glasses), $c \approx 1.5$.

We can distinguish three different regimes in the strain-stress response recorded during an indentation test:

1. For $p_m < 1.1\ Y$: full elastic response; there is no imprint left after the indenter is removed
2. For $1.1\ Y < p_m < c \cdot Y$: plastic deformation is constrained by the surrounding elastic matrix
3. $p_m = c \cdot Y$: a plastic region grows further as indentation progresses, leading to an increase in indentation contact area and almost no increase in p_m.

At the beginning of the indentation process, corresponding to the first regime, the response is purely elastic. For a spherical indenter, the loading curve follows the equation:

$$p_m = \left(\frac{4E_r}{3\pi}\right)\frac{a}{R}$$

Eq. 2.46

This equation is consistent with Hertz's theory, with R the radius of the indenter, a the radius of the contact circle between the indenter and the surface, and E_r the reduced modulus given in Eq. 2.18. This assumes a linear relationship between the mean contact pressure, called the "indentation

stress", and the ratio a/R, called the "indentation strain". Using either the Tresca or Von Mises yield criterion, we can show that plastic deformation starts when $p_m \approx 1.1\ Y$.

The second regime consists in a transition between purely elastic and elasto-plastic deformation. For high values of indentation strain, the plastic deformation, under the assumption of no work-hardening, progresses with little or no increase in p_m.

Measurements of hardness via indentation are thus done in a fully developed plastic zone, where the mean contact pressure is independent of the load and dependent only of material properties. The most frequently used definition of hardness is given by Meyer's law, which uses the mean pressure at full load:

$$H = \frac{P_{max}}{A}$$

Eq. 2.47

where A is the projected contact area.

For indentation with a sharp indenter, a substantial level of plastic flow is observed in the indented material, and the elastic strain is small enough to be neglected: the material can be considered as rigid-plastic. For blunt indenters, the material must be considered as elastic-plastic. The mode of plastic deformation is then a result of compression and the displaced volume is compensated by elastic strains outside the plastic zone. A model called the "expanding cavity" model has been developed by Johnson[140] to describe that situation (Fig. 2.42).

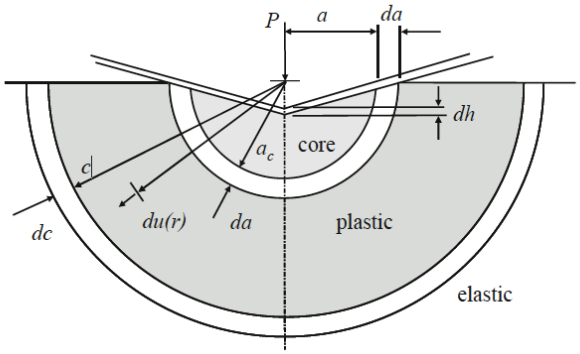

Fig. 2.42 – Expanding cavity model[140]; figure reproduced from Ref [122].

In that model, the contact between the indenter and the surface is surrounded by a first core, which is under hydrostatic stress and has a radius a_c; that core is in turn surrounded by a plastic zone of radius c. Everything else is considered elastic. An increment of penetration dh results in an expansion of the core by da. The volume displaced by the indenter is accommodated by a displacement of matter at the core interface, which causes, in turn, an expansion of the plastic cavity dc. For geometrical indentations (i.e., with a conical indenter), we have $da/dc = a/c$: the radius of the plastic zone increases at the same rate as that of the core.

The pressure within the core has been calculated as:

$$p = \frac{2Y}{3}\left[1 + ln\left(\frac{(E/Y)\,cot\,\alpha + 4(1-2\nu)}{6(1-\nu)}\right)\right]$$

Eq. 2.48

When the plastic material is no longer elastically constrained, the material takes the characteristics of a rigid-plastic solid, because elastic deformation becomes much smaller than plastic flow. Yield of such a material depends on the critical shear stress, calculated with either the Tresca or Von Mises criterion.

For two-dimensional (vs. axisymmetric) geometries, slip-line theory has been developed by Hill, Lee and Tupper[141]Fig. 2.43 to model indentation of a perfectly plastic material (Fig. 2.41).

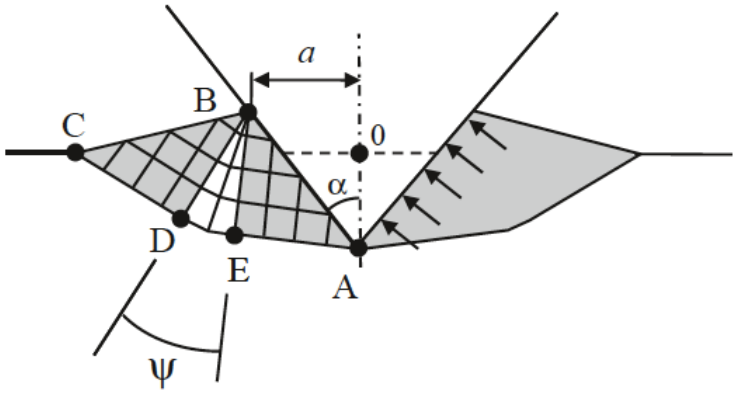

Fig. 2.43 – Illustration of the Slip-line theory[141] ; reproduced from Ref [122].

The volume of material displaced by the indenter is accommodated by upward and outward flow. Under the assumption of frictionless contact, the stress along the line AB is normal to the indenter. This type of indentation involves cutting along the line OA and creating new surfaces. The contact pressure is then:

$$p_m = 2\tau_{max}(1+\alpha) = H$$

Eq. 2.49

Using the Tresca yield criterion $\tau_{max} = 0.5 \cdot Y$, we get:

$$H = Y(1+\alpha) \Leftrightarrow c = (1+\alpha)$$

Eq. 2.50

A slightly higher value of c is found if the Von Mises criterion is used instead ($\tau_{max} \approx 0.58 \cdot Y$). For $\alpha = 90°$ and with the Von Mises criterion, this thus yields the expected value $c = 3$.

Historically, indentation methods are based on the measurement of the residual imprint dimensions, which are used to determine the hardness. However, for the very small marks

produced by nanoindentation, it is hard to measure their dimensions with sufficient accuracy. Therefore, the depth of penetration is used, and the area is extrapolated, knowing the indenter geometry, as in modulus measurement methods detailed above. The effect of compliance is here a less critical parameter than for the modulus measurement, because the related extra displacement is much smaller than the plastic deformation.

It is important to note that for ceramics, which are materials with a low ratio E/Y, the mean contact pressure under the condition of fully developed plastic zone measures the resistance of the material to combined plastic and elastic deformation. *Stricto sensu*, therefore, indentation is often not an exact measurement of hardness. The analysis of Oliver and Pharr can, however, be applied to determine the hardness – using the relation $H = P_{max}/A$ after a proper calibration of the area function of the tip – but there will be a systematic error (which decreases as the ratio E/Y increases). For most materials, that error is negligible, and the Oliver and Pharr method provides accurate hardness measurements.

It is alternatively possible to use the energy spent during indentation to measure the hardness. This method rests on the fact that an indentation consists of an elastic-plastic loading, followed by an elastic unloading and assuming that there is no reverse plasticity. A general power-law can describe both parts of the indentation:

$$P = C \cdot h^m$$

Eq. 2.51

The constant C depends on the nature of the contact, while $m = 2$ for a conical indenter. For the elastic-plastic part of the loading curve, C_L is given by:

$$C_L = \left[\frac{1}{\sqrt{\pi H \cdot tan^2\,\phi}} + \frac{2(\pi - 2)}{\pi}\sqrt{\frac{\pi}{4}}\frac{\sqrt{H}}{E_r}\right]^{-2}$$

Eq. 2.52

while for the (fully elastic) unloading part, C_U is given by:

$$C_U = \frac{2}{\pi} E_r \, tan\,\phi$$

Eq. 2.53

This energy-based approach considers the work done by the applied load P during the indentation (Fig. 2.44). During unloading, work is also done by the partial elastic recovery of the material. It appears that the amount of energy returned during the unloading is independent of the indenter's geometry and is a function of the ratio E_r/H.

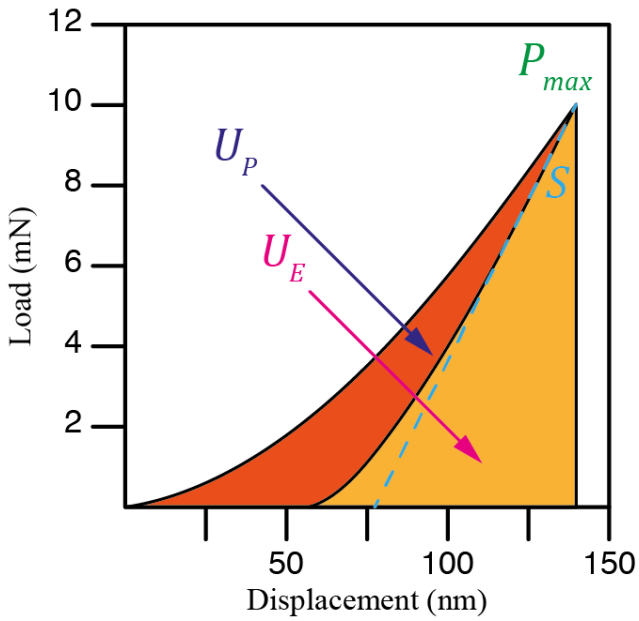

Fig. 2.44 – Indentation work during the loading (U_P+U_E) and the unloading (U_E); figure reproduced from Ref [142].

At maximal load, the two power-law curves intersect, and we have for a conical indenter:

$$P_{max} = C_L h_{max}^2 = C_U (h_{max} - h_r)^2$$

Eq. 2.54

The work of indentation is then calculated by integrating P with respect to h:

$$U_P = \int_0^{h_{max}} C_L h^2 dh - \int_{h_r}^{h_{max}} C_U (h - h_r)^2 dh = (C_L - C_U) \frac{h_{max}^3}{3}$$

Eq. 2.55

For rigid-plastic materials (high E/Y ratio), elastic recovery is negligible, and we can set $E_r = \infty$. In that case, $h_{max} = h_r$ and thus:

$$U_P = C_L \frac{h_{max}^3}{3} = \pi H \cdot tan^2 \phi \frac{h_{max}^3}{3}$$

Eq. 2.56

Since the volume of a cone of radius a and height h is given by $V = \pi \cdot a^2 \cdot h_{max}/3$ and knowing that $tan(\phi) = a/h$, we can transform Eq. 2.56:

$$U_P = \pi H \cdot \frac{a^2}{h_{max}^2}\frac{h_{max}^3}{3} = H\left(\frac{\pi a^2 h_{max}}{3}\right) = H \cdot V_{cone} \Leftrightarrow H = \frac{U_P}{V_{cone}}$$

Eq. 2.57

That value represents the amount of work required to produce a unit volume of indentation (or, more strictly, of corresponding displaced material); it is thus called "true hardness" since it can be viewed as a true measurement of resistance to plastic deformation.

For an elastic-plastic contact (i.e., for a small E/Y ratio), the volume of the indentation is the size of the residual impression $V_r = \pi \cdot a^2 \cdot h_r/3$ and the hardness is calculated as:

$$H = \frac{U_P}{V_r}$$

Eq. 2.58

This hardness is called the "apparent hardness". For an elastic-plastic material, the apparent hardness is smaller than the true hardness by a factor that depends on the ratio E_r/H.

The model can be improved by considering the elastic recovery process in more detail[142]: the shape of the indenter during unloading need no longer be assumed to be conical. Eq. 2.54 becomes:

$$P_{max} = C_L h_{max}^2 = C_U (h_{max} - h_r)^m$$

Eq. 2.59

The total work of indentation is calculated by integrating the loading part:

$$U_T = C_P \frac{h_{max}^3}{3}$$

Eq. 2.60

Integration of the unloading part gives:

$$U_E = \int_{h_r}^{h_{max}} C_U (h - h_r)^m dh = C_U \frac{(h_{max} - h_r)^{m+1}}{m+1}$$

Eq. 2.61

The work related to the plastic deformation is then:

$$U_P = U_T - U_E = C_L \frac{h_{max}^3}{3} - C_U \frac{(h_{max} - h_r)^{m+1}}{m+1}$$

Eq. 2.62

We can now define the ratios U_P/U_T and U_E/U_T:

$$\frac{U_P}{U_T} = 1 - \frac{3}{m+1}\left(1 - \frac{h_r}{h_{max}}\right)$$
$$\frac{U_E}{U_T} = 1 - \frac{U_P}{U_T}$$

Eq. 2.63

Finite element calculations have shown that for a conical indenter, m ranges between 1.27 and 1.36[143,144].

Cheng, Li and Cheng[143] found an empirical linear relationship between the ratio E_r/H and the ratio U_E/U_T:

$$\frac{H}{E_r} = \kappa \frac{U_E}{U_T}$$

Eq. 2.64

and we can define the ratio E_r^2/H by using Eq. 2.28 and Eq. 2.47:

$$\frac{E_r^2}{H} = \frac{\left(\frac{1}{2}\sqrt{\frac{\pi}{A}}\frac{dP}{dh}\right)^2}{\frac{P_{max}}{A}} = \left(\frac{dP}{dh}\right)^2 \frac{\pi}{4P_{max}}$$

Eq. 2.65

Combining Eq. 2.64 and Eq. 2.65 gives:

$$H = \kappa^2 \left(\frac{dP}{dh}\right)^2 \left(\frac{U_E}{U_T}\right)^2 \frac{\pi}{4P_{max}}$$

Eq. 2.66

Parameter κ requires a calibration with a known standard; E_r is known and dP/dh, U_E, U_T, and P_{max} are test parameters.

Many further models have been developed to measure the hardness from a nanoindentation test:

Ni et al.[145] extended the method based on the U_E/U_T ratio for spherical indenters, with the equation:

$$H = 0{,}276\left(\frac{h_{max}}{R}\right)^{1{,}24} \left(\frac{dP}{dh}\right)^2 \left(\frac{U_E}{U_T}\right)^2 \frac{1}{P_{max}}$$

Eq. 2.67

Hainsworth at al.[146] described the loading curve with the same power-law $P = C \cdot h^2$, but defined empirically the constant C as:

$$C = E\left(\phi_m\sqrt{\frac{E}{H}} + \varphi_m\sqrt{\frac{H}{E}}\right)^{-2}$$

Eq. 2.68

for a Berkovich indenter, ϕ_m = 0.194 and φ_m = 0.93.

Page and Pharr[147] proposed another method for the measurement of hardness, based on the P/S^2 parameter. This ratio is indeed directly proportional to H and independent of the tip geometry:

$$\frac{P}{S^2} = \frac{\pi}{4{E_r}^2}H$$

Eq. 2.69

This method is however sensitive on the accuracy of E_r and even a small variation of that parameter can alter significantly the measurement of H.

We have in summary exposed five different methods to measure the hardness. We can now compare their pros and cons, as well as the adequate use of each (Table 2.10).

Table 2.10 – Pros and cons of H indentation-based measurement methods.

Method	Equation	Pros	Cons	Principal use
OPM	Eq. 2.47	Simple method Adapted to automatization	Large error for materials with a large elastic recovery	Most situations, but inaccurate for hard materials
Cheng et al.	Eq. 2.66	Work-based method Consider the unloading part	Only for conical indenters	Adapted to all materials
Ni et al.	Eq. 2.67	Idem Cheng et al. Extension for spherical indenters	Only for spherical indenters	Adapted to all materials
Hainsworth et al.	Eq. 2.68	Accurate for stiff and hard materials	For Berkovich indenters only	Materials with a high elastic recovery
Page and Pharr	Eq. 2.69	Very simple method	Elastic modulus must be precisely known	Most situations

2.4.2.4 Toughness measurement

During a nanoindentation test, tensile stresses are induced in the specimen as the radius of the plastic zone increases. During unloading, additional stresses appear because of the elastic recovery of the material outside of the plastic zone; the end result is a state of residual stress in the indented material. Tensile stresses produced within the material can result in the formation of cracks, the presence of which can often be detected by examination of the indents after testing.

One distinguishes usually four different kinds of residual cracks around indents: radial (also called "Palmqvist cracks"), lateral, median and half-penny (Fig. 2.45).

Radial cracks are vertical half-circular cracks that occur at the surface and emanate from the corners of the residual imprint. These cracks are formed by a hoop stress and extend downward into the material, although they are generally shallow. Lateral cracks are parallel to the surface and occur beneath the surface. They are symmetric according to the load axis; they can often be deflected and extend to the surface, resulting in a surface ring. Median cracks are vertical circular cracks that form beneath the surface along the loading axis (lateral and median cracks are, thus, not directly visible after testing). Finally, if the load is high enough, median cracks may extend and join with radial cracks, forming a large half-penny crack.

The cracks can be subdivided into two categories: those which form on symmetry planes containing the indenter axis (radial and median cracks) and those which form on planes parallel to the surface (lateral crack). The sequence of initiation depends strongly of the indenter geometry, as well as of the material, but median cracks initiate generally first; their extension to the surface, forming half-penny cracks, is due to residual stresses in the elastically strained material surrounding the median cracks. Normal residual stresses are responsible for the propagation of lateral cracks.

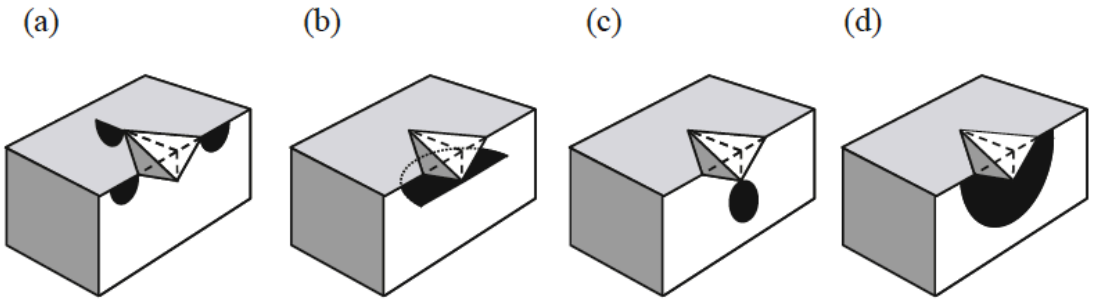

Fig. 2.45 – Indentation cracks; a) radial crack; b) lateral crack; c) median crack; d) half-penny crack; reproduced from Ref [142].

Such cracks can be subdivided into two categories: those that form on symmetry planes containing the indenter axis (radial and median cracks) and those that form on planes parallel to the surface (lateral crack). The sequence of initiation depends strongly of the indenter geometry, as well as of the material. This said, median cracks initiate generally first; their extension to the surface, forming half-penny cracks, is due to residual stresses in the elastically strained material surrounding the median cracks. Normal residual stresses are responsible for the propagation of lateral cracks.

In measuring fracture toughness, radial and half-penny cracks are of particular importance, because they constitute surface cracks that can be directly observed without milling material under the indent.

Palmqvist[148] was the first to demonstrate empirically that the length l of radial cracks could be related to toughness, on metal carbides. A theory describing the evolution of the lateral/radial crack system under Vickers indents was later developed by Lawn, Evans and Marshall[149], based on Griffith's fracture theory.

The Griffith analysis of fracture is based on consideration of potential energy minimization: cracks grow when the rate of release of strain energy U_s that accompanies crack growth exceeds the surface energy plus the rate of energy dissipation from processes that accompany crack formation (such as plastic deformation) U_γ required to create two new crack faces:

$$\frac{dU_s}{dc} \geq \frac{dU_\gamma}{dc}$$

Eq. 2.70

Where c is the crack length. Lawn et al. proposed a model by approximating the elasto-plastic field of a Vickers indentation generating a median crack into (i) the stress field of the same indentation at full load and (ii) the residual stress field present after plastic deformation and complete unloading (Fig. 2.46)

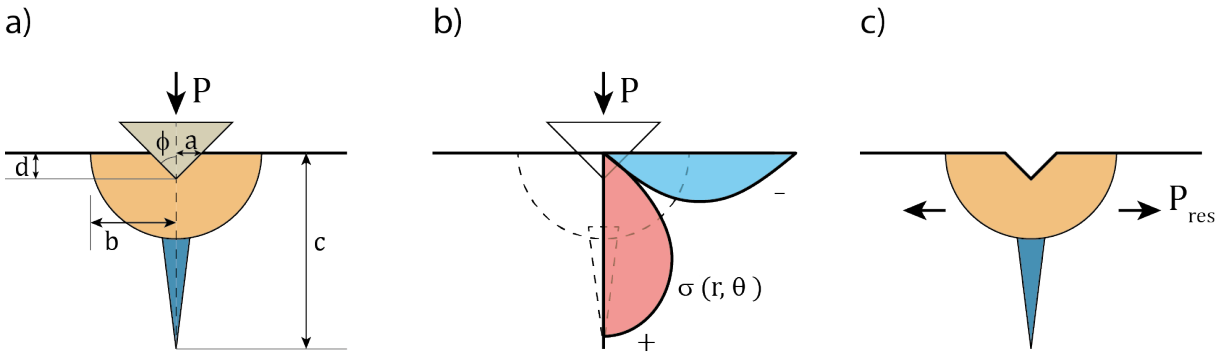

Fig. 2.46 – Lawn analysis of median crack system; a) plastic zone and crack configuration at full load; b) distribution of the elastic stress field at full load; c) residual stress after complete unload. Picture redrawn from Ref [149].

The elastic field (Fig. 2.46-b) operates outside the plastic zone, reaches a maximal intensity at full load and goes to zero at complete unload. The residual field (Fig. 2.46-c) results from the mismatch of tensile forces applied on the surrounding matrix by plastically deformed the material within $r \leq b$; it is maximal at full load and remains as the indenter is removed.

Lawn et al. used the stress intensity factor for center-loaded penny cracks to derive the stress intensity factor for each of those two stress fields:

$$K = \chi \frac{P}{c^{3/2}}$$

Eq. 2.71

with χ the proportionality factor, which depends both on the indenter geometry and on the material.

The residual stress field is evaluated by:

1. virtually removing a half-sphere of material, of radius b, under the indenter;
2. deforming the removed material plastically by indentation with penetration d and contact radius a. The volume being constant, and δV characterizing the volume of the imprint, the half-sphere strain can be expressed as:

$$\frac{\delta V}{V} = \frac{\frac{2}{3}a^2 d}{\frac{2}{3}\pi b^3} = \frac{1}{\pi}\frac{a^2 d}{b^3} = \frac{1}{\pi}\left(\frac{a}{b}\right)^3 cot\,\phi$$

Eq. 2.72

3. the half-sphere is elastically restored to its original radius b, by applying a hydrostatic compression:

$$p_b = B\frac{\delta V}{V} \Rightarrow p_b = \frac{E}{3(1-2\nu)}\frac{1}{\pi}\left(\frac{a}{b}\right)^3 cot\,\phi$$

Eq. 2.73

4. the half-sphere is then reinserted, and the interface coherence is restored. The constraining pressure on the half-sphere is compressive but reduced to a fraction of p_b ($1/2$ for an infinite matrix). The magnitude of the force is obtained by integrating the horizontal stress component over the zone cross section within the crack plane:

$$P_{res} = \frac{\pi b^2}{2} p_b = \frac{E}{6(1-2\nu)}\left(\frac{a}{b}\right)^3 b^2\, cot\,\phi$$

Eq. 2.74

The stress intensity factor for the residual field component is then:

$$K_{res} = f(\alpha)\frac{P_{res}}{c^{3/2}} = \chi_{res}\frac{P}{c^{3/2}}$$

Eq. 2.75

where $f(\alpha)$ is an angular function compensating the effects of the free surface and its value is close to unity. With $H = P/\,a^2$ the proportionality coefficient χ_{res} is then expressed as:

$$\chi_{res} = f(\alpha)\frac{E}{6(1-2\nu)}\frac{a}{b}\frac{a^2}{P}cot\,\phi = f^{\circ}(\alpha)\frac{E}{H}\frac{a}{b}cot\,\phi$$

Eq. 2.76

where the $6(1-2\nu)$ term has been incorporated in the $f°(\alpha)$ function. The a/b ratio can be related to the E/H ratio by using the expanding cavity model that was developed to model the measurement of hardness[150] (Fig. 2.42):

$$\frac{E}{H} = \frac{9}{2}\frac{\left[(1-\nu)\left(\frac{b}{r_0}\right)^3 - \frac{2}{3}(1-2\nu)\right]}{\left[1 + ln\left(\frac{b}{r_0}\right)^3\right]}$$

Eq. 2.77

where r_0 is the radius of the cavity. A log-log plot of b/r_0 versus E/H gives a nearly linear function, i.e. it is possible to approximate Eq. 2.77 with a power law:

$$\frac{b}{r_0} = C \cdot \left(\frac{E}{H}\right)^m$$

Eq. 2.78

The cavity volume being in our case the volume of the imprint, Eq. 2.78 becomes

$$\frac{b}{a} = \left(\frac{E}{H}\right)^m \left(\frac{cot\,\phi}{\pi}\right)^{\frac{1}{3}}$$

Eq. 2.79

The final form of χ_{res} is then:

$$\chi_{res} = f'(\alpha)\left(\frac{E}{H}\right)^{1-m} cot\,\phi^{\frac{2}{3}}$$

Eq. 2.80

Lawn et al. proposed an empirical value of $m = 0.5$.

Lawn et al. evaluated similarly the stress field at peak load, by integrating a point-load Boussinesq stress field $\sigma(r,\alpha) = g(\alpha)\cdot P/r^2$, $g(\alpha)$ being the angular function represented in Fig. 2.46-b, for $b \leq r \leq c$[151,152].

$$K_e = P \cdot f(\alpha) \cdot g(\alpha) \sqrt{\frac{2}{c}} \int_b^c r\sigma(r) \frac{dr}{\sqrt{c^2 - r^2}} = f(\alpha)g(\alpha)\, ln \left\{ \frac{c}{b} \left(1 + \sqrt{1 - \frac{b^2}{c^2}} \right) \right\} \frac{P}{c^{\frac{3}{2}}}$$

Eq. 2.81

Because $c >> b$, Eq. 2.81 reduces to

$$K_e = f(\alpha)g(\alpha)\, ln \frac{2c}{b} \frac{P}{c^{\frac{3}{2}}} = \chi_e \frac{P}{c^{\frac{3}{2}}}$$

Eq. 2.82

At equilibrium, both components must be summed, and the critical toughness is then $K_c = K_{res} + K_e$. The authors observed a net dominance of K_{res} over K_e, and because of the reversibility of the elastic term, the equilibrium crack length c at complete unload depends only on χ_{res}. They confirmed experimentally the predominance of K_{res} over K_e.

Laugier[153] extended this model for half-penny cracks, that consist of median cracks propagated up to the surface, and which are very often observed on ceramics. The fracture toughness is now given by:

$$K_c = x_v \sqrt{\frac{a}{l}} \left(\frac{E}{H} \right)^{2/3} \frac{P}{c^{3/2}}$$

Eq. 2.83

with x_v = 0.015 for a Vickers indenter and x_v = 0.016 for a Berkovich indenter.

Niihara et al.[154,155] proposed two different modified equations, one for radial cracks, the other for half-penny cracks:

$$K_{C,HP} = A_1 \left(\frac{E}{H} \right)^{\frac{2}{5}} \frac{P}{c^{\frac{3}{2}}}$$

$$K_{C,R} = A_2 \left(\frac{E}{H} \right)^{\frac{2}{5}} \frac{P}{a\sqrt{l}}$$

Eq. 2.84

with A_1 and A_2 being respectively the constants for half-penny and radial cracks.

When indenting very small particles and generating a crack, the Berkovich indenter is most of the time inadequate and a much sharper cube corner tip is needed. Field and Tada [156,157] investigated fracture toughness measurements performed on very small particles, using such indenters. They

proposed to determine the crack length c from the loading curve, such that no crack length measurement is required.

The energy approach has been investigated for indentation toughness by Zhang et al.[158]. Here, the toughness is calculated by determining similar parameters as in measurement of the hardness: U_T and U_E:

$$K_C = \lambda \left(\frac{U_T}{U_E}\right)^{\frac{1}{2}} \frac{P_{max}}{c^{\frac{3}{2}}}$$

Eq. 2.85

The constant λ has been calibrated and $\lambda = 0.0695$.

We have described four indentation methods to measure the fracture toughness based on Lawn's derivation. We can now summarize their pros and cons, as well as the adequate use of each in Table 2.11.

Table 2.11 – Pros and cons of K indentation-based measurement methods

Method	Equation	Pros	Cons	Principal use
Lawn et al.	Eq. 2.71	Simple method Simple analysis	Analysis can be complicated (more than one crack-type) Not the most accurate model For Palmqvist cracks only	Adapted to brittle materials
Laugier	Eq. 2.83	Simple method Simple analysis	Idem Lawn For half-penny cracks	Adapted to brittle materials
Niihara et al.	Eq. 2.84	Simple method Simple analysis For both Palmqvist and half-penny cracks Most accurate model	For Berkovich and cube corner only	Adapted to brittle materials
Zhang et al.	Eq. 2.85	Work-based method E and H are not required	Determination of crack length can be complicated	Adapted to brittle materials

2.4.3 Micromechanical Tests

If nanoindentation is a relatively convenient way to measure fracture toughness at the micron scale, it has been strongly criticized and can lead to error in measurements. As a result, other micro-mechanical methods have been developed, based on other loading modes (scratching, impact, etc.) or on the rupture of pre-cracked or notched specimens having one of specific geometries.

The measurement of K_C via a scratch test has been proposed by Akono et al.[159]. Toughness in the sense of this test is a function of the horizontal force F_T, the perimeter of the indenter p and the horizontal projected load bearing contact area A:

$$K_C = \frac{F_T}{\sqrt{2pA}}$$

Eq. 2.86

Another method, based on the splitting of FIB milled pillars, has been developed by Sebastiani et al.[160]:

$$K_C = \gamma \frac{P_c}{R^{\frac{3}{2}}}$$

Eq. 2.87

where P_c is the load at failure, R is the pillar radius and γ is a calibration constant, which depends on the material and is evaluated by numerical techniques.

Frutos et al.[161] used repeated nano-impacts to propagate a crack with the aim of measuring the fracture toughness of alumina. In this case, it was possible to follow the evolution of the crack, progressing from radial to half-penny for each impact.

The most common mechanical test used to measure toughness at the microscale consists in cutting a notched cantilever beam out of the sample and testing it to fracture in bending. The simplest crack initiator is a straight notch. Iqbal et al.[162], Di Maio and Roberts[163], and Kupka et al[164] developed such a method. In this case, if one assimilates the notch to a crack, the fracture toughness is then easily determined by the general equation

$$K_{IC} = \sigma_c \sqrt{\pi a} \cdot F\left(\frac{a}{b}\right)$$

Eq. 2.88

where a is the initial crack length (i.e. the depth of the notch), and $F(a/b)$ is a geometrical factor. Iqbal used this method to determine the anisotropic fracture toughness of monocrystalline NiAl;

they machined 8 µm long beams in two different orientations using FIB and measured two different toughness values: 3.52 MPa·m$^{0.5}$ for the "soft" orientation and 5.12 for the "hard" orientation. Di Maio and Roberts machined pentagonal (truncated triangle) straight-notched beams in silicon, orienting the notch along a (111) fracture plane; they obtained a toughness of 1.1 MPa·m$^{0.5}$, coherent with literature references for the material. They transposed then the method to CVD-deposited WC on a steel substrate and measured a fracture toughness of 3.2 MPa·m$^{0.5}$. Kupka et al. measured the fracture properties of brittle grain boundaries in aluminium lithium alloys using notched micro-cantilever beams.

Mueller et al.[165] have replaced the straight notch by a chevron-notch (Fig. 2.47). For that special geometry, cracks nucleate and propagate in a stable way before fracture, with the advantage that fracture occurs (i) in an area unaffected by FIB effects and (ii) by propagation of a "real", sharp crack instead of a notch.

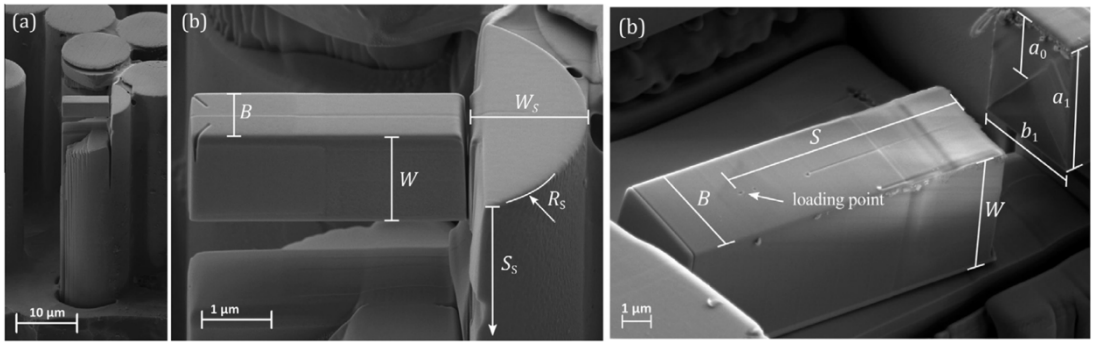

Fig. 2.47 – Chevron-notched beam; a-b) chevron-notched beam in polycrystalline alumina fibers; c) chevron-notched beam in fused quartz; figure reproduced from Ref [165].

Mueller at al. measured in this way the fracture toughness of polycrystalline alumina to find K_{IC} = 2.3 MPa·m$^{0.5}$, and of fused quartz, giving K_{IC} = 0.65 MPa·m$^{0.5}$, both in agreement with literature values.

The cantilever beam can also be used to test the resistance of interfaces[166] or coatings[167,168].

A variation of the cantilever beam is the clamped beam (Fig. 2.48), where both extremities are fixed, and a straight notch is milled using the FIB in the middle of the beam. Jaya and Jayaram[169] experimented that configuration, as well as Cui and Vinci[170] who used a triangular notch. The geometrical factor is determined via numerical FE simulations.

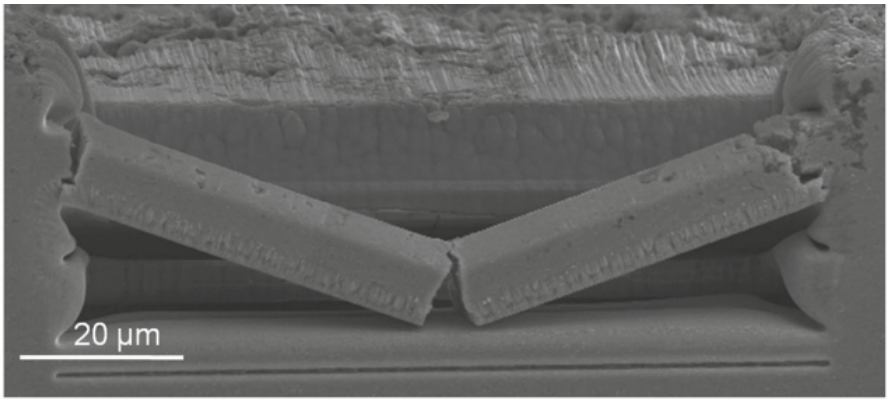

Fig. 2.48 – Clamped beam Si specimen; reproduced from Ref [169].

Jaya and Jayaram used that method to measure the toughness of NiAl and silicon; this gave values of K_{IC} = 2.1 MPa·m$^{0.5}$ for Si, which is higher than most reported values, and 3.8 MPa·m$^{0.5}$ for NiAl, in accordance with reference data. Cui and Vinci adapted the method for bowtie-shaped beams with a chevron-notch (Fig. 2.49); they measured the fracture toughness of fused quartz by applying a cyclic load to cause progressive crack extension, and found K_{IC} = 0.62 MPa·m$^{0.5}$, a value coherent with the literature (and the value measured at the microscale by Mueller et al.).

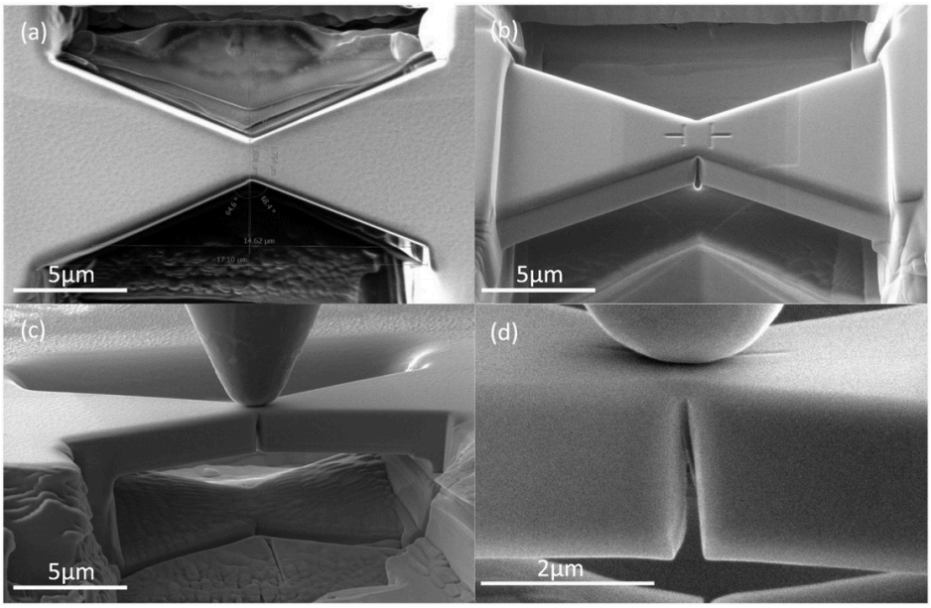

Fig. 2.49 – Fused quartz bowtie specimen; figure reproduced from Ref [170].

Another creative method that has been used to measure fracture toughness is the double cantilever beam (Fig. 2.50)[171]. This method has been applied with good results to various materials including SiC, GaAs and CrN-based coatings.

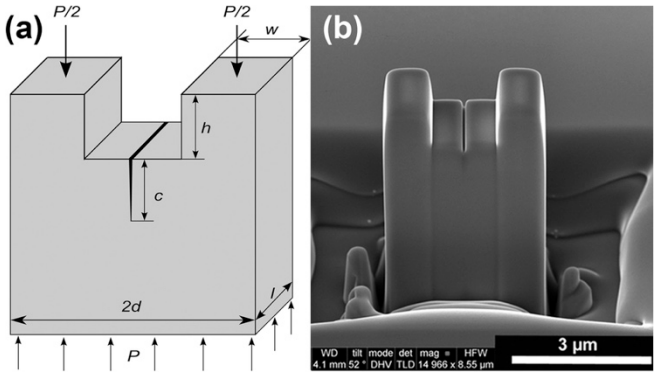

Fig. 2.50 – Double cantilever beam (SiC); figure reproduced from Ref [171].

In practice, after machining, the specimen is loaded in compression, up to failure at critical load P_c, in a nanoindentation apparatus using a flat punch, which pushes on the two edges protruding on top of the specimen (Fig. 2.50). The fracture toughness is then calculated by the following equation:

$$K_{IC} = \sqrt{3}\frac{(e-\mu h)}{bd^{\frac{3}{2}}}P_c$$

Eq. 2.89

where $e = \frac{1}{2}(d-w)$, μ is the coefficient of friction between the indenter and the sample, and b is the thickness of the beam. A value of K_{IC} = 3.6 MPa·m$^{0.5}$ was obtained for SiC, and 0.57 MPa·m$^{0.5}$ for GaAs. The toughness of columnar-grown CrN coatings was also measured in this way, giving K_{IC} = 1.75 MPa·m$^{0.5}$, as was that of a CrAlN/Si_3N_4 coating, which gave 3.26 MPa·m$^{0.5}$.

B. Merle and M. Göken[172] used a bulge test to propagate a crack and then measure the toughness of thin films: a pre-crack is introduced in a membrane, which is deformed by the pressure of a gas, causing the membrane to bulge, which in turn provides a driving force for crack propagation (Fig. 2.51).

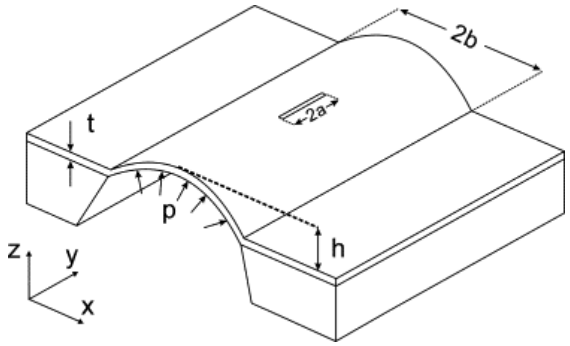

Fig. 2.51 – Bulge test; figure reproduced from Ref [172].

This method was used to measure the fracture toughness of amorphous CVD deposited silicon nitride, giving K_{IC} = 6.3 MPa·m$^{0.5}$.

In surveying the literature, no results were found for micro-mechanical tests on carbides.

2.5 Concluding remarks

Carbides constitute a very important class of materials, notably for the machining industry, where high hardness, high stiffness, sufficient toughness and often resistance to elevated temperature are key parameters. In practice, basic binary MC carbides are generally deemed sufficiently hard and stiff materials to withstand such extreme operating conditions as are found in applications of tool

steel. Their toughness, which is often low, is improved by combining the carbides with a hard but tough metallic matrix, or by using them as coating material over a tougher substrate. Given that machining often constitutes an important part of the price of engineering components (up to 25%[173]), interest in developing more efficient cutting tools remains high.

The most investigated option consists in using harder and stiffer reinforcements, be it in cemented carbides or tool steel. With carbides, an interesting possibility to increase their intrinsic mechanical properties is to use their mutual solubility, or in other words alloying of MC carbides. Many systems have been investigated during the 1970s and 1980s, including carbonitrides; most of the publications presented the evolution of Vickers microhardness versus composition. Under the assumption that the increase in hardness is related to the carbide bond structure, Jhi et al.[55] proposed a complete physical interpretation based on atomic simulation and band structure.

As a result of that work and of progress in *ab initio* materials simulation, numerical investigations of carbide systems have proliferated in recent years, aiming to predict not only the hardness, but also other important mechanical properties, such as the Young's modulus or the fracture toughness. In parallel, and with the development of nanoindentation techniques, several authors have tried to correlate mechanically the predictions of atomic simulations, by indenting bulk carbides.

With this thesis, we aim to go one step further in measuring directly the properties of carbide reinforcements embedded in their matrix. We also aim to optimize both hardness and Young's modulus by processing and characterizing ternary and quaternary MC carbides.

CHAPTER 3:

MICROSTRUCTURES & PROCESSING

DESCRIPTION OF CORRECTIONS BROUGHT TO THE SUBMITTED THESIS VERSION: Table 3.13 has been corrected for errors present in the original thesis version.

This chapter first describes the processing methods that we applied to produce carbide particles reinforcing iron, then reports the microstructures that we obtained and the different analyses that were used for characterization of their microstructure. Five binary MC carbides (M = Ti, V, Ta, Nb, W) have been produced, as well as five ternary MM'C carbides (MM' = TiW, TiV, TiTa, TiNb, TaV) and, finally, the quaternary Ti-Ta-V-C system.

3.1 In situ carbide formation

Taking as a reference the tool steel industry, where carbides are frequently produced *in situ* by precipitation within a liquid iron phase, samples of this work were prepared by arc-melting high-purity (binary) cast iron together with selected amounts of transition metal. Carbides are then produced *via* a chemical reaction between the metallic elements and carbon in a liquid composed mainly of iron. In such complex systems, several carbides with various morphologies can be formed, depending on the temperature, the cooling rate and the composition. In order to obtain the desired composition, as well as a shape and size amenable to mechanical testing of the particles, additional heat treatment was occasionally applied, using the dedicated software ThermoCalc® as a guide for interpretation and design of heat-treatment schedules.

3.1.1 Design of carbide particles reinforcing iron: raw materials and carbide compositions

Four ternary titanium-based carbides, namely (Ti,M)C, with M = W, Ta, V and Nb, as well as an additional ternary (Ta,V)C, and a quaternary (Ti,Ta,V)C MC carbide have been investigated. We chose these five transition metals because, among the large number of possible compositions, those systems are known to produce very strong carbides and because those are among the most common transition carbides used in industry. The carbides are formed *in situ* from high-purity powders, granules or chips of the metallic elements. In order to reduce the total surface, granules are preferred rather than powders. Table 3.1 summarizes the main features of the selected materials.

Table 3.1 – Raw materials used for carbide formation

	Purity	Shape	Supplier
Fe	99.98%	chips	Sigma Aldrich, St-Louis, US
Ti	99.99%	granules	ABCR, Karlsruhe, DE
W	99.9%	powder	Alfa Aesar, Haverhill, US
V	99.7%	granules	ABCR, Karlsruhe, DE
Nb	99.9%	powder	Wah Chang, Albany, US
Ta	99.98%	powder	ABCR, Karlsruhe, DE

Carbon in cast iron was selected as the carbon source. The alloy was produced by melting pure iron chips in a graphite crucible within a custom-made induction furnace setup, powered by a CELES® 12 kW, 22A power source. The crucible is cylindrical, with an aperture of 2 cm, and is made of EDM 200 high-quality graphite. The temperature is set at 1500°C and the process lasts 5 minutes, in order to allow carbon diffusion into liquid iron. The solidified rod is then chemically analyzed by the Combustion Infrared Detection Technique (LECO® CS844) to determine the carbon content: an average composition of 5.5 wt% of carbon was measured. In this process, the iron dissolves a portion of the crucible (as predicted by the phase diagram, Fig. 3.1) and begins to melt once its carbon content is high enough. The liquid phase, once formed, becomes then richer in carbon and reaches a maximal composition between 5 and 5.5 wt% at that specific temperature, this concentration being the maximum solubility of graphite in liquid iron at 1500°C (Fig. 2.3).

The carbide-containing samples are designed to have a carbide volume fraction, ϕ_{car}, equal to 0.4. The respective masses of each element are then calculated from that parameter.

$$\phi_{car} = \frac{V_{car}}{V_{car} + V_{matrix}} = \frac{\frac{m_{car}}{\rho_{car}}}{\frac{m_{car}}{\rho_{car}} + \frac{m_{matrix}}{\rho_{matrix}}}$$

Eq. 3.1

where V represents the volume, m the mass and ρ the density, respectively of the carbide and of the matrix. The carbide density is assumed to be either known (binary carbides) or is otherwise approximated using the simple rule of mixtures from densities of relevant binary densities (for both ternary and quaternary carbides). The total mass of the sample is also fixed at $m_{tot} = m_{car} + m_{matrix} \approx 1.5$ g, this choice being made simply because of the furnace size limitations. We assume that the entire carbon amount present in the cast iron was involved in alloying element carbide formation (with, thus, no formation of cementite), and for simplicity we consider the matrix as pure iron with $\rho_{matrix} = \rho_{iron}$ (at room temperature this is justified by the fact that carbide-forming alloying additions will lower the carbon equilibrium concentration in iron even lower than its value in the binary Fe-C system).

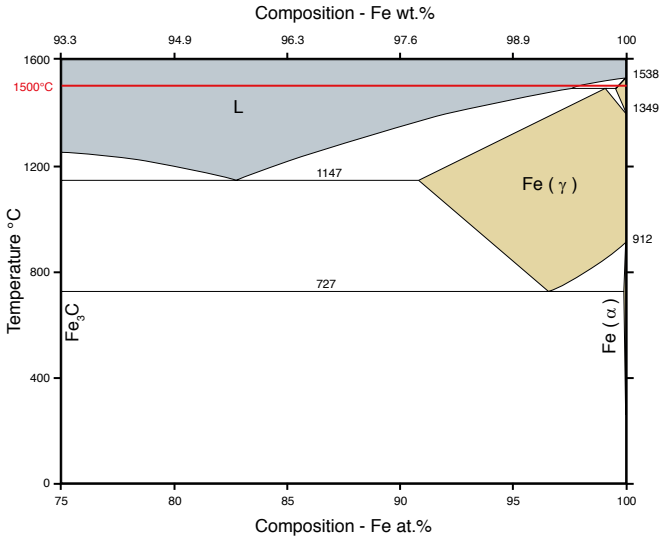

Fig. 3.1 – C-Fe partial phase diagram. The process temperature, 1500°C, is outlined.

The only remaining unknown parameter is then the carbide mass:

$$m_{car} = \frac{m_{tot}}{1 + \frac{\rho_{iron}}{\rho_{car}}\left(\frac{1}{\phi_{car}} - 1\right)}$$

Eq. 3.2

The carbide mass m_{car} is also linked according to its desired composition. For a quaternary carbide of $\mathrm{M^1}$, $\mathrm{M^2}$ and $\mathrm{M^3}$ metallic elements, we define the composition as $(\mathrm{M^1_xM^2_yM^3_{1-x-y}})\mathrm{C}$, where x and y are the atomic fraction. For a ternary compound, $y = 1 - x$. The total number of moles N of atoms contained in m_{car} is obtained as:

$$N = \frac{m_{car}}{M_{mol}\left(M_x^1 M_y^2 M_{1-x-y}^3 C\right)} = \frac{\sum_i m_{M^i} + m_C}{\sum_i b_i M_{mol}(M^i) + M_{mol}(C)}$$

Eq. 3.3

where $b_i = x, y, 1-x-y$ for $i = 1, 2, 3$. The required mass of each element is then given by:

$$m_{M^i} = N \cdot b_i \cdot M_{mol}(M^i)$$
$$m_C = N \cdot M_{mol}(C) \leq 0.055 \cdot m_{matrix}$$

Eq. 3.4

In systems containing vanadium, an extra amount of 11.8 at% V is systematically added to the desired composition, to compensate for the large solubility of V in Fe. This value was calculated using ThermoCalc for pure cast iron containing 5.5 wt% of C.

ThermoCalc was also used to determine the phases that should appear for a given system. An example of phase fraction calculation is given in Fig. 3.2 for the ternary composition $Ti_{0.5}Ta_{0.5}C$.

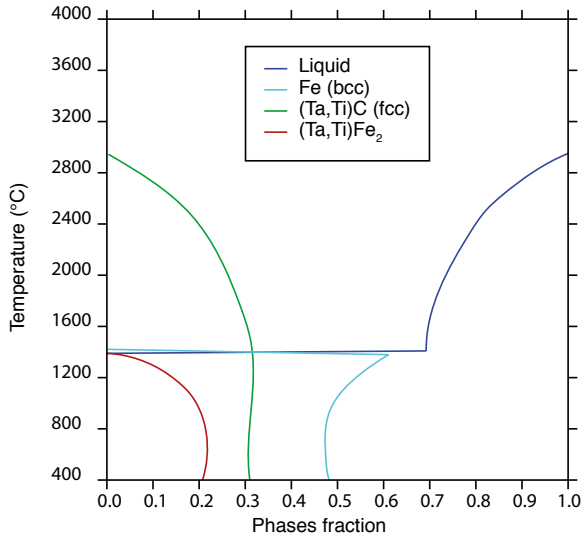

Fig. 3.2 – Phases fraction for the $Ti_{0.5}Ta_{0.5}C$ composition, based on ThermoCalc predictions.

More generally, ThermoCalc, as a thermodynamic calculation software, can be used to calculate phase diagrams, equilibrium phase fraction (for a given composition) and phase compositions (at a fixed temperature). We use it as a support tool when designing our ternary and quaternary compositions, to get an idea of the expected phases that should be formed in a given system, and to determine the theoretical compositions of our samples.

3.1.2 Arc Melting

The formation of carbide reinforcements by an *in situ* process requires a specific furnace:

- The temperature should be high enough to melt metals of high fusion temperature (T ≥ 2500°C);

- The process should be done under a controlled atmosphere, to avoid the formation of oxides.

The arc melter furnace is one of the best options, because it is possible to reach temperatures higher than 3000°C, and to operate under gettered Argon. The small laboratory-scale arc melter brings with it some limitations, however, which include:

- The size of the sample: typically, samples of < 5 g are well melted, while larger samples are more difficult to melt entirely. This value is further decreased to < 2 g in our systems due to the very high melting temperature of transition metals;
- The crucible electrode is water-cooled, and a strong temperature gradient exists within the sample, from the top to the bottom in contact with the crucible, during the cooling, which also occurs relatively fast;
- The tip electrode is made of tungsten, small particles of which may contaminate the sample during the process;
- The peak sample temperature is unknown.

We used an Edmund BÜHLER (Bodelshausen, DE) laboratory arc melter, model MAM-1. Usage and the underlying principle of an arc melter furnace are relatively simple: an electric current passes from a tungsten electrode to a copper crucible through an argon atmosphere, creating an arc that heats the sample, as schematically shown in

Fig. 3.3.

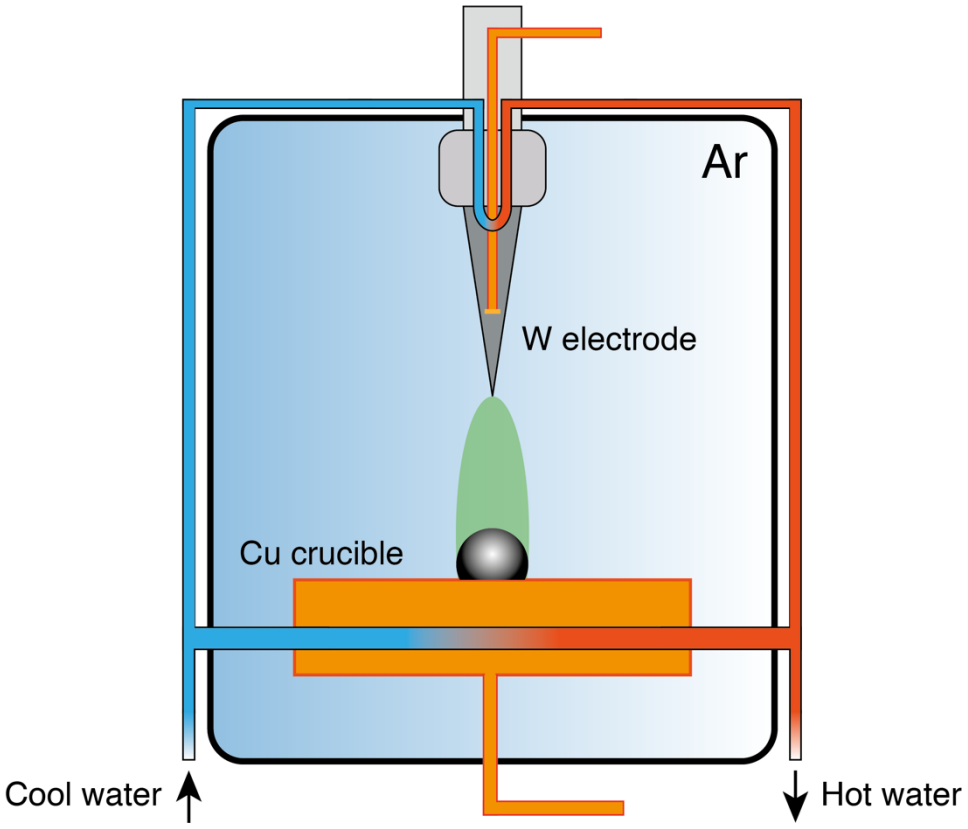

Fig. 3.3 – Simplified schema of a laboratory arc melter furnace, similar to the MAM-1 BÜHLER model we used for our processing.

The temperature of the sample in the furnace depends on the current, the weight of the sample, its electrical conductivity and its distance from the tungsten electrode. As stated previously, the exact temperature is unknown.

The design of the furnace requires a cooling system that prevents the crucible and the tip from melting; that cooling influences however strongly the solidification process of the sample, as it imposes a relatively high cooling rate and promotes then the formation of out-of-equilibrium microstructures.

The melting procedure can be summarized as:

1. The sample components are cleaned with acetone, as is the inside of the furnace chamber;
2. A primary vacuum of 10^{-2} mbar is applied, the chamber is then filled with 99.9999% extra pure Argon;
3. Five cycles of vacuum-Argon are done to purge the pipes, and the vacuum is progressively improved up to 10^{-3} mbar. The chamber is then filled with Ar;
4. A piece of pure Titanium is molten, acting as an oxygen getter;
5. A first piece of compacted transition metallic powders or granules is molten. The compaction avoids a dispersion of the small particles when the arc is created;
6. That sample is melted and cooled, at least 5 times, turning it in order to ensure a good homogeneity of its microstructure;
7. The metallic piece is then molten with the cast iron, in order to form the carbides.
8. The process is repeated at least 5 times to promote a good homogeneity, rotating the sample.

Then, the sample is analyzed in a scanning electron microscope (SEM).

3.1.3 Sample preparation and analysis

Before being mechanically tested, the sample must be adequately prepared. The metal piece is first cut in half alongside the thermal gradient of the arc melter. That specific cut allows to observe the different microstructures that can be formed at different cooling rates.

The sample is then embedded in a conductive polymeric resin, containing carbon filler to avoid charging effects in the SEM. The thickness of the resin is kept as small as possible, typically < 10 mm, to minimize the global sample compliance during the mechanical tests.

The embedded sample is then polished with monocrystalline diamond particles, from 9 μm down to ¼ μm. After the 1 μm polish, the sample exhibits a mirror surface, but the last ¼ μm step is crucial to reduce the surface roughness and allow to measure meaningfully tip penetrations of a few nanometers.

The sample is analyzed in a SEM: the microstructure is observed and investigated (phase fraction, morphology, etc.) and the phase compositions are measured by EDX within the particles. For a given phase, several particles are tested, and the average value is then calculated. The amount of carbon being difficult to determine accurately, EDX is used to measure the ratio of transition

metals in carbide particles, with a typical precision of ± 1.5 at%. Elemental mapping is performed to confirm the overall composition of the sample.

Finally, a XRD analysis is performed on flat surface to detect the crystalline structure of the phases and to confirm the EDX analyses as well as ThermoCalc prediction.

The various apparatuses, equipment and consumables used for sample preparation and analysis are:

- Saw: PRESI® (Le Locle, CH) Mecatome T180, equipped with a diamond blade;
- Resin: STRUERS® (Ballerup, DK) PolyFast thermosetting phenolic resin with carbon filler;
- Coater: PRESI® Mecapress 3;
- Polishing: STRUERS® DAP-7, equipped with an additional VEXTA® counter-rotating motor;
- Diamond particles: PRESI® Diamond suspension, polycrystalline particles;
- SEM: ZEISS® (Oberkochen, DE) Merlin SEM, equipped with a Gemini II column. We used the microscope in SE mode, with a voltage of 2 kV and a probe current of 350 pA;
- EDX: OXFORD Instruments® (Abingdon-on-Thames, GB) X-Max^N Silicon Drift Detector, with ad detector size of 80 mm^2, mounted on the ZEISS Merlin SEM. We used a standard tension of 10 kV. The analysis software is ETAS® INCA V7.0;
- XRD: PHILIPS® (Amsterdam, NL) X'Pert X-ray diffractometer, equipped with a Cu-Kα source, angles 2θ from 10° to 90°.

3.1.4 Heat-treatment

In order to verify whether a carbide particle is suitable for mechanical testing, three criteria were taken into consideration: size, homogeneity and composition.

The size is the most crucial parameter: if a particle is too small, it is then impossible to apply a load with sufficient precision, and/or the applied stress field extent can exceed the dimensions of the particle and overflow into the matrix. The limit of the particle size depends on the test: a modulus measurement test can be done on particles as small as ~1 μm, whereas a toughness test is unthinkable for particles smaller than 10 μm, because there is no room for crack propagation. In general, tests inducing only elastic deformation can be performed on very small particles, but once plasticity or cracks are involved, the minimal particle dimensions rise.

Homogeneity in composition is another important factor in collecting meaningful data. Within error of the performed analyses, the composition should be constant inside the tested zone. A different composition is often found near the interface between particle and the matrix, as compared to the particle core; if the core is sufficiently large, the test is done on the core (only).

The composition of the particles should be as close as possible to the aimed-for values. Regarding the microstructure, as the melting process imposes rapid cooling, the microstructure can often deviate from thermodynamic equilibrium predictions, such that other phases can appear or

predicted phases might not have formed. This was ensured as was the composition, using SEM analyses coupled with EDX, thus defining the particles suitable for testing.

If the previous requirements are not fulfilled, a simple way to increase the size of the particles, make them homogeneous or change their composition consists in applying an adequate heat treatment. Heating the sample promotes a more stable microstructure: the particles grow, reducing the particle-matrix interfacial area; they also become more homogeneous, reducing the composition gradient and their composition moves closer to the thermodynamic prediction. The phenomenon is governed by solid state diffusion, which becomes increasingly important as the temperature rises. The selected temperature is then chosen to be as high as possible, while still in the region of stability of the desired solid phase. Heat-treating temperatures used here varied from 1200°C to 1500°C depending on the system. ThermoCalc predictions were used as a guide in defining the proper temperature.

The duration of the heat treatment is also crucial: since diffusion is a statistical phenomenon, based on vacancy-atoms exchanges, it requires time to induce changes in a micron-scale microstructure. The heat treatments that we applied lasted typically from 2h to 72h, depending on the material and on the temperature of the treatment.

Two kinds of furnace were used: a tubular resistive and an induction furnace. The former is made of an alumina tube, surrounded by electrical resistances; the tube is sealed, and vacuum is applied with a turbomolecular pump. As the tube is large and not perfectly sealed, the best vacuum did not exceed $5 \cdot 10^{-3}$ mbar. Titanium sponge was introduced inside the furnace close to the sample to serve as an oxygen getter and the pump was continuously running during the treatment. That furnace allowed us to apply long heat treatments with a maximal temperature of 1500°C. The second furnace is a simple induction furnace: a coil generates a magnetic field that drives the movement of induced currents, which heat the sample in a quartz tube under Argon. As drawbacks, heat treatments longer than 2 hours cannot be performed, and the cooling rate is faster than a resistive furnace, since the tube is less well insolated from a thermal standpoint.

Once the first heat treatment was performed, the sample was analyzed again by SEM and EDX and eventually a second heat treatment (at different temperature or holding time) was performed. The cycle was repeated unless the requirements of size and composition were satisfied. In case a heat treatment was performed, important parameters as temperature and holding time are specified for each sample in the next section.

Once the desired composition and microstructure are obtained, the sample is submitted to a last polishing step before being analyzed in detail by SEM, EDX and XRD, before subsequent mechanical characterization.

3.2 Carbide microstructures

Five binary carbides, five ternary systems of carbide particles embedded in steel and an additional quaternary carbide system were investigated as summarized below:

- Binary: TiC, WC, TaC, VC and NbC;

- Ternary: $(Ti_xW_{1-x})C$, $(Ti_xV_{1-x})C$, $(Ti_xTa_{1-x})C$, $(Ti_xNb_{1-x})C$ and $(Ta_xV_{1-x})C$;
- Quaternary: $(Ti_xTa_yV_{1-x-y})C$

The composition of ternary and quaternary carbides systems was varied and tailored in order to cover the entire range of composition. Collected EDX and XRD spectra, as well as the phase diagram calculated with ThermoCalc (except for the $(Ti_xW_{1-x})C$ system), are provided in Appendix C.

3.2.1 Binary carbides

Starting with the systems containing binary carbides, Fig. 3.4 depicts the microstructure of TiC carbides grown *in situ* in a steel matrix.

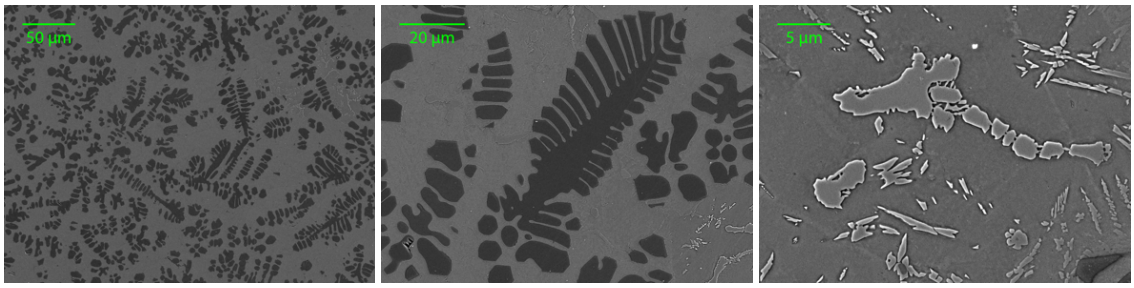

Fig. 3.4 – Microstructure of TiC particles embedded in a steel matrix, raw from arc melter.

TiC particles, which appear in black in the SEM images (Fig. 3.4 left & center) are dendrites, typical of nucleation and growth of a primary phase within the liquid phase. The microstructure is homogeneous over the sample and is not affected by the thermal gradient associated with the arc melter furnace. Regarding the steel matrix, EDX analyses revealed that about 10 at% of Ti remains in solution, coherently with the Fe-Ti phase diagram, which exhibits such a solubility for Ti in Fe at 1290°C. Finally, another second phase is present in the microstructure as suggested by the light grey particles illustrated in Fig. 3.4-c. According to the EDX and XRD results, this phase was identified as Fe_2Ti. These particles can be found in random areas over all the surface of the sample. Image analysis of Fig. 3.4-a gives a TiC volume fraction of 32.1%.

TiC particles are homogeneous in composition and EDX analysis did not show any signal of impurity elements. Their size, in the range of 20-60 µm satisfied well the requirements for testing.

The microstructure observed in WC/Fe samples produced by arc melting is reported in Fig. 3.5.

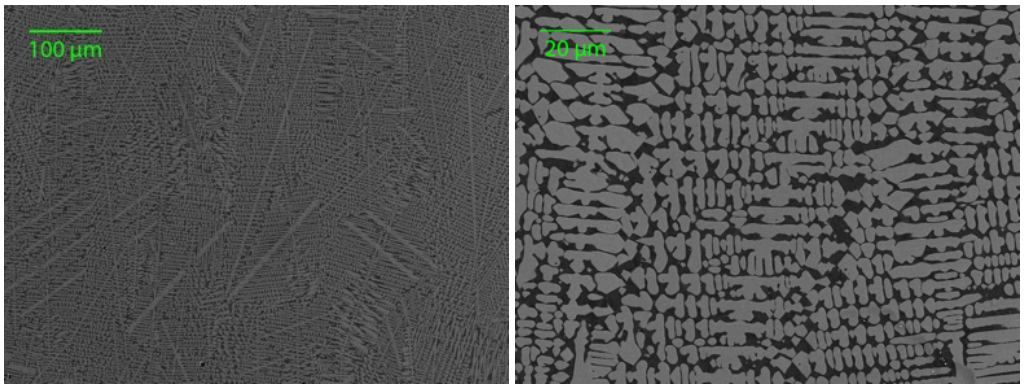

Fig. 3.5 – Fe/WC microstructure, after arc melting.

Despite the homogeneity of the microstructure and the proper size of the particles embedded in iron, the dendritic particles, whose phase fraction exceeds 40 vol%, are composed of a ternary (Fe,W)C carbide, identified using EDX and XRD data as the Fe_3W_3C phase. The WC phase does not form during the arc melting process, probably because of the high cooling rate, such that formation of WC requires a subsequent heat treatment. Therefore, the sample was submitted to heat treatment at 1400°C for 2h in the induction furnace; the new microstructure is given in Fig. 3.6.

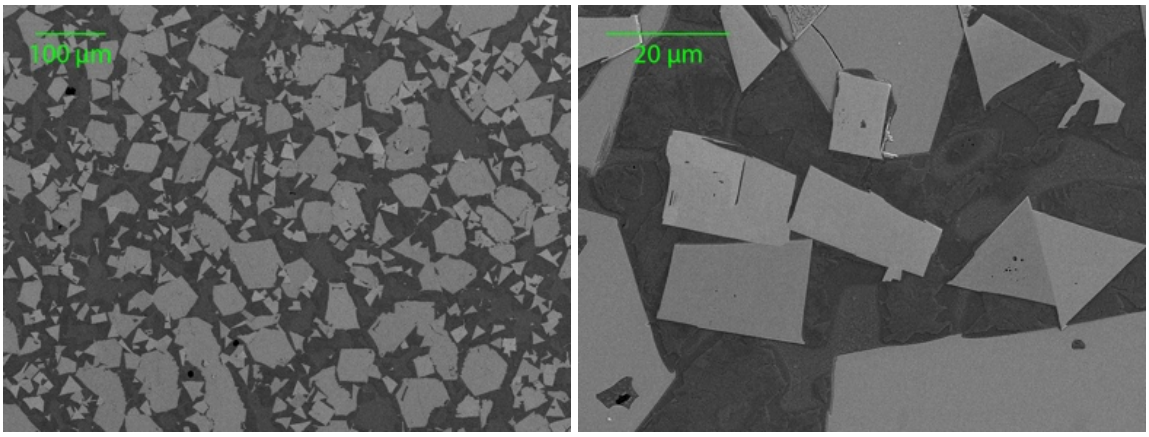

Fig. 3.6 – Fe/WC heat-treated at 1400°C/2h.

After the heat treatment, SEM micrographs show the presence of grey angular particles of pure WC and of light grey rounded particles of Fe_3W_3C. The size of the WC particles (15-20 µm) is adequate for our mechanical tests, as well as their homogeneity. An analysis of Fig 3.6-left reveals the following phase volume fraction: 48.9% of second phases, divided in this way: 25.1 vol % of WC and 74.9 vol % of Fe_3W_3C.

The VC system did not require any heat treatment after the melting process, as the VC particles were sufficiently large for our tests. The microstructure of the sample is given in Fig. 3.7.

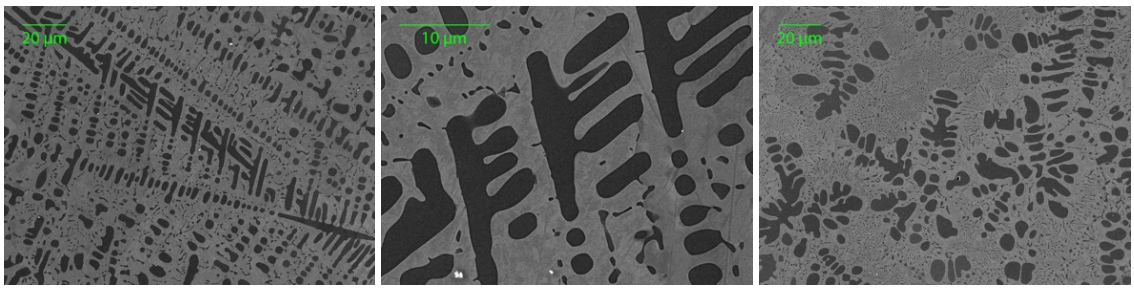

Fig. 3.7 – Fe/VC microstructure, after arc melting.

The largest black particles are composed of pure VC, as are the smaller eutectic-like particles. The sample is homogeneous in terms of composition, even if the morphology of the VC particles changes over the specimen volume. Dendrites are found at the bottom, near the cool copper plate of the arc melter (Fig 3.7-left), while the top of the specimen is mainly made of spheroidal particles (Fig 3.7-right). EDX reveals that the matrix contains around 10 at% of vanadium. According to the Fe-V phase diagram, V can be soluble in Fe up to 20 at%, depending on the temperature. As mentioned in the previous section, an extra amount of 11.8 at% of vanadium with respect to iron was added to compensate for such high solubility. Image analyses of Fig 3.7-a and Fig 3.7-c reveal a VC volume fraction of 28.5% and 29.4%.

The microstructure of the iron/TaC sample after the melting process is given in Fig. 3.8.

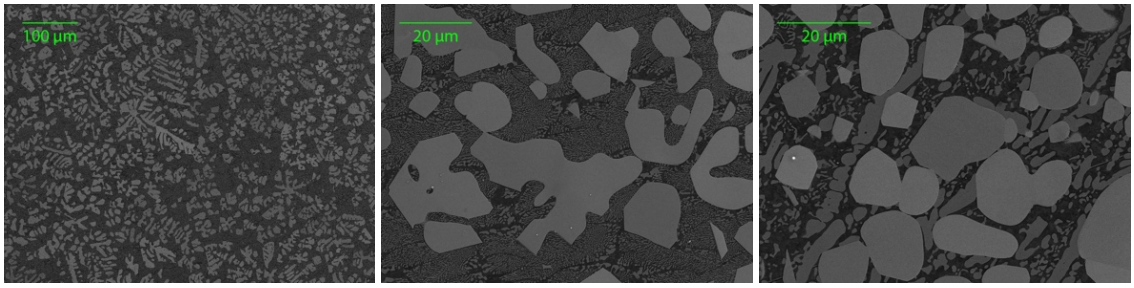

Fig. 3.8 – Fe/TaC microstructure, after arc melting.

The big grey particles of Fig. 3.8-center are composed of TaC, while the fishbone-like phase consists of the Laves phase Fe_2Ta, accordingly both to EDX and XRD analyses. In the microstructure shown in Fig. 3.8-c, we can also identify large (several tens of micrometers) spheroidal particles of TaC. Even though one can distinguish differences in contrast, the EDX analyses confirm that the particles are all composed of TaC, with the same tantalum to carbon ratio. A possible explanation for the different contrast could be that there is a dependence of brightness on crystal orientation. Dark grey particles, as well as the small particle in Fig. 3.8-right, are composed of Fe_2Ta. The composition of TaC particles is homogeneous over the sample, but their morphology changes with location, with more dendritic particles at the bottom of the specimen (Fig. 3.8-a). EDX analyses reveal a small amount of tantalum in the matrix, around 0.88 at%, coherently with the Ta-Fe phase diagram. Analysis of Fig. 3.8-b gives a 44.3% TaC volume fraction.

Finally, the microstructure of the NbC system after the arc melter process is presented in Fig. 3.9.

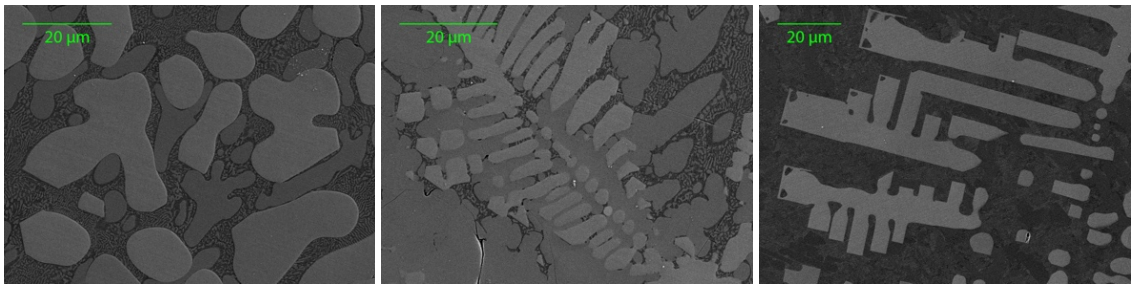

Fig. 3.9 – Fe/NbC microstructure, after arc melting.

Once again, it is possible to identify light grey particles composed of NbC, dark grey particles, as well as eutectic particles composed of Fe_2Nb. The morphology of NbC particles evolves along the sample, from a rounded shape at the top (Fig. 3.9-left), to dendrites (Fig. 3.9-center) as one moves further towards the center of the sample, and then to faceted dendrites close to the bottom of the specimen (Fig. 3.9-right). The facets of this phase show clearly the cubic crystalline structure of NbC, typically observed when the growth velocities of the different crystalline orientation are different. Nb in the matrix was not detected by EDX. Observations are coherent with Nb-Fe phase diagram, where the solubility of Nb in Fe tends to zero at low temperatures. Image analysis reveals a final NbC volume fraction of 46.3%.

From now on, we use two different notations for our samples: (i) the theoretical (i.e., aimed-for) composition is written, for example, Ti90W10C and means that the metallic elements were weighted in order to have a 90/10 atomic ratio and to form a MC carbide (there is then one atoms of carbon for each atom of metal). (ii) the measured and calculated compositions are written, for example, $Ti_{89}W_{11}C$ and we omit the subscript $_{100}$ for C, in order to simplify the notation.

3.2.2 $(Ti_xW_{1-x})C$ ternary carbides

With the aim of covering systematically the entire range of compositions, we designed five different $(T_xW_{1-x})C$ samples, aiming to reach a theoretical composition from 10 to 90 at% of W. The final, measured composition featured less tungsten that expected, with x varying stoichiometrically from 34 at% up to 89 at%. Table 3.2 lists those measured values, including SEM micrographs and the real phase compositional values obtained by EDX analyses.

Table 3.2 – Summary of the microstructure obtained for ternary $(Ti_xW_{1-x})C$ particles embedded in steel.

Theoretical composition	Microstructures		Phases composition (according to EDX analyses)
Ti90W10C	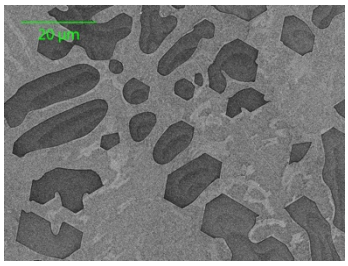	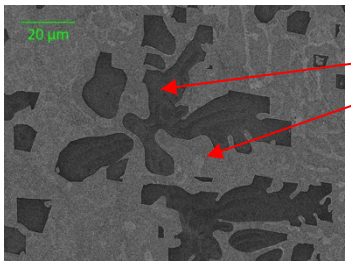	$Ti_{89}W_{11}C$ $Fe_2(Ti,W)$ Matrix: Ti – 6.6 at% W – 1.2 at%
Ti75W25C	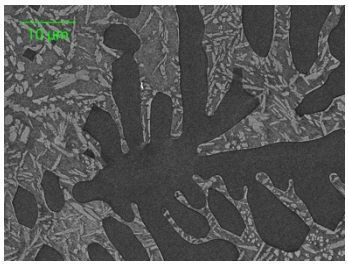	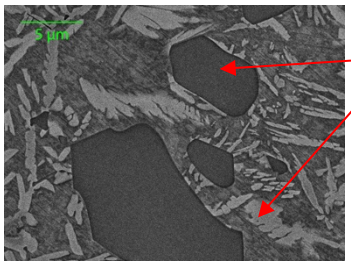	$Ti_{81}W_{19}C$ $Fe_2(Ti,W)$ Matrix: Ti – 3.5 at% W – 3.4 at%
Ti50W50C	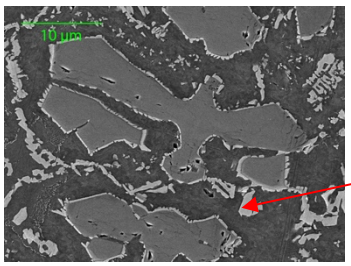	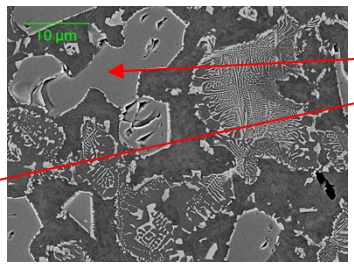	$Ti_{71}W_{29}C$ Fe_3W_3C Matrix: Ti – 0.1 at% W – 7.2 at%
Ti25W75C	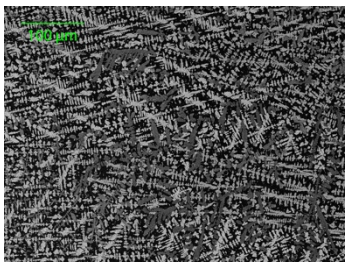	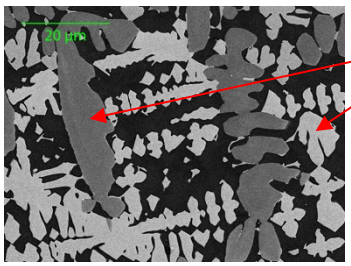	$Ti_{54}W_{46}C$ Fe_3W_3C Matrix: Ti – 0.12 at% W – 3.4 at%
Ti10W90C	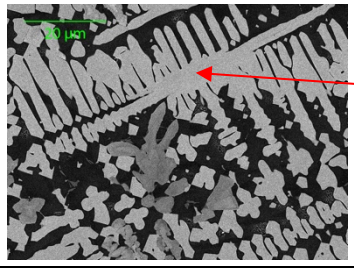	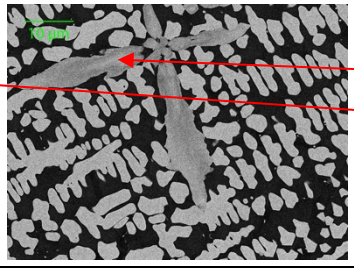	$Ti_{34}W_{66}C$ Fe_3W_3C Matrix: W – 3.0 at%

All the microstructures have in common the presence of both the ternary (Ti,W)C carbide and an iron-containing phase such as Fe_2Ti for higher amounts of Ti or Fe_3W_3C as the theoretical

amount of W exceeds Ti. The (Ti,W)C particles are large enough to be tested and the variation of the composition for a given (Ti,W)C particle was assessed by EDX to be within instrumental error (±1.5 at%). Therefore, those samples do not require a complementary heat treatment before testing. The range of compositions in the $(Ti_xW_{1-x})C$ system is well covered with x varying from 34 up to 89 at%, although the phase diagram predicts a maximum content of 50 at% of W in the cubic phase (Ti,W)C[84]. The measured tungsten content is lower in comparison with the theoretical composition (compare the first and third columns of Table 3.2) , especially for W-rich samples; that could be a consequence of Fe_3W_3C phase formation, which lowers the tungsten content in the carbide. If we compare these compositions with ThermoCalc predictions (Table 3.3), we still observe a difference in the W-content of the (Ti,W)C particles. The temperature of 1200°C was chosen in order to be in the dual solid phase Fe + (Ti,W)C domain.

Table 3.3 – Comparison of (Ti,W)C theoretical, measured and predicted compositions.

Theoretical	Measured	ThermoCalc Database: TCFE9 T°: 1200°C
Ti90W10C	$Ti_{89}W_{11}C$	TiC
Ti75W25C	$Ti_{81}W_{19}C$	$Ti_{97}W_3C$
Ti50W50C	$Ti_{71}W_{29}C$	$Ti_{81}W_{19}C$
Ti25W75C	$Ti_{54}W_{46}C$	$Ti_{69}W_{31}C$
Ti10W90C	$Ti_{34}W_{66}C$	$Ti_{67}W_{33}C$

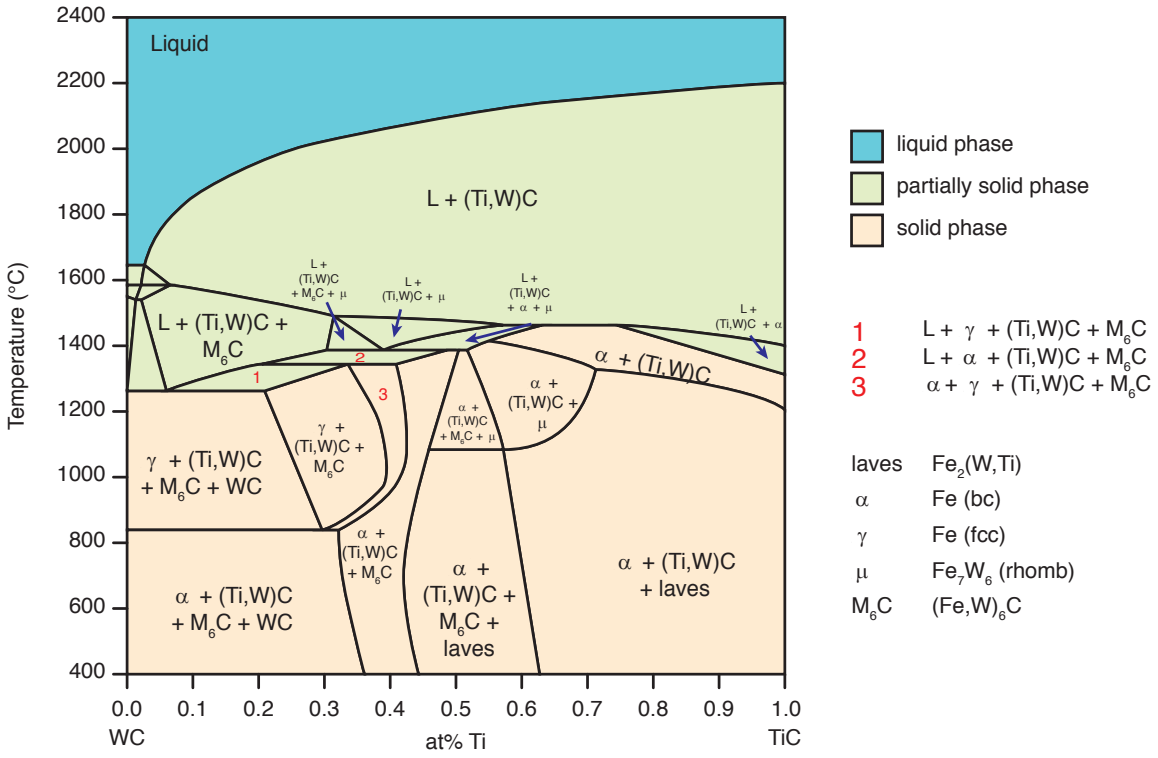

Fig. 3.10 – Pseudo-binary TiC-WC diagram in an iron matrix (from ThermoCalc).

The pseudo-binary Fe/TiC-WC phase diagram obtained by ThermoCalc is reported in Fig. 3.10, where it is plotted as a function of temperature and of the TiC content. As seen, WC should precipitate for W concentrations above 65 at%: this is not observed in our samples; therefore, we can assume that our particles are metastable, and that their formation is likely associated with the high cooling rate imposed by the arc melter furnace. This was confirmed by performing heat treatments that led to the decomposition into microstructures containing metastable W-rich carbides towards the equilibrium microstructure. The presence of a (Fe,W)C ternary carbide is also predicted by ThermoCalc, in the form of a M_6C carbide.

3.2.3 $(Ti_xV_{1-x})C$ ternary carbides

This second system probes the mutual solubility of Ti and V; nine different (Ti,V)C ternary compositions were produced covering the entire compositional range. As for the previous system, Table 3.4 summarizes the different microstructures of ternary carbides in a steel matrix and compares the theoretical (Ti,V)C composition with the experimentally values obtained by EDX.

Table 3.4 – Summary of the microstructure obtained for ternary $(Ti_xV_{1-x})C$ particles embedded in steel.

Theoretical composition	Microstructures		Phases composition (according to EDX analyses)
Ti95V5C	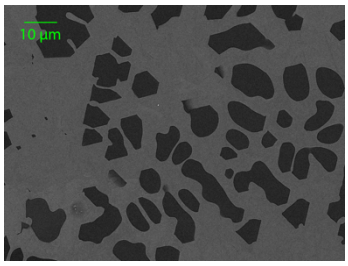	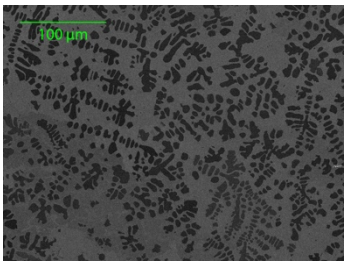	$Ti_{90}V_{10}C$ Matrix: Ti – 8.0 at% V – 10.3 at%
Ti75V25C	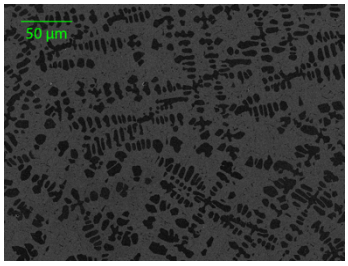	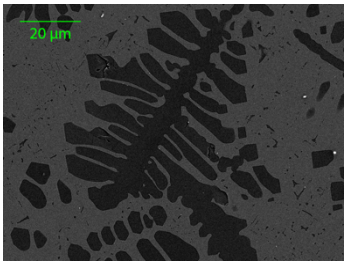	$Ti_{81}V_{19}C$ Matrix: Ti – 3.6 at% V – 13.2 at%

Ti50V50C	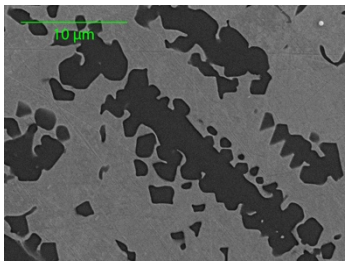	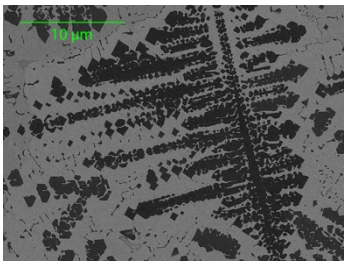	$Ti_{75}V_{25}C$ Matrix: Ti – 0.9 at% V – 9.0 at%
Ti40V60C	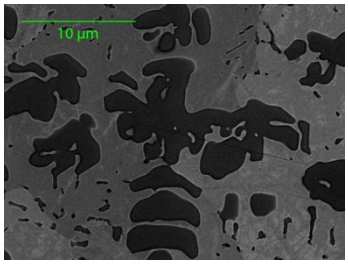	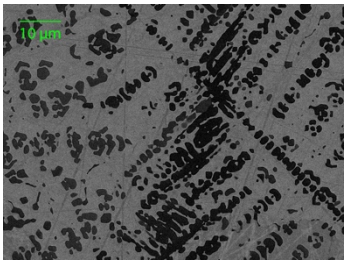	$Ti_{71}V_{29}C$ Matrix: Ti – 8.4 at% V – 14.9 at%
Ti35V65C	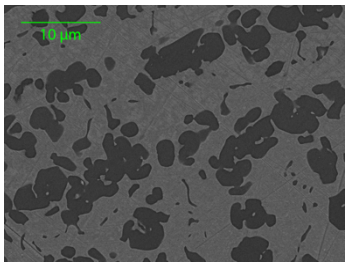	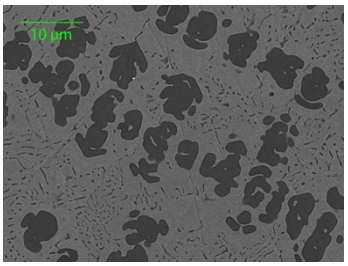	$Ti_{47}V_{53}C$ Matrix: Ti – 0.7 at% V – 17.0 at%
Ti25V75C	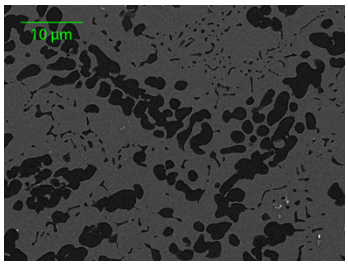	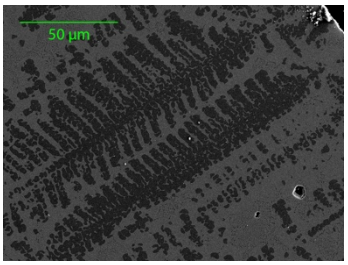	$Ti_{34}V_{66}C$ Matrix: V – 18.0 at%
Ti15V85C	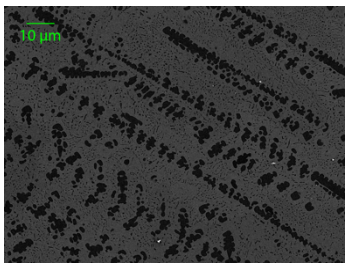	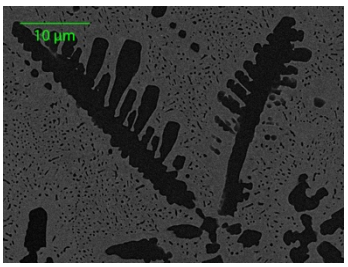	$Ti_{26}V_{74}C$ Matrix: Ti – 0.3 at% V – 20.0 at%
Ti10V90C	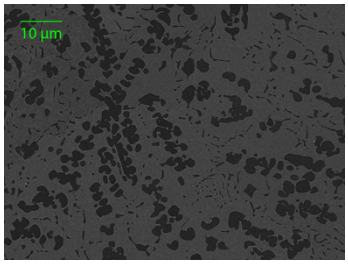	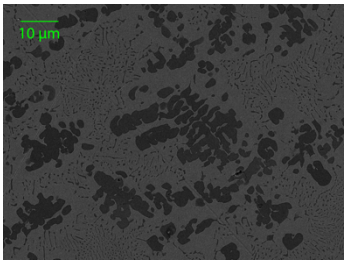	$Ti_{23}V_{77}C$ Matrix: V – 13.0 at%

Ti2V98C	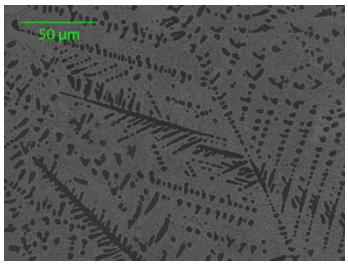	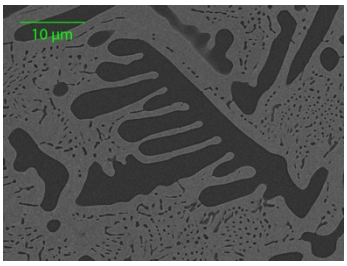	$Ti_4V_{96}C$ Matrix: V – 18.6 at%

All the compositions exhibited (Ti,V)C particles fulfilling requirements of size, homogeneity and composition and hence amenable to mechanical testing. Therefore, no additional heat treatments were performed. We explored compositions ranging from 5 to 98 at% of V. According to EDX results, all the (Ti,V)C particles contain a tiny amount of Fe, below 1 at%. The vanadium content in carbides is smaller than the predicted values, with the exception of Ti95V5C. The observation is not surprising, if we consider the high solubility of V in Fe, in many case higher than the amount of 11.8 at% we add during the processing. The particles have the characteristic dendritic morphology, although the dendrites are more fragmented in comparison with the previous system.

When comparing the measured (Ti,V)C compositions with predicted values from ThermoCalc, we observe an acceptable concordance, except for the low-vanadium compositions, Table 3.5. As for the previous system, the temperature was chosen to correspond to a domain of the phase diagram exhibiting a mixture of Fe and (Ti,V)C carbide in a solid state.

Table 3.5 – Comparison of (Ti,V)C theoretical, measured and predicted compositions.

Theoretical	Measured	ThermoCalc Database: SSOL2 T°: 600°C
Ti95V5C	$Ti_{90}V_{10}C$	TiC
Ti75V25C	$Ti_{81}V_{19}C$	$Ti_{99}V_1C$
Ti50V50C	$Ti_{75}V_{25}C$	$Ti_{71}V_{29}C$
Ti40V60C	$Ti_{71}V_{29}C$	$Ti_{70}V_{30}C$
Ti35V65C	$Ti_{47}V_{53}C$	$Ti_{40}V_{60}C$
Ti25V75C	$Ti_{34}V_{66}C$	$Ti_{35}V_{65}C$
Ti15V85C	$Ti_{26}V_{74}C$	$Ti_{19}V_{81}C$
Ti10V90C	$Ti_{23}V_{77}C$	$Ti_{13}V_{87}C$
Ti2V98C	$Ti_4V_{96}C$	$Ti_3V_{97}C$

3.2.4 $(Ti_xTa_{1-x})C$ ternary carbides

For this third ternary system, we produced five (Ti,Ta)C ternary carbides, ranging from 10 at% to 90 at% of Ta. As with the previous system, the two binary TiC and TaC carbides are totally soluble at high temperatures. Table 3.6 summarizes the different phases that could be distinguished by analyzing the microstructure in the SEM, together with the main EDX results.

Table 3.6 – Summary of the microstructure obtained for ternary $(Ti_xTa_{1-x})C$ particles embedded in steel.

Theoretical composition	Microstructures		Phases composition (according to EDX analyses)
Ti90Ta10C	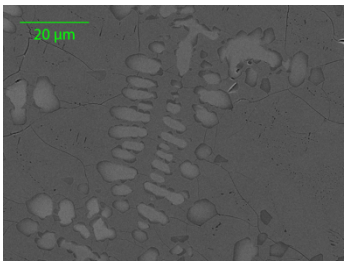	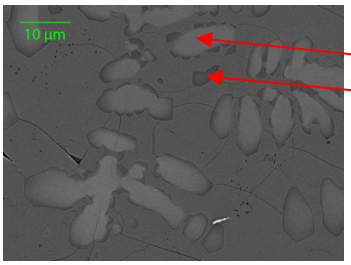	$Ti_{81}Ta_{19}C$ $Ti_{10}Ta_{90}C$ Matrix: Fe_2Ti
Ti75Ta25C	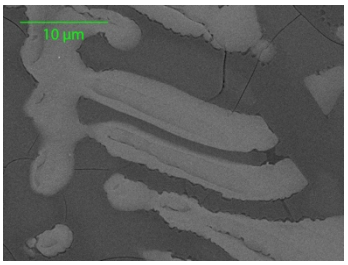	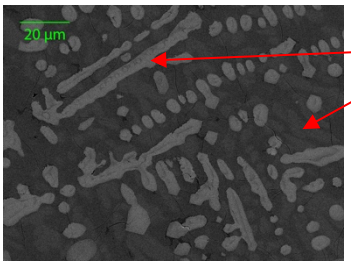	$Ti_{69}Ta_{31}C$ $Fe_{52}Ta_{11}Ti_{14}C_{33}$ Matrix: Fe_2Ti
Ti60Ta40C	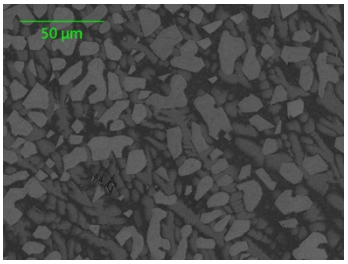	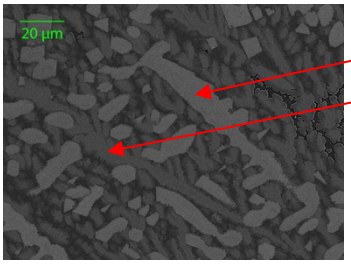	$Ti_{42}Ta_{58}C$ $Fe_2(Ti,Ta)$ Matrix: Ti – 5.5 at% Ta – 0.2 at%
Ti25Ta75C	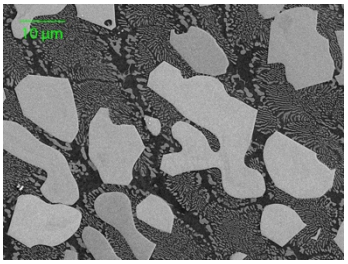	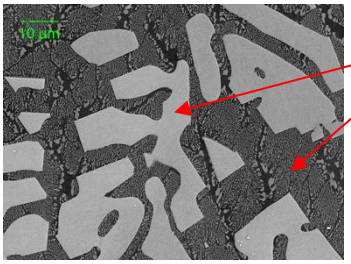	$Ti_{22}Ta_{78}C$ $Fe_2(Ti,Ta)$ Matrix: Ti – 1.6 at% Ta – 0.5 at%

Ti10Ta90C	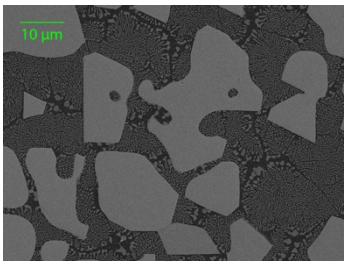 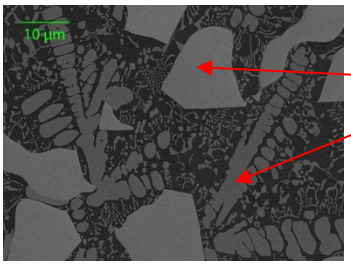	$Ti_{10}Ta_{90}C$ Fe_2Ta Matrix: Ta – 0.6 at%

As with the (Ti,W)C system, we observe the presence of an iron-containing phase in all the samples, this phase being present in addition to the desired ternary carbide. Both theoretical and measured compositions match relatively well with the predicted ThermoCalc values, except for the Ti60Ta40C composition (see Table 3.7). Such small deviations can be explained by (i) an out-of-equilibrium structure, caused by the rapid cooling of the samples, (ii) the presence of other phases (Fe_2Ta, Fe_2Ti) and (iii) partial solubility of Ta in the matrix (up to 4 at% according to the Ta-Fe phase diagram). The ternary (Ti,Ta)C particles fulfill the requirements on size, composition and compositional homogeneity necessary for mechanical tests and have therefore not been subjected to additional heat treatment.

We observed in Ti90Ta10C a difference in composition between the border and the center of the sample; yet, the particles are large enough in the middle to perform the mechanical tests. The morphology of the ternary carbides is again mostly dendritic, with the presence of more spheroidal particles for some compositions such as Ti10Ta90C, particles of which are located close to the top of the sample. Besides the ternary carbide phase, we can observe the presence of a fishbone-like phase in Fe/$Ti_{22}Ta_{78}C$ and Ti10Ta90C, as well as the Laves phase Fe_2Ta in the $Ti_{42}Ta_{58}C$ composition. The Ti-richest composition contains also a second kind of particle with a Ti10Ta90C composition, but its volume fraction is much smaller than for the other carbides.

Table 3.7 – Comparison of (Ti,Ta)C theoretical, measured and predicted compositions.

Theoretical	Measured	ThermoCalc Database: TCFE9 T°: 1300°C
Ti90Ta10C	$Ti_{81}Ta_{19}C$	$Ti_{89}Ta_{11}C$
Ti75Ta25C	$Ti_{69}Ta_{31}C$	$Ti_{74}Ta_{26}C$
Ti60Ta40C	$Ti_{42}Ta_{58}C$	$Ti_{59}Ta_{41}C$
Ti25Ta75C	$Ti_{22}Ta_{78}C$	$Ti_{25}Ta_{75}C$
Ti10Ta90C	$Ti_{10}Ta_{90}C$	$Ti_9Ta_{91}C$

3.2.5 $(Ti_xNb_{1-x})C$ ternary carbides

The fourth ternary system that was investigated is based on the mutual solubility at high temperature of the two binary carbides TiC and NbC. Six compositions were investigated in that

specific ternary system, from a theoretical value of 2 to 80 at% of Nb with respect to Ti. Table 3.8 summarizes the different microstructures observed, as well as the identified phases with their respective compositions as analyzed by EDX. In some cases, a thermal treatment was necessary in order to obtain a good compositional homogeneity; details are reported in Table 3.8.

Table 3.8 – Summary of the microstructure obtained for ternary $(Ti_xNb_{1-x})C$ particles embedded in steel.

Theoretical composition	Microstructures		Phases composition (according to EDX analyses)
Ti98Nb2C	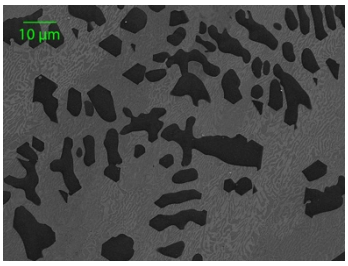	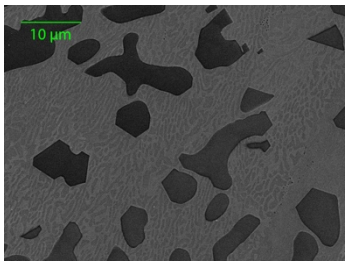	$Ti_{93}Nb_7C$ Fe_2Ti Matrix: Ti – 7.0 at%
Ti90Nb10C	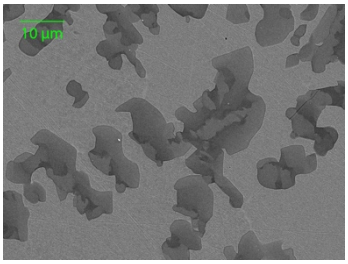	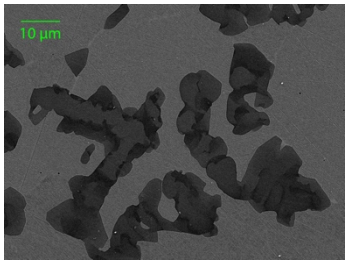	$Ti_{72-82}Nb_{18-28}C$ $Ti_{76}Nb_{24}C$ (Average) Matrix: Ti – 2.8 at% Nb – 0.3 at%
Heat treatment: 1250°C – 72h			
Ti70Nb30C	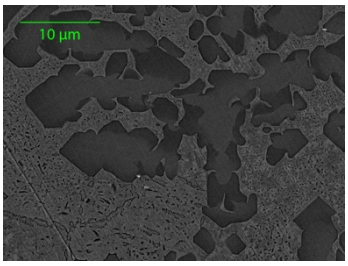	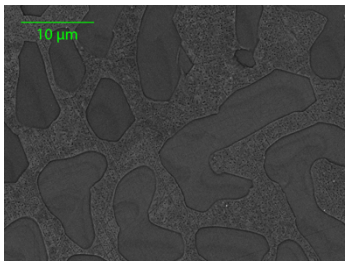	$Ti_{70-80}Nb_{20-30}C$ $Ti_{73}Nb_{27}C$ (average) Matrix: Ti – 5.0 at%
Heat treatment: 1350°C – 1h			
Ti50Nb50C	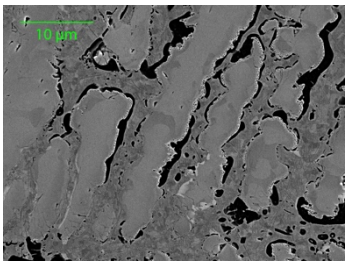	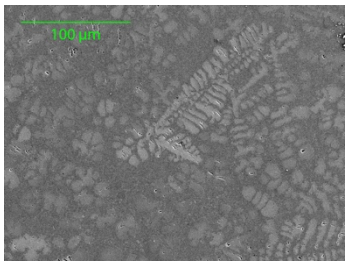	$Ti_{39-50}Nb_{50-61}C$ $Ti_{43}Nb_{57}C$ (average) Matrix: Nb – 0.5 at%
Heat treatment: 1200°C – 48h			

Ti30Nb70C	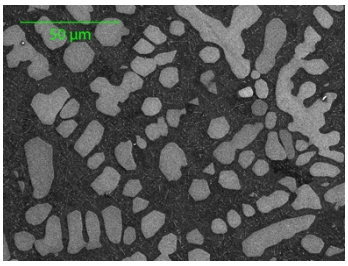	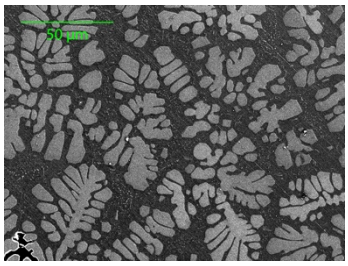	$Ti_{23}Nb_{77}C$ Matrix: Ti – 0.3 at% Nb – 1.0 at%
Ti20Nb80C	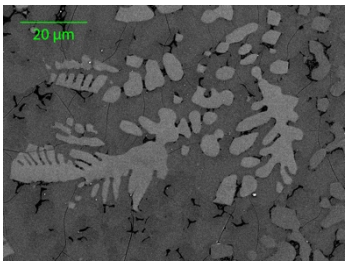	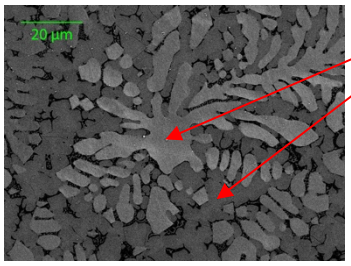	$Ti_{10}Nb_{90}C$ $Fe_2(Ti,Nb)$ Matrix: Ti – 1.8 at% Nb – 1.4 at%

The microstructures in this system share a dendritic morphology for the ternary (Ti,Nb)C carbide. Spheroidal particles are present in Nb-rich samples (Ti30Nb70C and Ti20Nb80C), close to the top of the sample. The size of (Ti,Nb)C carbide particles fulfils the requirements for mechanical tests. Although thermal treatment were performed, some ternary (Ti,Nb)C particles are definitely not homogeneous, especially at higher Ti amount (Ti90Nb10C, Ti70Nb30C and Ti50Nb50C); EDX analyses revealed a range of compositions of carbide particles for each of these three samples. However, since the average composition is constant over the sample, the dispersion being acceptably small, we nonetheless test those particles, trying to focus, if possible, on the particle core, which seems more homogeneous than the rim. This system is one in which the formation a second particle phase is less marked, as only the two extremal compositions exhibit the presence of, respectively, Fe_2Nb Laves phase for Ti98Nb2C and a quaternary iron-containing carbide for Ti20Nb80C. A small amount of niobium in the matrix is outlined by EDX analyses, corresponding to the solubility of Nb in Fe, as given by the Fe-Nb phase diagram (~ 5 at% at 1394°C).

The relatively good agreement that we found between the theoretical and observed compositions, as well as with those predicted by ThermoCalc at 1350°C is given in Table 3.9.

Table 3.9 – Comparison of (Ti,Nb)C theoretical, measured and predicted compositions.

Theoretical	Measured (average)	ThermoCalc Database: SSOL2 T°: 1350°C
Ti98Nb2C	$Ti_{93}Nb_7C$	$Ti_{97}Nb_3C$
Ti90Nb10C	$Ti_{76}Nb_{24}C$	$Ti_{88}Nb_{12}C$
Ti70Nb30C	$Ti_{73}Nb_{27}C$	$Ti_{69}Nb_{31}C$
Ti50Nb50C	$Ti_{43}Nb_{57}C$	$Ti_{54}Nb_{46}C$
Ti30Nb70C	$Ti_{23}Nb_{77}C$	$Ti_{36}Nb_{64}C$
Ti20Nb80C	$Ti_{10}Nb_{90}C$	$Ti_{13}Nb_{87}C$

3.2.6 $(Ta_xV_{1-x})C$ ternary carbides

The fifth and last ternary system is (Ta,V)C, of which we produced nine different compositions, from 8 at% up to 96 at% V. Table 3.10 presents the various microstructures of the different specimens and reports the compositions that we measured by EDX analysis. For some of the samples, a thermal treatment was performed, parameters of which are reported in the same table.

Table 3.10 – Summary of the microstructure obtained for ternary $(Ta_xV_{1-x})C$ particles embedded in steel.

Theoretical composition	Microstructures	Phases composition (according to EDX analyses)
Ta75V25C	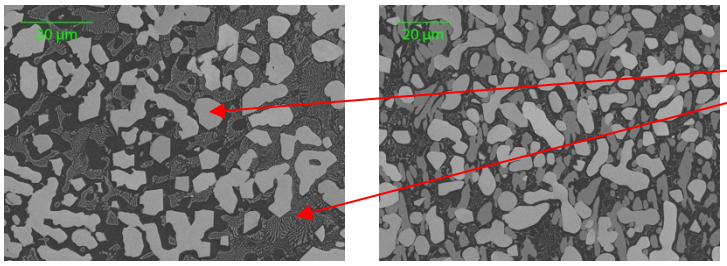	$Ta_{90}V_{10}C$ $Fe_2(Ta,V)$ Matrix: Ta – 1.0 at% V – 20.0 at%
Ta75V25C	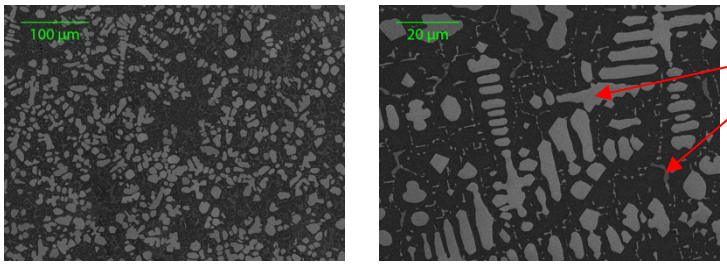	$Ta_{92}V_8C$ $Fe_2(Ta,V)$ Matrix: Ta – 1.3 at% V – 13.0 at%
Ta50V50C	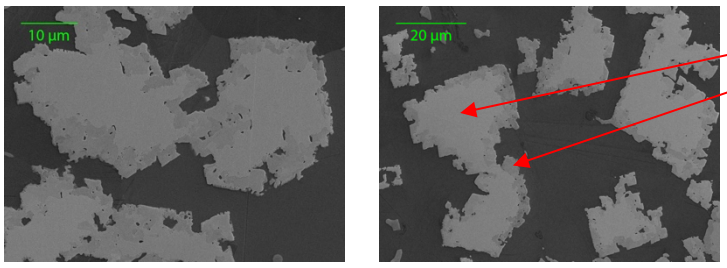	$Ta_{69}V_{31}C$ $Ta_{52\text{-}58}V_{48\text{-}42}C$ Matrix: Ta – 0.2 at% V – 15.0 at%
Heat treatment: 1400°C – 2h		

Ta50V50C	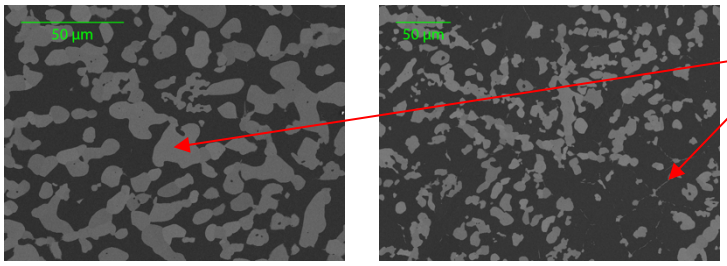	$Ta_{77}V_{23}C$ $Fe_2(Ta,V)$ Matrix: Ta – 0.3 at% V – 21.0 at%
Heat treatment: 1400°C – 72h		
Ta35V65C	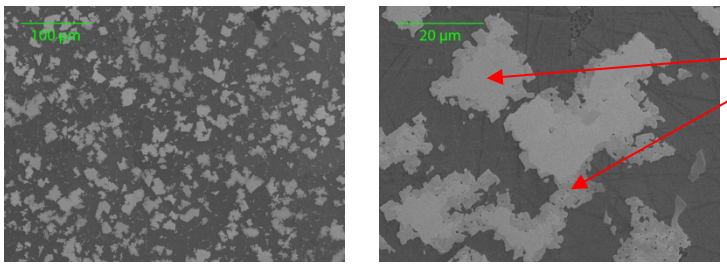	$Ta_{53}V_{47}C$ $Ta_{30-48}V_{70-52}C$ Matrix: Ta – 0.2 at% V – 17.0 at%
Heat treatment: 1400°C – 2h		
Ta25V75C	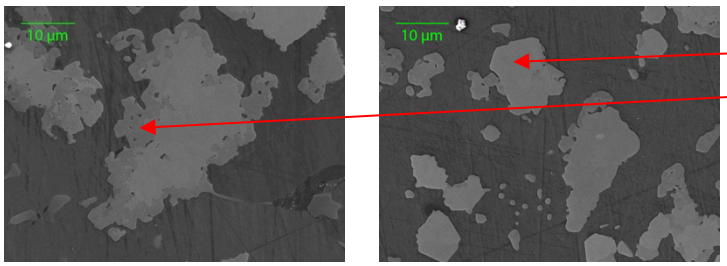	$Ta_{39}V_{61}C$ $Ta_{32}V_{68}C$ Matrix: Ta – 0.3 at% V – 18.0 at%
Heat treatment: 1400°C – 2h		
Ta10V90C	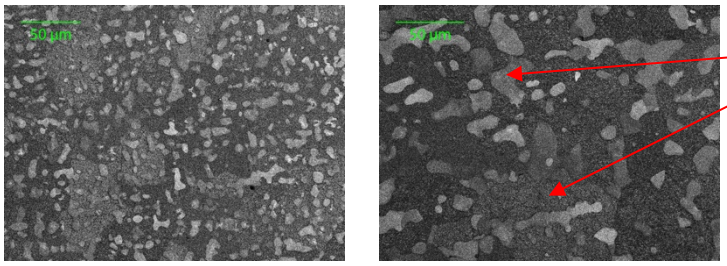	$Ta_{13}V_{87}C$ $Ta_4V_{96}C$ Matrix: Ta – 0.1 at% V – 14.6 at%
Heat treatment: 1350°C – 2h		
Ta10V90C	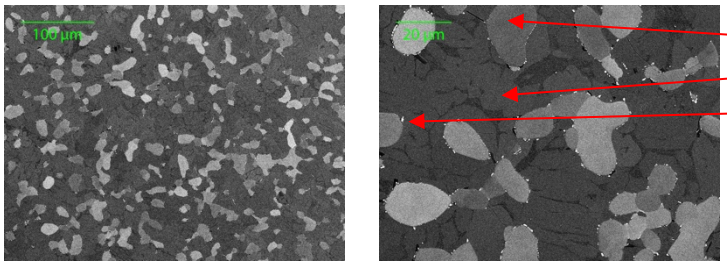	$Ta_{18}V_{82}C$ Fe_2V VC Matrix: Ta – 0.3 at% V – 28.0 at%
Heat treatment: 1400°C – 72h		

Ta2V98C	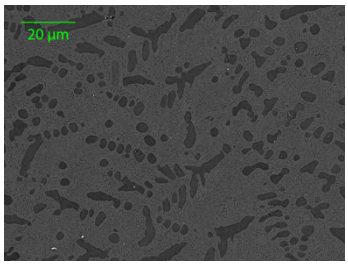	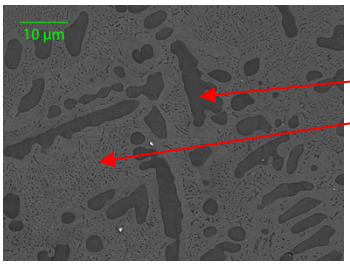	$Ta_4V_{96}C$ VC Matrix: V – 18.6 at%

From Ta-rich to V-rich compositions, the nine (Ta,V)C samples exhibit various microstructures. The first two samples share the same theoretical composition; however, the vanadium solubility was not compensated for in the first sample, while it was for the second sample, by adding the extra amount of 11.8 at% of V. The microstructures of the two samples are very dissimilar. In the first, we observe the presence in Ta92V8C of light grey, somewhat faceted dendrites, as well as a eutectic-like second phase, namely the Laves Fe_2Ta phase. A third phase, of the quaternary carbide (Fe,Ta,V)C, is also present. The microstructure of the second Fe/Ta75V25C specimen, which contains more vanadium, consists mainly in faceted dendrites of the ternary carbide (whose composition is slightly richer in vanadium in comparison with the previous composition), together with the presence of tiny (Fe,Ta,V)C particles.

Three other samples, namely the first Ta50V50C (heat treated at 1400°C for 2h), Ta35V65C and Ta25V75C, exhibit roughly the same microstructure, mainly composed of ternary carbide particles, with no additional particle phase present. The ternary carbide particles are characterized by a fragmented faceted dendritic morphology, with a different and inhomogeneous composition at the rim of the particle in comparison with the core, which is homogeneous. Because the core is sufficiently wide and its composition is known, composition gradients near the rim do not constitute an issue for the mechanical tests.

In the case of Fe/Ta50V50C system, another thermal treatment was performed by increasing the holding time, with the aim of investigating variations in carbide composition and homogeneity. The resulting microstructure is different, showing a coexistence of the ternary (Ta,V)C carbide, in the form of dendrites, and a quaternary iron-based carbide within smaller particles.

The two twin Fe/Ta10V90C samples, of the same composition but heat treated differently, exhibit a rather similar microstructure, consisting of spheroidal particles of different ternary (Ta,V)C compositions. For the first specimen (1350°C for 2h), large $Ta_{13}V_{87}C$ particles are present, in parallel with smaller $Ta_4V_{96}C$. For the second sample (1400°C for 72h under vacuum), tiny binary VC particles nucleate at the matrix/particle interface. Both specimens contain the Laves Fe_2V phase.

The last sample, Fe/Ta2V98C is characterized by dendrites of ternary (Ta,V)C carbide and pure VC forming a eutectic phase.

A comparison with ThermoCalc predictions at 1100°C and theoretical carbide stoichiometry values is given in Table 3.11:

Table 3.11 – Comparison of (Ta,V)C theoretical, measured and predicted compositions.

Theoretical	Measured	ThermoCalc Database: TCFE9 T°: 1100°C
Ta75V25C	$Ta_{92}V_8C$	$Ta_{88}V_{12}C$
	$Ta_{90}V_{10}C$	$Ta_{88}V_{12}C$
Ta50V50C	$Ta_{69}V_{31}C$	$Ta_{69}V_{31}C$
	$Ta_{77}V_{23}C$	$Ta_{69}V_{31}C$
Ta35V65C	$Ta_{53}V_{47}C$	$Ta_{47}V_{53}C$
Ta25V75C	$Ta_{39}V_{61}C$	$Ta_{35}V_{65}C$
Ta10V90C	$Ta_{13}V_{87}C$	$Ta_{13}V_{87}C$
	$Ta_{18}V_{82}C$	$Ta_{13}V_{87}C$
Ta2V98C	$Ta_4V_{96}C$	$Ta_{3.5}V_{96.5}C$

For this system, the measured vanadium content of the ternary carbides is in good agreement with the predicted values. Discrepancies with the theoretical values are mostly explained by the solubility of V and by the presence of both Laves and (Fe,Ta,V)C phases.

3.2.7 $(Ti_xTa_yV_{1-x-y})C$ quaternary carbides

A quaternary system was investigated, combining the three (explored) ternary (Ti,Ta)C, (Ti,V)C and (Ta,V)C systems. The three binary TiC, VC and TaC carbides exhibit a total mutual solubility at T > 1500°C, and a homogeneous quaternary phase is predicted by ThermoCalc within the entire range of compositions.

Initially, we designed six quaternary specimens with their compositions equally spaced between TiC and $Ta_{77}V_{23}C$. The latter composition, situated within the ternary (Ta,V)C system, was chosen because it might exhibit attractive mechanical properties according to the VEC-based criterion of Jhi et al., exposed in Chapter 2 and discussed in the next chapters. A first series of samples was produced, with no correction for the solubility of vanadium in iron: that series is labelled "A". A second batch of specimens, labelled "B" was then prepared, by correcting the vanadium content with a fixed amount corresponding to 11.8 at%. Finally, a last series of samples, corrected for the vanadium solubility, was produced and thermally treated at 1400°C for 24h. Table 3.12 summarizes the different compositions and the processing cycle of the 18 quaternary specimens that were produced.

Table 3.12 – Labelling and processing of quaternary Fe/(Ti,Ta,V)C specimens.

	Sample 1	Sample 2	Sample 3	Sample 4	Sample 5	Sample 6
Theoretical composition	Ti80Ta15V5C	Ti67Ta24V9C	Ti53Ta34V13C	Ti40Ta44V16C	Ti27Ta54V19C	Ti13Ta64V23C
Label "A"	Raw from arc melter, no correction for V solubility in Fe					
Label "B"	Raw from arc melter, corrected for V solubility (extra amount of 11.8 at% of V)					
Label "C"	Corrected for V solubility (extra 11.8 at% of V) and heat-treated at 1400°C/24h					

Among those 18 specimens, only 12 fulfil the requirements for mechanically testing, namely the six "A" samples, plus Samples 2B, 3B, 4B, 1C, 2C and 3C.

In order to represent this quaternary system, we use a pseudo-ternary TiC-TaC-VC phase diagram, shown in Fig. 3.11. On the edge of the triangle, we report the ternary carbides described above in this chapter. The microstructures of these 12 compositions are presented in Table 3.13:

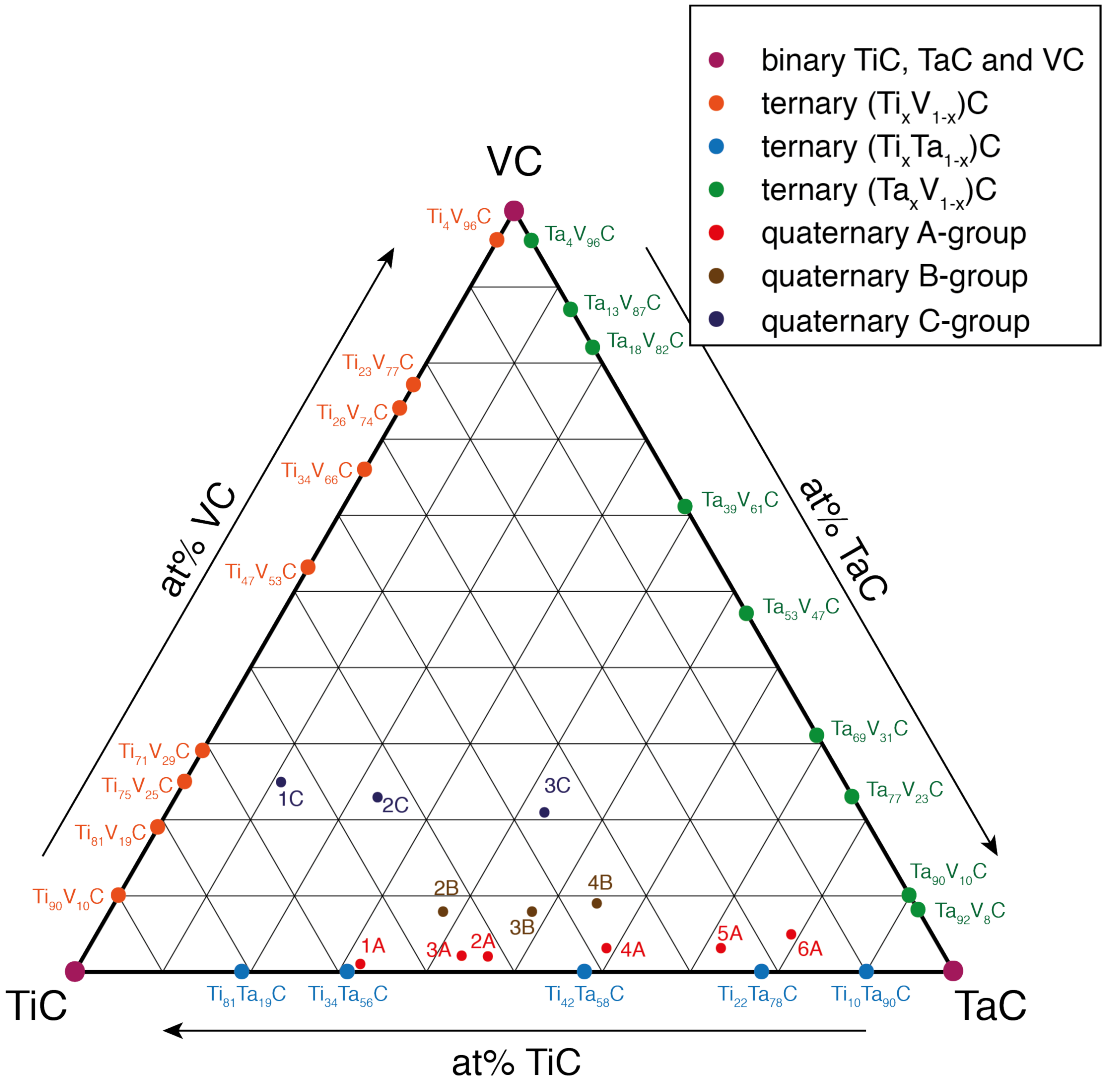

Fig. 3.11 – Pseudo-ternary TiC-TaC-VC compositions. On the edge, we report the composition of the three ternary systems forming the boundaries.

Table 3.13 – Summary of the microstructure obtained for quaternary $(Ti_xTa_yV_{1-x-y})C$ particles embedded in steel. CHANGED by correction of micrographs and specification of the heat treatment

Sample	Microstructures		Phases composition (according to EDX analyses)
1A	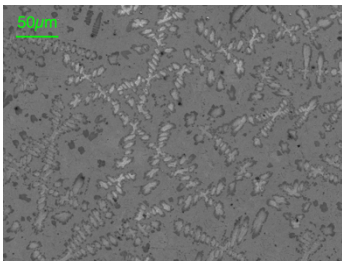	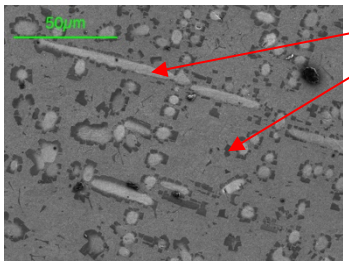	$Ti_{67}Ta_{32}V_1C$ $Ti_{97}V_3C$ Matrix: Ti – 0.5 at% Ta – 0.7 at%
2A	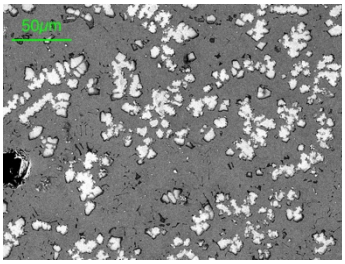	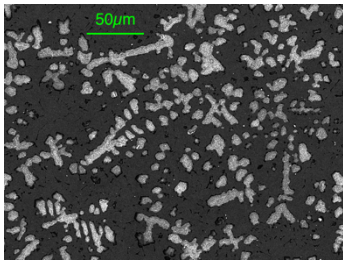	$Ti_{52}Ta_{46}V_2C$ Matrix: Ti – 0.4 at% V – 0.9 at%
3A	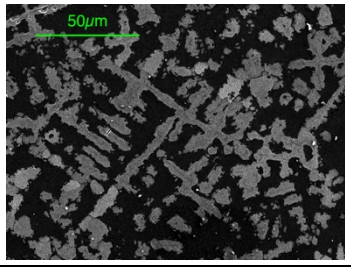	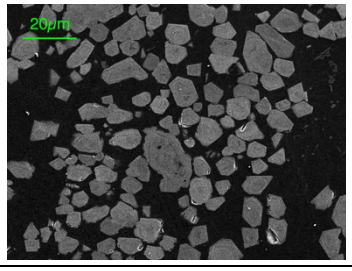	$Ti_{55}Ta_{43}V_2C$ Matrix: Ti – 0.4 at% Ta – 0.1 at% V – 2.7 at%
4A	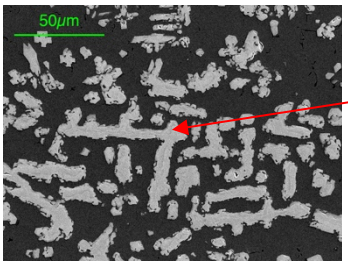	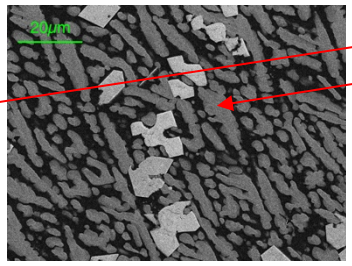	$Ti_{38}Ta_{59}V_3C$ $Fe_{45}Ta_{13}Ti_7V_4C_{31}$ Matrix: Ti – 0.2 at% Ta – 0.1 at% V – 2.8 at%
5A	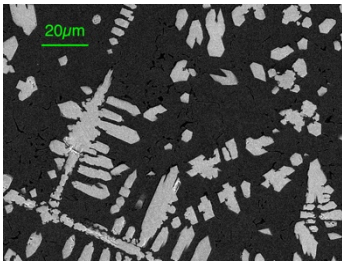	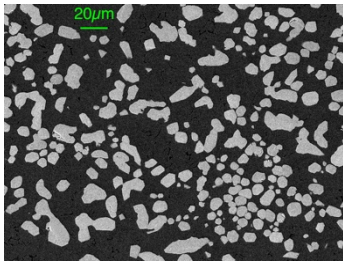	$Ti_{25}Ta_{72}V_3C$ Matrix: Ti – 0.1 at% Ta – 0.1 at% V – 2.8 at%

6A	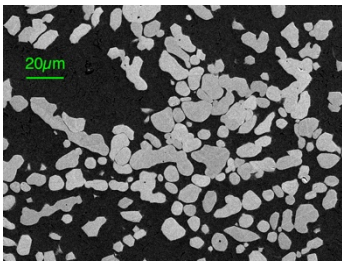	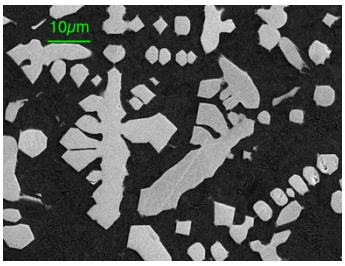	$Ti_{16}Ta_{79}V_5C$ Matrix: Ti – 0.05 at% Ta – 0.1 at% V – 3.0 at%
2B	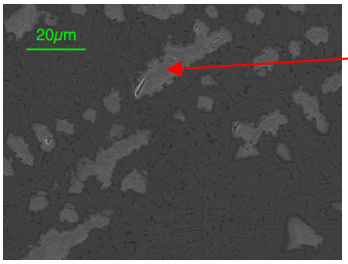	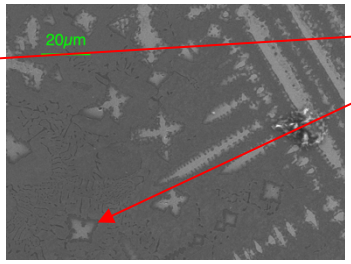	$Ti_{54}Ta_{38}V_8C$ $Fe_{80}Ti_1V_5C_{14}$ Matrix: Ti – 0.2 at% Ta – 0.05 at% V – 7.3 at%
3B	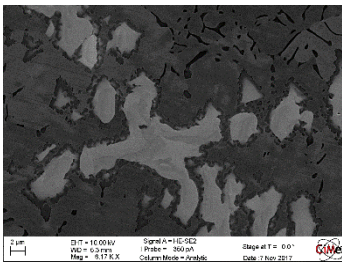	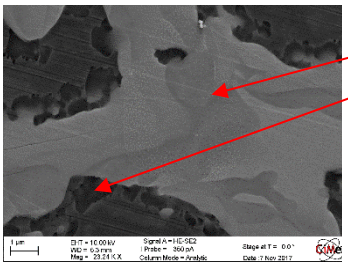	$Ti_{44}Ta_{48}V_8C$ $Ti_{67}Ta_7V_{26}C$ Matrix: Ti – 0.2 at% Ta – 0.1 at% V – 6.0 at%
4B + heat treatment 2h @ 1500°C	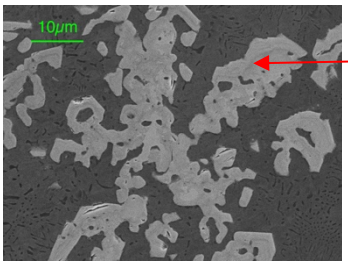	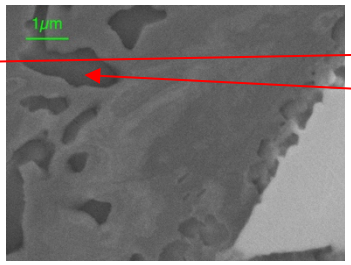	$Ti_{36}Ta_{55}V_9C$ $Ti_9Ta_{10}V_{31}C_{50}$ Matrix: Ta – 0.5 at% V – 7.0 at%
1C	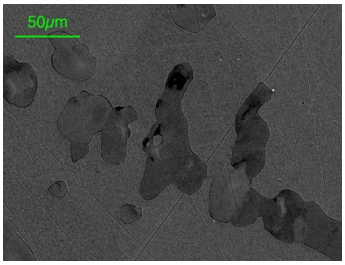	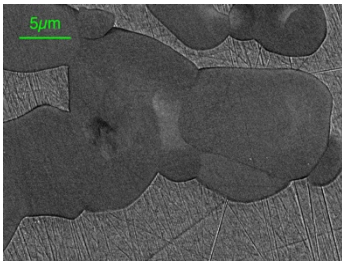	$Ti_{64}Ta_{11}V_{25}C$ Matrix: Ti – 0.5 at% V – 8.4 at%
2C	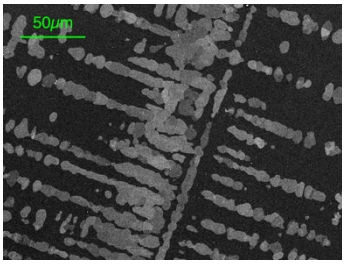	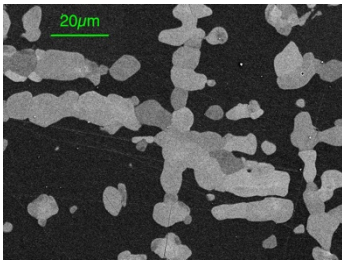	$Ti_{54}Ta_{23}V_{23}C$ Matrix: Ti – 0.2 at% Ta – 0.1 at% V – 9.0 at%

3C	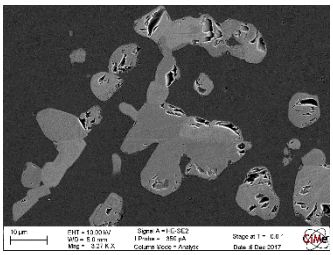	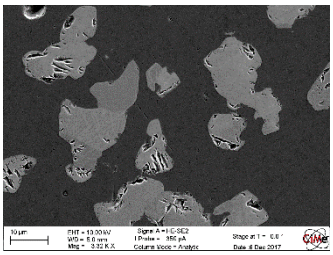	$Ti_{36}Ta_{43}V_{21}C$ Matrix: Ti – 0.1 at% V – 11.7 at%

The microstructures of the twelve quaternary samples are rather different, and similarly to the (Ta,V)C system, it is difficult to define a common microstructure type. Depending on the sample, we can observe either (i) homogeneous particles with a composition that we can consider as constant (2A, 3A, 5A, 6A, 4B, 1C), or (ii) particles having a different composition at the sample border (1A, 2B, 3B, 3C). The iron-containing carbide was found in Specimen 4A. Finally, Specimen 2C exhibits some heterogeneities in terms of grey levels, suggesting the presence of compositional variations within the carbide; EDX analysis reveals that the composition varies by ~1 at%, such that for purposes of this work we can consider it as a constant composition. Most of the quaternary (Ti,Ta,V)C carbides exhibit a characteristic dendritic morphology, with the presence of more spheroidal particles close to the top of the sample (3A, 5A, 6A, 2C). The particles meet the three criteria defined above for mechanical testing suitability.

CHAPTER 4:

HARDNESS

DESCRIPTION OF CORRECTIONS BROUGHT TO THE SUBMITTED THESIS VERSION:
This chapter has been corrected by replacement herein of (invalid) hardness measurement values, which were initially reported, with new measurements produced by Dr. Deillon using the standard nanoindentation model developed by Oliver & Pharr (instead of Cheng's model) for all the carbide compositions. The modified experimental methods are given in Section 4.1, and the new results in Section 4.2.

Dr Léa Deillon performed the new set of hardness measurements, as well as the analysis based on the standard Oliver & Pharr model.

This and the two next chapters aim to present in turn the three mechanical properties we have investigated, namely the hardness, the elastic modulus (Chapter 5) and the fracture toughness (Chapter 6) of MC carbides in steel. For each property, the methods used to measure it are firstly described, followed then by the results. A discussion, aiming not only to interpret the results, but also first to assess the measurement accuracy, is then presented at the end of each chapter.

Hardness measurements, as opposed to elastic modulus data, are not sensitive to the matrix compliance because, provided indents are sufficiently small in comparison with the particle size, data that are measured are related only to plastic deformation within the carbide particle; not knowing the load train or substrate elastic compliance has no importance. A traditional hardness test measures the imprint left by an indenter after unloading, i.e. after recovery of elastic deformation, including in the matrix. We still have here to address the issue of particle size, however: plastic deformation imposes that a threshold load be exceeded, which depends on the indenter geometry, and the size of the imprint relative to that of the particle, since the stress field

associated with the indentation must be entirely contained within the particle. Therefore, particles should have dimensions in excess of ≈ 15-20 μm to be tested.

The "standard" Oliver and Pharr analysis was used. As for the elastic modulus described in the next chapter, all systems of Chapter 3 (binary, ternary and quaternary carbides) have been tested and (updated) hardness values will be presented hereunder as a function of carbide composition. The discussion will first assess the method accuracy and, in a second step, attempt to determine whether existing theory from electronic considerations provides a viable interpretation of observed trends.

4.1 Hardness measurement: methods

We start this chapter by giving a description of the experimental procedure that was used to measure the hardness of carbide particles.

4.1.1 Nanoindentation apparatus: Hysitron TI 950 TriboIndenter

Because all our mechanical tests are based on, or involve, nanoindentation, our nanoindenter constituted the key data-generating apparatus of this thesis. For that reason, we start with a description of the setup, including the heads, the tips and the stages that we used during the project.

We used a HYSITRON® (Minneapolis, US) TI 950 TriboIndenter apparatus composed of three main parts, namely the frame, the stage and the heads. A granite frame is used in order to supply a rigid, dimensionally stable skeleton for the nanoindenter, the material contributing to thermal stability and reducing environmental noise and resonant frequencies. All the measurements are performed within an acoustic enclosure designed to block air currents and act as a thermal buffer; a piezo-electric active vibration isolation system completes the frame. The X/Y stage has a lateral resolution of 500 nm to allow for precise and repeatable positioning of the probe. The nanoindenter can accommodate three different heads, and the head-support constitutes the Z-axis stage, with a micro-stepping resolution of 3.1 nm. One of the three slots hosts an optical camera system, with a 10x MITUTOYO® (Toru Nakagawa, JP) objective lens and a ALLIED® (Exton, US) color CCD Camera. The two remaining slots are dedicated to nanoindentation sensors, in our case a low-load cell and a high-load cell. The low-load head is a HYSITRON® TriboScanner characterized by a maximum force of 13.3 mN. It is used to perform scanning probe microscopy (SPM) imaging and indentations. The high-load head, used here for fracture toughness exclusively, is a HYSITRON® MultiRange NanoProbe, characterized by maximal load and displacement of respectively 2.45 N and 84.4 μm.

In addition, we used a NEWPORT® (Irvine, US) M-GON40-U ±5° tilt stage, in order to correct for sample surface inclination in the most severe direction (N-S or W-E), to bring it as parallel as possible to the X/Y plane of the nanoindenter.

We used four types of nanoindentation tip:

- Two low-load Hysitron® Berkovich diamond tips (E = 1140 GPa and ν = 0.07), with a half-angle of 65.27°.
- Two low-load Hysitron® conospherical diamond tips (E = 1140 GPa and ν = 0.07), with a cone angle of 90° and a nominal tip radius between 0.5 and 1.5 μm (1.09 μm for the first tip, 1.33 for the second, measured on fused quartz);
- A low-load Hysitron® cube corner diamond tip (E = 1140 GPa and ν = 0.07), with a half angle of 35.27° and a < 50 nm tip radius;
- A high-load SYNTON® (Nidau, CH) cube corner diamond tip (E = 1140 GPa and ν = 0.07), with a half angle of 35.27° and a < 50 nm tip radius.

We used two different references when calibrating the tip area function:

- Fused quartz, provided by Hysitron® as a standard sample. This sample has a reduced modulus E_r of 69.6 ± 5% GPa, a hardness H of 9.25 ±10% GPa and a Poisson's ratio ν of 0.17;
- Silicon carbide, 4H α-SiC, in the form of a 330 μm wafer, provided by University Wafer (Boston, US), with a <0001> orientation of elastic modulus E = 410 GPa, measured hardness H = 35 GPa and Poisson's ratio ν = 0.14[xviii]

4.1.2 The Oliver and Pharr analysis for hardness

The hardness of binary carbides was measured following the standard Oliver and Pharr method, which is based on deriving the ratio of the maximal load to the imprint contact area calculated, knowing the indenter geometry, from the unloading segment of the measured indenter load-displacement curves. Here, the indenter is a Berkovich diamond tip. The area function was calibrated on fused quartz, and the load function is a standard trapezoidal curve with 5s loading/unloading segments and a 2s holding time.

The peak load was chosen by performing indents on the 5 binary carbides with different P_{max} values, ranging from 4 to 10 mN. The objective was to keep the peak load as low as possible yet perform indentations deep enough such that results are not affected by indentation size effects.

Hardness measurements are then performed on carbide particles produced in this work (i.e, embedded in steel). A minimum of six particles was tested for each composition; the precise number of indents used to calculate the (average) measured hardness is reported for each composition in the tables below.

All samples were previously aligned with a single tilting stage: according to the angle measured during SPM, this was corrected to be less than 0.5°. A SPM image with an area of 20x20 μm^2 was

[xviii] Values for E and ν of α-SiC from www.matweb.com/search/DataSheet.aspx?MatGUID=dd2598e783ba4457845586b58c8ea9fb

collected on each tested particle; the locations of the indentation were chosen by "clicking" directly on the spots that had to be indented on the SPM image. A time delay of 150 seconds was set before the first indent and 90 seconds between each tests in order to increase the spatial accuracy. Once all the indents were performed, a final SPM scan was done to verify that the indents were correctly located.

The hardness is then calculated by means of Eq. 2.47. The area function A(h_c) is calculated with the Oliver & Pharr method, defining contact depth h_c as $h_c = h_{max} - \varepsilon \frac{P_{max}}{S}$. For a Berkovich tip, ε = 0.75, and S is the unloading contact stiffness, defined as the derivative of P(h) at h=h_{max}. In practice, the unloading indentation curve is fitted between 20% and 95% of P_{max} with a power-law.

4.2 Hardness measurements: results

Examples of load-displacement curves performed with a Berkovich indenter on several different particles are given in Fig. 4.1:

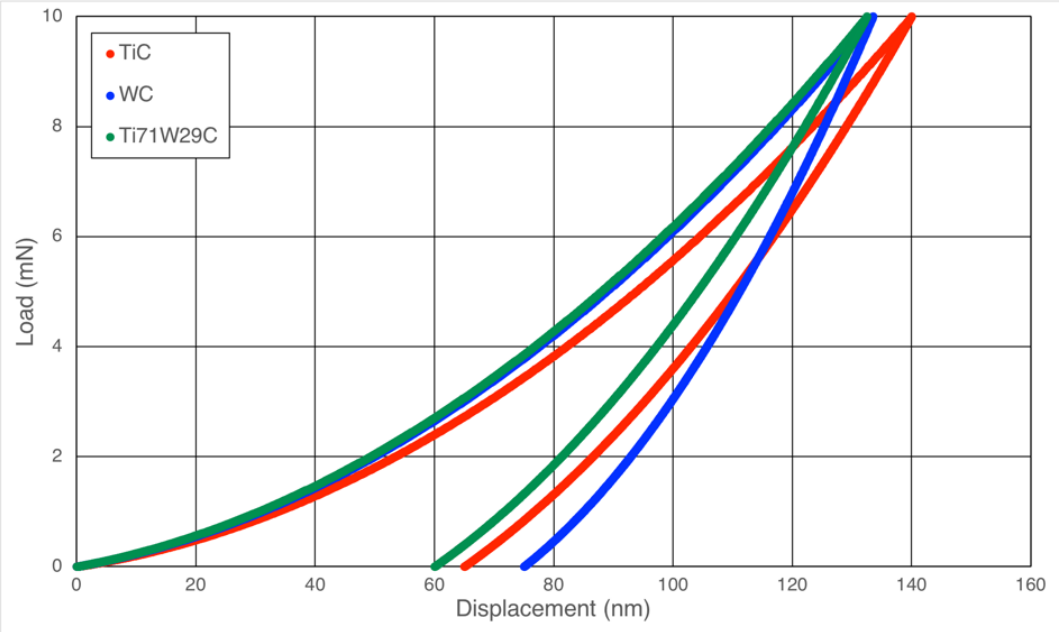

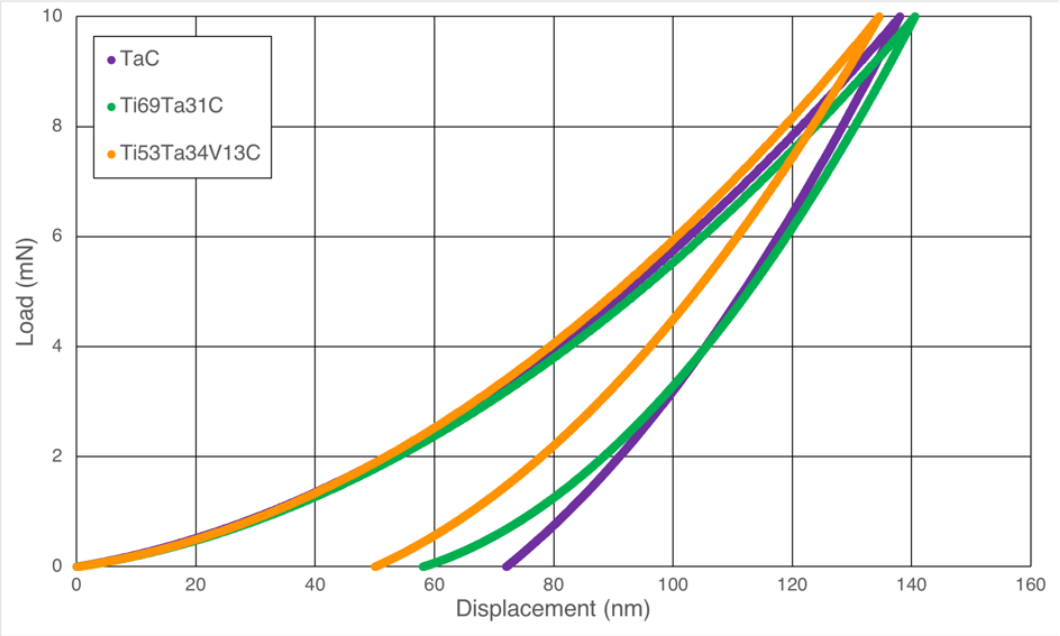

Fig. 4.1 – a) Comparison of load-displacement curves in the Ti-W-C system; b) comparison of load-displacement curves for a binary, a ternary and a quaternary composition.

4.2.1 The Oliver and Pharr analysis for hardness measurement

The results for binary carbides are given in Table 4.1. Reported values are the mean hardness, $\overline{H}$, over all measurements conducted, as well as the standard deviation σ and the number of measurements n for each composition.

Table 4.1 – Hardness measurements on TiC, WC, TaC, VC and NbC, obtained with Berkovich indentation and Oliver & Pharr analysis CHANGED.

	TiC	WC	TaC	VC	NbC
P_{max} (mN)	6	6	6	6	6
$\overline{H}$ (GPa)	30.9	31.1	31.6	30.4	25.7
σ (GPa)	0.7	3.4	0.8	0.9	1.2
n (-)	24	14	17	9	19

Hardness results of the ternary systems calculated using the Oliver & Pharr method are displayed in Tables 4.3 - 4.7 together with graphic representations of the hardness evolution as a function of carbide composition in Figs. 4.3 – 4.7. In those graphic representations, the vertical error is given by the measured hardness values' standard deviation and the horizontal uncertainty by the estimated uncertainty in EDX data (± 3%), this estimation being an addition of uncertainty inherent to EDX measurements (± 1.5%), plus variations in concentrations measured within and between particles, also roughly equal to ± 1.5%. The VEC evolution with composition is inserted for discussion in the next section.

Table 4.2 – Hardness measurements for ternary $(Ti_xW_{1-x})C$ particles embedded in steel. CHANGED

	$Ti_{89}W_{11}C$	$Ti_{81}W_{19}C$	$Ti_{71}W_{29}C$	$Ti_{54}W_{46}C$	$Ti_{34}W_{66}C$
n (-)	56	48	58	29	24
H (GPa)	31.9 ± 0.9	32.1 ± 0.8	34.2 ± 1.1	33.9 ± 1.3	36.4 ± 1.5

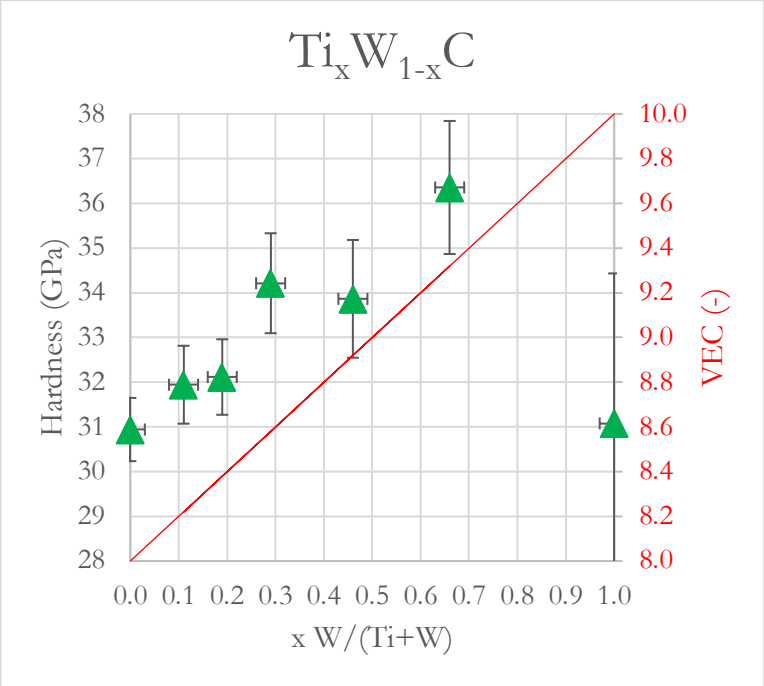

Fig. 4.2 – Hardness of the (Ti,W)C ternary system. CHANGED

Table 4.3 – Hardness measurements for ternary (Ti_xV_{1-x})C particles embedded in steel. CHANGED

	$Ti_{90}V_{10}C$	$Ti_{82}V_{18}C$	$Ti_{76}V_{24}C$	$Ti_{71}V_{29}C$	$Ti_{49}V_{51}C$	$Ti_{35}V_{65}C$	$Ti_{27}V_{73}C$	$Ti_{23}V_{77}C$	$Ti_4V_{96}C$
n (-)	60	57	58	50	52	52	32	46	48
H (GPa)	31.2 ± 0.8	31.9 ± 0.5	32.3 ± 0.5	32.9 ± 0.6	33.1 ± 0.7	33.1 ± 1.0	32.1 ± 0.7	31.9 ± 0.7	29.3 ± 1.5

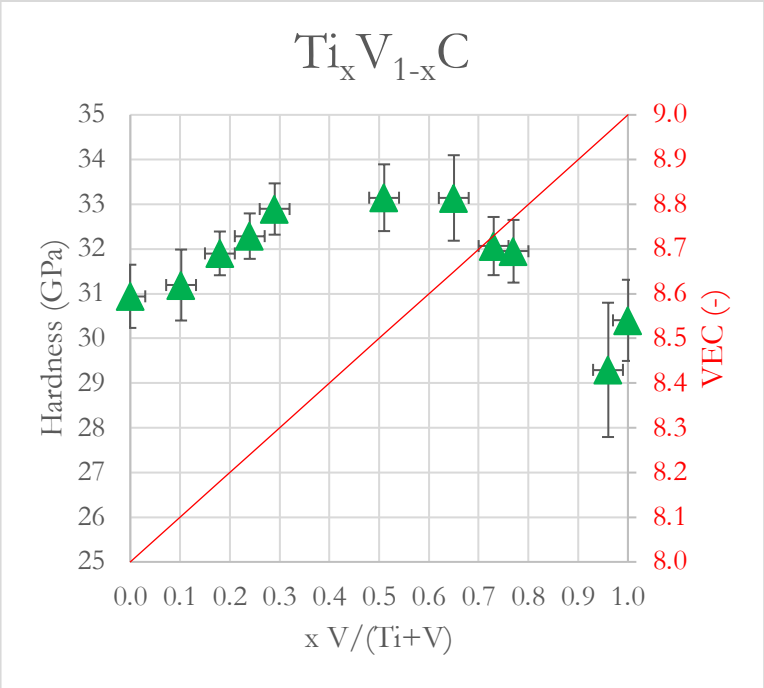

Fig. 4.3 – Hardness of the (Ti,V)C ternary system. CHANGED

Table 4.4 – Hardness measurements for ternary (Ti_xTa_{1-x})C particles embedded in steel. CHANGED

	$Ti_{85}Ta_{15}C$	$Ti_{69}Ta_{31}C$	$Ti_{42}Ta_{58}C$	$Ti_{22}Ta_{78}C$	$Ti_{10}Ta_{90}C$
n (-)	60	70	70	56	67
H (GPa)	29.5 ± 0.6	29.2 ± 0.8	30.7 ± 0.7	33.4 ± 1.5	32.7 ± 0.9

Table 4.5 – Hardness measurements for ternary (Ti_xNb_{1-x})C particles embedded in steel. CHANGED

	$Ti_{93}Nb_7C$	$Ti_{77}Nb_{23}C$	$Ti_{75}Nb_{25}C$	$Ti_{45}Nb_{55}C$	$Ti_{23}Nb_{77}C$	$Ti_{10}Nb_{90}C$
n (-)	50	57	67	57	71	50
H (GPa)	30.8 ± 0.8	31.9 ± 0.9	32.1 ± 0.6	31.3 ± 0.9	31.3 ± 0.9	32.3 ± 1.0

Table 4.6 – Hardness measurements for ternary (Ta_xV_{1-x})C particles embedded in steel. CHANGED

	$Ta_{92}V_8C$	$Ta_{90}V_{10}C$	$Ta_{77}V_{23}C$	$Ta_{69}V_{31}C$	$Ta_{53}V_{47}C$	$Ta_{39}V_{61}C$	$Ta_{18}V_{82}C$	$Ta_{13}V_{87}C$	$Ta_4V_{96}C$
n (-)	89	58	72	76	76	90	59	97	36
H (GPa)	32.4 ± 0.9	36.1 ± 1.0	34.6 ± 0.7	32.7 ± 1.0	33.5 ± 0.7	31.6 ± 0.8	30.9 ± 1.5	31.6 ± 0.9	31.2 ± 0.6

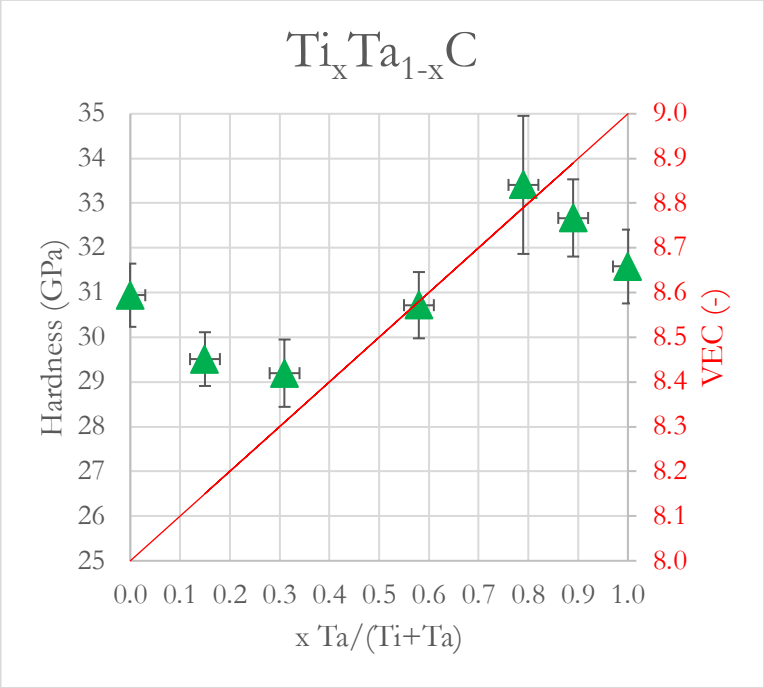

Fig. 4.4 – Hardness of the (Ti,Ta)C ternary system. CHANGED

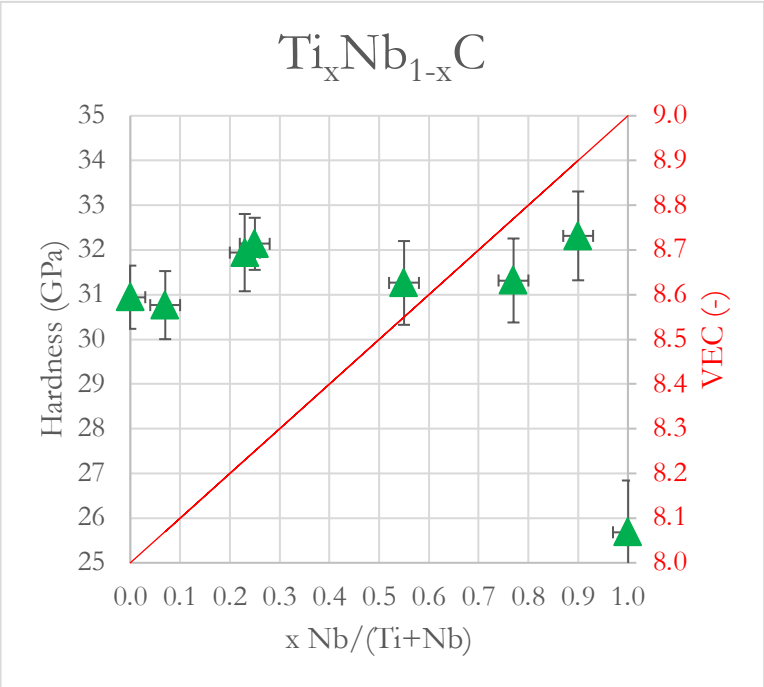

Fig. 4.5 – Hardness of the (Ti,Nb)C ternary system. CHANGED

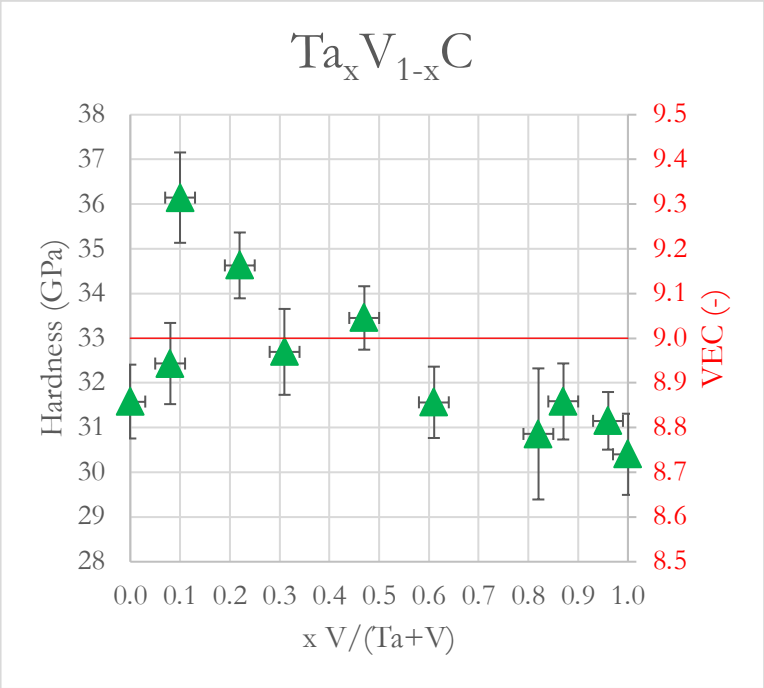

Fig. 4.6 – Hardness of the (Ta,V)C ternary system. CHANGED

Finally, hardness results for the twelve quaternary ($Ti_xTa_yV_{1-x-y}$)C carbides are given in Table 4.7.

Table 4.7 – Hardness measurement on ($Ti_xTa_yV_{1-x-y}$)C quaternary compositions. CHANGED

	1A	2A	3A	4A	5A	6A
	$Ti_{67}Ta_{32}V_1C$	$Ti_{55}Ta_{44}V_1C$	$Ti_{49}Ta_{49}V_2C$	$Ti_{39}Ta_{58}V_3C$	$Ti_{28}Ta_{69}V_3C$	$Ti_{17}Ta_{79}V_4C$
n (-)	53	48	48	60	59	54
H (GPa)	32.0 ± 0.6	30.9 ± 1.0	30.9 ± 1.1	32.4 ± 0.9	30.4 ± 0.9	30.3 ± 1.2

	2B	3B	4B	1C	2C	3C
	$Ti_{54}Ta_{38}V_8C$	$Ti_{44}Ta_{48}V_8C$	$Ti_{38}Ta_{53}V_9C$	$Ti_{65}Ta_{11}V_{24}C$	$Ti_{54}Ta_{22}V_{24}C$	$Ti_{36}Ta_{43}V_{21}C$
n (-)	49	48	59	79	76	84
H (GPa)	31.0 ± 0.9	31.3 ± 1.0	32.0 ± 1.1	32.2 ± 1.2	32.0 ± 1.1	32.0 ± 1.2

4.3 Hardness measurements: discussion

The hardness of carbides varies with many parameters including the carbide porosity, composition and crystalline orientation. Values in the literature therefore cover a certain range (see Chapter 2, Section 2.2.4). In that range of reported values, monocrystalline dense carbides tend to exhibit the highest hardness values, pointing to the importance of porosity and/or grain boundaries in the obtained value. One should also take into consideration that hardness can be strongly influenced by anisotropy, as measured by Mearky on TiC[6].

In this section, we will first discuss the accuracy of the method that was used to measure H. Unlike the elastic modulus, hardness is not a measurement of the stiffness of the material, but rather an indication of its resistance to permanent deformation. For that reason, the effect of the extra load-train compliance is not as important an issue here as it is for the elastic modulus (see next chapter).

Secondly, we will discuss the observed hardness evolutions as a function of carbide composition, referring in particular to the theory developed by Jhi et al.[55].

4.3.1 Comparison between Oliver & Pharr analysis and literature

Table 4.8 presents a comparison between hardness measurement derived from the Oliver & Pharr analysis ("OPM hardness") and corresponding values found in the literature.

Table 4.8 – Comparison among hardness results of binary carbide particles, analyzed with Oliver & Pharr method and the range of values found in the literature. CHANGED

	TiC	WC	TaC	VC	NbC
H_{OPM} (GPa)	30.9 ± 0.7	31.1 ± 3.4	31.6 ± 0.8	30.4 ± 0.9	25.7 ± 1.2
H_{lit} (GPa)	19.0[14] – 35.0[70]	19.0[80] – 30.0[81]	14.0[10] – 26.0 [77]	19.0[11] – 33.0[73]	27.2[12] – 29.4[12]
$H_{lit-ind}$ (GPa)	~ 32.0 [xix]	23.0 – 30.0 [xx]	17.8 – 26.3 [xxi]	33.3 [xxii]	24.5 [xxiii]

[xix] Q. Yang et al., Journal of Alloys and Compounds, 309 (2000) L5–L9
[xx] T.E. Buchheit et al., Mechanics of Materials, 42 (2010) 599–614
[xxi] S.R. Bakshi et al., Materials Science and Engineering, A528 (2011) 1287–1295
[xxii] L. Wu et al., Journal of Alloys and Compounds, 548 (2013) 60-64
[xxiii] L. Wu et al., Journal of Alloys and Compounds, 561 (2013) 220-227

OPM hardness values measured here are in some cases coherent in comparison with literature values, in other cases do not agree, the deviation being non-systematic: presently measured values agree with the literature for TiC and VC, while exceeding literature values for WC and TaC, and lying lower than literature values for NbC. Reasons for the discrepancy are not easy to pinpoint: one can invoke differences in the measurement method used, or in the microstructure or composition of the carbide, or also with anisotropic carbides such as WC in the crystal orientation. Most literature values are gathered using micro-Vickers measurements, in which the measured residual imprint area is used to compute the hardness from the measured peak load. Another possibility is that, despite finding a plateau in the present measurements above a certain load, this plateau value still be characteristic of hardness values amplified by a size effect. For this reason, a separate line is added to Table 4.8, giving literature values of hardness, $h_{lit-ind}$, gathered exclusively by nanoindentation methods.

The contact area $A(h_c)$ constitutes a key parameter for hardness measurements, and all the sources of error affecting the displacement (initial penetration, thermal drift, surface roughness, etc.) have an effect on the computed contact area. Calibration of the indenter requires here extra care, since H is directly proportional to A^{-1} (while E_r, for example, is only proportional to $A^{-1/2}$). In practice, it is very difficult to calibrate accurately the indenter for small displacements, and so we preferred identifying a threshold depth above which the hardness was observed to remain constant. A new calibration was also performed after testing ~1/3 of the samples, to observe that identical results were obtained, indicating in turn that there is no significant indenter tip blunting.

One possible source of systematic error in the present measurements is the potential, with the present steel-embedded carbide particles, for an added plastic (permanent) residual indenter displacement resulting from the particle sinking into the matrix via plastic deformation of the latter. The resulting added displacement will indeed have the effect of increasing the total residual displacement after subtraction of elastic deformation and therefore the computed contact area, causing the computed hardness to be smaller than it would with a sample of bulk carbide. Were residual indenter displacements resulting from such plastic particle sinking into the matrix significant, however, their values should increase with the applied load: this is not the case here, since measurements were only computed once reaching a plateau over a range of peak load values; i.e., in the absence of such an effect. Hence, as long as the particle does not indent plastically (or, viewed differently, sink permanently into) the matrix, matrix deformation will only bring added compliance to the load train. This will lead to an increase of the elastic recovery during unloading, thus potentially raising uncertainty but not causing systematic error on H. We note that this question has been addressed by Buchheit et al. in Mechanics of Materials 42 pp.599-614, 2010 in experiments where similar nanoindentation measurements of hardness and modulus were conducted on particles of equally hard particles (including WC) embedded in far more compliant polymeric matrices, to show that reliable hardness measurements could be obtained, with ranges of uncertainty in data similar to what is recorded here.

4.3.2 Evolution of the hardness for ternary compositions

The hardness of ternary carbides is reported here using values that were measured using the Oliver & Pharr method; relative deviations with this method proved to be within ± 2%. Although

this does not preclude higher levels of imprecision in measurements, we deem that this is an indication that present results are sufficiently precise to appreciate differences among compositions explored here.

We observe that the maximum hardness *H* in the (Ti,V)C system is located near VEC=8.5-8.7, not very far from the composition where VEC ≈ 8.4 and the analysis developed by Jhi et al. predicts a peak in carbide hardness based on consideration of numerically predicted values for the c_{44} elastic (directional, shear) modulus of cubic carbide or nitride crystals simulated by means of *ab initio* pseudopotential density functional theory. The maxima that we observe for (Ti,W)C and (Ti,Ta)C are on the other hand situated at far higher VEC values and thus cannot be said to agree with that prediction (in fact in the (Ti,Ta)C system near VEC = 8.4 the hardness rather passes through a minimum). The (Nb,Ti)C system shows no significant variation in measured hardness across the range of compositions explored except for the downward jump for binary NbC; here again the prediction by Jhi et al. of a maximum in hardness at VEC = 8.4 is not observed. And finally, data for the (Ta,V)C system, where the VEC is constant yet measured hardness values show strong variations, prove unequivocally that other factors than the VEC are at play in governing the hardness of carbides. The lack of agreement of present data with the VEC criterion of Jhi et al. is apparent also if one superimposes present data over those of Holleck[100] (see graph presented in Fig. 2.30) in Fig. 4.9, where microhardness values given by Holleck were converted into GPa (noting also that their definition of hardness is different from that used here, in that residual and not contact areas were used, causing an upward deviation in hardness if the former tend to fall below the latter).

The explanation that was proposed by Jhi et al. for the existence of this peak can be schematically summarized as follows. The effect on orbitals of the pure shear deformation along directions corresponding to cubic elastic constant c_{44} of a MC cubic crystal is sketched in Fig. 4.8. As outlined by Jhi et al., the σ M-C bonds, formed by the pairing of two electrons coming respectively from a p sub-orbital of the carbon atom and a d-e_g orbital of the metal atom (more precisely, the electron is localized in a hybridized sp^3d^2 orbital), are deformed in shear along the *44* orientation of the cubic crystal such that their overlap decreases: the crystal resists deformation that decreases in this way the bonding energy. Therefore, an increase of the density of such bonds has a positive (increase) effect on the shear modulus G. On the other hand, shear strain (along that direction) tends also to increase the overlap of π M-M bonds, formed by the pairing of two d-t_{2g} electrons, in the direction perpendicular to shearing, while it tends to separate them in the shearing direction. Because these M-M bonds are non-bonding, they do not contribute to the crystal cohesion in the undeformed state. Therefore, their increased separation in the shearing direction does not have a significant effect on the mechanical properties, while the increased overlap in the perpendicular direction suggests a negative effect on c_{44}: this assists the deformation. Therefore, as long as only d-e_g states are occupied, corresponding to M-C bonds, the shear modulus (and then the hardness) are expected to increase. On the other hand, when starting to fill also the d-t_{2g} states, forming M-M bonds, the hardness starts to decrease. This transition happens at VEC ≈ 8.4, suggesting that this is where G and hence the hardness should peak.

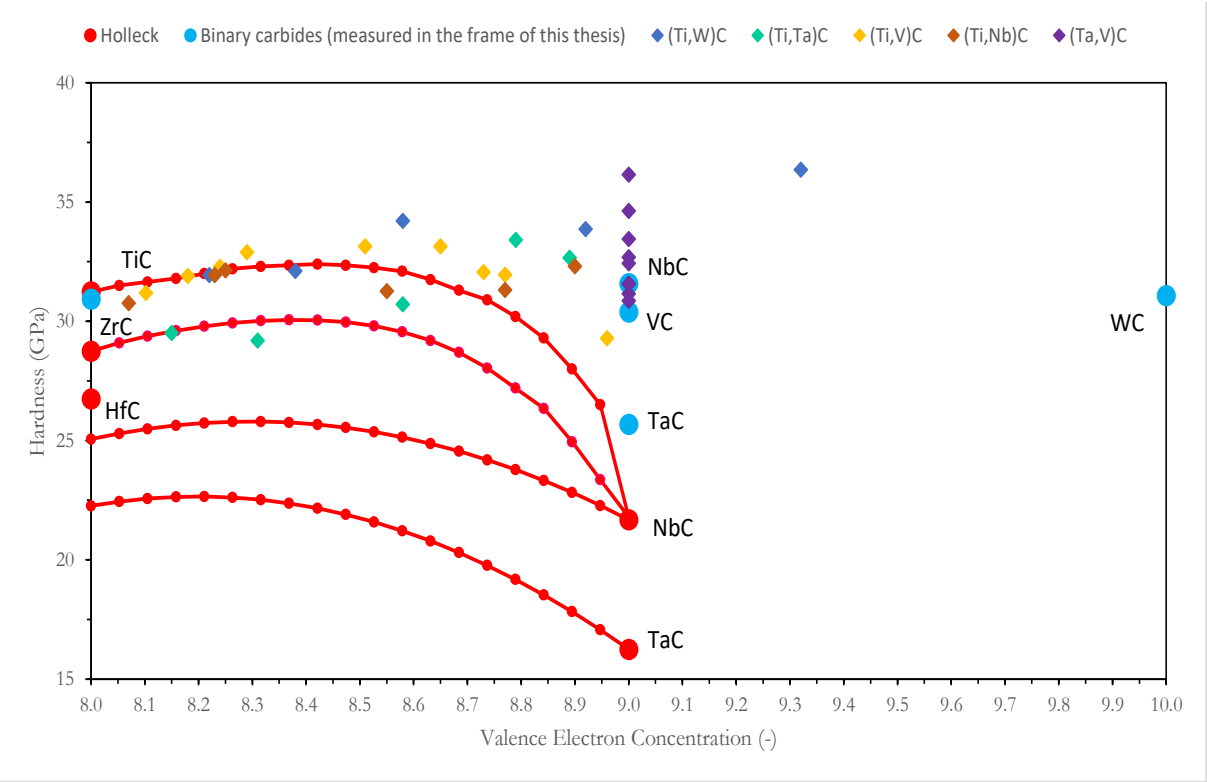

Fig. 4.7 – Completion of Holleck graph for hardness evolution of ternary carbides and carbonitrides with the hardness measurement performed in the frame of this thesis for the five (Ti,Nb)C, (Ti,Ta)C, (Ti,V)C, (Ti,W)C and (Ta,V)C ternary systems. CHANGED

As seen, present data do not agree with this prediction, especially if one considers the fifth ternary system, namely (Ta,V)C, for which the VEC is constant and equal to 9, both Ta and V belonging to Group V. According to the analysis of Jhi et al., all e_g states are occupied at such a high value of VEC, and we should then have a linear evolution of the hardness, linked to the gradual replacement of Ta atoms by V atoms, with no change in VEC and hence no change in the effects noted above. Our measurements of hardness for this specific ternary system show strong variations in measured hardness, with a high peak near 10 at.% V), Fig. 4.6. We now consider possible causes for discrepancy between the theory of Jhi et al. and data for carbides explored here.

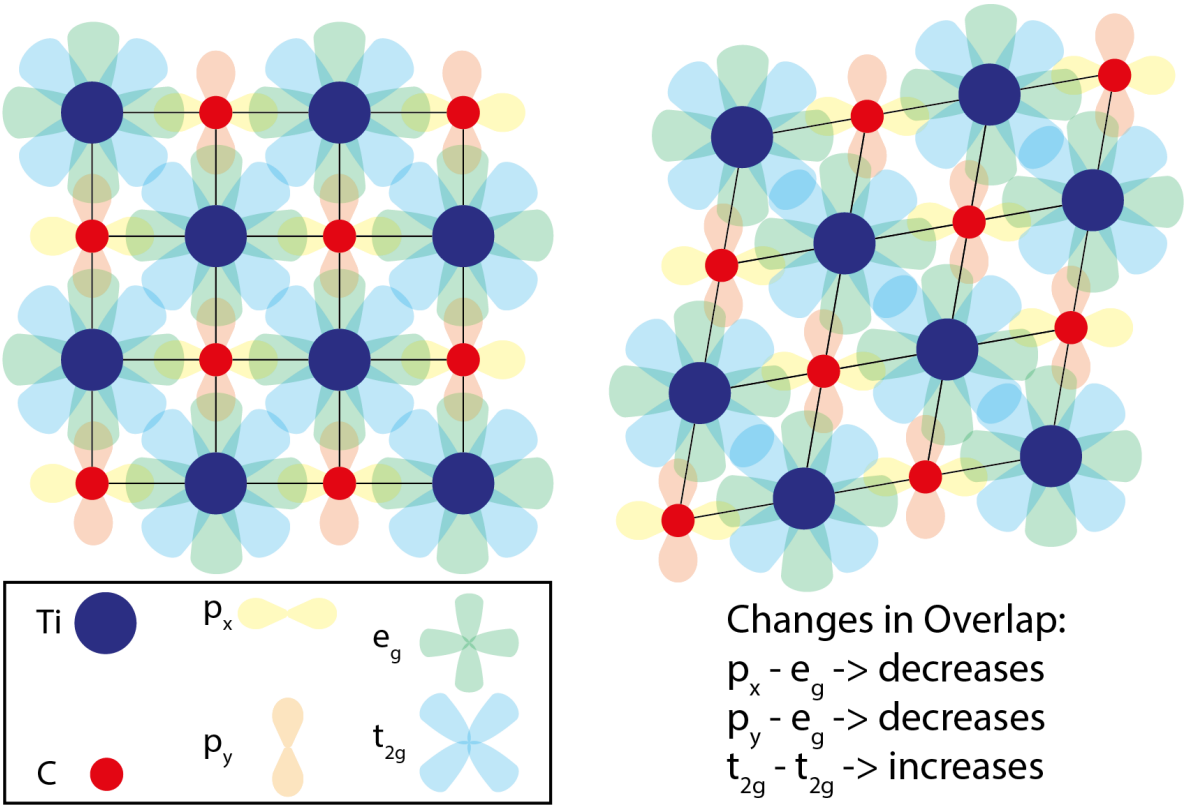

Fig. 4.8 – Evolution of the overlap with a shear strain in the xy plane.

Possibly, the difference in M-C bond strength between the two metals is another important parameter, as the strength of the Ta-C bond is different (and higher) than the strength of V-C bonds. As outlined by Gao[11], based on Gilman's theory, the bond strength of covalent ceramics can be extrapolated from the difference, in terms of energy, between the highest occupied state and the lowest unoccupied state, because breaking a bond requires moving a pair of electrons from the valence band up to the conduction band. DOS plots can then be used in order to determine the energy gap between these two states (Appendix D).

Another possible effect comes from the fact that, as a different atom is substituted within a MC cubic lattice, the difference in atom size may also play a role. If we assimilate the M-C bond to a spring, replacing an atom of M by an atom of M' will lead to the replacement of six M-C bonds by six new M'-C bonds, characterized by a different "spring constant" (which is directly linked to the bond strength). The new M' atom is located in the center of an octahedron, i.e. its equilibrium position remains the same, but the "springs" need to be either stretched or compressed to accommodate the difference in size.

Finally, a last possible effect might be the probability that an electron occupies a high-energy antibonding state. For this to be possible, the electron must overcome the gap energy, by tunneling. For high values of the VEC, the highest occupied state moves closer to the lowest antibonding state and the probability for an electron to tunnel into it increases. The effect on mechanical properties of the occupation of antibonding states was highlighted in Chapter 2 with the evolution of the bulk modulus along the fifth period.

To summarize, we observe a variation in hardness with composition for all five ternary systems. All the systems exhibit a non-linear behavior, with the presence of a maximal hardness for

intermediate compositions, and peak hardness values at compositions that do not agree with Jhi's theory.

4.3.3 Hardness evolution for quaternary compositions

A campaign of hardness measurements was also performed on quaternary (Ti,Ta,V)C carbides, thus exploring a portion of the compositional space situated between the three ternary (Ti,Ta)C, (Ti,V)C and (Ta,V)C systems.

Data are given in Table 4.7. As seen, in general, the addition of a third metallic element does not significantly impact the measured carbide hardness. Indeed, the reported hardness values for the twelve quaternary compositions that we have investigated all range from 30.3 to 32.4 GPa. If we compare those values with the hardness of the three related binary carbides TiC (30.9 GPa), VC (30.4 GPa) and TaC (31.6 GPa), we can conclude that there is no strong practical interest (or penalty), in terms of hardness, in producing a quaternary carbide, particularly given that ranges of measurement variations with composition match experimental uncertainty (see Table 4.9).

4.3.4 Conclusion

Pooling data from this work, the highest hardness has been obtained by mixing TiC and WC; indeed, the ternary composition $Ti_{34}W_{66}C$ exhibited a hardness of 36.4 GPa, which represents a gain of 5.5 GPa in comparison with TiC. It is interesting to note that this specific composition is metastable: indeed, at such a high amount of tungsten, thermodynamics predict the precipitation of WC; we assume that the fast cooling rate associated with the arc melting process is a possible explanation to the formation of this out-of-equilibrium phase. Another, similarly high, peak hardness was found in the (Ta,V)C system, namely in the carbide containing 10%VC; neighbouring compositions, however, showed values clearly lower than that. Overall, those are high hardness values; however, all fall short of the value 40 GPa, which is often considered as the threshold value above which materials can be qualified as being superhard.

CHAPTER 5:

ELASTIC MODULUS

Elastic modulus measurements were confronted with the major issue that the surrounding steel matrix adds compliance to the loadtrain, which lowers the apparent value of E that is measured when indenting the material making the particles well below the intrinsic stiffness of that material. We explored several different methods in order to overcome this challenge: we tried to correct the Oliver and Pharr method by using an analysis proposed by King for thin films over a substrate and we also milled un-notched cantilever beams and tested them in bending in order to eliminate the effect of the matrix. In the end, we designed our own method, based on ultra-low load spherical indentation, to measure E under conditions where it was possible to neglect the matrix-induced extra-compliance effect.

We measured in this way the modulus of five binary carbides: TiC, VC, TaC, NbC and WC, and these measurements were used to assess the accuracy of our method, by comparison with the respective literature values of those carbides. The mixed compositions within all the five ternary and some of the quaternary systems were then characterized. As will be seen, the elastic modulus evolution exhibits various behaviors depending on the system. We conclude by comparing measurements with the measured evolution of hardness and with predictions of atomic bonding theory, reviewed in Chapter 2: .

5.1 Elastic modulus measurement methods

In this section, the nanoindentation apparatus is firstly described in detail. That apparatus was used not only for elastic modulus measurements, but also to determine hardness and fracture toughness. We then provide experimental details, as well as the analyses used to measure E.

5.1.1 The Oliver and Pharr method and King's analysis

The elastic modulus of carbides was first evaluated by the standard method that Oliver and Pharr developed in 1992. Indents were done with a calibrated Berkovich diamond tip. The elastic modulus was then extrapolated from the unloading curve, by measuring the slope at P_{max}, as described in Chapter 2 (Section 2.4.2).

Calibration of the tip, necessary to determine the area function, was done on the reference substrates, of polished fused quartz and SiC. A perfect Berkovich tip has a contact area given by:

$$A(h_c) = 24.5\ h_c^2$$

Eq. 5.1

A real indenter, which is always blunted at its tip, is better approximated by a polynomial function:

$$A(h_c) = 24.5\ h_c^2 + C_1 h_c + C_2 h_c^{\frac{1}{2}} + C_3 h_c^{\frac{1}{4}} + C_4 h_c^{\frac{1}{8}} + C_5 h_c^{\frac{1}{16}}$$

Eq. 5.2

The calibration is realized by doing a series of 100 indents on the reference material, with an increasing peak load. We produced indents from 615 µN up to 12'000 µN with a step size of 115 µN on the fused quartz reference sample. Each indent was then analyzed, and the area function was calculated, the modulus and the Poisson's ratio being fixed. The contact area was plotted as a function of the contact depth h_c. The polynomial coefficients C_i are then calculated by fitting the data with the function given in Eq. 5.2. In doing so, it is better to have only a few non-zero coefficients because when too many coefficients are finite, the fitting polynomial will start to fit the noise and develop inflection points.

Our Berkovich tip is well fitted with a two-parameters polynomial, as per calibration on fused quartz:

$$A_{FQ}(h_c) = 24.5\ h_c^2 + 599.86\ h_c$$

Eq. 5.3

In measuring the modulus of MC carbides, once the sample is correctly placed onto the nanoindenter X/Y stage, one particle is selected with help from the optical image provided by the camera. Then a scan of the surface is performed with the tip, keeping a constant contact load of 2 µN. This SPM capability of the nanoindenter transducer allows to apply the load with a positioning precision of ~100 nm.

A drift analysis is then performed: the tip is set in contact with the specimen and the displacement is measured for 40 seconds. Because of the large difference in size between the tip (a few μm^3) and the sample (~ 3 cm^3), as soon as the contact is established, thermal equilibration occurs. Therefore,

even a small difference in temperature between the tip and the sample can induce a measureable movement of the tip by thermal dilatation on either side of the contact point. That effect, called thermal drift and typically on the order of 0.1 nm/s, is then corrected for each indent according to the measured drift rate.

The load function used for all the tests is a simple trapezoidal curve, composed of three segments:

- A loading part, conducted with a constant loading rate of 2 mN/s;
- A plateau lasting 2 seconds;
- An unloading part, conducted with an unloading rate of -2 mN/s.

The unloading curve is fitted with a power-law from which the slope at P_{max} is calculated, allowing to determine the reduced modulus E_r (Eq. 2.28). The power law used to fit the unloading part of the indentation curve counts three parameters: A, m and an offset h_f accounting for the plastic deformation, in the following function:

$$P(h) = A\left(h - h_f\right)^m$$

Eq. 5.4

The slope of the unloading curve at h_{max} can be directly calculated from the power-law:

$$S = \left.\frac{dP(h)}{dh}\right|_{h=h_{max}} = mA \cdot \left(h_{max} - h_f\right)^{m-1}$$

Eq. 5.5

Knowing E_r, the modulus of the material is then extracted using Eq. 2.18.

The Oliver and Pharr analysis was developed for bulk materials and proved to be inaccurate for particles embedded in more compliant and softer matrix: it then leads to underestimate the particle elastic modulus. For that reason, we used a corrected version of this method, initially proposed by King for flat punch indents and extended to conical indenters by Saha and Nix, in order to correct the Oliver and Pharr analysis so as to account for the added compliance caused by the substrate.

This model adds an extra term in Eq. 2.18, which accounts for the fact that the measured reduced modulus is not only a combination of both sample and indenter properties, but should also include properties of the substrate (Eq. 2.38). In our case, we consider carbide particles as a thin film (Fig. 5.1) that is not uniform, in the sense that the film is fragmented, and its thickness is not constant (the particles have a complex shape and are not always aligned with the polished surface).

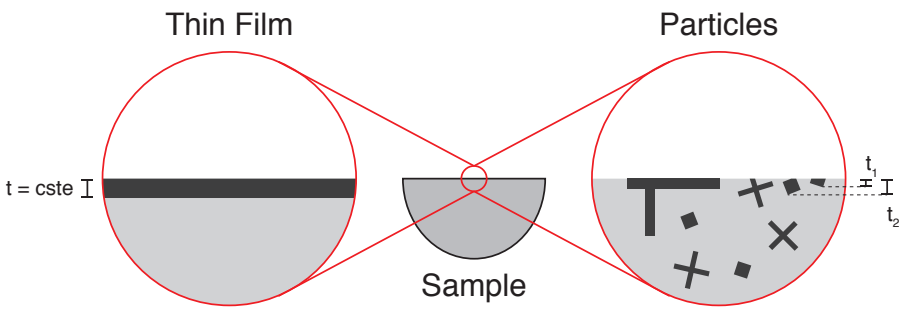

Fig. 5.1 – Thin film vs particles configuration.

If the measurement on particles can be locally assimilated to a thin film measurement, the particle thickness along the indentation axis varies along the particle and must be determined, for example by FIB-milling. We measured the local thickness by performing FIB-tomography on a few tested particles: a rectangular cross-section is cut, encompassing the particle, and a high-resolution SE picture of the cross-section is taken; a new cut is performed, followed by a new picture; the process is repeated until all the particle has been milled. We can then reconstruct a 3D picture of the particle and measure its thickness at different locations, especially under the indentation. Because that process proved to be very time-consuming, we characterized only three binary carbides in this way, namely TiC, TaC and VC, testing three different particles for each carbide.

Eq. 2.38 requires knowledge of the mechanical properties of the matrix (E_s and ν_s). In our samples, the matrix is not homogeneous because it contains ~ 40 vol% of carbide particles. As a first approximation, it is possible to use the modulus of iron (E = 200 GPa), but a more sophisticated micro-composite model would be more appropriate. Therefore, the Hashin-Shtrikman[174] composite model was used to determine the matrix properties: we assumed the presence of 40 vol% carbide particles in the matrix and we calculated its composite modulus using thi mean-field model developed for an isotropic material uniformly reinforced with isotropic spheres of different modulus. Both bulk and shear moduli of the composite, B_c and G_c, are first bounded, as a function of the properties of the matrix and of the reinforcements:

$$B_{Fe} + \frac{V_{car}}{\frac{1}{B_{car} - B_{Fe}} + \frac{V_{Fe}}{B_{Fe} + \frac{4G_{Fe}}{3}}} \leq B_c \leq B_{car} + \frac{V_{Fe}}{\frac{1}{B_{Fe} - B_{car}} + \frac{V_{car}}{B_{car} + \frac{4G_{car}}{3}}}$$

$$G_{Fe} + \frac{V_{car}}{\frac{1}{G_2 - G_{Fe}} + \frac{6V_{Fe}(B_{Fe} + 2G_{Fe})}{5G_{Fe}(3B_{Fe} + 4G_{Fe})}} \leq G_c \leq G_{car} + \frac{V_{Fe}}{\frac{1}{G_{Fe} - G_{car}} + \frac{6V_{car}(B_{car} + 2G_{car})}{5G_{car}(3B_{car} + 4G_{car})}}$$

Eq. 5.6

G_{Fe} = 77.5 GPa and B_{Fe} = 166 GPa are found in the literature[xxiv]. G_{car} and B_{car} are calculated from E_{car} and ν_{car}, under the assumption of an isotropic material made of isotropic phases:

$$B_{car} = \frac{E_{car}}{3(1 - 2\nu_{car})}$$

$$G_{car} = \frac{E_{car}}{2(1 + \nu_{car})}$$

Eq. 5.7

[xxiv]Source: matweb.com; search: iron, Fe; 26.03.2018 / 09:40

The Hashin and Shtrikman model gives us a lower and a higher bound for substrate B and G moduli. We used the lower bound, because it corresponds to the case of strong particles embedded in a more compliant matrix. The Young's modulus of the sample matrix is then calculated from:

$$E_s = \frac{9B_cG_c}{3B_c + G_c}$$

Eq. 5.8

We use an iteration process, starting with $E_s = E_{iron}$; the carbide elastic modulus E_{car} is then calculated with Eq. 2.38. E_s is then re-evaluated by using the new value of E_{car} and Eq. 5.6 & Eq. 5.8; E_{car} is calculated again with Eq. 2.38 and from this E_s is recalculated. That procedure is then repeated until convergence of E_s. During all the process, the Poisson's ratio of the substrate, ν_s, is assumed constant and $\nu_s = \nu_{iron} = 0.29$[xxiv].

5.1.2 Cantilever beams

In another attempt to eliminate the effect of the matrix surrounding the carbide particles, the carbide particle elastic modulus was measured by carving and bending triangular un-notched cantilever beams within the particles. To this end, a micro-cantilever beam is milled from the polished surface of a carbide particle. As few beams have been produced in this way, and similar beams were tested to measure the carbide fracture toughness, the complete method will be explained in the fracture toughness chapter (Chapter 6), where it was more extensively used to test similarly shaped and carved chevron-notched cantilever beams.

A sketch of the test is shown in Fig. 5.2. The beam is loaded elastically by a cube-corner tip, using the low-load head of the nanoindenter up to P = 5 mN. The load-displacement curve for such a test is a straight line. The elastic modulus E is given by:

$$E = \frac{P_{max}L^3}{3I\delta_{max}}$$

Eq. 5.9

Where P_{max} is the peak load (5 mN), δ_{max} the maximal deflection, L is the distance between the origin of the beam and the point of the load application, and I is the moment of inertia; for a triangular beam, $I = H \cdot B^3/12$, with H and B the beam height and width. While applying the load, both the displacement δ_{max} and the load P_{max} are measured. The dimensions of the beam, L, B and H are determined from SEM images.

This method proved to give a good approximation of the carbide elastic modulus but was very sensitive to the SEM-measured dimensions. Moreover, milling such beams was very time consuming and not adapted for evaluation of a large number of particles. Only a few tests were thus conducted using this approach.

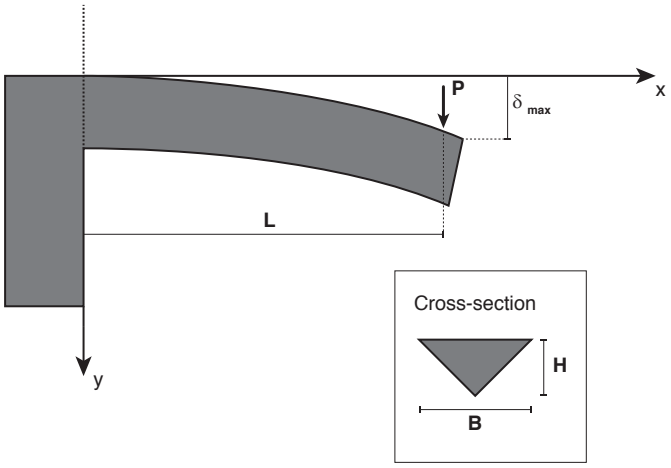

Fig. 5.2 – Sketch of an un-notched cantilever beam in bend testing.

5.1.3 Ultra-low load spherical indentation

A third method, used here in systematic fashion, was developed within the frame of this project in order to measure the elastic modulus of embedded particulate carbide reinforcements. Our method aims to overcome the issue of the extra compliance coming from the matrix, without requiring the use of onerous FIB machining, which automatically renders the method unsuitable for testing a large number of carbide compositions. This method is based on nanoindentation solely.

The matrix can be seen as an additional spring, placed in series with two other springs representing the carbide and the indenter. The spring constants could be ordered as follow: $k_{mat} < k_{car} < k_{ind}$, the matrix being much more compliant (by *virtue* both of its modulus and size than the carbide or the diamond. As load is applied, the three springs are deformed. A procedure used to calibrate the compliance was proposed by Oliver & Pharr, but cannot be applied here because it requires a large indent, which is not compatible with the size of our particles. Moreover, the procedure would have to be performed for each particle, because the compliance is a function of both the particle thickness and of what lies underneath, two parameters that vary widely from particle to particle. Rather than calibrating the extra matrix-induced compliance, we chose to use testing conditions that make it negligible.

Because the effect of the compliance is, in a first approximation, proportional to the applied load, the extra displacement, h_{cp}, that it induces on the indenter can be written as:

$$h_{cp} = C_m \cdot P$$

Eq. 5.10

Where C_m is the extra matrix-induced compliance and P the applied load. Our approach consisted in using ultra-low loads, typically $P < 1$ mN, in order to render h_{cp} negligible compared to the displacement induced b deformation at the point of indenter and carbide contact.

By decreasing the load, the penetration depth decreases as well: for example, at 1 mN, the penetration of the indenter in a carbide particle is only ~10-20 nm, depending on tip geometry and on the material. The resolution of the apparatus is such that this displacement range is below uncertainty or noise of the apparatus. For such small penetrations, all the indenters deviate from their ideal geometry and can in a first approximation be considered as blunted and hence roughly spherical. For that reason, we chose to use a spherical indenter and treat our measurements by using Hertz's analysis of the elastic contact between a sphere and a surface. We used a large spherical diamond tip, with a radius $R > 1$ μm.

The total displacement h_{tot} measured during the indentation is the sum of three terms:

$$h_{tot} = h_0 + h_{cp} + h_{ind}$$

Eq. 5.11

where h_0 is an offset due to the initial contact established with the tip at 2 μN, h_{cp} is due to matrix deformation, and h_{ind} is the particle penetration depth. Using Hertz's analysis (Eq. 2.22) and the definition of compliance Eq. 5.8 & Eq. 5.9, we can rewrite this as:

$$h_{tot}(P) = h_0 + C_m \cdot P + \left(\frac{P}{\frac{4}{3} E_r \sqrt{R}} \right)^{2/3}$$

Eq. 5.12

The easiest way to determine $\mathrm{E_r}$ would then be to fit a function $f_1(P) = c + b \cdot P + (P/a)^{2/3}$ to our data, the constant a containing all the particle-relevant elastic information, b being the global load-train compliance and c the offset.

Reference materials are used to calibrate the radius of the indenter R. To this end, a series of indents is performed on the SiC reference, chosen because it is closer to MC carbides in its stiffness value. The reference being bulk SiC, we are not concerned by the effect of extra matrix-induced compliance and the second coefficient in the $f_1(P)$ function, b, is zero. Fig. 5.3-a shows an example of the load-displacement curve of an indent performed on SiC; the deformation is purely elastic, as confirmed by the superposition of both loading and unloading curves. Fig. 5.3-b gives an example of the fit accuracy. The local, nanoscale indenter radius is then calculated from the resulting a fitting parameter, knowing E_r (Eq. 5.12).

By examination of function f_1, it is seen that if the load is low enough, the last term, proportional to $P^{2/3}$, will dominate over the second term, which is linear in P and has a coefficient that decreases as the matrix stiffness increases. Hence, if the particle is embedded within a relatively stiff matrix and the load is kept sufficiently low, the linear term becomes negligible and the simplified fitting function f_2, which implicitly neglects the effect of the matrix compliance, can be used. By using sufficiently low loads, we found indeed that the effect of the extra-compliance due to the matrix becomes negligible ($b = 0$), making it possible to use a simplified $f_2(P) = c + (P/a)^{2/3}$ function, containing only two fitting parameters. Reducing the number of fitting parameters has the advantage of avoiding mathematical issues due to the fact that an infinity of solutions exists for

the fit of a given curve if too many parameters are involved. And, indeed, it proved to be impossible to determine single and clear values for both b and a when fitting function f_1 to the data.

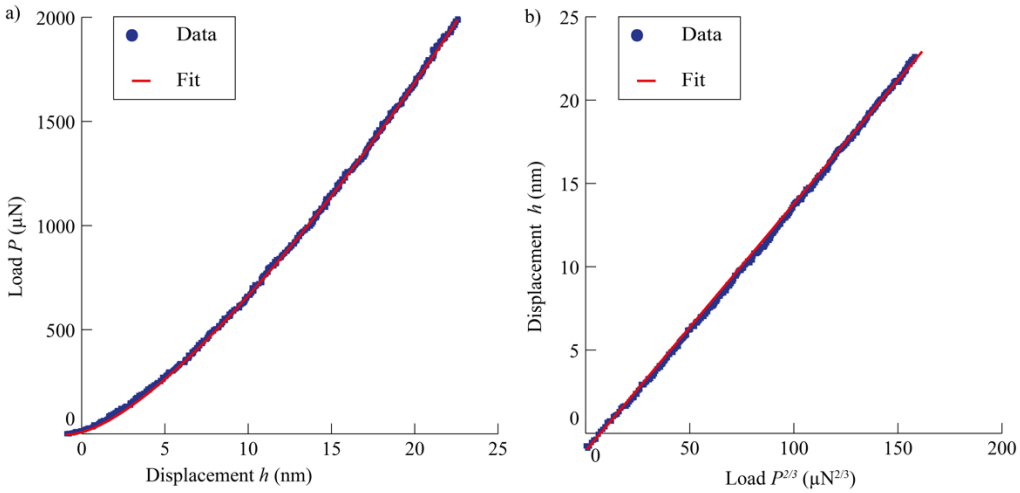

Fig. 5.3 – a) Elastic indentation on a SiC (0001) wafer; b) Accuracy of a fit on the total displacement related to the indentation of SiC by a spherical tip.

The theoretical error in the a parameter is easily calculated: we consider an indentation performed on an ideal particulate sample, for which both the extra matrix-induced compliance and the elastic modulus are known, with a spherical indenter of fixed radius R. If we compare analyses of the load-displacement curve done with both $f_1(P)$ and $f_2(P)$ functions, it appears that the quantity $h - c$ must be constant, and the a-parameter calculated with $f_2(P)$, called $\hat{a}$, must be different from a, in order to compensate for the extra matrix-induced compliance. The ratio $\hat{a}/\,a$ can be easily calculated and depends on both the matrix-induced compliance b and the parameter a, which is a function of the particle elastic modulus and of the indenter radius:

$$\frac{\hat{a}}{a} = \frac{P}{a}\left[b \cdot P + \left(\frac{P}{a}\right)^{\frac{2}{3}}\right]^{-\frac{3}{2}}$$

Eq. 5.13

Error in the a parameter is plotted in Fig. 5.4. The three colors, red, green and blue, correspond respectively to three increasing values of a; for a tip radius of 2 µm, a = 4 TPa·nm$^{0.5}$ represents fused quartz, a = 18 TPa·nm$^{0.5}$ SiC and a = 8 TPa·nm$^{0.5}$ an intermediate material. The solid lines represent a stiff matrix, with C_m = 1 nm/mN, compatible with a steel matrix, while the dashed lines represent a more compliant matrix with C_m = 5 nm/mN (e.g. an aluminium matrix). For ultra-low loads (P < 150 µN), and for stiff matrices (C_m = 1 nm/mN), the error on a for carbide-like materials ($a \approx 18$) is smaller than 5%.

The minimal load required for a given error in the a parameter can also be easily estimated by inverting Eq. 5.13:

$$P = a\left(\frac{\left(\frac{\hat{a}}{a}\right)^{-\frac{2}{3}} - 1}{ab}\right)^3$$

Eq. 5.14

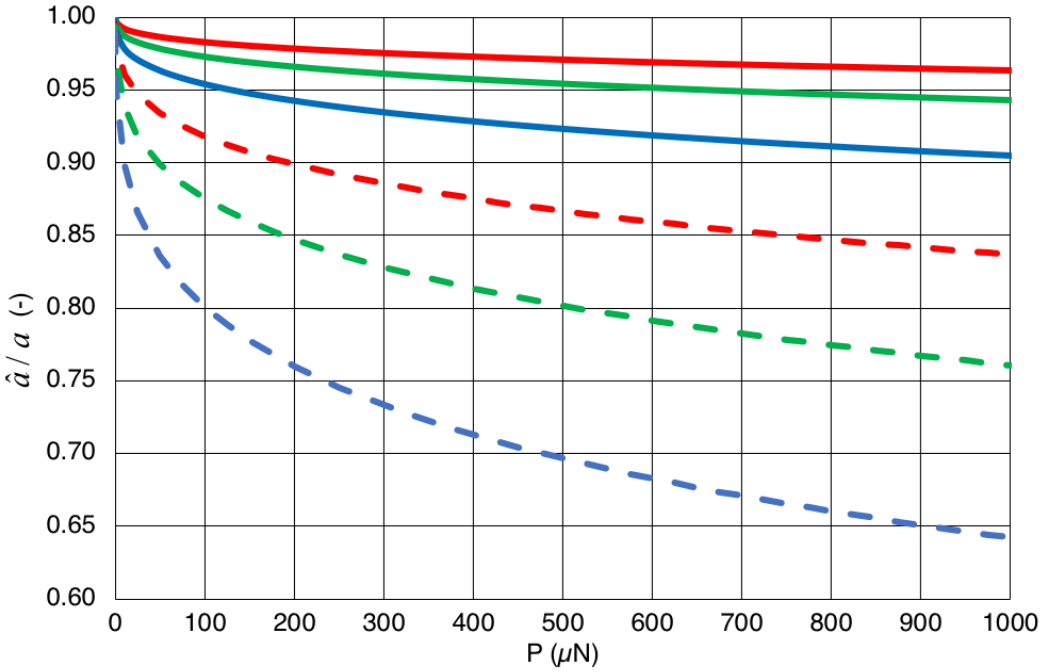

Fig. 5.4 – Estimation of the theoretical error on the a parameter caused by elastic surrounding matrix deformation; Red: a = 4; Green: a = 8; Blue: a = 18; Solid line: C_m = 1 nm/mN; Dashed line: C_m = 5 nm/mN; the limit representing an error of 5% for a = 4 and C_m = 1 nm/mN is represented by the grey line.

Note that the load below which it is possible to neglect the effect of the extra-compliance depends then not only on the matrix stiffness, but also on the particle modulus. If the matrix is too compliant, it is almost impossible to reach the limit of 5% (dashed lines in Fig. 5.4). By contrast, for a less stiff particle material such as fused quartz, it is possible to neglect the matrix compliance for loads higher than 1 mN (red solid line in Fig. 5.4).

Our method consists then in performing a large set of indents (> 50) for each composition, on different particles, each indent having a load function characterized by several load-unload cycles, with a peak load situated between 2 and 3 mN.

The entire set of displacement-load curves is then fitted by imposing:

- The fitting equation is $f_2(P) = c + (P/a)^{2/3}$, c being the offset corresponding to the point of initial contact between the indenter and the sample, with a then containing all the elastic information;

- All the loading/unloading parts of the indents are considered separately, and the first loading part of each indent is systematically rejected, as it can exhibit a small amount of plastic deformation during initial contact and depending on the surface roughness;
- The fitted part of the curve covers the interval of load values from 50 to 100 µN, such that we can neglect the linear elastic compliance load-train;
- The offset c is fitted separately for each indent;
- Parameter a is fitted for the entire set of data, i.e. it is constrained to keep the same value for all the curves of the set.

The reason for fitting the entire set together with a single value of a is to eliminate the effect of thermal drift, which is a statistical error, and by this increase the accuracy of the fit. For a set of N loading/unloading curves, we have thus to determine $N + 1$ parameters by means of N fits. An example is given in Fig. 5.5, with a set of 50 different indents performed on SiC or TiC.

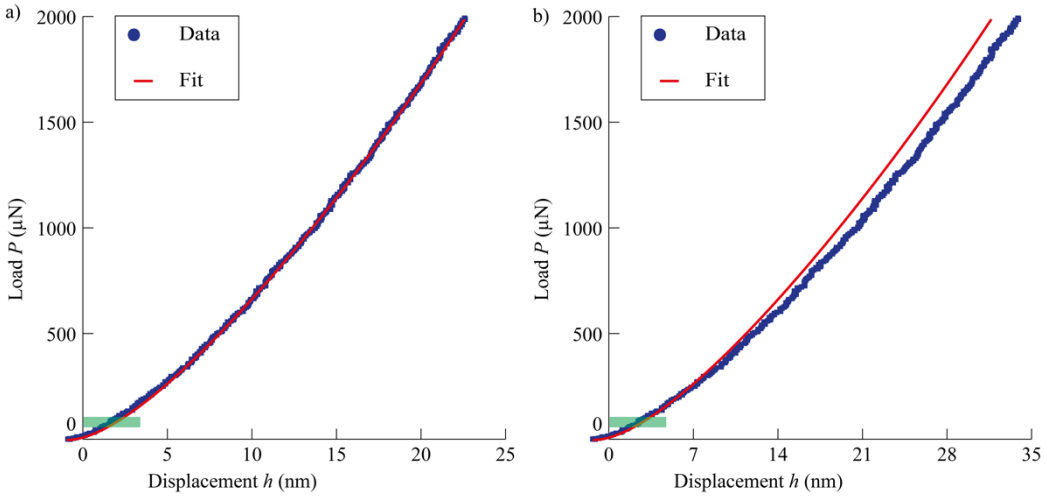

Fig. 5.5 – Example of fitting equation. h in nm and P in µN. The blue points represent the 50 superposed indents; the red points are used for the fit and the red line corresponds to the fitted equation. a) fit on SiC wafer; b) fit on TiC particles in a steel matrix.

The difference in displacement at peak load is different in both cases: for SiC, which is a bulk material, the difference is very small and can be explained by the frame compliance (which is not corrected here). For TiC particles, the deviation at peak load becomes important and is due to the matrix compliance, which cannot be neglected anymore at 3 mN.

5.2 Elastic modulus measurements: results

The elastic modulus was measured for binary, ternary and quaternary carbide compositions. We first present the Oliver and Pharr results for Berkovich indents in binary carbides, in order to demonstrate the underestimation of the elastic modulus caused by matrix deformation. We then give the results gathered using King's analysis for TiC, VC and TaC binary carbides. Next, we present the measurements done by bending cantilever beams of TiC, VC and TaC. Finally, we give the results obtained with our own spherical indentation method, for binary, ternary and quaternary systems.

5.2.1 Oliver & Pharr and King's analysis

The Oliver & Pharr analysis is based on the unloading part of the indent, which is purely elastic if we assume no reverse plasticity. We present, for illustration, the detailed calculations for a TiC particle.

Nine indents were performed on a single TiC particle, with a maximal load of 10 mN, arranged according to a *3x3* grid with a 3 μm step size. That spacing is sufficient to ensure that the strain field associated with each indent does not interfere with that of neighbor indents. The power-law fitting parameters, as well as S and h_{max} are given for the 9 indents on the TiC particle in Table 5.1:

Table 5.1 – Power-law fitting parameters for indents on a TiC particle embedded in steel.

Parameter	Indent 1	Indent 2	Indent 3	Indent 4	Indent 5	Indent 6	Indent 7	Indent 8	Indent 9
$A\left(\frac{\mathrm{mN}}{\mathrm{nm}^m}\right)$	24.93	25.80	25.56	24.00	23.79	30.30	23.66	25.91	22.64
m (-)	1.377	1.369	1.372	1.384	1.383	1.329	1.391	1.360	1.384
h_f (nm)	60.85	61.03	62.32	60.28	61.20	63.48	67.41	62.73	61.64
h_{max} (nm)	138.6	138.8	139.9	138.4	140.0	142.0	144.6	142.5	143.2
S (μN/nm)	177.2	176.1	176.9	177.1	175.6	169.2	180.1	170.5	169.6

With the contact stiffness S thus calculated, we can determine the contact depth h_c.

$$h_c = h_{max} - \varepsilon \frac{P_{max}}{S}$$

Eq. 5.15

Where the parameter $\varepsilon = 0.75$ for a paraboloid of revolution and accounts for deflection of the surface along the contact perimeter. By inserting Eq. 5.3 & Eq. 5.5 into Eq. 2.28, it is now possible to determine E_r:

$$E_r = \frac{\sqrt{\pi} \cdot mA \cdot \left(h_{max} - h_f\right)^{m-1}}{2\sqrt{24.5\, h_c^2 + 599.86\, h_c}}$$

Eq. 5.16

The TiC Young's modulus is then calculated with Eq. 2.18. The results for the indents performed on a TiC particle are given in Table 5.2:

Table 5.2 – Contact depth, contact area and reduced modulus for nine indents on a TiC particle.

	Indent 1	Indent 2	Indent 3	Indent 4	Indent 5	Indent 6	Indent 7	Indent 8	Indent 9
h_c (nm)	96.3	96.2	97.5	96.1	97.3	97.7	103.0	98.5	99.0
$A(h_c)$ (µm²)	0.285	0.284	0.291	0.283	0.290	0.292	0.321	0.297	0.299
E_r (GPa)	294.0	292.5	290.4	294.5	288.9	277.2	281.3	277.2	274.6
E (GPa)	381.9	379.3	375.7	382.8	373.1	353.2	360.1	353.2	348.8

That procedure was repeated on at least five different particles, in order to provide a range of values accounting for potential effects of anisotropy. Table 5.3 gives final results, obtained by following the same procedure, for the five binary carbides. The values intervals represent the min/max measured moduli for each binary carbide.

Table 5.3 – Elastic modulus measurements by the Oliver & Pharr analysis on TiC, VC, TaC, NbC and WC particles embedded in steel.

	TiC	WC	TaC	VC	NbC
E (GPa)	345-393	497-524	389-396	344-361	405-419

We also applied King's analysis to measurements performed on 3 different particles of TiC, VC and TaC. That model requires prior determination of the thickness t of the particle under the

indentation. The α parameter in Eq. 2.38 is a function of the $\sqrt{A}/t$ ratio, and was empirically determined by Saha and Nix[129]:

$$\alpha\left(\frac{\sqrt{A}}{t}\right) = -0.378 - 0.005\left(\frac{\sqrt{A}}{t}\right) + 0.347\left(\frac{\sqrt{A}}{t}\right)^{\frac{1}{2}} + 1.197\left(\frac{\sqrt{A}}{t}\right)^{\frac{1}{4}}$$

Eq. 5.17

As described in the previous section, the elastic modulus is calculated by an iterative process based on the Hashin-Shtrikman model.

The detailed results are presented in Table 5.4:

Table 5.4 – Elastic modulus measurements of TiC, VC and TaC particles embedded in steel. The matrix is considered as a carbide/steel composite and its modulus is determined with the Hashin-Shtrikman model.

	TiC			VC			TaC		
	Ind. 1	Ind. 2	Ind. 3	Ind. 1	Ind. 2	Ind. 3	Ind. 1	Ind. 2	Ind. 3
t (μm)	3.02	3.42	4.03	3.87	3.62	4.01	4.24	4.99	4.65
$\sqrt{A}$ (nm)	533.6	533.2	582.7	567.3	579.1	565.8	564.7	575.8	568.4
α (-)	0.48	0.52	0.44	0.50	0.53	0.49	0.48	0.44	0.46
h (nm)	138.9	139.43	138.9	144.6	146.4	144.3	141.5	142.8	141.8
E_r (GPa)	295.1	294.5	296.9	285.7	285.0	286.4	309.9	310.5	309.5
E (GPa)	467.2	453.1	451.8	435.2	440.4	433.0	484.9	475.9	477.5

5.2.2 Elastic modulus measurement with cantilever beams

In a first approach to eliminate effects of the matrix deformation, cantilever beams were machined in TiC, TaC and VC (one for each composition). The elastic modulus is calculated with Eq. 5.7. The beam dimensions, as well as the maximal displacements measured are presented together with the calculated E values in Table 5.5. The errors on E are calculated from Eq. 5.7, by assuming a measurement uncertainty on B, H and L from the SEM image analysis of ± 5%.

Table 5.5 – Elastic modulus measurements based on the bending of TiC, VC and TaC cantilever beams.

	TiC	VC	TaC
δ_{max} (nm)	450.7	402.3	615.7
B (μm)	5.0	5.2	4.9
H (μm)	2.6	2.5	2.7
L (μm)	15.2	14.6	16.6
E (GPa)	490 ± 27	430 ± 24	490 ± 30

5.2.3 Ultra-low load spherical indentation method

As described in the previous section, this new method consists in fitting an entire set of indentations, performed on the same sample but in different particles, with a power-law function. Each loading/unloading curve is fitted separately for the offset h_0, but the a parameter of $f_2(P) = c + (P/a)^{2/3}$ is forced to be the same for the entire set.

The measurements for the binary carbides are given in Table 5.6:

Table 5.6 – Elastic modulus measurements on binary carbides, based on ultra-low load spherical indentation.

	TiC	VC	TaC	NbC	WC
a (TPa·nm$^{0.5}$)	19.5 ± 0.15	13.8 ± 0.25	14.8 ± 0.20	16.6 ± 0.37	26.8 ±0.14
R (nm)	1972 ± 43	1065 ± 33	1065 ± 33	1065 ± 33	1972 ± 43
E_r (GPa)	329 ± 4	318 ± 6	339 ± 6	383 ± 7	452 ± 5
M (GPa)	461 ± 6	440 ± 9	481 ± 10	574 ± 13	746 ± 10
ν (-)[5]	0.19	0.22	0.24	0.22	0.24
E (GPa)	445 ± 6	419 ± 9	454 ± 10	546 ± 13	703 ± 10

The uncertainties on a and on the indenter radius R are calculated from the R-squared correlation coefficient and propagated to E_r, M and E according to standard uncertainty

propagation methods. The measured curves are compared with the fitting functions and the R-squared coefficient is calculated from the residuals, by using the general definition:

$$"R^2" = 1 - \frac{SS_{res}}{SS_{tot}} = 1 - \frac{\sum_i (y_i - f_i)^2}{\sum_i (y_i - \bar{y})^2}$$

Eq. 5.18

where y_i are the measured displacement values, f_i are the fitted displacement values and $\bar{y}$ is the mean displacement. A statistical approach makes sense here, because each set of data contains a sufficient number of indentation loading/unloading curves (typically N > 500). The R-squared coefficient can then be used to determine the uncertainty on the derived value of a:

$$err(a) = \sqrt{\frac{(1 - "R^2") \sum_i (y_i - \bar{y})^2}{(N-1) \sum_i (x_i - \bar{x})^2}}$$

Eq. 5.19

where x_i represents each measured load and $\bar{x}$ the mean load.

Results for the five ternary systems are presented in Tables 5.7-5.11. A graphic representation of the elastic modulus evolution with composition is shown in Figs. 5.6-5.10. A representation of the carbide indentation modulus M is preferred instead of E, because the Poisson's ratio was not known for ternary and quaternary compositions. Nevertheless, an estimation for E calculated from the binary MC carbide Poisson's ratios using the rule of mixtures is given for each composition.

Table 5.7 – Elastic modulus measurements in the $(Ti_xW_{1-x})C$ ternary system, based on ultra-low load spherical indentation.

	$Ti_{89}W_{11}C$	$Ti_{81}W_{19}C$	$Ti_{71}W_{29}C$	$Ti_{54}W_{46}C$	$Ti_{34}W_{66}C$
a (TPa·nm$^{0.5}$)	20.0 ± 0.17	20.9 ± 0.16	21.8 ± 0.21	23.0 ± 0.15	25.0 ±0.21
R (nm)	1972 ± 43	1972 ± 43	1972 ± 43	1972 ± 43	1972 ± 43
M (GPa)	480 ± 7	509 ± 7	542 ± 8	589 ± 9	669 ± 10
ν (-)	0.19	0.20	0.20	0.21	0.22
E (GPa)	463 ± 7	490 ± 7	520 ± 8	563 ± 8	636 ± 10

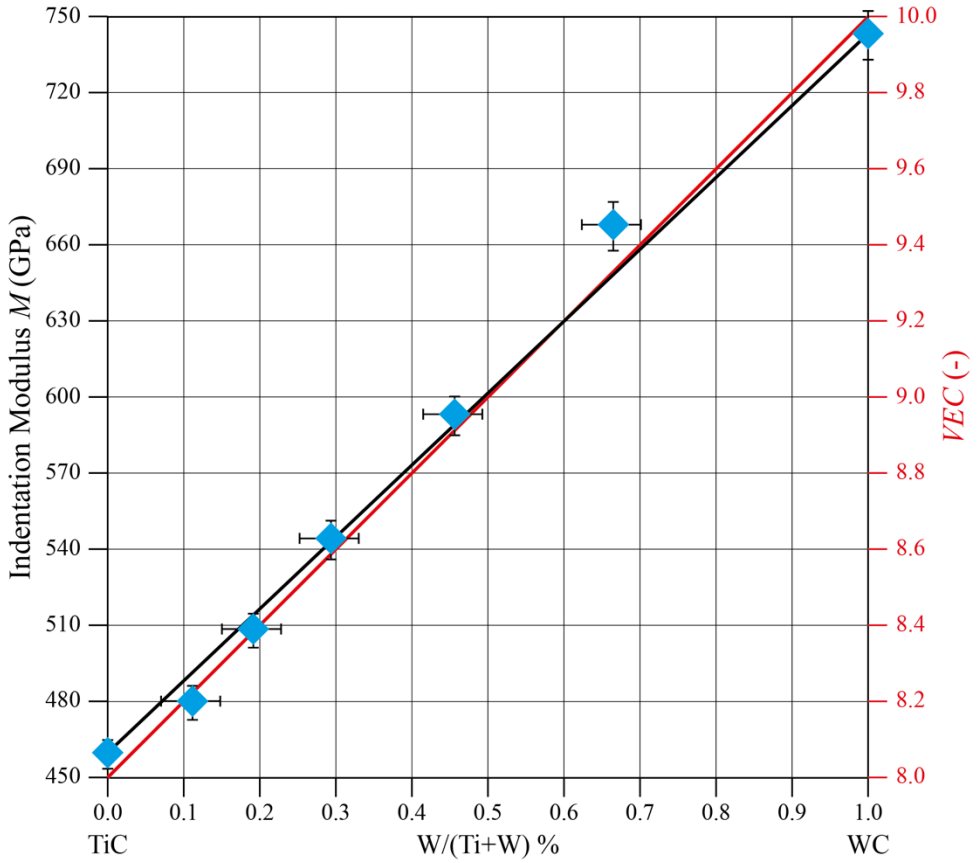

Fig. 5.6 – Indentation Modulus evolution in the (Ti,W)C ternary system.

Table 5.8 – Elastic modulus measurements in the $(Ti_xV_{1-x})C$ ternary system, based on ultra-low load spherical indentation.

	$Ti_{90}V_{10}C$	$Ti_{81}V_{19}C$	$Ti_{75}V_{25}C$	$Ti_{71}V_{29}C$	$Ti_{47}V_{53}C$	$Ti_{34}V_{66}C$	$Ti_{26}V_{74}C$	$Ti_{23}V_{77}C$	$Ti_{4}V_{96}C$
a ($TPa \cdot nm^{0.5}$)	15.2 ± 0.19	21.0 ± 0.19	21.5 ± 0.13	15.7 ± 0.19	20.9 ± 0.15	19.8 ± 0.16	19.2 ± 0.13	19.1 ± 0.19	18.9 ± 0.17
R (nm)	1065 ± 33	1972 ± 43	1972 ± 43	1065 ± 33	1972 ± 43	1972 ± 43	1972 ± 43	1972 ± 43	1972 ± 43
M (GPa)	501 ± 13	514 ± 7	533 ± 8	527 ± 13	509 ± 7	473 ± 7	453 ± 6	447 ± 7	443 ± 6
ν (-)	0.19	0.19	0.19	0.20	0.20	0.21	0.21	0.21	0.22
E (GPa)	483 ± 12	495 ± 7	513 ± 7	507 ± 13	488 ± 7	453 ± 6	433 ± 6	427 ± 6	422 ± 6

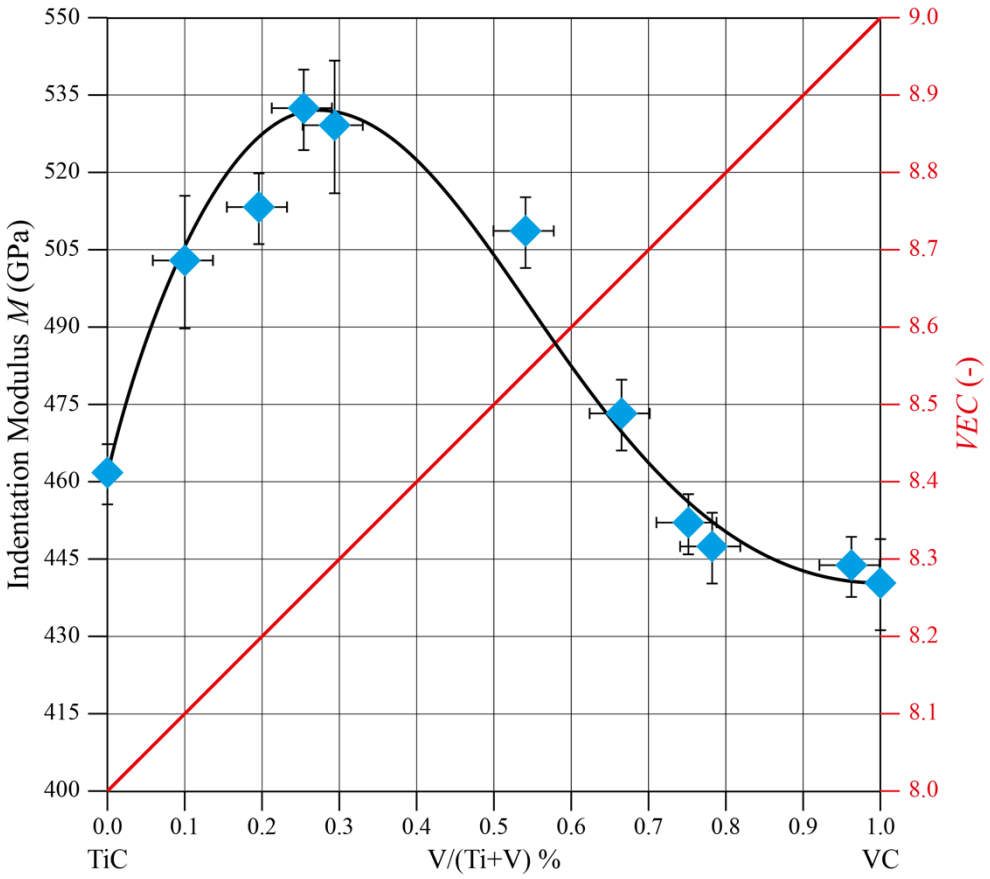

Fig. 5.7 – Indentation Modulus evolution in the (Ti,V)C ternary system.

Table 5.9 – Elastic modulus measurements in the (Ti_xTa_{1-x})C ternary system, based on ultra-low load spherical indentation.

	$Ti_{81}Ta_{19}C$	$Ti_{69}Ta_{31}C$	$Ti_{42}Ta_{58}C$	$Ti_{22}Ta_{78}C$	$Ti_{10}Ta_{90}C$
a ($TPa \cdot nm^{0.5}$)	14.9 ± 0.22	15.0 ± 0.22	15.8 ± 0.23	15.8 ± 0.19	15.6 ± 0.20
R (nm)	1065 ± 33	1065 ± 33	1065 ± 33	1065 ± 33	1065 ± 33
M (GPa)	489 ± 10	492 ± 10	531 ± 11	530 ± 10	520 ± 10
ν (-)	0.20	0.20	0.22	0.23	0.24
E (GPa)	470 ± 10	472 ± 10	506 ± 11	502 ± 10	491 ± 10

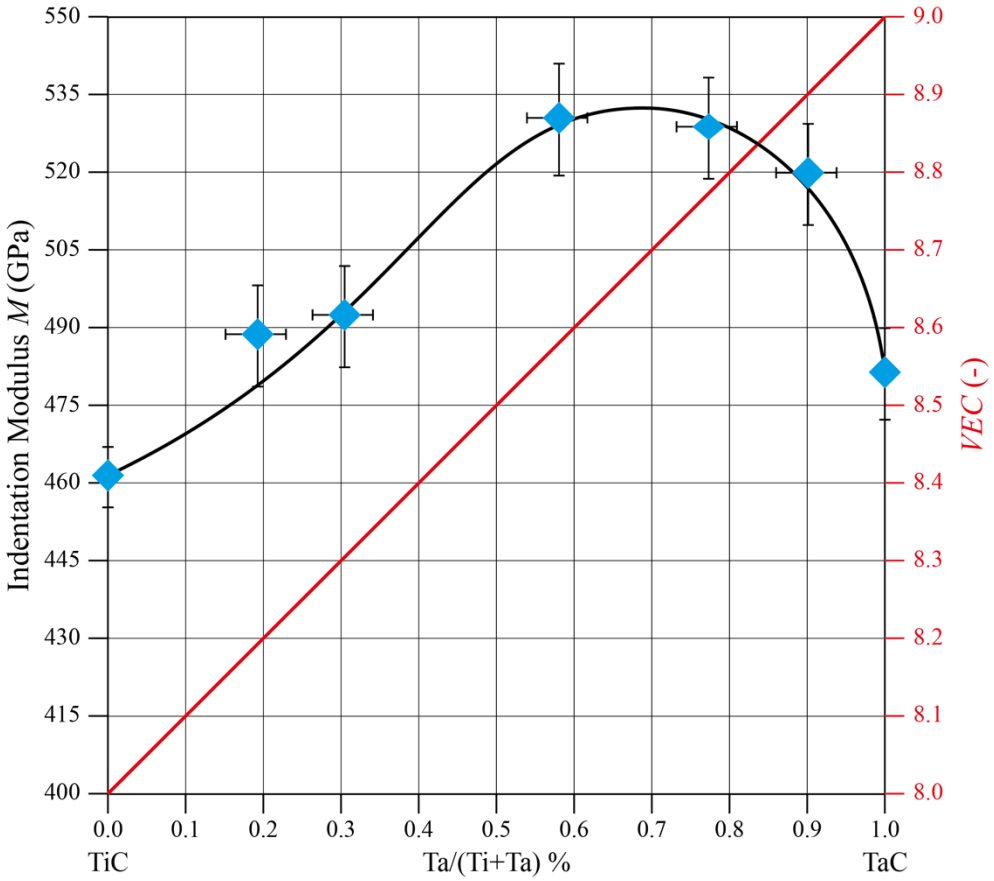

Fig. 5.8 – Indentation Modulus evolution in the (Ti,Ta)C ternary system.

Table 5.10 – Elastic modulus measurements in the (Ti_xNb_{1-x})C ternary system, based on ultra-low load spherical indentation.

	$Ti_{97}Nb_3C$	$Ti_{76}Nb_{24}C$	$Ti_{73}Nb_{27}C$	$Ti_{43}Nb_{57}C$	$Ti_{23}Nb_{77}C$	$Ti_{10}Nb_{90}C$
a (TPa·nm$^{0.5}$)	14.4 ± 0.25	14.8 ± 0.25	14.9 ± 0.22	15.6 ± 0.27	16.1 ± 0.29	16.5 ± 0.23
R (nm)	1065 ± 33	1065 ± 33	1065 ± 33	1065 ± 33	1065 ± 33	1065 ± 33
M (GPa)	463 ± 10	485 ± 10	489 ± 10	521 ± 11	545 ± 12	568 ± 12
ν (-)	0.19	0.19	0.19	0.20	0.21	0.22
E (GPa)	446 ± 10	467 ± 10	470 ± 10	499 ± 11	521 ± 12	542 ± 12

Table 5.11 – Elastic modulus measurements in the $(Ta_xV_{1-x})C$ ternary system, based on ultra-low load spherical indentation.

	$Ta_{92}V_8C$	$Ta_{90}V_{10}C$	$Ta_{77}V_{23}C$	$Ta_{69}V_{31}C$	$Ta_{53}V_{47}C$	$Ta_{39}V_{61}C$	$Ta_{18}V_{82}C$	$Ta_{13}V_{87}C$	$Ta_4V_{96}C$
a (TPa·nm$^{0.5}$)	14.7 ± 0.20	14.9 ± 0.23	15.0 ± 0.20	15.1 ± 0.18	15.2 ± 0.14	14.8 ± 0.20	14.1 ± 0.21	14.0 ± 0.21	13.8 ± 0.18
R (nm)	1065 ± 33	1065 ± 33	1065 ± 33	1065 ± 33	1065 ± 33	1065 ± 33	1065 ± 33	1065 ± 33	1065 ± 33
M (GPa)	481 ± 10	490 ± 10	493 ± 10	498 ± 10	503 ± 10	482 ± 10	450 ± 9	445 ± 9	440 ± 9
ν (-)	0.24	0.24	0.24	0.23	0.23	0.23	0.22	0.22	0.22
E (GPa)	453 ± 9	462 ± 10	465 ± 10	471 ± 10	477 ± 10	457 ± 10	427 ± 9	423 ± 9	419 ± 9

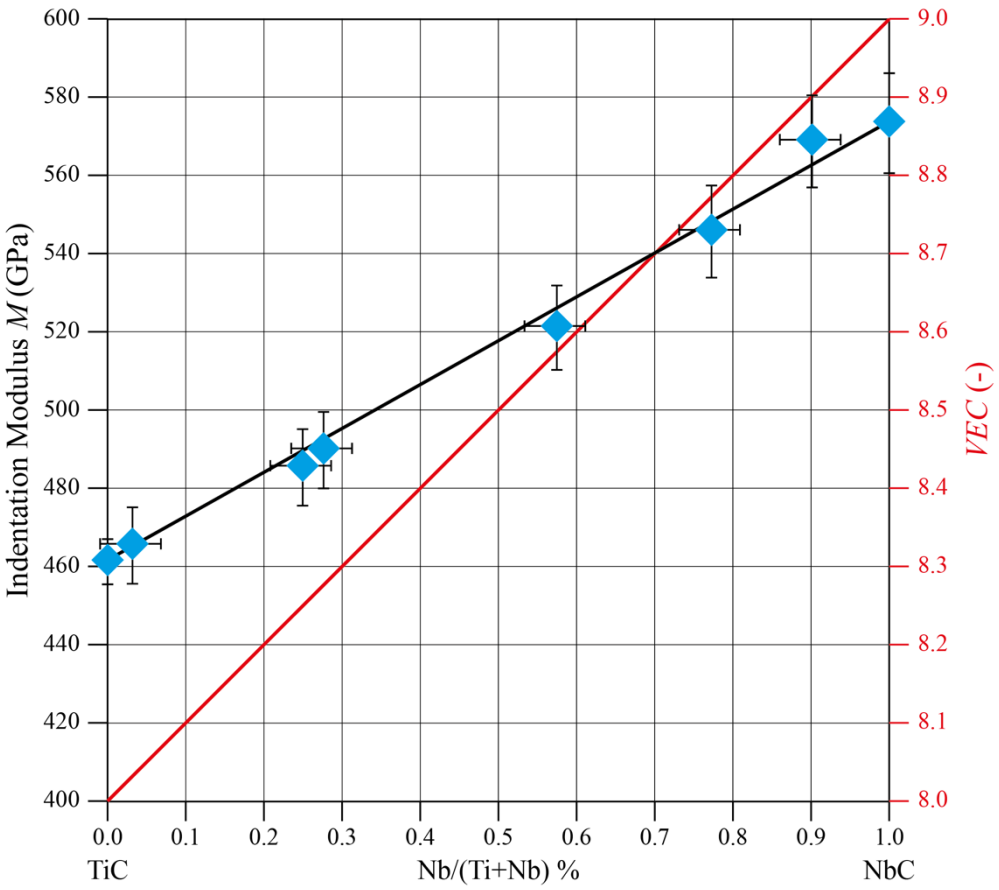

Fig. 5.9– Indentation Modulus evolution in the (Ti,Nb)C ternary system.

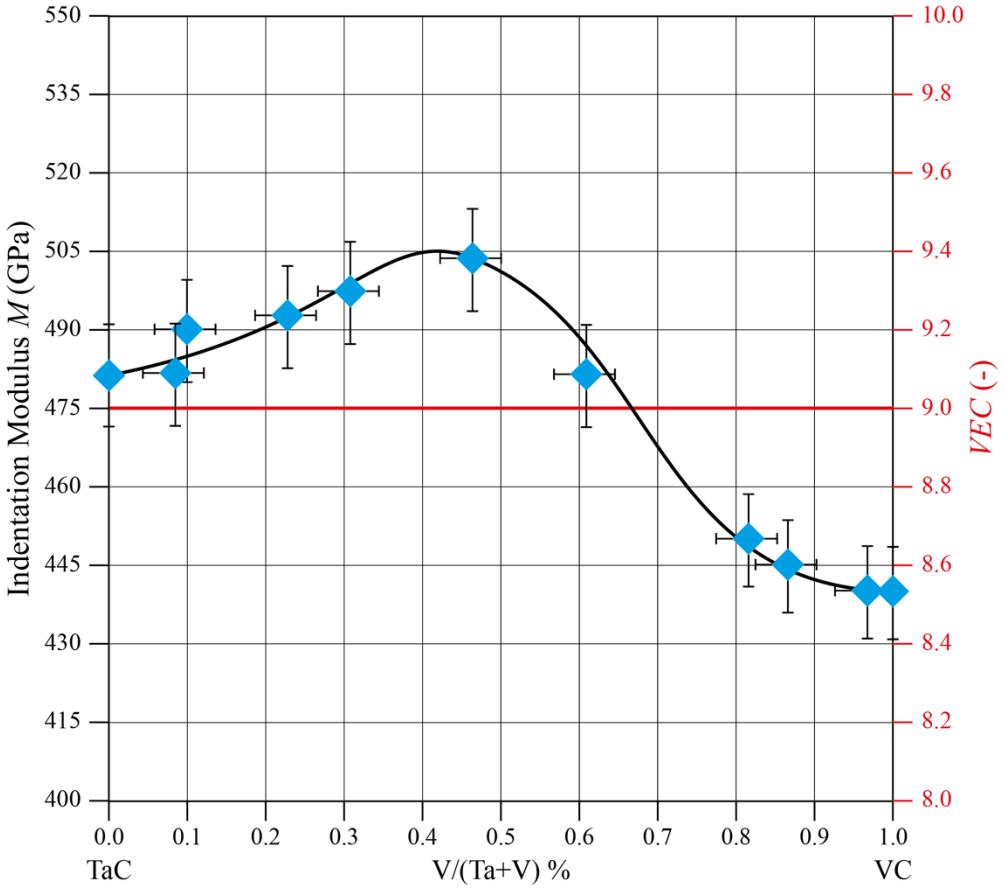

Fig. 5.10 – Indentation Modulus evolution in the (Ta,V)C ternary system.

The results for the twelve quaternary $(Ti_xTa_yV_{1-x-y})C$ alloy particles are presented in Table 5.12. Fig. 5.11 represents a ternary TiC-TaC-VC diagram summarizing all the measurements performed on the three TiC, TaC and VC binary carbides, on the three ternary $(Ti_xTa_{1-x})C$, $(Ti_xV_{1-x})C$ and $(Ta_xV_{1-x})C$ systems, and on the quaternary compositions that were explored here.

Table 5.12 – Elastic modulus measurement on $(Ti_xTa_yV_{1-x-y})C$ quaternary compositions, based on ultra-low load spherical indentation.

	1A	2A	3A	4A	5A	6A
a ($TPa \cdot nm^{0.5}$)	20.9 ± 0.24	21.5 ± 0.35	21.3 ± 0.27	22.4 ± 0.23	22.3 ± 0.31	21.8 ± 0.22
R (nm)	1972 ± 86	1972 ± 86	1972 ± 86	1972 ± 86	1972 ± 86	1972 ± 86
M (GPa)	511 ± 8	532 ± 9	523 ± 8	566 ± 8	562 ± 9	542 ± 8
ν (-)	0.20	0.21	0.21	0.22	0.23	0.23
E (GPa)	490 ± 8	509 ± 9	500 ± 8	539 ± 8	532 ± 9	513 ± 8

	2B	3B	4B	1C	2C	3C
a (TPa·nm$^{0.5}$)	22.1 ± 0.19	22.7 ± 0.19	22.6 ± 0.26	22.0 ± 0.17	23.1 ± 0.20	25.0 ± 0.26
R (nm)	1972 ± 86	1972 ± 86	1972 ± 86	1972 ± 86	1972 ± 86	1972 ± 86
M (GPa)	552 ± 8	577 ± 8	571 ± 9	549 ± 8	590 ± 9	669 ± 10
ν (-)	0.21	0.22	0.22	0.20	0.21	0.22
E (GPa)	528 ± 8	549 ± 8	543 ± 9	527 ± 8	564 ± 9	637 ± 10

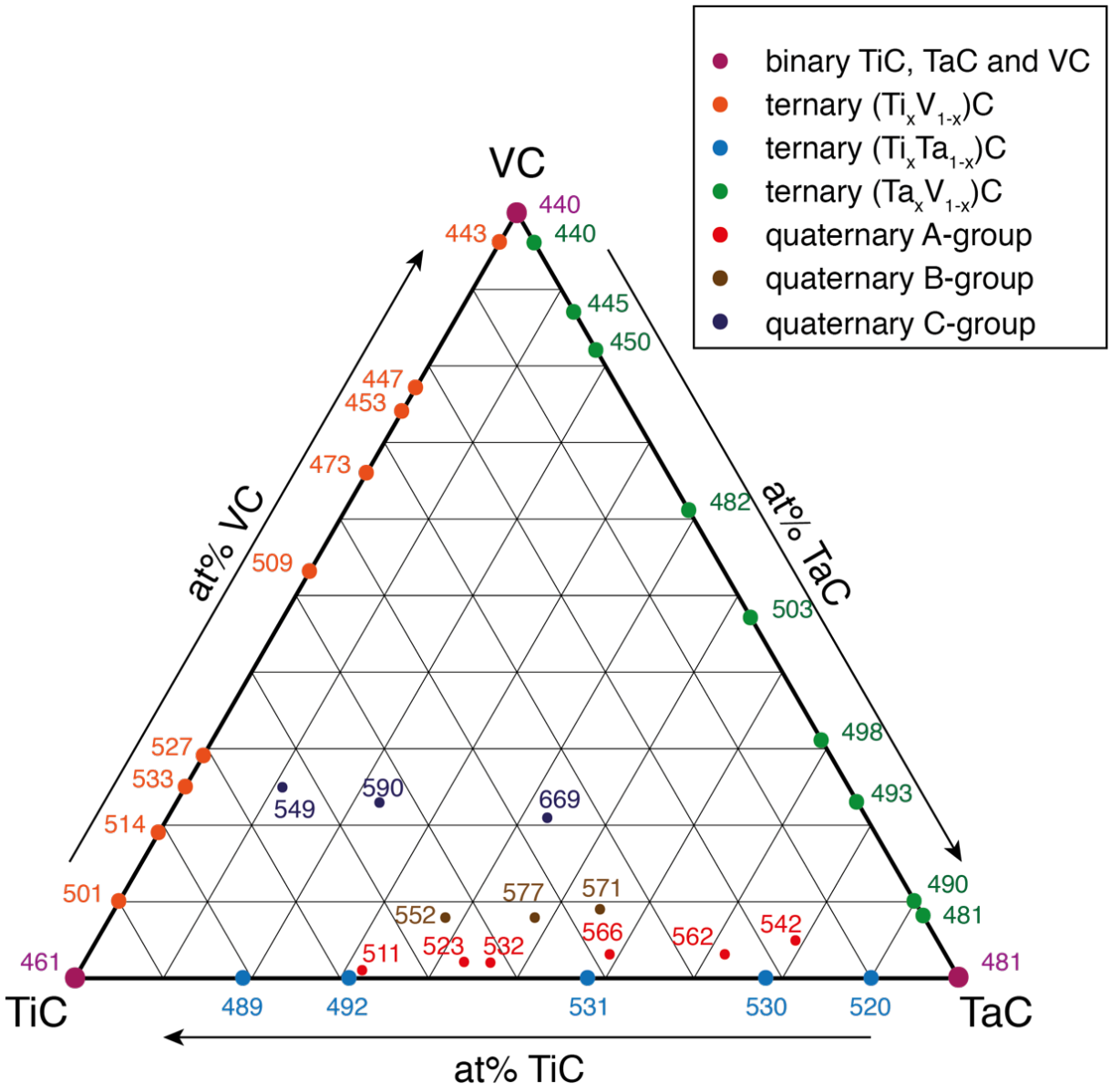

Fig. 5.11 – Indentation Modulus of the (Ti,Ta,V)C quaternary system, all values in GPa.

5.3 Elastic modulus measurements: discussion

As seen in Chapters 1 and 2, one often finds for carbides a large range of values for experimentally measured values of E reported in the literature. Such a big interval is mainly due to the material itself, as the elastic modulus is sensitive to the microstructure and varies notably as a function of porosity and carbide stoichiometry. For single crystals, anisotropy is a further factor impacting the elastic modulus measurement, as E can exhibit large variations depending on the crystal orientation.

The measurement method itself is another source of uncertainty. In general, normalized measurements done on large macro-scale specimens (e.g. in tensile tests) can provide an estimation of the modulus of elasticity with a typical error of 1-2%[175]. When dealing with micron-scale specimens, the measurement procedure is completely different, as are the sources of error. Because we use the contact between an indenter and the surface of the material, both have an important role, and in this case, most of the error on the measurement can be distributed between tip and surface effects. For that reason, measurements based on nanoindentation provide generally less accurate results than macro-scale tests. The aim of this section is then firstly to identify all the parameters that can induce uncertainties in the present elastic modulus measurement. In a second step, we examine the elastic modulus evolution with changes in ternary/quaternary carbide composition.

5.3.1 Accuracy of the Oliver & Pharr analysis

The Oliver & Pharr analysis is the classical indentation method and constitutes, as such, a good starting point to discuss the accuracy of nanoindentation-based E measurements.

The parameters that could have an effect on the final value can be divided into three groups: (i) those related to the material, (ii) those related to the testing method and (iii) those related to the indenter tip. The surface is the most important parameter as concerns the material to be tested: at such a small scale, and given the small penetration depth, the surface must be as flat and homogeneous as possible. The sample is prepared for the indentation by mechanical polishing: different diamond particles with decreasing sizes are used successively until ¼ of a micron; that last step, if done correctly, allows to reduce the surface roughness to a few nanometers. Such roughness constitutes the first source of error, because it varies randomly over the surface and can induce, by creating sites of stress concentration, local plastic deformation.

Although the penetration is small, the stress field associated with an indentation has an influence over a much larger depth; depending on what lies below the imprint (pores, second phases, etc.), the result will be affected. Residual stresses are another common source of error, which in the present material are present due to differential phase contraction during cooldown of the sample from processing temperatures, or during metallographic preparation by deformation during the

polishing process; the interaction of the indentation stress field with residual stresses modifies the response of the material and thus biases the measurement.

Sinking-in and piling-up effects can appear when the surface is drawn underneath the indenter; the presence of one or the other effect is linked to the E/Y ratio, as well to the strain-hardening properties of the material. Both phenomena can have an important effect on the measurement of the properties, because they induce changes in the contact area (Fig. 5.12).

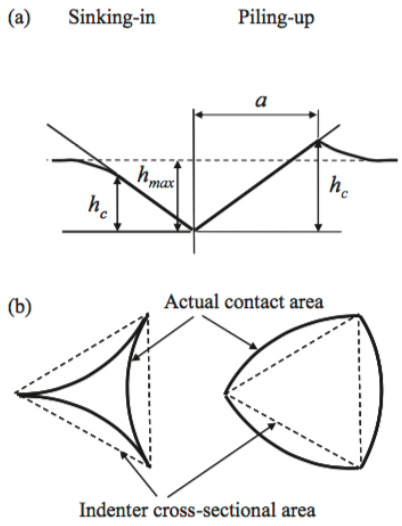

Fig. 5.12 – Sinking-in and piling-up effects; figure reproduced from Ref [176].

Thermal-drift constitutes the most important test-related source of error. As explained before, it results from the thermal equilibration sets in when the indenter and the material are in contact, leading to a deformation by thermal expansion or contraction of the indenter. The drift rate is generally not constant during the indentation; a typical value for a contact between a diamond tip and a carbide surface leads to a drift rate of ~ 0.1 nm/s. When doing a series of indents, the drift rate decreases, as the thermal equilibrium is progressively reached. The fact that the thermal drift is never constant during the indent constitutes a severe issue, and a drift correction, based on a constant drift rate, becomes complicated.

Before indenting the material, it is necessary to establish contact between the tip and the material (to measure the thermal drift among others). To this end, we defined a pre-load of 2 μN: the contact is considered as established when the load cell measures this specific value. Even if the pre-load is small, however, there is always a corresponding penetration of the tip; depending on the surface roughness, that offset can vary and should be corrected to measure accurately the elastic modulus.

The last source of error linked to the test can be attributed to the apparatus compliance; when we try to measure a mechanical property related to the elastic behavior of the material, compliance is always an issue. The extra-displacements due to the compliance are proportional to the load and are consequences of the reaction forces during the loading. It is possible to correct this by the Oliver & Pharr calibration method presented in Chapter 2. As explained, in the case of particles embedded in a soft matrix, the compliance issue becomes the biggest uncertainty error.

The last category of error arises from the indenter and its deviation from an ideal shape: it is indeed impossible to machine a perfect indenter, especially at its tip. At high resolution, the tip of an indenter is always more nearly spherical than pointed, with a typical radius of 100 nm (one can

find more expensive high-quality tips with a smaller radius of 50 nm). The error due to the indenter geometry becomes important when the penetration depth decreases, as outlined in Fig. 5.13.

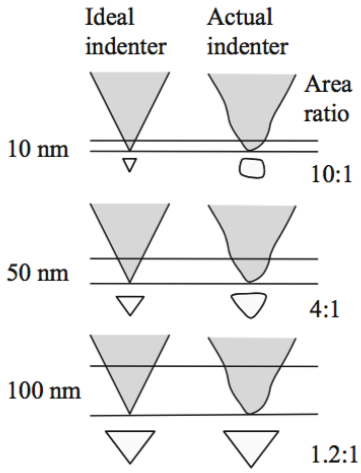

Fig. 5.13 – Indenter geometry effect; figure reproduced from Ref [176].

Calibration of the tip area function is always required, but the function is based on a fit of several indents performed on a reference material at different loads. Depending on the quality of the fit, and the interval of penetrations, contact area values can constitute an important source of error. Moreover, for indents performed with a penetration depth smaller than the tip radius, analysis schemes designed for a conical tip are no more valid; rather, in such situations, Hertz's analysis can provide a more accurate description of the underlying physics.

The indentation size effect describes the differences in measurement with variation of the penetration depth. Such size effects can have various origins, such as the presence of a thin oxide film, friction between the indenter and the sample, or the area function of the indenter. Friction and adhesion constitute then a last source of error, since at small scales, surface forces become important and can have an impact on the shape of the load-displacement curve, depending on the indented material.

For most of these sources of error, standard procedures have been developed in order to reduce the impact on the measurement. For example, the initial penetration can be easily corrected, and precise calibrations can be performed to determine the area function and the apparatus compliance.

This said, it is not possible to correct completely all these sources of error; moreover, the total error being the sum of all the possible uncertainties, nanoindentation-based elastic modulus measurements uncertainties can easily reach 10%, well above usual error in macro-mechanical tests.

We consider now the repeatability of the Oliver & Pharr analysis on bulk materials and on particles. For fused quartz and SiC, a series of 196 Berkovich indents at 10 mN have been done along a *14x14* grid pattern, the rows and columns being spaced by 10 µm; the total area of 130x130 μm^2 can be considered as homogeneous and the total required time for a series of indents is approximatively 6 hours. Given the conditions, we can consider that each indent was performed under the same conditions and the results can then be compared.

Each indent was analyzed using the OPM procedure, with the same calibration for the machine compliance and for the area function of the indenter. The results for the elastic modulus, including the min/max values, as well as the average μ and the standard deviation σ are presented in Table 5.13.

Table 5.13 – Repeatability of standard nanoindentation tests on bulk fused quartz (FQ) and SiC reference samples.

	FQ	SiC
E_{min} (GPa)	68	396
E_{max}(GPa)	76	441
μ (GPa)	70.1	416
σ (GPa)	0.6	4.9

We can measure the interval for each material: 8 GPa for fused quartz and 45 GPa for silicon carbide. These ranges correspond more or less to 10% of the mean value. If we compare now the mean values with the literature references for the elastic moduli (E_{FQ} = 70 GPa; E_{SiC} = 410 GPa), agreement is much better; when we average a large number of curves, the effect of statistical sources of error such as thermal drift or the offset tends to zero.

To conclude, the reasons explaining why the Oliver & Pharr analysis is widely used to measure elastic moduli are linked with its accuracy when several indents are performed under the same conditions. Combined with a cautious calibration of the apparatus and of the indenter tip, this method can be used to measure the modulus of bulk materials with good accuracy.

If we try now to extend the method to particles embedded in a soft matrix and treated as a thin film, severe complications arise. The substrate or the matrix play an important role when we try to measure elastic properties. The load applied by the indenter induces a displacement that is used to measure the modulus of elasticity; however, in that case, the displacement is not entirely situated in a single phase, as was the case for a bulk material. Rather, it is the sum of (i) the penetration of the indenter within the film or the particle, and (ii) the indenter displacement caused by the finite substrate/matrix compliance. If the stiffness of the matrix is higher than the particle stiffness, it could be possible to neglect it, under certain conditions, because the part of the displacement due to the matrix would be small in comparison with the penetration into the particle. For the opposite situation, as is the case for carbides embedded in a steel matrix, the extra displacement due to the deformation of the matrix is too large to be neglected. The Oliver & Pharr analysis is then no longer accurate: resulting values characterize the modulus of elasticity of a composite material of carbide combined with steel.

Operationally, the indentation procedure is identical to that described for measurements performed on bulk materials. Hence, all the listed possible sources of errors are found again; however, the microstructure of hard particles in a soft matrix introduces an additional source of error, arising due to uncertainty in the surroundings of the region surrounding the particle that was tested. Unlike a bulk homogeneous material, we have now the presence of interfaces between the matrix and the particle; these boundaries are easily seen at the surface, but they form a complex 3D structure that is unknown below the surface. When indenting, the stress field associated with the penetration must remain within the particle, otherwise the result will be a combination of the particle and the matrix properties. This means that the maximal load is limited by such considerations, particularly if we produce several indents in each particle. Another supplementary source of error is directly linked to the polishing procedure: indeed, due to the high hardness difference between carbides and steel, it is nearly impossible to obtain a flat surface in metallographic polishing; the particle surface has a slightly convex shape, as it is harder to remove

material from the carbide than from the matrix. That feature will introduce differences within a set of indents inside the same particle, as the indents closer to the particle border will have a different alignment with the indenter than the indents performed in the center of the particle, due to the convex morphology of the particle surface. The last, but important, source of variability consists in the anisotropy between the single crystal particles: indeed, each polished particle exhibits a different crystalline orientation, leading to differences in the measurements.

All these additional sources of error decrease the accuracy of the measurement but remain small in comparison with the effect of the extra-compliance brought by deformation of the matrix. Table 5.14 presents the average value and standard deviation of the elastic modulus measured on a given TiC particle, as well as the same quantities measured similarly for a set of data gathered from 5 different particles.

Table 5.14 – Elastic modulus measurement and Oliver & Pharr analysis on TiC particles.

	TiC (1 particle)	TiC (5 particles)
E_{min} (GPa)	349	345
E_{max} (GPa)	382	393
μ (GPa)	367	368
σ (GPa)	13.6	17.1

The standard deviation is more important in that case than for bulk material measurements, and it increases when different particles are analyzed together.

If we consider now the results obtained for the TiC, VC, TaC, NbC and WC binary carbides with the Oliver & Pharr analysis, we can compare the values with literature references in Table 5.15:

Table 5.15 – Binary carbides particles elastic modulus measurement performed with the Oliver & Pharr analysis method (OPM) compared with literature values.

	TiC	WC	TaC	VC	NbC
E_{OPM} (GPa)	345-393	497-524	389-396	344-361	405-419
E_{lit} (GPa)	451[5]	696[5]	472[9]	430[7]	537[5]

Obviously, the modulus of elasticity is largely underestimated, as it oscillates between 72% and 87% of the reference values that can be found in the literature, thus betraying the effect of the matrix compliance. We conclude that for this study, the Oliver & Pharr analysis cannot be used to measure the modulus of elasticity with sufficient precision.

5.3.2 Accuracy of King's correction

The correction proposed by King and adapted by Saha and Nix addresses the calculation of the elastic modulus from the reduced modulus. In the classical Oliver & Pharr approach, the reduced modulus is considered as a combination of both the material and the indenter deformations; King added an additional term to account for deformation of a substrate. The procedure used to calculate the reduced modulus is given by the Oliver & Pharr method, and consequently, the above discussion of the sources of error inherent to the OPM remains: King's analysis constitutes only a correction of that method.

An additional parameter is now required to calculate the elastic modulus, namely the thickness of the film or the local thickness of the particle just below the indenter (at fixed total sample thickness). That parameter is directly used in Eq. 2.38 and serves also to determine the α parameter, according to Eq. 5.15. The square root of the contact area is directly given by the area function of the indenter, and the penetration h is measured on the indentation curve. The critical parameter is then the indented phase thickness, which is unknown and not constant in the case of particles (as opposed to a thin film). Indeed, because they are randomly oriented, and because of their irregular morphology, the thickness of a particle can only be defined locally as the length between the polished surface and the particle/matrix interface. A possible approach to measure this consists in making perpendicular cuts in a FIB-equipped SEM; we can then reconstruct the interface between the matrix and the particle underneath the surface. That procedure is easier with faceted particles; in the case of a parallelepipedic dendritic arms, two cuts suffice to characterize the thickness of the particle.

Once t has been measured, we can use King's analysis to calculate the Young's modulus of the particle. A comparison between Oliver & Pharr analysis, King's correction and literature values for TiC, VC and TaC is given in Table 5.16:

Table 5.16 – Comparison between Oliver & Pharr, King's correction, bending beams and literature values for TiC, VC and TaC elastic modulus. All values in GPa.

	TiC	VC	TaC
E_{OPM}	345-393	344-361	389-396
E_{King}	452-467	433-440	476-485
E_{Beams}	490 ± 27	430 ± 24	490 ± 30
E_{lit}	451	430	472

The correction proposed by King and improved by Saha and Nix was also explored in an attempt to correct the data obtained with the OPM to take into account the compliance of the matrix. The approach proved to measure accurately the modulus of elasticity, on the condition that the thickness of the particle or of the film be known. For this reason, it is one of the most used nanoindentation method to determine the Young's modulus of thin films. When dealing with

particles, the method is however more complicated, as mentioned before, given the non-constant thickness of the particles normal to the indent coupled with their irregular shape. Also, the FIB-milling step represents a strong limitation to the efficiency of the process, because it cannot be automated.

5.3.3 Carved beam bending

In Table 5.16, we compare also the values obtained by bending TiC, VC and TaC cantilever beams. The agreement is good for VC, but the values for TiC and TaC are overestimated by the beam bending method. That method proved to be very sensitive to the beam dimension measurements, and for that reason, its accuracy is not optimal. Moreover, the time required to machine each beam makes the method both expensive and labour-intensive. For that reason, it was not further used.

5.3.4 Accuracy of the spherical indentation method

Here we use elastic indents performed with a conospherical indenter, the tip of which is treated as (different) spherical indenter in order to measure the elastic modulus of particles embedded in steel at very low load, so low that Hertzian indentation physics dominate the process. The usual sources of error of standard indentation methods, listed previously, again apply to measurements produced by this method.

In order to illustrate the error due to the initial contact and to the thermal drift, Fig. 5.14-a presents five different indentations performed on the same TiC particle. A zoom on the area corresponding to the peak load and maximal displacement outlines the displacement offset, representing roughly 1-2 nm. For a standard high-load ($P \approx 10$ mN) indentation, the difference is negligible, but here, it represents 5% of the displacement at peak load P_{max}.

Fig. 5.14-b represents subtractions between two similar indentations, performed on the same particle, at the same location: $h_d(P) = h_1(P) - h_2(P)$. According to Eq. 5.11, such a difference should in principle be written as:

$$h_d(P) = \left(h_{0,1} - h_{0,2}\right) = constant$$

Eq. 5.20

However, we can see that $h_d(P)$ is not constant; thermal drift is mainly responsible for that behavior.

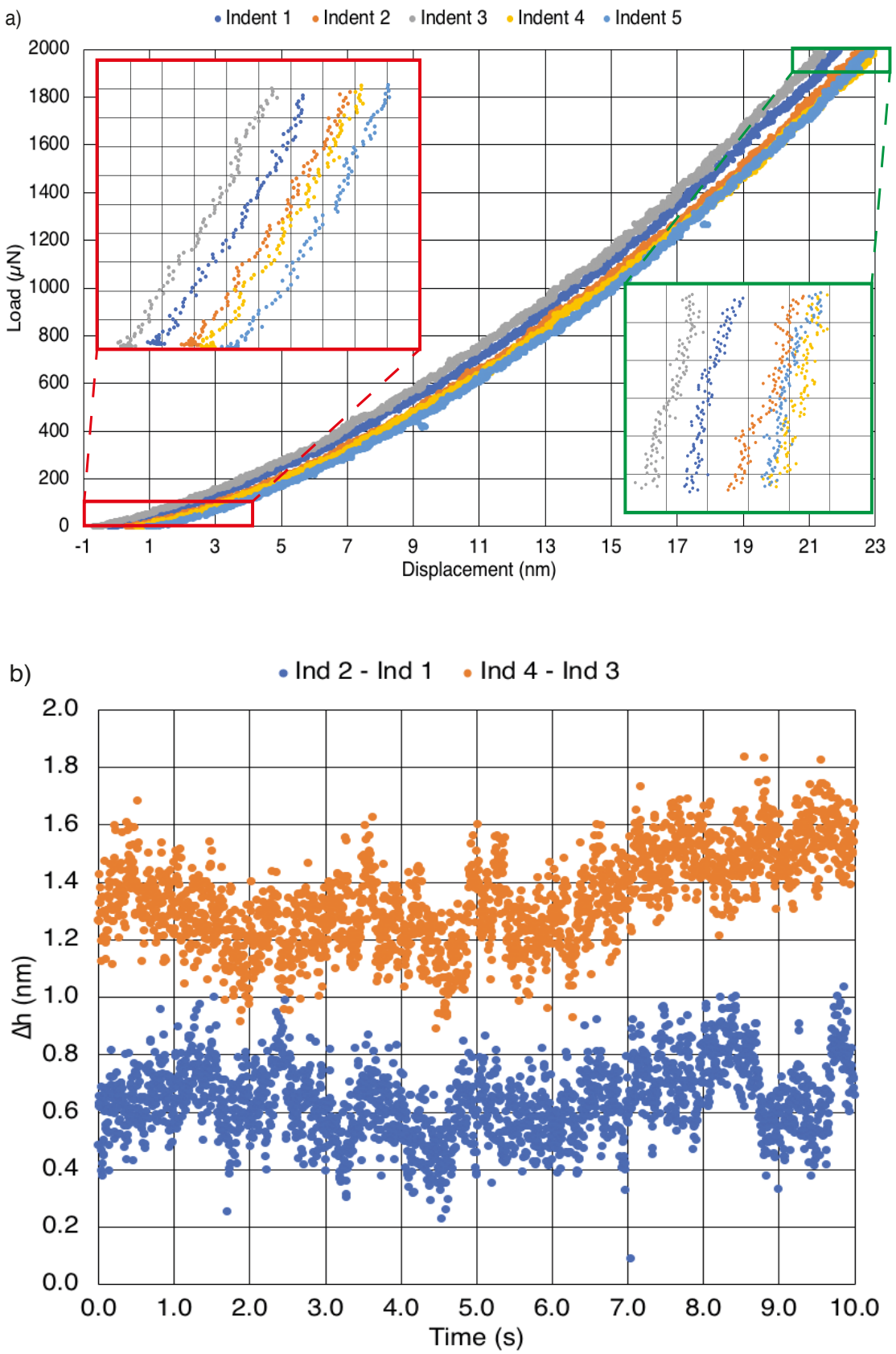

Fig. 5.14 – a) Superposition of comparable indent curves; b) Subtraction of comparable indent curves.

Reducing the influence of thermal drift requires a short test, and thus a high loading rate. The offset cannot be avoided during the test, but that parameter is well determined by the fitting procedure and does not constitute a critical issue. Particularly for such small displacements, thermal drift, initial penetration and surface roughness constitute the most important sources of error. Because we consider the tip as a sphere, the area function of the indenter is not a problem anymore, as long as we can determine accurately the (apparent) tip radius.

The problem of initial penetration is solved by determining the offset separately for each indent. The load-displacement curves can then be accordingly corrected:

$$P = \frac{4}{3} E_r \sqrt{R} (h_{tot} - h_0)^{\frac{3}{2}} = a \cdot h^{\frac{3}{2}}$$

Eq. 5.21

with $P(h = 0) = 0$. Because h_0 is independent of P, it can be easily fitted – if data agree with this purely Hertzian indentation law.

The problem of surface roughness is solved by cycling the indents: each indentation consists of a series of 5 load/unload cycles. The first load allows to establish the contact with the surface of the sample, leading to a small amount of plastic deformation, which flattens somewhat surface roughness; the next cycles are then purely elastic. When analyzing the data, we thus simply exclude the first load.

Thermal drift can be an important issue when indenting at a typical depth of ~20 nm: the drift can easily exceed 2 nm during the test, representing 10% of the total displacement. We know that the drift becomes smaller with the number of indents on the same sample, because after the tip is in contact with the surface, thermal equilibrium is gradually reached; it is then possible to minimize this effect by doing a first series of indents that we will not analyze, but whose usefulness is chiefly to give time for thermal equilibration. It is also possible to correct the drift by measuring the drift rate; this reduces the error, but not completely, because the drift rate varies during the test. The most efficient way to deal with the drift consists in averaging several indents, because the time variation of the drift rate tends to be cancelled statistically. That is the reason explaining why we need to fit the second parameter of the power law, a, as a single constant over the entire set of indents.

A comparison between the results obtained with spherical low-load indentation and literature for the five binary carbides is given in Table 5.17:

Table 5.17 – Comparison between the elastic modulus measurement of binary carbide based on spherical indentation and literature values.

	TiC	WC	TaC	VC	NbC
E_{sph} (GPa)	445 ± 6	703 ± 10	454 ± 10	419 ± 9	546 ± 16
E_{lit} (GPa)	451	696	472	430	537

The moduli of elasticity measured with our spherical indentation method are in good agreement with the reverence values. The method accuracy can also be considered as good, since the error is less than < 3% of the modulus across the range of measurements.

If we compare the different methods used to measure the elastic modulus and their agreement with literature data, both King's model and the spherical indentation method proposed here are able to measure E with sufficient precision, given the difficulty of a measurement at a such small scale. If the correction proposed by King allows to quantify the effect of the matrix deflection under the particle, in practice it is inconvenient with particles. By comparison, the spherical method is based on the fact that at very small loads we can neglect the effect of the matrix deformation altogether, rather than measure it, removing the influence of this factor. That method also has the important advantage that it can easily be performed efficiently over a large number of particles and samples. Finally, King's correction being based on the OPM method, it requires an indent that deforms plastically the material, and requires a conical indenter and an area function calibration; such indents being much larger than what ones corresponding to a purely elastic indentation, it introduces a lower bound on the size of particles that can be characterized.

5.3.5 Evolution of the modulus for ternary compositions

Having compared different methods used to measure the Young's modulus of the present carbide particles, we turn now to results obtained for the five ternary systems using the ultralow load indentation method.

For ternary and quaternary systems, we examine the indentation modulus M rather than E, because the ternary carbide Poisson's ratio is not known. The evolution of M is represented versus the composition in Figs 5.6-5.10. In the light of the underlying literature exposed in Chapter 2, it is of interest to convert the atomic composition into the corresponding valence electron concentration (VEC). This is easily done if we know the number of valence electrons for each element composing the carbide and then use the simple rule of mixtures. The indentation modulus is represented for the five systems as a function of VEC in Fig. 5.15. Because the valence of tantalum and vanadium is the same, the VEC of the (Ta,V)C system is constant and equal to 9, causing data points to be aligned along the ordinate axis direction.

One observes that two of the five systems – (Ti,W)C and (Ti,Nb)C – exhibit a linear evolution of the modulus, across the range between the moduli of TiC, and WC or NbC, respectively. The three other systems: (Ti,V)C, (Ti,Ta)C and (Ta,V)C show strong deviations from linearity, with the presence of a maximum at a value of the VEC that is far from being a constant (the maximum present in the (Ta,V)C ternary system is only visible in Fig. 5.10, because of the constant VEC value characterizing this system).

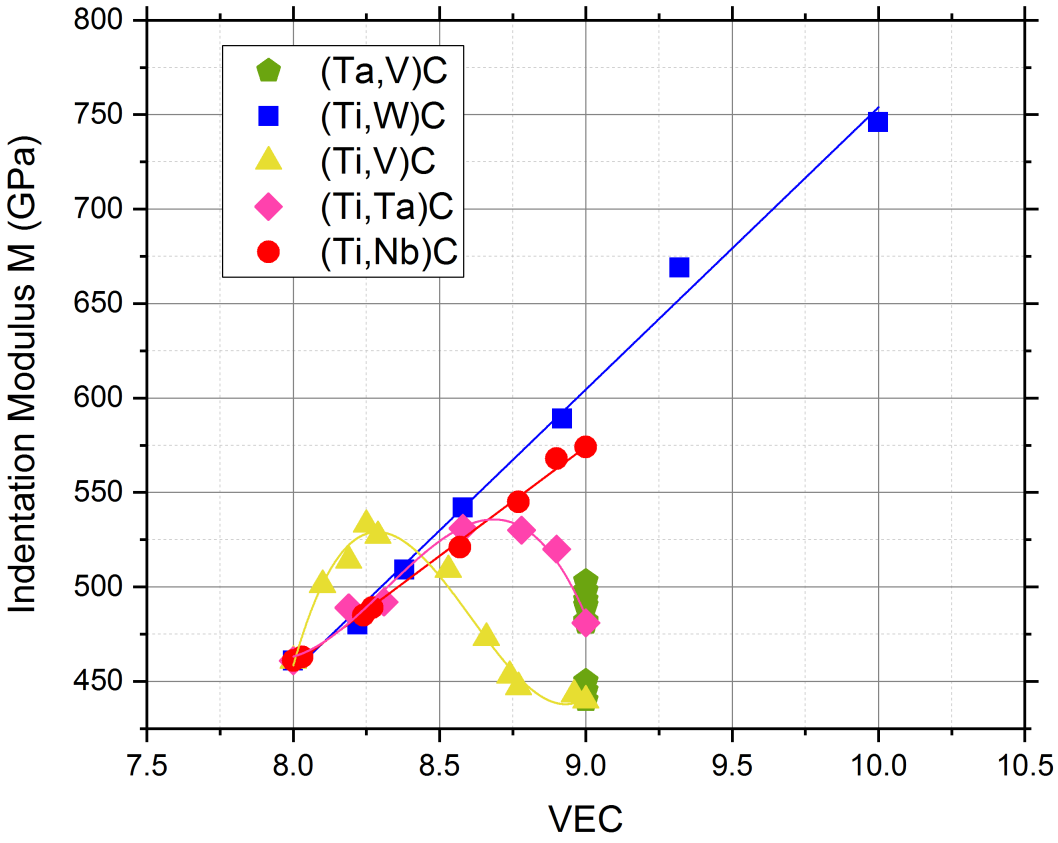

Fig. 5.15 – Indentation modulus as a function of VEC.

The disagreement between the analysis proposed by Jhi et al. and the present data can have several sources. Jhi et al.'s analysis predicting maximum stiffness at VEC = 8.4 is based on a pure shear deformation. The indentation modulus *M* is, rather, close to Young's modulus, which is related, for an isotropic material, to the shear modulus $G(x)$ and the bulk modulus $B(x)$, x being any parameter upon which it depends, such as the composition, by the relation:

$$E(x) = \frac{9B(x) \cdot G(x)}{G(x) + 3B(x)}$$

Eq. 5.22

As outlined in Chapter 2, the bulk modulus B increases monotonically with the VEC, without the presence of a maximum and unlike G. Indeed, if we assume a hydrostatic dilatation, it is evident that all the M-C bonds are equally stretched in the three x,y and z directions, resisting similarly to the deformation; the non-bonding t_{2g} orbitals are also moved away from each other, but because they are non-bonding, they do not affect the resistance to the deformation. As the VEC increases, the density of M-C bands – resisting the deformation –increases also, resulting in a rise of B. For higher values of VEC, t_{2g} orbitals are filled, resulting in a weaker π M-M bond and the increase in bulk modulus is less important. The evolution of B with the composition thus does not exhibit a maximum but rather deviates only somewhat from linearity as B increases more at the beginning (low values of VEC) than at the end (high values of VEC).

It is easily shown using Eq. 5.22 that, provided $B(x)$ is not a constant, the maximum of $E(x)$, if it exists, is not located at the same composition as for the shear modulus $G(x)$. It is thus clear that

the evolution of E with composition is not expected to show the same peak at VEC ≈ 8.4 as was predicted by Jhi et al. for c_{44} and, by extension, for both G and the hardness. This proved to be the case for our five systems, as two of them exhibit a linear evolution, while three are characterized by the presence of a maximum.

The evolution of the indentation modulus for the (Ti,W)C system is presented again in Fig. 5.16, together with DFT calculations (Details are given in Appendix D).

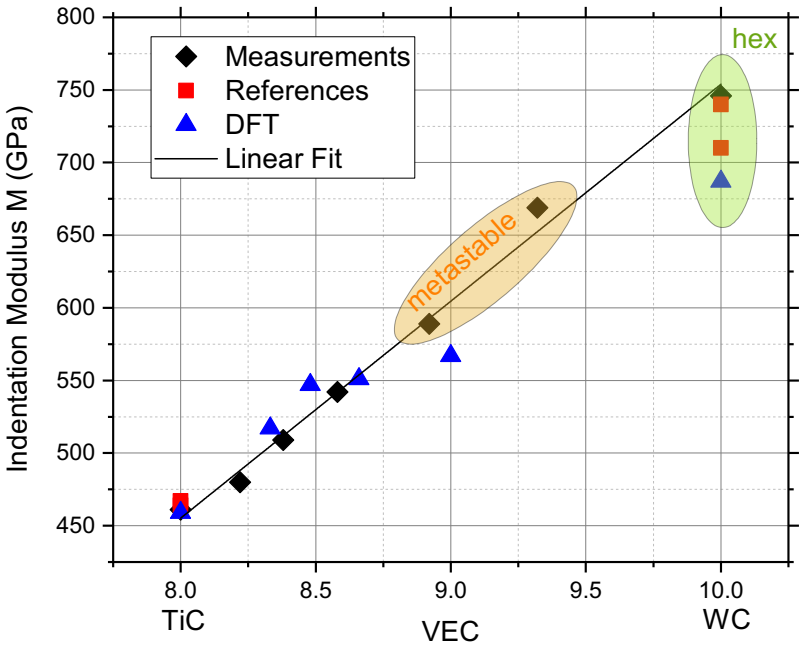

Fig. 5.16 – Evolution of M vs VEC for the (Ti,W)C system.

For that specific ternary system, we (this was chiefly the work of Dr. Goran Zagar, in our laboratory at EPFL) ran our own DFT calculations in parallel with the measurements. One can observe that both agree for this system, for a VEC < 9. We observe a linear evolution of the indentation modulus with the composition for our measurements. The XRD analysis confirmed the fcc structure for all the compositions, except for pure WC which is hexagonal. We observe that for the DFT simulation, the modulus increases linearly up to VEC ≈ 8.4, corresponding to saturation of d-e_g bonds. When more electrons are added, the indentation modulus M rises again, but more slowly. Our measurements do not exhibit a such change at VEC ≈ 8.4; the slope is similar before and after the saturation, suggesting a stronger M-M bond for a metastable structure. More investigations would be necessary for a firm conclusion to be reached (measuring precisely the lattice size for the metastable carbides and comparing the value with the predicted lattice size evolution could give more information about the validity of the simulations and the nature of M-M bonding).

The evolution of E in the (Ta,V)C system, characterized by a constant value of VEC = 9 and yet showing a clear maximum in E (Fig. 5.11), illustrates again that the VEC is not the only parameter governing intrinsic mechanical properties of MC carbides. Other parameters. Other parameters, namely both changes in bond strength and in atomic size, can influence the Young's modulus, as atoms are gradually replaced in the crystal structure of the carbide. Relevant information can be found in DOS plots or by measuring changes in lattice size (all these data, when available, are provided in Appendix D). It is, however, complex to quantify the effect of each phenomenon.

The last parameter which may influence the elastic modulus of all the systems and depends on the VEC is related to the antibonding empty states, as already mentioned in the previous chapter. In the octahedron configuration, an electron can not only occupy an e_g bonding or a t_{2g} non-bonding state, but also an e_g antibonding state. The energy increase is in the following order: E(e_g-bonding) < E(t_{2g}) < E(e_g-antibonding) (Fig 2.12). Each electron has then a probability of occupying an antibonding state, which induces a strong negative effect over the elastic modulus (cf the example of RhC in Chapter 2). Because our measurements of M involved only (small) elastic deformation (unlike hardness which involves plastic deformation and breaking of atomic bonds), this phenomenon has only a limited effect, as suggested by the very high elastic modulus of WC. Indeed, WC is characterized by the highest VEC (10) among all the carbides we investigated, and it is then the most susceptible to be affected by the antibonding phenomenon. It is also the carbide that exhibits the highest elastic modulus (E = 696 GPa), suggesting that it is not affected by this phenomenon.

5.3.6 Evolution of the modulus for quaternary compositions

In order to visualize the evolution of the indentation modulus with composition, with such a parameter varying over more than one dimension, we use as in Chapter 4 the pseudo-ternary TiC-TaC-VC diagram and reduce it to several pseudo-binary sections; in total, we look at six different cuts, as shown in Fig. 5.17. They all possess a maximum in the evolution of M with composition, which by fitting polynomial equations seems to be located at ~50 at% of V and ~70 at% of Ta.

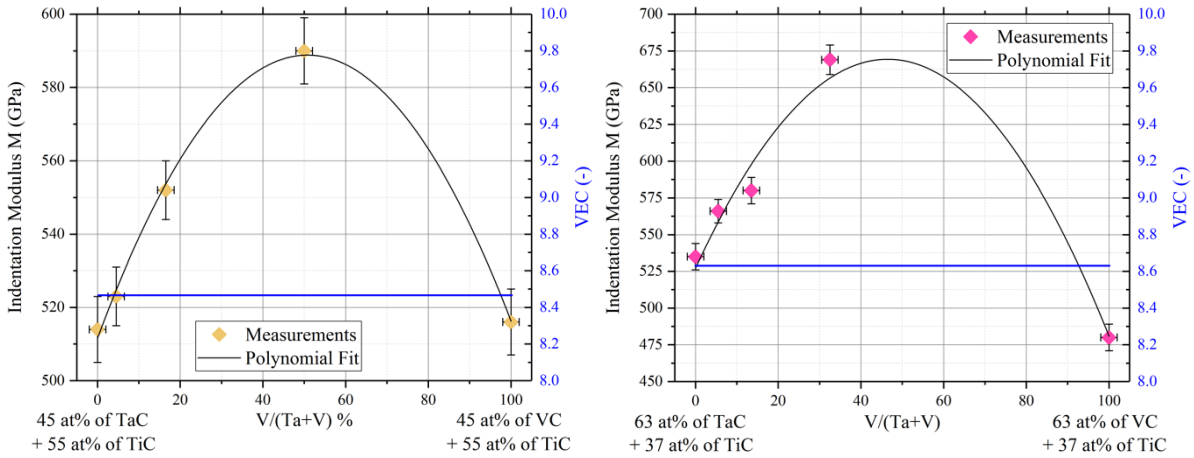

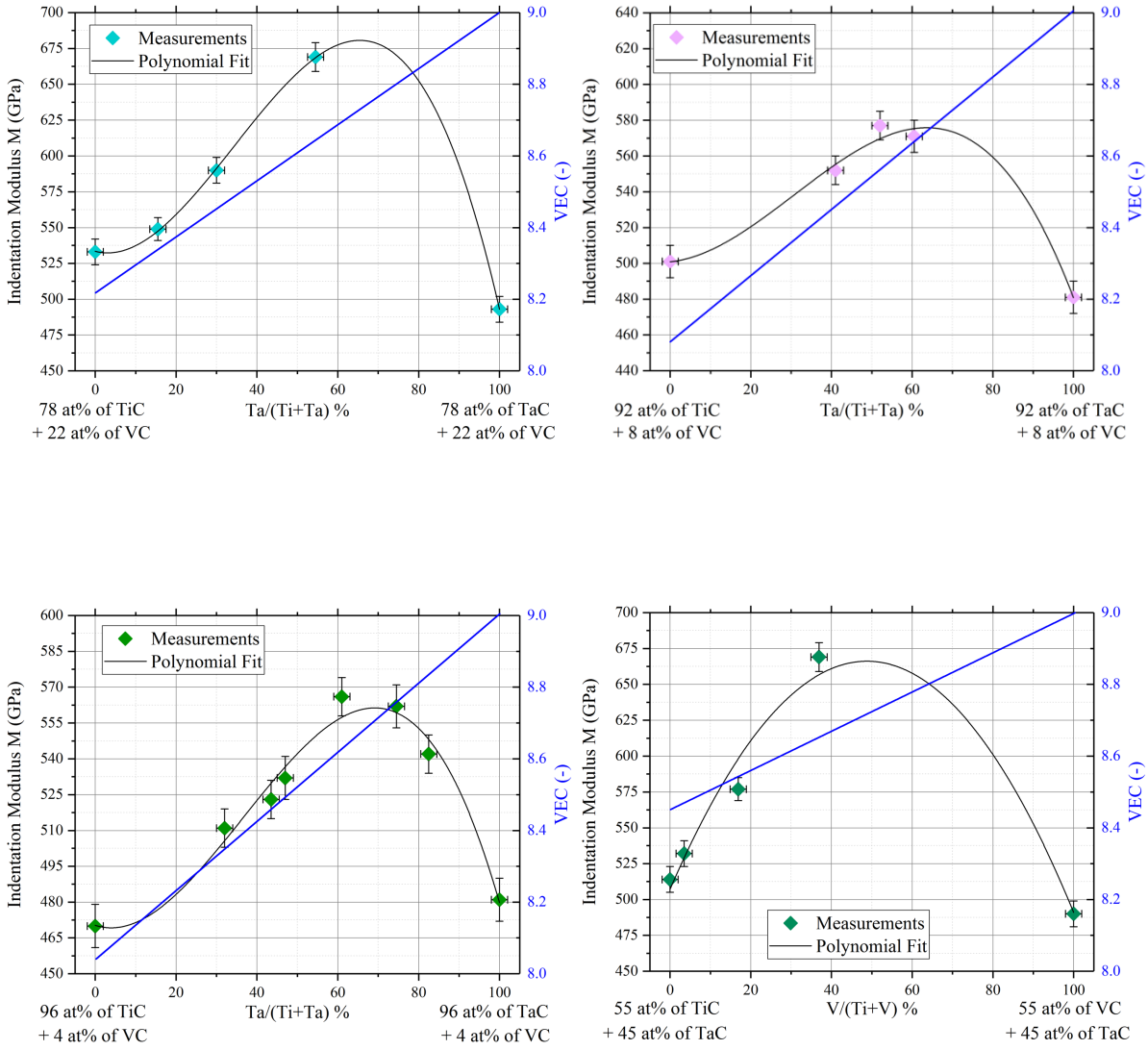

Fig. 5.17 – Pseudo-binary cuts in the TiC-TaC-VC diagram.

Parallel cuts can be directly superimposed and compared with the corresponding ternary system, Fig. 5.18:

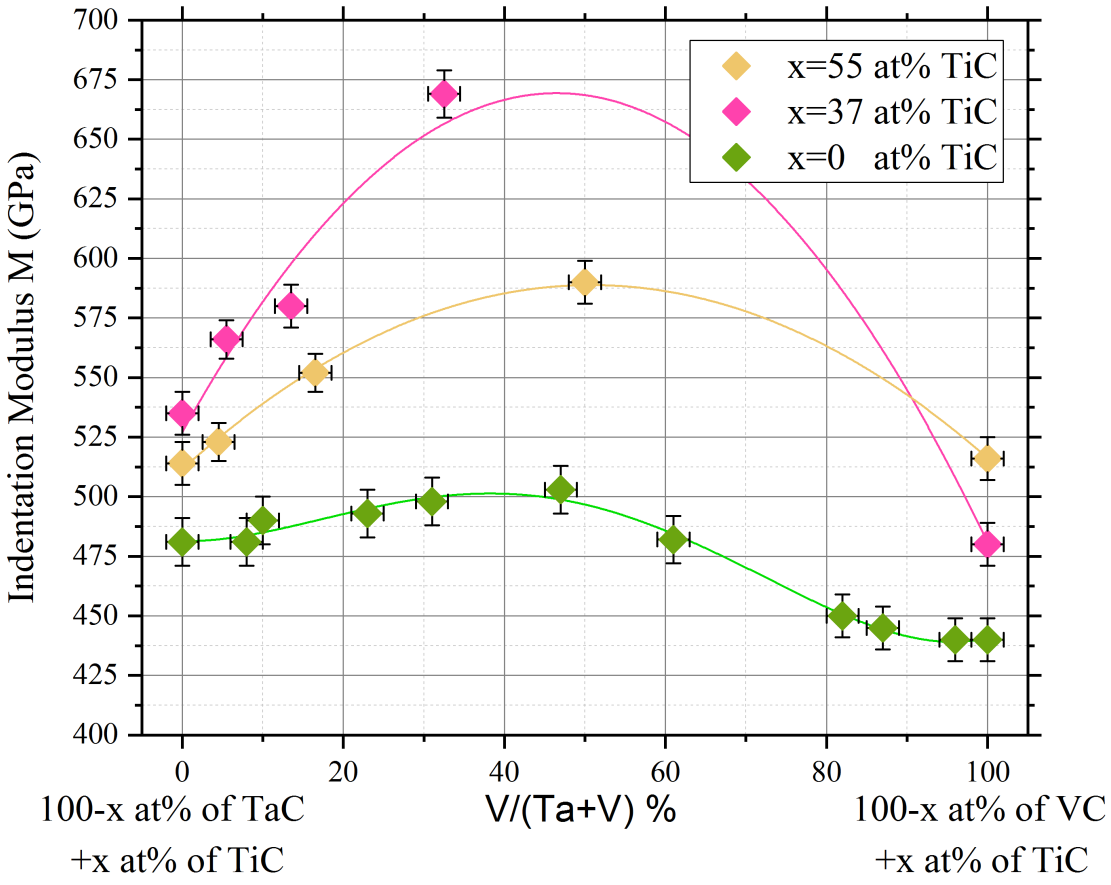
x=55 at% TiC
x=37 at% TiC
x=0 at% TiC
Indentation Modulus M (GPa)
700
675
650
625
600
575
550
525
500
475
450
425
400
0
20
40
60
80
100
100-x at% of TaC
+x at% of TiC
V/(Ta+V) %
100-x at% of VC
+x at% of TiC

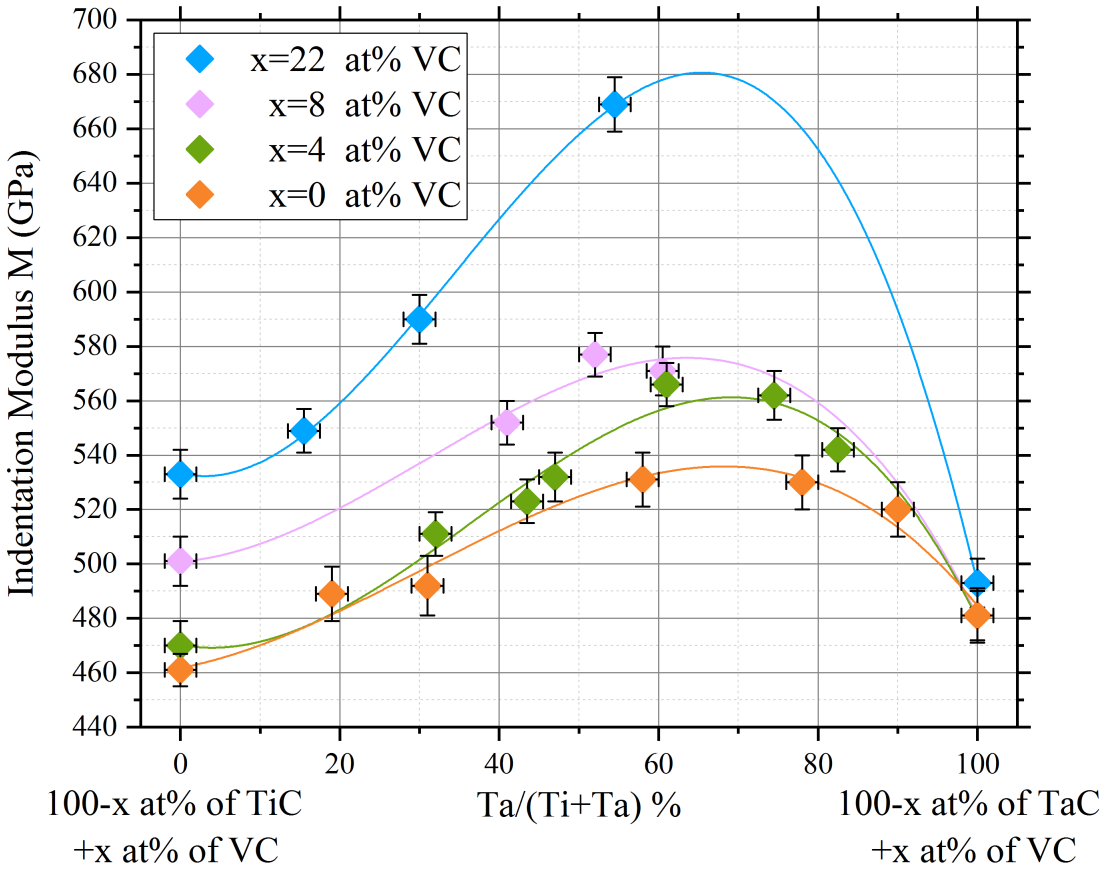
x=22 at% VC
x=8 at% VC
x=4 at% VC
x=0 at% VC
Indentation Modulus M (GPa)
700
680
660
640
620
600
580
560
540
520
500
480
460
440
0
20
40
60
80
100
100-x at% of TiC
+x at% of VC
Ta/(Ti+Ta) %
100-x at% of TaC
+x at% of VC

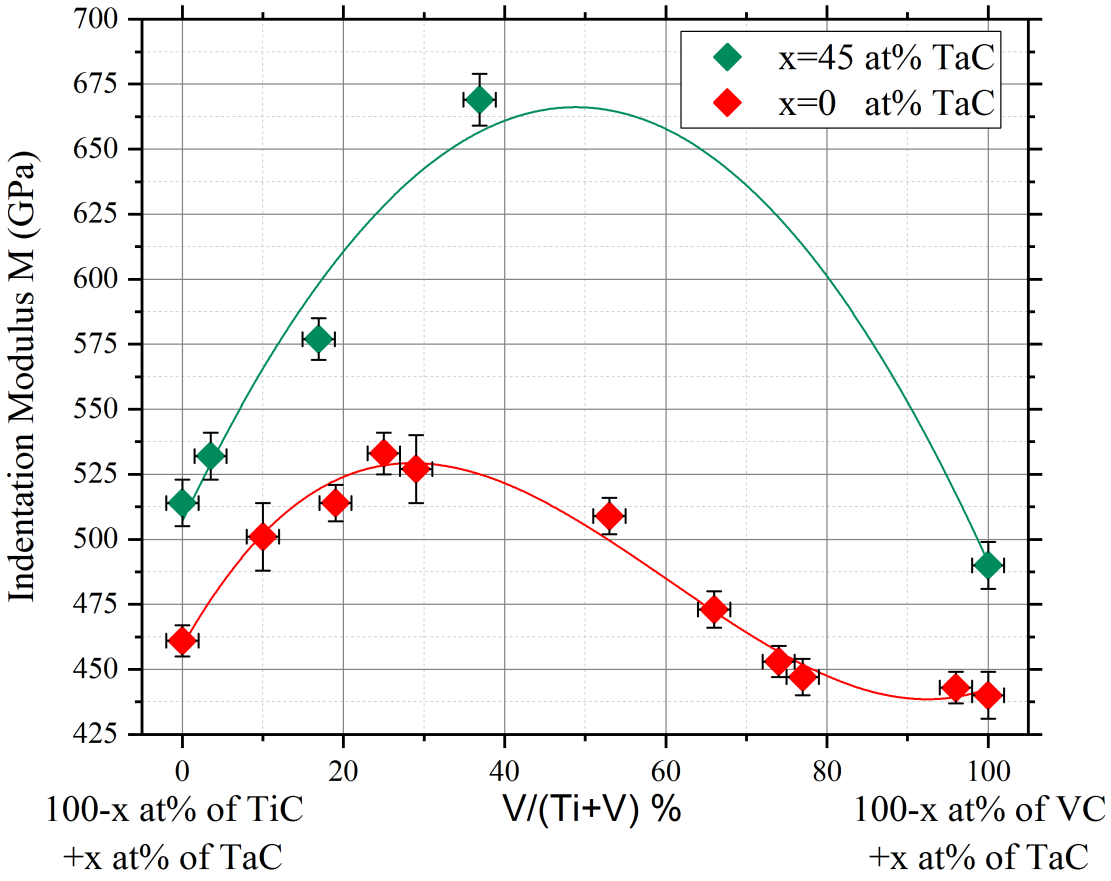

Fig. 5.18 – Comparison of parallel pseudo-binary cuts.

As was noted for the hardness, if we consider mixed TiC-TaC carbides, the addition of supplementary vanadium has a positive effect over the indentation modulus, with a supposed maximum for an intermediate V content value. As we have not explored compositions richer in V we cannot affirm that we have found the optimum within this system; however, the lower mechanical properties of VC suggest however that the elastic modulus will likely decrease for higher V contents. In Fig. 5.18-b we also can see that the behavior of the modulus when the Ta/Ti ratio changes is similar for different V contents; however, the value at the maximum increases from ~540 GPa for 0 at% V up to ~670 GPa when the carbide contains 22 at% V, this being a significant increase and a high stiffness.

In conclusion, the data collected over the course of this investigation show that monocrystalline binary MC carbide particles precipitated from steel exhibit interesting variations in their resistance to elastic deformation: their elastic indentation modulus, which closely approximates Young's modulus, is high in comparison with that of other materials and can be increased significantly by adding a third or even a fourth alloying element. Variations with composition are significant: one obtains a ~50% improvement over TiC by adding 27% of vanadium and 62% of tantalum, thus forming a quaternary carbide. At the optimal composition found in this work, this yields a carbide with an indentation modulus as high as of 670 GPa (corresponding to E = 630-640 GPa).

CHAPTER 6:

FRACTURE TOUGHNESS

DESCRIPTION OF CORRECTIONS BROUGHT TO THE SUBMITTED THESIS VERSION: A part of this chapter is affected by the hardness value correction. Indeed, the indentation toughness equation is based on both the elastic modulus and the hardness of the tested material (although, as the equation contains the *E/H* ratio to the power 2/5, the results are only slightly affected). We have thus recalculated all the indentation toughness values and redrawn corresponding graphics.

I performed all the measurements, with the chevron-notched method and by nanoindentation. I recalculated the fracture toughness with new hardness values measured by Dr Léa Deillon.

The fracture toughness of MC carbides explored in this work was measured by two different methods: (i) propagating a crack in a chevron-notched bending cantilever beam, or (ii) by generating cracks whiles indenting a polished particle surface with a cube corner indenter (i.e., measuring the indentation toughness). We present the two experimental procedures used to measure the fracture toughness, present the results for binary and ternary compositions, and then discuss the method accuracy, comparing results obtained with the two methods. Finally, we examine the evolution of fracture toughness with carbide composition.

6.1 Toughness measurement methods

In this section, we start by describing the procedure for the chevron-notched cantilever beam. In a second part, we describe the method used to generate cracks with a nanoindenter, as well as the Lawn-based analysis method that was used to calculate the indentation toughness.

6.1.1 Chevron-notched cantilever beam

The fracture toughness of MC carbide particles was first measured by means of the chevron-notched test, as developed for microscale testing in our group and based on the bending of a FIB-machined triangular cantilever beam.

The first part of the test consists in carving a beam out of a particle with a known crystalline orientation. Polished particles were first analyzed by EBSD (electron back-scattered diffraction), in our case, here using a FEI® (Hillsboro, US) XLF-30 (EBSP) with a OXFORD Instruments Nordlys II(S) EBSD detector. The tension was set at 30 kV and the current at 5 nA. Analysis of Kikuchi bands formed by the diffraction of back-scattered electrons allows to determine the crystal orientation of each single crystal particle. We used the EBSD post-processing software Tango, developed by Oxford Instruments and designed for the generation of orientation maps. A mapping of a selected sample area is performed and the orientation of all the particles contained within this area is determined. The surface quality is a very important parameter in obtaining a signal from which one can index the different Kikuchi bands; for that reason, a careful final polish with ¼ μm diamond particles was applied. Exposure of characterized material volumes to Ga^+ ions used in the FIB, is mostly avoided in the test, this being important as implanted ions contaminate the material, alter its mechanical properties and make impossible any EBSD measurement. The orientation analysis is therefore always performed before the FIB-machining process. It is thus possible to identify the plane orientation parallel to the polished surface. The other directions are generally determined by analyzing the faceted morphology of the particles, knowing that cubic crystal dendrites tend to grow along the <100> direction.

The selected particles must then be machined, in order to give them the required chevron-notched bend beam geometry. The procedure is entirely performed within a ZEISS NVision 40 CrossBeam high-resolution SEM equipped with a Ga liquid metal ion source FIB. The SEM and FIB column voltages are always respectively 2 kV and 30 kV. The electron beam current is also constant and set at 350 pA. The ion beam current varies during the procedure, depending on the precision that is required.

The FIB-milling process can be summarized as follows and the different steps are illustrated in Fig. 6.1 a-g:

1. We start by milling two parallel rectangular pits (Fig. 6.1 a,b). The pit depth and width must be large enough to avoid the pit being completely filled by milled material redeposition while milling with the ion gun. Because of the large volume of material to be removed, we use a high current of typically 26 nA.
2. In a second step, we mill the free extremity of the beam (Fig. 6.1-c), with the same milling conditions as for the first step.
3. The sample is then tilted at 45° so as to machine the triangular section. We start by milling one side of the beam (Fig. 6.1-d) and then the sample is rotated by 180° and the second side is similarly milled.
4. This step is repeated several times (Fig. 6.1-e), while decreasing the milling current from 13 nA down to 300 pA. Small currents are required in order to mill precisely the triangular beam geometry.

5. Once the beam is finished, we mill the notch. We us several stage tilt angles, ranging from 45° to 30° (the angle of the ligament corresponds to the double of the tilt angle). The sharper the ligament, the weaker the beam, and the easier it becomes to initiate a crack during the test. It was found that the ligament angle need to be sharper than 90°, as that value was not sharp enough to initiate stable crack growth on bent WC beams. The notch is fibbed from both sides, by rotating the sample by 180° (Fig. 6.1-f). We use ultra-low currents, typically 10 pA, in order to have the thinnest notch possible (as this aids crack nucleation).
6. With the notch carved, the sample is tilted again to its original position. The last step consists in fibbing shallow benchmarks (Fig. 6.1-g), which are used during SPM scanning in the nanoindenter to find the load application point.
7. Once the chevron-notched beam is ready, we measure its dimensions in the SEM;

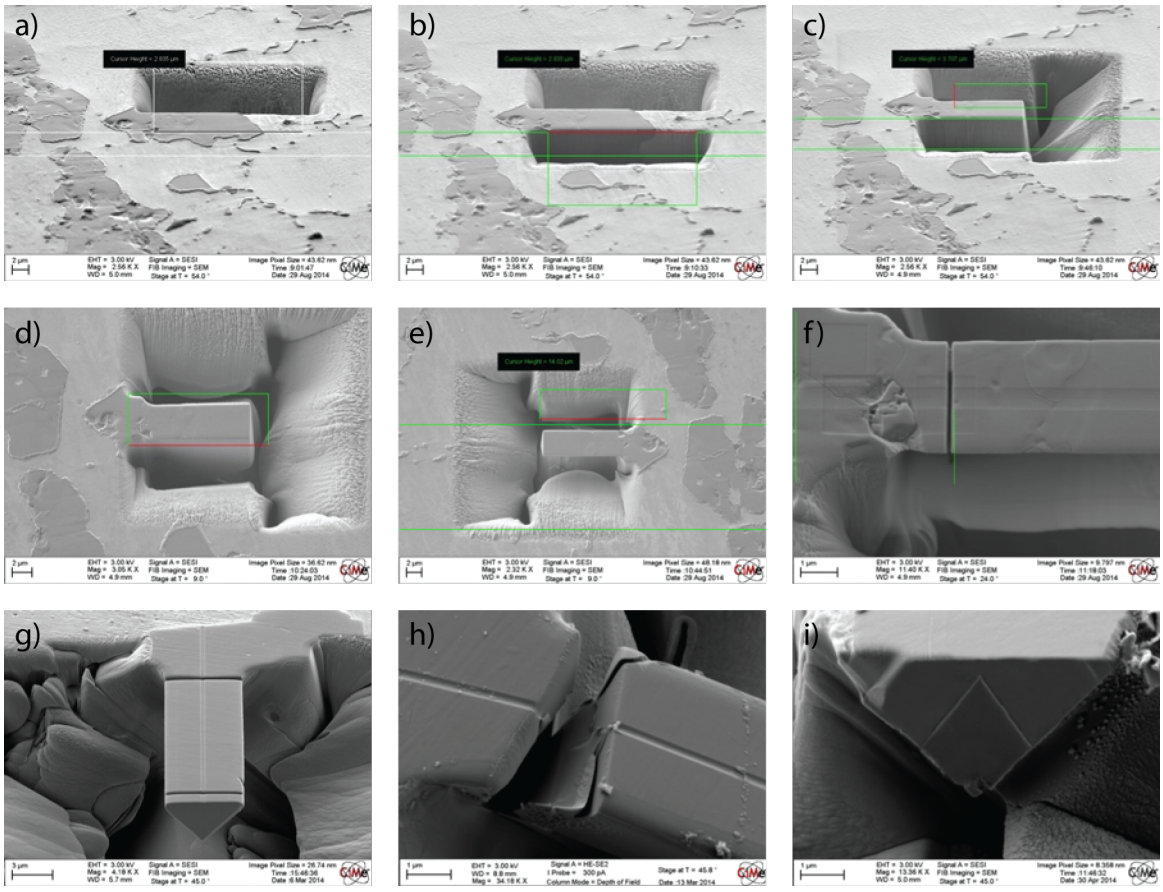

Fig. 6.1 –a-g) Shaping of the beam; h) Out-of-the-plane fracture; i) in-plane fracture.

The beam is then tested under the nanoindenter. We start by correcting the X/Y beam alignment with two perpendicular ±5° tilt stages. We measure the misalignment by scanning a neighboring particle along two orthogonal directions normal to the indentation direction. The correction process is repeated until the misalignment is smaller than 0.1° in both directions. The beam is then scanned along the beam, and the point of load application is chosen at the intersection of the two

benchmarks. The load is applied at a very slow loading rate of 0.5 μN/s, in order to detect and measure stable crack propagation.

When the beam is loaded in bending, stresses – normal to the notch – promote the formation of a crack at the apex of the ligament and then its growth in Mode I. The tip of cracks growing within chevron-notched beams can be considered as being in plane strain; also, since this is the directly known quantity, we use the indentation modulus $M = E/(1-\nu^2)$ instead of E in toughness calculations.

Once initiated, the crack goes through the notch; we assume that the crack front remains straight during its propagation (Fig. 6.2). The width of the crack front $b(a)$ is calculated from geometrical considerations:

$$\frac{b(a)}{b(a_1)} = \frac{a-a_0}{a_1-a_0}$$
$$\frac{b(a_1)}{B} = \frac{W-a_1}{W} = \left(1-\frac{a_1}{W}\right)$$
$$b(a) = B\left(1-\frac{a_1}{W}\right)\frac{a-a_0}{a_1-a_0}$$

Eq. 6.1

where parameters present in Eq. 6.1 are described in Fig. 6.2.

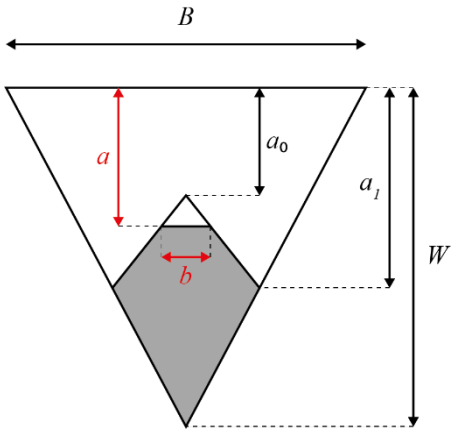

Fig. 6.2 – Geometry of the notched section for a triangular beam.

The increasing crack front width serves to stabilize crack growth, because the rate of elastic strain energy released, G, then initially decreases with increasing a. Indeed, Griffith's criterion tells us that the crack propagates spontaneously when:

$$G = \frac{P^2}{2b}\frac{\partial C}{\partial a}$$

Eq. 6.2

where C is the specimen compliance. We can thus express the stress intensity factor K_I for a chevron-notched specimen as:

$$K_I = \sqrt{GM} = \sqrt{\frac{P^2}{2b}\frac{\partial C}{\partial a}M} = P\sqrt{\frac{1}{2B\left(1-\frac{a_1}{W}\right)}\frac{a_1-a_0}{a-a_0}\frac{\partial C}{\partial a}M} = \frac{P}{B\sqrt{W}}\sqrt{\frac{1}{2(1-\tilde{a}_1)}\frac{\tilde{a}_1-\tilde{a}_0}{\tilde{a}-\tilde{a}_0}\frac{\partial C_v}{\partial \tilde{a}}}$$
$$= \frac{P}{B\sqrt{W}}Y$$

Eq. 6.3

where the "tilde" symbol represents a dimensionless quantity, normalized by W, and C_v is a dimensionless compliance, $C_v = C \cdot B \cdot M$.

For each sample, the compliance evolution and from there the relevant derivative is calculated by an elastic finite element analysis performed with the software Abaqus® (Dassault Systèmes, Vélizy-Villacoublay, FR). The compliance is calculated for thirty different crack lengths. The critical plane strain fracture toughness K_{IC} is determined at the peak load and at Y_{min}, where instability sets in:

$$K_{IC} = \frac{P_{max}}{B\sqrt{W}}Y_{min}$$

Eq. 6.4

6.1.2 Indentation fracture toughness

Due to the large number of samples to be characterized, and because the chevron-notched method is expensive and time-consuming, we used another, more conventional, measurement method, based on nanoindentation, to estimate the fracture toughness of the carbide particles. Indentations are known to generate cracks if the material is brittle enough; it is then possible to correlate the length of these cracks with the applied load and deduce the toughness.

The method classically used to measure toughness from indents consists of three steps:

1. Indentation of the material with a sharp indenter and generation of cracks;
2. SEM analysis of the indentation to measure crack length;
3. Analysis of the crack length and determination of K.

In practice, the generated cracks can form a messy system, with different crack geometries appearing simultaneously; hence, one must be careful and define criteria that enable one to consider a test as valid or not.

The first challenge consists in the generation of cracks, since we have particles of relatively small size. Indeed, a crack must propagate within a limited volume entirely contained within the particle: if the crack is stopped by an interface, for example the boundary of the particle with the matrix, or if it propagates into the matrix, the test cannot be considered as successful. For these reasons, we must apply the lowest load able to generate measurable cracks in the present carbide particles.

The sharpest available indenter has a cube-corner geometry and 3-fold symmetry. In comparison with a standard Berkovich tip, characterized by a semi-angle of 65.3°, the cube corner is a three-sided pyramid with perpendicular faces and a semi-angle of 35.3°. With that kind of tip, it is possible to generate cracks in a carbide particle with a load of 50 mN, whereas more than 500 mN are generally required for a Berkovich indenter. We performed indents on all the compositions that exhibited particles large enough to support the imprint and the cracks generated by a load of 50 mN. For each testable composition, at least 10 different particles were tested.

Once the indents have been performed, an accurate picture of the crack system is needed to be able to determine the toughness. Each indent is observed separately within a SEM microscope to identify cracks and then find the crack type, i.e. radial, median, lateral or half-penny, as well as its length. In some cases, we performed FIB-tomography to observe whether those cracks had propagated below the surface (looking for both lateral and median cracks).

At this point, a decision could be made as to whether an indent can be analyzed or not. An example of a valid test is presented in Fig. 6.3. On the contrary, the indent is rejected if:

1. There is no crack;
2. The crack is stopped by an interface or a defect (Fig. 6.3-center);
3. The crack system is too irregular, for examples because there is superposition of different crack types (Fig. 6.3-right).
4.

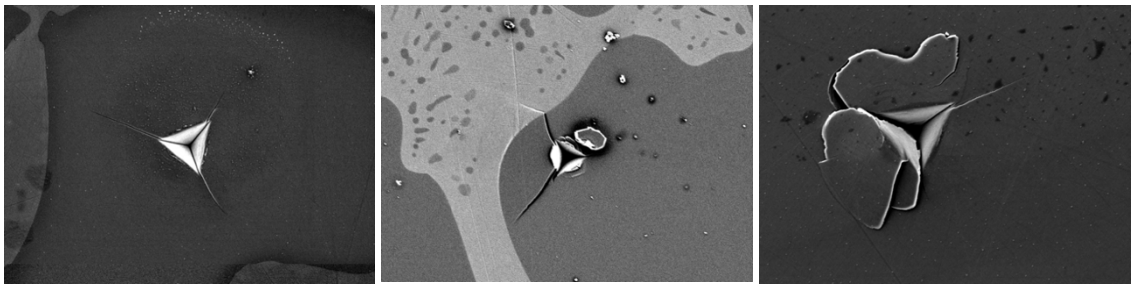

Fig. 6.3 – link) Valid test; center) propagation stopped at an interface;
right) messy cracks system (lateral cracks) on various compositions.

Many equations have been derived to analyze indentation cracks. For radial and half-penny cracks, we used the Niihara equations (Eq. 2.84), which have been reviewed by Schiffmann[177] as the most accurate to calculate the toughness of hard materials via this method. Table 6.1 summarizes the equation and the parameters used for each type of cracks.

Table 6.1 – Equations and parameters used for radial and half-penny crack analysis.

	Radial cracks	Half-penny cracks
	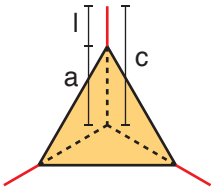	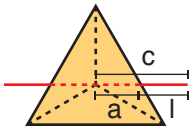
Equation	$K_C = A\left(\frac{E}{H}\right)^{\frac{2}{5}} \frac{P}{a\sqrt{l}}$	$K_C = A\left(\frac{E}{H}\right)^{\frac{2}{5}} \frac{P}{c^{\frac{3}{2}}}$
	A constant:	
Berkovich	0.010	0.035
Cube Corner	0.023	0.079

6.2 Toughness measurement results

The fracture toughness was measured with two different methods: the chevron-notched microbeams and nanoindentation. The first method has the advantage to correlate the toughness with the crystalline orientation, but it necessitated a major amount of work to test all the different compositions by making fibbed beams. The second method is certainly more adapted to a large number of samples, but on the other hand, the results cannot be separated according to the orientation, and as is well known, indentation toughness needs to be interpreted with caution.

6.2.1 Chevron-notched cantilever beam

Using this method, we have tested three samples from the (Ti,W)C system: binary TiC and WC carbides, as well as an intermediate composition, $Ti_{81}W_{19}C$. For each composition, several beams were machined, probing, if possible, different crystal orientations.

The critical dimensions required to analyze the fracture toughness of a chevron-notched cantilever beam are depicted in Fig. 6.4:

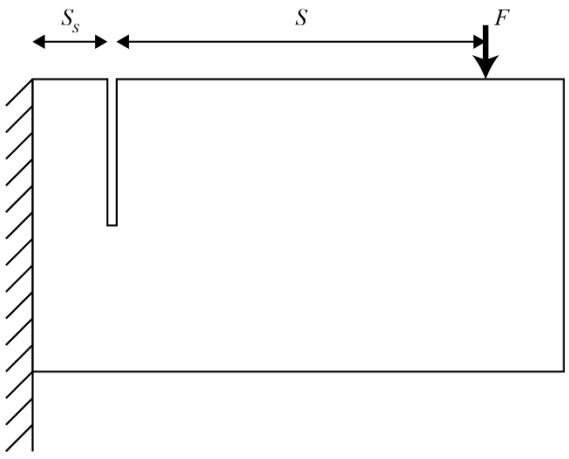

Fig. 6.4 – Critical dimensions of a chevron-notched beam.

The dimensions of tested beams are given in Table 6.2; the notch orientation corresponds to the crystal plane of the notch:

Table 6.2 – Chevron-notched beam dimensions and notch orientations.

	Beam #	Notch orientation	S (μm)	S_S (μm)	B (μm)	W (μm)	a_0 (μm)	a_1 (μm)	V (μm³)
TiC	1	(100)	12.1	3.8	4.8	3.3	0.8	1.8	125
	2	(100)	19.2	5.1	7.8	5.4	0.9	2.8	508
	3	(111)	10.0	2.7	5.6	4.6	0.7	2.6	163
$Ti_{81}W_{19}C$	1	(100)	10.5	1.8	4.0	3.7	0.7	1.6	92
	2	(100)	17.9	1.9	5.1	3.8	0.6	2.3	190
	3	(100)	11.1	1.1	2.5	1.8	0.4	1.0	27
	4	(110)	21.1	1.5	5.3	2.7	0.8	1.9	158
	5	(110)	10.9	1.4	3.2	2.3	0.4	1.1	45
WC	1	(1$\underline{1}$00)	6.0	2.8	2.4	1.8	0.6	1.3	19
	2	(1$\underline{1}$00)	11.5	1.6	3.9	3.2	0.6	2.3	83

Since our samples are machined from particles embedded in a much softer metallic matrix, the compliance measured in the test might also include a contribution due to matrix deformation. We assume that the compliance C_0 due to matrix deformation is independent of the crack length a; the total compliance is then $C(a) = C_0 + C_b(a)$, where C_b is the compliance of the beam. The matrix compliance is then irrelevant since we only consider the derivative $dC(a)/da$. To determine the compliance of the beam, finite element modelling was used, giving C_b. As the crack grows through the ligament of a chevron notch, the sample compliance continuously increases, so that, as should be, dC/da is a monotonically increasing function of the crack length a.

Given the lack of precision inherent to FIB milling, each beam was measured and modelled separately, with its own dimensions. The final result of the FE simulation is the $C(a)$ function. An example is given in Fig. 6.5.

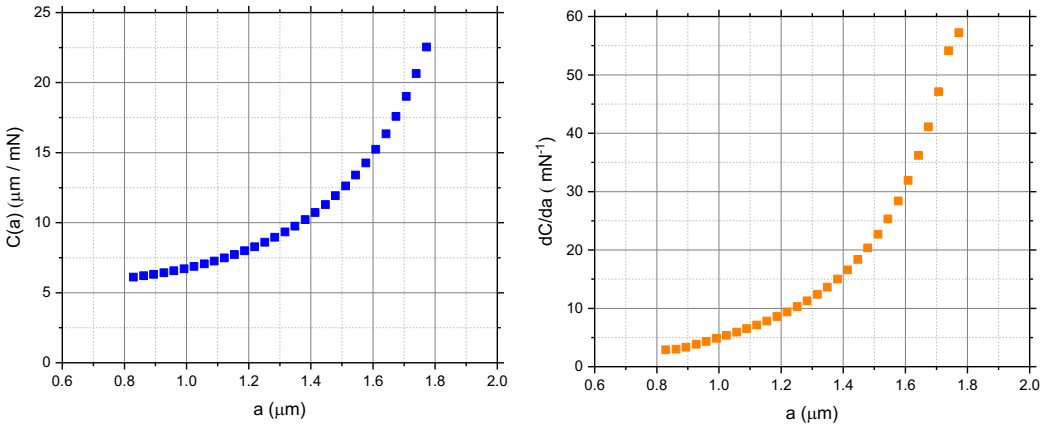

Fig. 6.5 – $C(a)$ and $dC(a)/da$ functions obtained from FE simulation ($Ti_{81}W_{19}C$, beam n°4).

The fracture toughness is measured at the minimum and can be expressed in terms of G_c or K_c:

$$G_c = P_c^2 \cdot min[Y_G(a)]$$
$$K_c = P_c\, min[Y_K(a)]$$

Eq. 6.5

where P_c is the critical load at failure and Y_G, Y_K are two geometrical functions that depend on the crack length:

$$Y_G(a) = \frac{1}{2b}\frac{\partial C}{\partial a} = \frac{W}{2B(W-a_1)}\frac{a_1 - a_0}{a - a_0}\frac{\partial C}{\partial a}$$
$$Y_K(a) = \sqrt{\frac{M \cdot W}{2B(W-a_1)}\frac{a_1 - a_0}{a - a_0}\frac{\partial C}{\partial a}}$$

Eq. 6.6

And M is the indentation modulus. Both Y functions reach a minimum at $a = a_c$, when the cracked chevron-notched sample becomes unstable (Fig. 6.6). The well-known relationship $K = \sqrt{G \cdot M}$ for plane strain is verified.

The minimal values of Y_G and Y_K are obtained from the FE simulation; the peak load is directly determined on the loading curve. The results are given in Table 6.3.

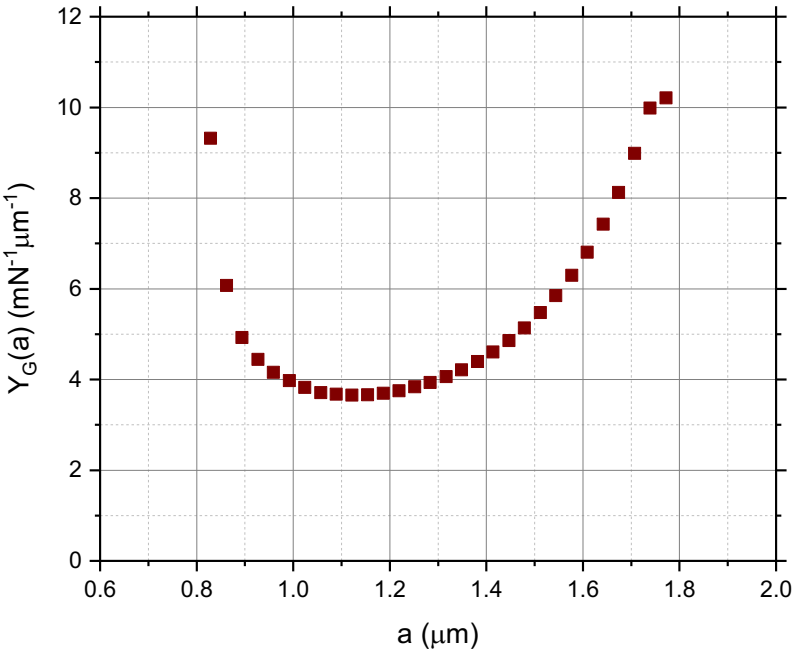

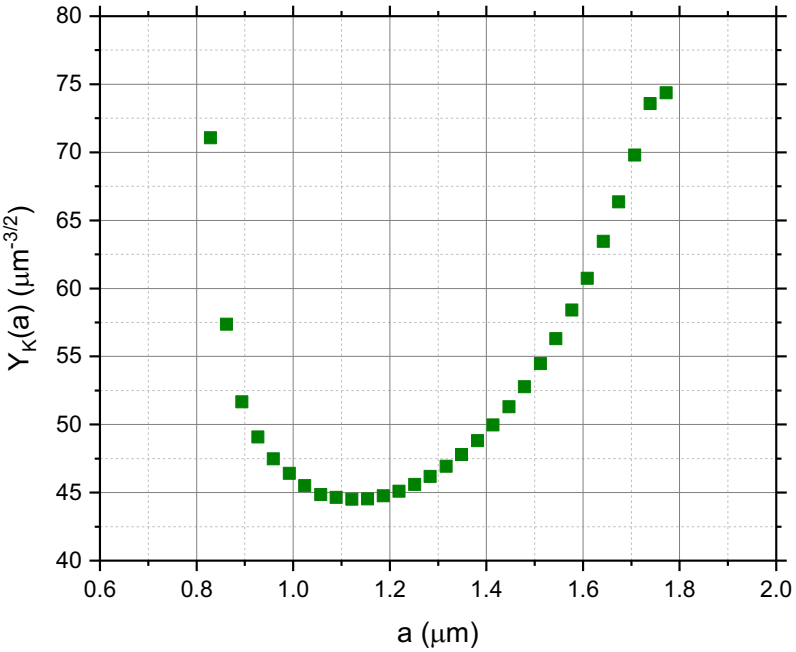

Fig. 6.6 – $Y_G(a)$ and $Y_K(a)$ functions ($Ti_{81}W_{19}C$, beam n°4).

Table 6.3 – Fracture toughness measurement for chevron-notched cantilever beams.

	Beam #	Notch orientation	P_c (μN)	$min(Y_G)$ (μm^{-1}·mN^{-1})	$min(Y_K)$ (μm$^{-3/2}$)	G_c (J·m^{-2})	K_c (MPa·m$^{1/2}$)
TiC	1	(100)	139	0.51	15.27	9.8	2.12
	2	(100)	261	0.08	6.22	5.8	1.64
	3	(111)	374	0.09	6.26	11.9	2.34
$Ti_{81}W_{19}C$	1	(100)	127	0.50	16.53	8.1	2.10
	2	(100)	90	1.27	26.22	10.3	2.36
	3	(100)	26	13.46	85.38	9.1	2.22
	4	(110)	83	3.53	43.73	24.3	3.63
	5	(110)	110	2.20	34.55	26.6	3.80
WC	1	(1$\underline{1}$00)	37	46.21	185.68	63.26	6.87
	2	(1$\underline{1}$00)	131	5.07	61.53	87.08	8.06

6.2.2 Indentation fracture toughness

Indents are performed with a 50 mN load on the different binary and ternary carbides. Some compositions have not been tested, because the size of the particles was not large enough to contain the cracks, which were then stopped at the interface, making the test invalid. For each tested composition, several indents are performed. Examples of SEM crack analysis and measurements are given in Fig. 6.7 for radial cracks and in Fig. 6.8 for half-penny cracks.

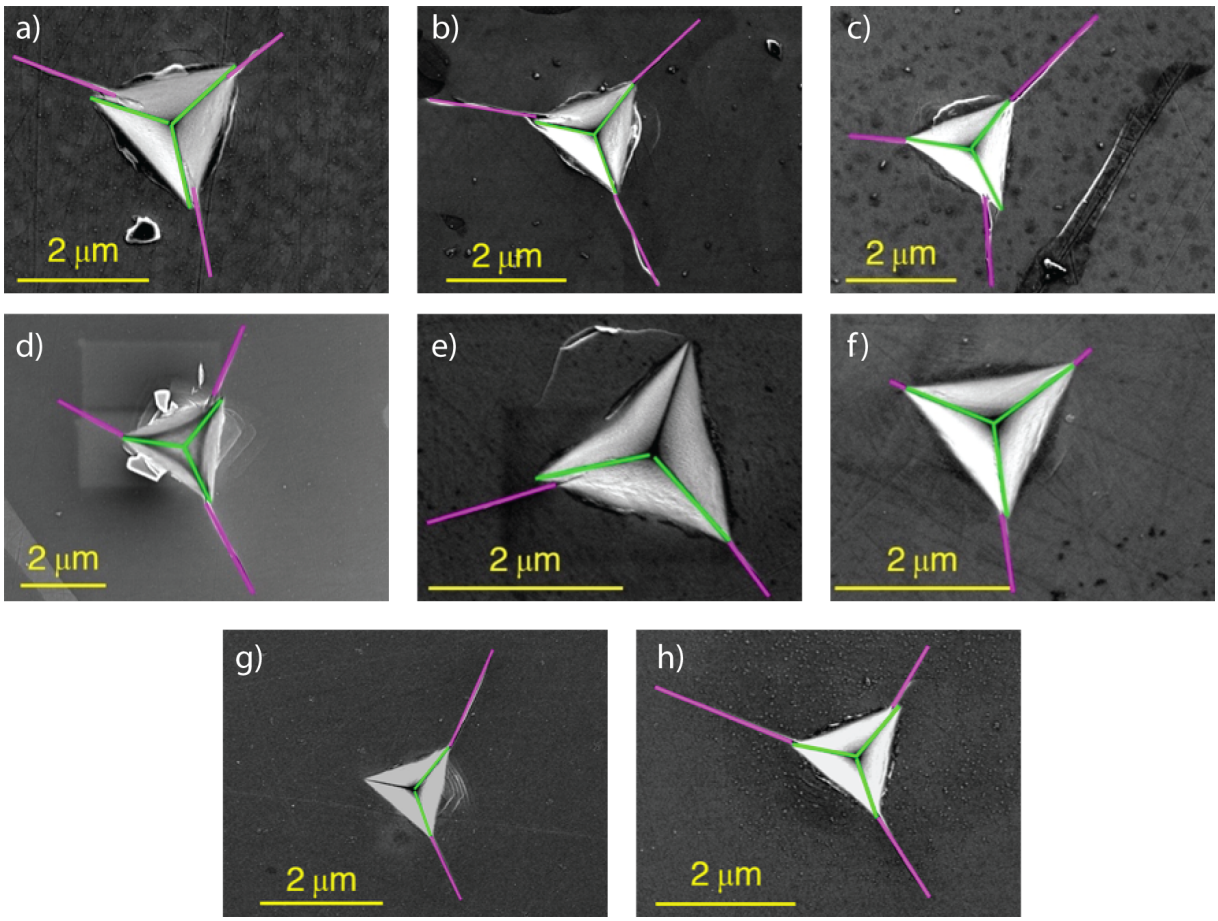

Fig. 6.7 – Examples of Palmqvist crack analysis and measurements for indentation toughness; a) $Ta_{13}V_{87}C$; b) $Ta_{39}V_{61}C$; c) $Ta_{69}V_{31}C$; d) $Ti_4V_{96}C$; e) $Ti_{22}Ta_{78}C$; f) $Ti_{73}Nb_{27}C$; g) $Ti_{90}V_{10}C$; h) $Ti_{90}V_{10}C$.

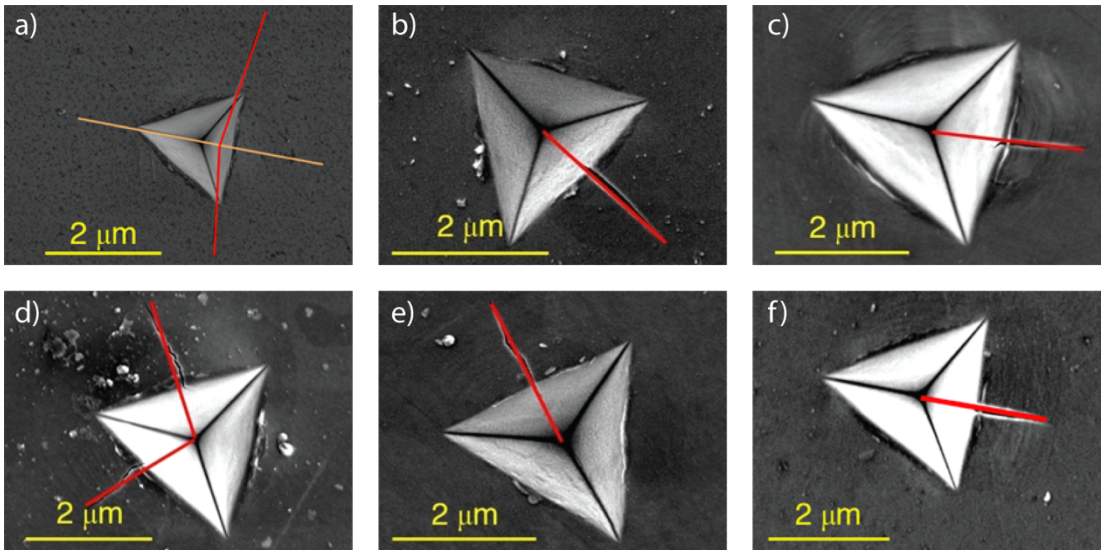

Fig. 6.8 – Examples of half-penny crack analysis and measurements for indentation toughness; a) $Ti_{10}Ta_{90}C$; b) $Ti_{69}Ta_{31}C$; c) $Ti_{76}Nb_{24}C$; d) $Ti_{76}Nb_{24}C$; e) $Ti_{81}Ta_{19}C$; f) $Ti_{93}Nb_{7}C$.

The indentation fracture toughness is then calculated with Niihara's equations. The values corresponding to the indents presented in Fig. 6.7 & Fig. 6.8 are detailed in Table 6.4:

Table 6.4 – Examples of measurement of indentation toughness based on crack analysis. CHANGED

	Indent #	Composition	E (GPa)	H (GPa)	c (µm)	a (µm)	l (µm)	K_c (MPa·m$^{1/2}$)
Radial cracks	a	$Ta_{13}V_{87}C$	423	31.6	-	1.38	1.40	2.0
	b	$Ta_{39}V_{61}C$	457	31.6	-	1.09	1.69	2.4
	c	$Ta_{69}V_{31}C$	471	32.7	-	1.17	1.60	2.3
	d	$Ti_{4}V_{96}C$	422	29.3	-	1.47	2.01	1.6
	e	$Ti_{22}Ta_{78}C$	502	33.4	-	1.21	1.06	2.7
	f	$Ti_{73}Nb_{27}C$	470	32.1	-	1.11	0.48	4.4
	g	$Ti_{90}V_{10}C$	483	31.2	-	0.92	1.46	3.1
	h	$Ti_{90}V_{10}C$	483	31.2	-	0.94	1.53	3.0
Half-penny cracks	a	$Ti_{10}Ta_{90}C$	491	32.7	2.18	-	-	3.6
	b	$Ti_{69}Ta_{31}C$	472	29.2	2.16	-	-	3.8
	c	$Ti_{76}Nb_{24}C$	467	31.9	2.28	-	-	3.4
	d	$Ti_{76}Nb_{24}C$	467	31.9	2.18	-	-	3.6
	e	$Ti_{81}Ta_{19}C$	470	29.5	2.20	-	-	3.7
	f	$Ti_{97}Nb_{3}C$	446	30.8	2.14	-	-	3.7

For the radial and half-penny cracks, we averaged a, l or c for each indent when there was more than one crack. The fracture toughness was determined for most of the binary and ternary compositions; graphic representations as a function of composition for ternary carbides are presented in Figs 6.9-13.

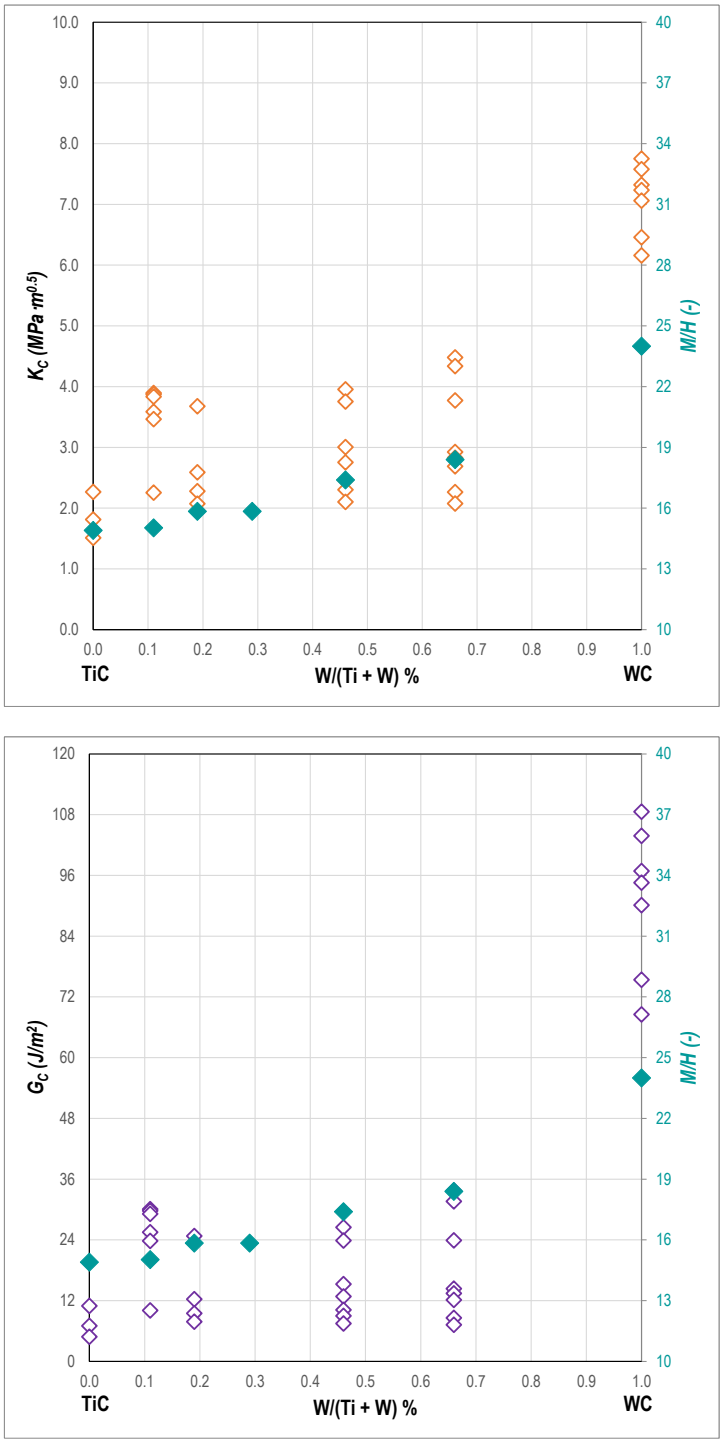

Fig. 6.9 – K_c and G_c for the (Ti,W)C ternary system. CHANGED

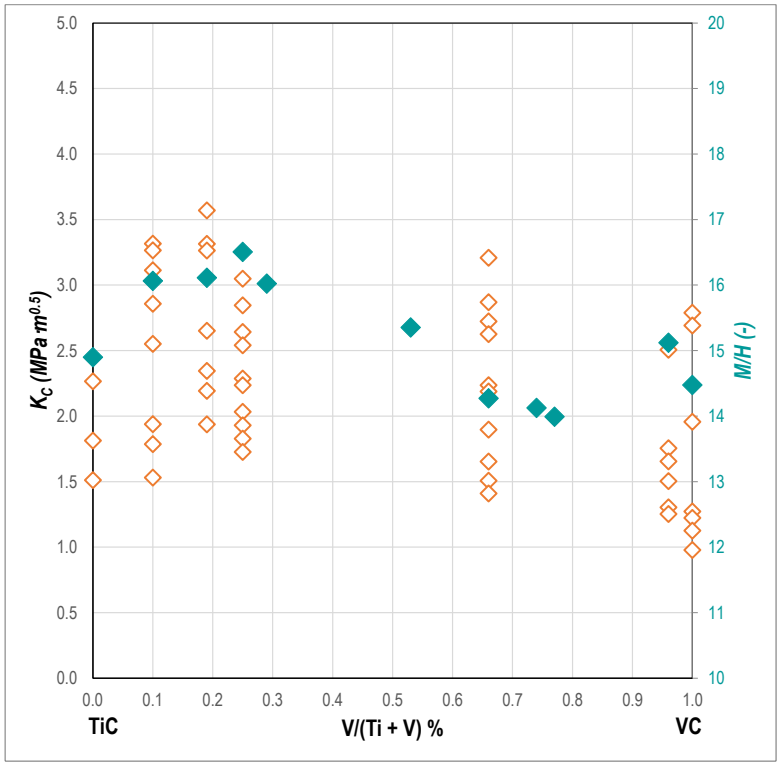

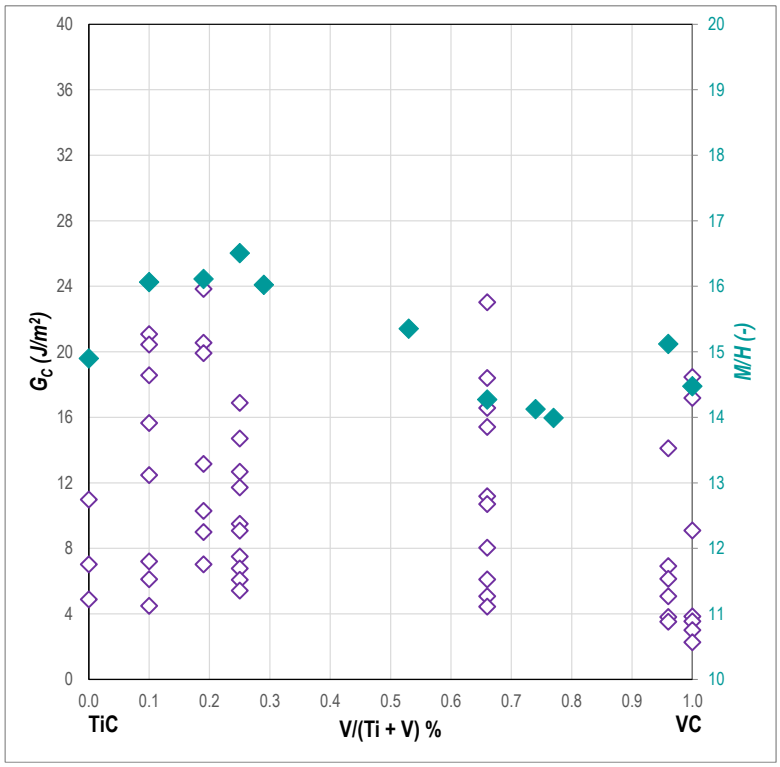

Fig. 6.10 – K_c and G_c for the (Ti,V)C ternary system. CHANGED

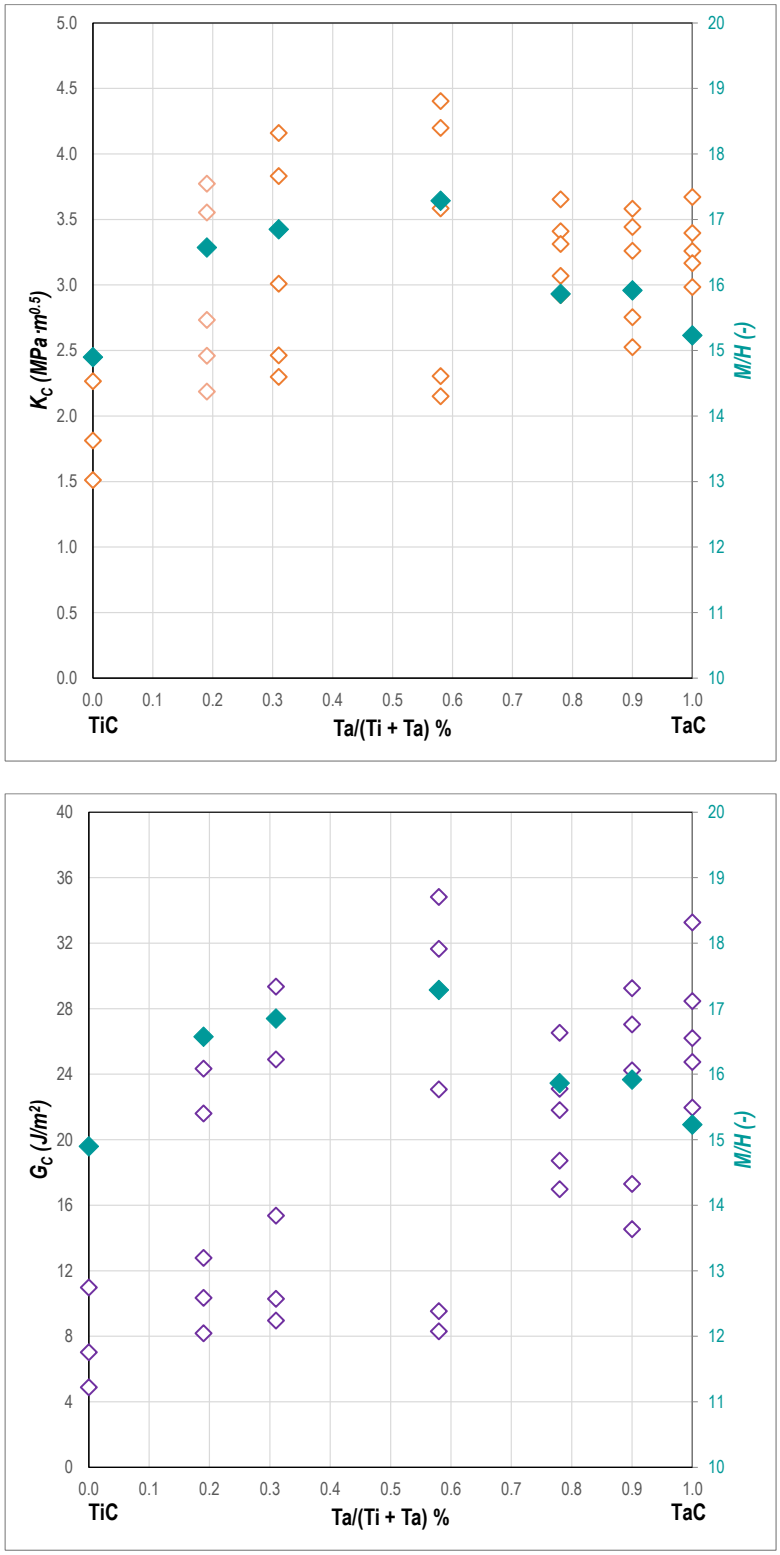

Fig. 6.11 – K_c and G_c for the (Ti,Ta)C ternary system. CHANGED

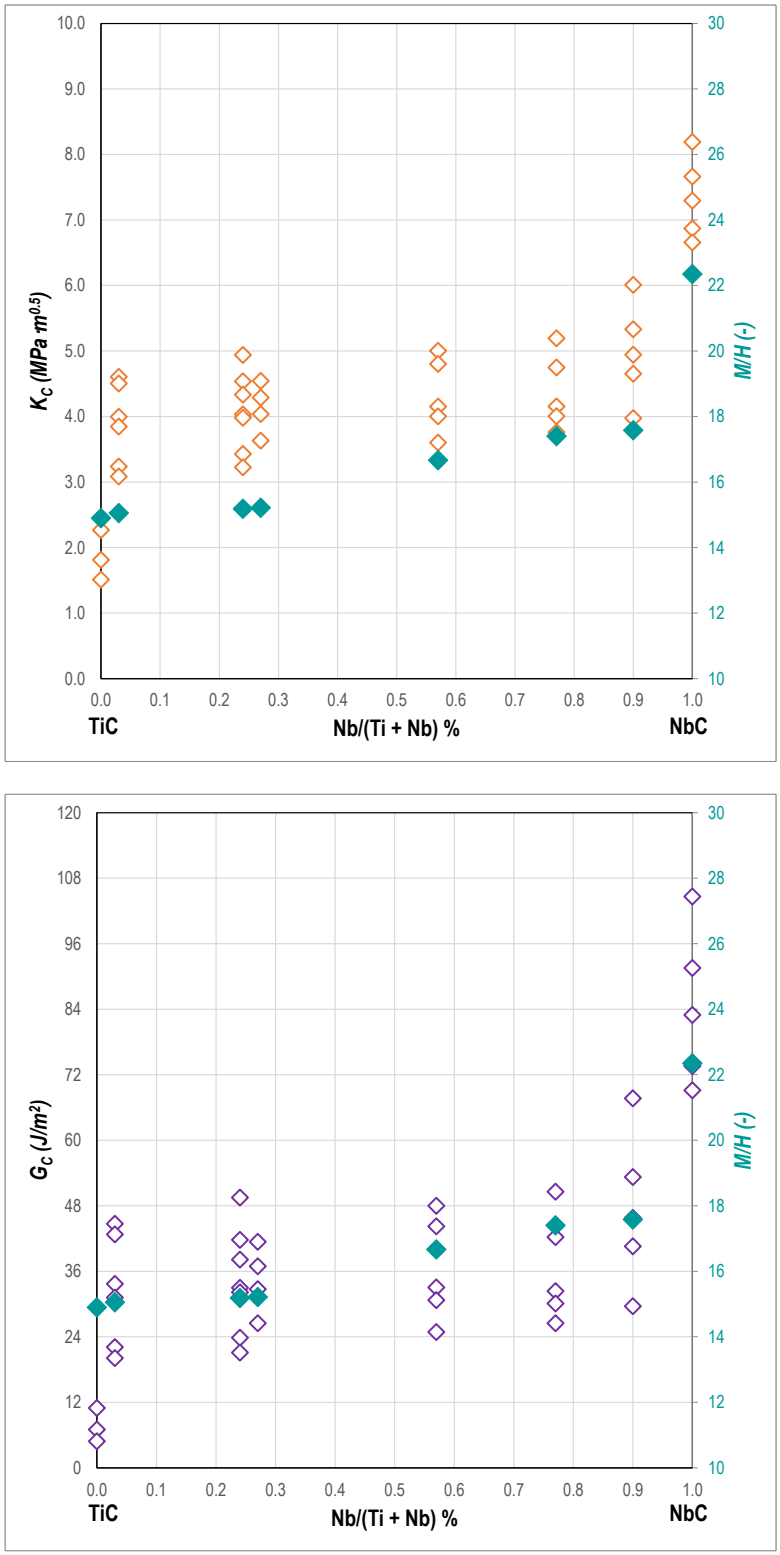

Fig. 6.12 – K_c and G_c for the (Ti,Nb)C ternary system. CHANGED

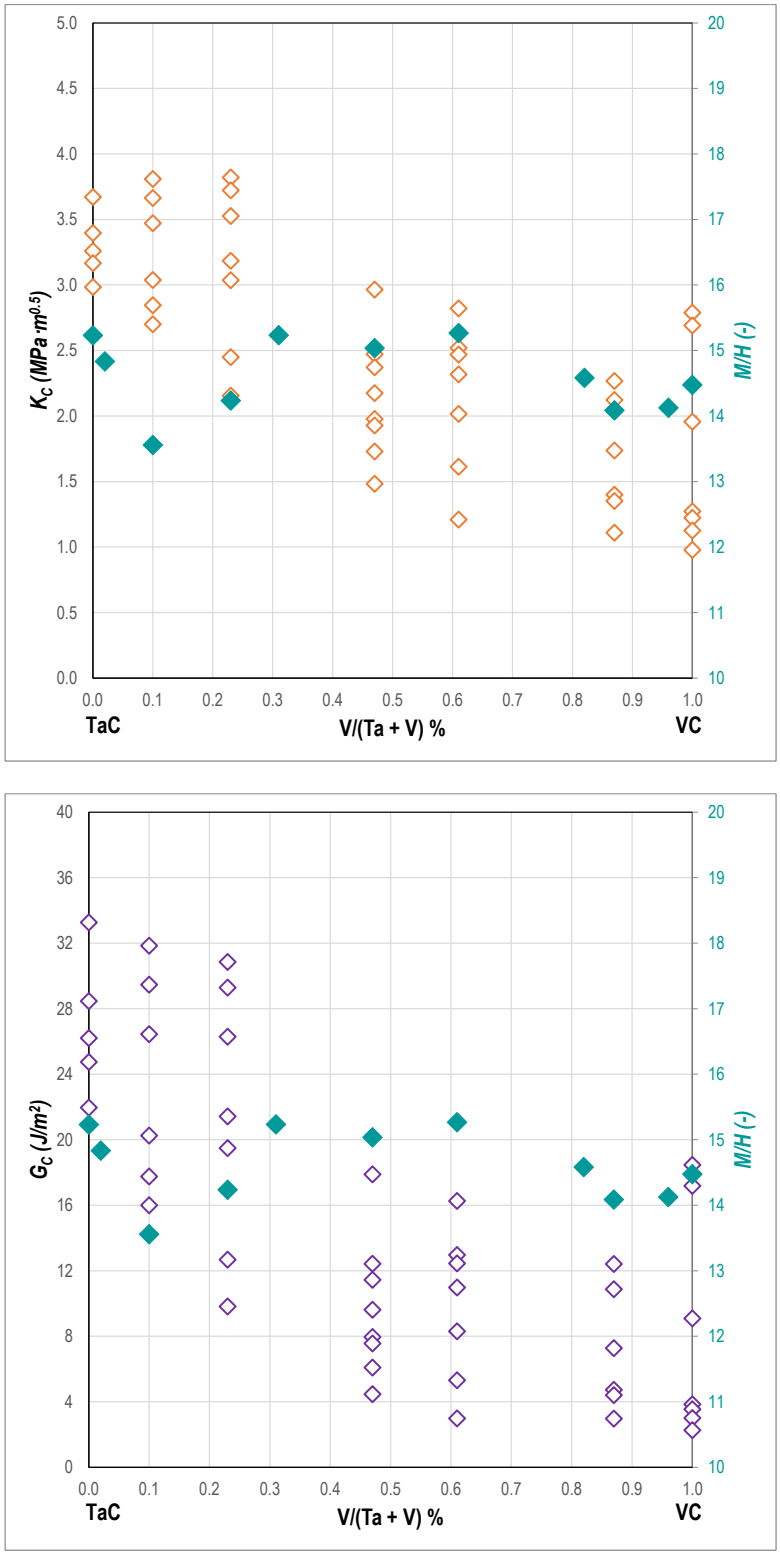

Fig. 6.13 – K_c and G_c for the (Ta,V)C ternary system. CHANGED

6.3 Fracture toughness measurements: discussion

In contrast to E and H, which were properties relatively well defined and "easy" to measure in practice once procedures are established, the fracture toughness is a much more complex quantity to measure. It is also more difficult to interpret: the elastic modulus can be directly related to the elastic stretching of atomic bonds and the hardness to localized elastoplastic deformation, whereas the fracture toughness involves more erratic and complex mechanisms, namely the propagation of a crack, with the ensuing breaking of atomic bonds, creation of new free surfaces, with strong variations in the amount of yielding in front of the crack or in the stress state around the crack tip (plane stress/strain assumptions).

Also, relatively few fracture toughness data are available in the literature for binary carbides of this work. We thus assess the accuracy of these two methods by comparing their results for the (Ti,W)C ternary system. The four other ternary systems are then presented in terms of results from nanoindentation toughness measurements (only) and effects of composition are briefly discussed in a third and last section.

6.3.1 Experimental difficulties associated with micro-tests

Most fracture toughness measurement methods are based on pre-cracked specimen geometries, both methods used here create the crack during the test. The reason for this is that producing a pre-crack is challenging in brittle materials, and even more so especially at the microscale. At the microscale, pre-cracked samples have been produced by machining: the machining of a pre-crack constitutes then a crucial step for the success of the test, and a first important source of error. For macro-samples, standards describe usually the sample geometry and a skilled operator can generally produce a notch that fulfils the requirements; for micro-samples on the other hand, FIB milling is generally the only tool available to machine the specimen, making it much more complicated (or impossible) to produce an acceptably sharp notch. We therefore opted to use methods by which a (real) crack is produced during the test. All data reported here thus give values of toughness measured, not at the initiation of crack propagation as is most usually done, but either on a propagating crack (the chevron-notched method), or at arrested cracks (indentation toughness).

In micro-tests, furthermore, positioning the sample is a challenge. Indeed, due to the small dimensions of the sample, the load is often applied via an indenter tip, and approaching (or even scanning) the specimen can easily break it; moreover, precision in the location of the application point of the load is important. If the test is performed within a SEM, it is possible to visualize simultaneously the tip and the sample; however, the spatial representation is limited (because the picture is taken from a single perspective). Otherwise one can use Scanning Probe Microscopy (SPM), which consists in a scan of the sample by the indenter tip, in tapping mode at low load. Both methods have a maximal lateral precision of roughly 200 nm in the point of load application.

Finally, the dimensions of the sample are also important in the determination of the fracture toughness; here too the (relative) precision is less at the microscale than with macrosamples.

Crack propagation is also an issue within monocrystalline samples. In anisotropic single crystals, the fracture toughness can be strongly dependent on the crack plane and on the crack propagation direction. Covalent materials are often characterized by cleavage planes, i.e. specific crystallographically defined planes that are preferably broken, towards which cracks have a tendency to deviate, making it difficult to force the crack to propagate in a given plane.

Fracture toughness measurements based on nanoindentation differ from tests conducted on notched samples in that they do not require a special geometry and can be performed directly on a crack-free polished surface. The cracks are generated by the tensile components of the complex indentation stress field, and this can happen during either the loading or the unloading part of the indentation process. *Stricto sensu*, nanoindentation fracture toughness does not measure the onset of crack propagation, but rather a set of length and load conditions that the propagation of a crack to stop. Determining the fracture toughness requires then a complete analysis of the cracks formed during the indent, which is not necessary for pre-cracked samples. Most of the error comes from that analysis, because in practice the crack system associated with an indent can be very messy and different crack types can be simultaneously generated around a single indent.

6.3.2 Chevron-notched test data

The use of chevron-notched samples for the measurement of toughness at the microscale was pioneered in our group on nanocrystalline alumina fibers and fused quartz, two materials that can be considered as isotropic, to demonstrate the method and assess its accuracy[178]. The method proved to give accurate measurements of the fracture toughness of these materials; however, it requires care during each of its steps. In later work, its extension towards testing silicon was attempted, to find that it was more difficult to implement in this (covalently bonded) solid because crack initiation proved difficult.

As described before, the method can be divided into four successive steps: (i) milling of the beam (rectangular or triangular), including the triangular notch; (ii) testing the notched beam in a nanoindentation apparatus; (iii) determining post-test required quantities (dimensions of the notch, point of application of the load) and finally (iv) FE simulation of the sample to determine its compliance versus crack length. Each step is important and can determine the success or the failure of the test.

The milling part is obviously important, because it determines the dimensions of the beam, as well as the quality of the notch. We used only triangular beams, as these are more convenient to mill such beams along a flat sample surface. Because the ion beam is characterized by a Gaussian dispersion, especially for high currents, the milled faces of the sample are never strictly parallel to the beam. FIB-milling also produces a large quantity of redeposited material, obviously commensurate in volume to the amount of milled material. These two effects can modify the final shape of the sample in comparison with the aimed-for geometry. It is however possible to reduce such problems by milling with successively decreasing currents, in order to obtain a final morphology as precise as possible, coupled with lowered levels of ion implantation. The notch is always milled with the lowest current available, for precision, and also to produce a notch as thin as possible, as this is an important parameter in initiating the crack and guiding its propagation.

The test itself must be performed very carefully. Indeed, the required scanning procedure can easily break the beam if performed incorrectly. The source of the problem consists in the two pits on both sides of the beam; while scanning, the contact load is set to a low but constant value (2 μN), and because of the large depth difference between the beam and the pit, the indenter tends, if it meets the pit, to dive into it, as it aims to keep the contact load. Because of the conical geometry of the indenter, a non-negligible force is then suddenly applied on the beam, which can be (or rather, has been) sufficient to break it. To avoid this, we developed a special scanning procedure:

- We first scan the particle laterally, far from the beam, and we correct the alignment with a tilt stage;
- We then scan the particle parallel to the beam, still far from it, and we correct the sample alignment with a second tilt stage;
- Since the particle surface is flat, we scan the beam, the indenter moving always parallel to the beam axis. We never performed in tests reported here a lateral scan of the beam.

The use of a cube corner indenter, with a smaller angle than a Berkovich tip, allows to reduce the load applied on the beam during the scanning, this being a significant advantage.

Experimental error on the point of load application is the principal parameter that can influence the measurement. With this scanning procedure, the point of application is chosen from a SPM image. At the end of the FIB-milling process, we place linear marks that are visible during the scanning to help us. The precision of the apparatus is approximately a circle of 200 nm diameter in which the indent is performed. An example is given in Fig. 6.14. Two typical load-displacement curves are shown in Fig. 6.15:

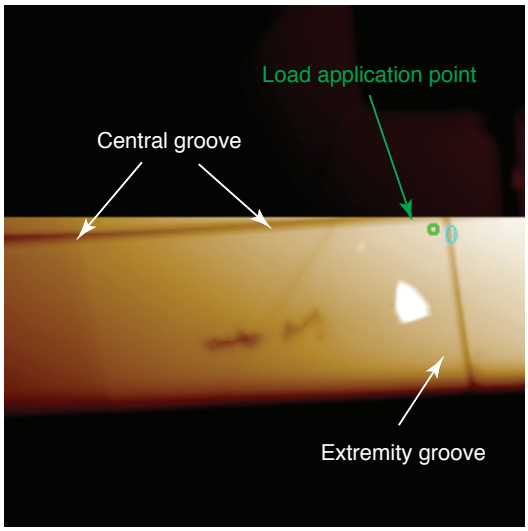

Fig. 6.14 – 10x10 μm SPM image of a chevron beam, with indication of the point of load application. The scan is performed from the bottom of the picture up to the top; the scan is stopped since the central groove is observed in order to start the test while the tip is properly situated over the beam.

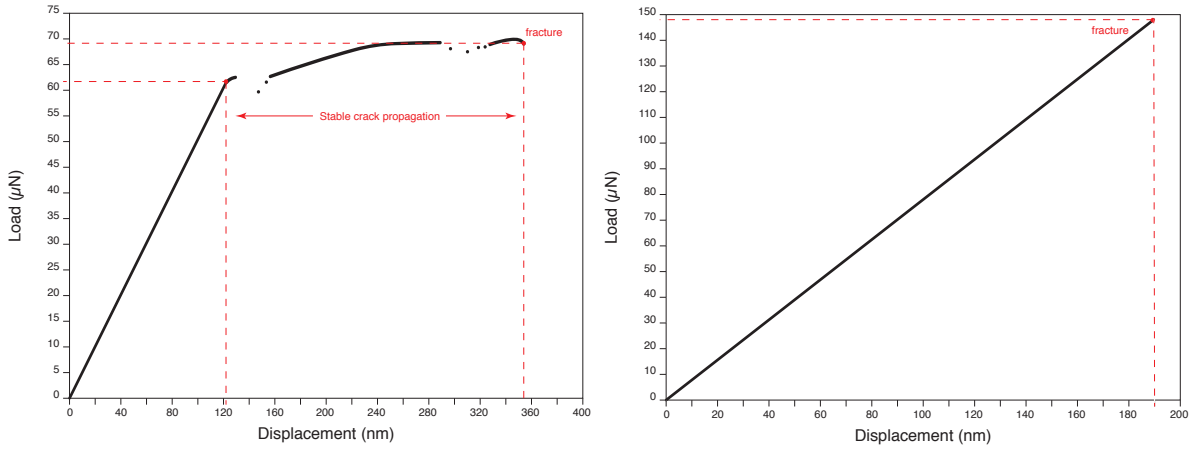

Fig. 6.15 – Load-displacement curve of a successful test (left) and for a failed test (right).

A failed test is usually characterized by a fully linear curve, i.e. there is no stable crack propagation, which causes deviations from linearity in the load/displacement curve. In that case, the sample breaks instantaneously when peak load is reached. On the contrary, a successful test exhibits a pop-in, indicating that the apex of the notch was broken, followed by a limited amount of stable crack propagation. Continued crack propagation necessitates an increase in load and generates a non-linear signal, which stops when the crack becomes unstable, upon which fracture occurs followed by immediate unloading. The indenter tip can often slide at the beginning of the test; in that case, the very first part of the curve is not linear, an effect that is not important if this initially non-linear signal is followed by a linear loading curve (Fig. 6.16).

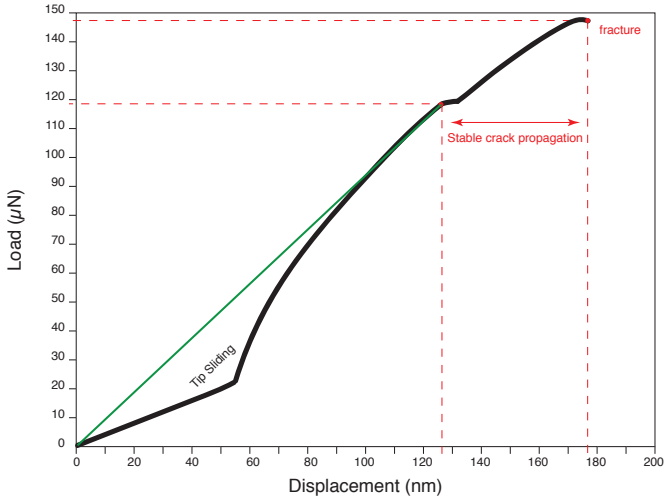

Fig. 6.16 – Load-displacement curve illustrating tip sliding.

The load-displacement curves are then used to determine the load at which the crack propagation becomes critical, and the corresponding stress intensity factor is deduced using finite element computations of the compliance calibration curve for the test sample in question.

It is only possible to measure the dimensions of the notch once the beam has been broken; at that time, it is also possible to determine more precisely the point of load application, because the indenter tip leaves a mark on the beam. In general, all the dimensions are important for finite element simulation and hence for the calculation of the fracture toughness. In this work, all relevant sample dimensions were measured by SEM analysis. In doing so, we can also determine whether the crack propagated in the notch plane or if cleavage deviated it into another plane. In conclusion, the biggest source of error for that method comes from the measurement of beam dimensions.

The complete procedure has required a large number of tests to be optimized for the testing of carbides. We performed 35 tests on TiC particles, with unfortunately only four successful tests; (milling a single beam takes approximately 5 hours). By improving the method along the way, the success rate increased significantly for WC and the ternary (Ti,W)C carbide: for WC, 50% of the samples were successful, and 5 of 8 worked for the ternary carbide.

Counterbalancing the difficulty in conducting and optimizing the test, advantages of the chevron-notched beams are multiple. Data provide a correct measurement of fracture toughness (measured with a propagating sharp crack), contrary to data generated with a pre-notched sample, which is loaded until the crack propagates from a notch, the tip of which is blunt on the scale of the test; in that sense, the chevron-notched test remains more similar in going from macro- to micro-scale testing. Secondly, the method allows to measure the fracture toughness anisotropy in single crystals because it is possible to pre-determine the crystalline orientation of the notch-plane. In this work, we used an EBSD equipped microscope to determine the orientation of the surface, using in addition the faceted dendritic morphology of the particles as an aid in determining other orientation directions. Finally, the method is not affected by the gallium contamination that accompanies FIB-milling. It is well known that gallium ions are implanted in a thin layer below the milled surface (to depths typically extending a few tens of nanometers); the presence of such ions can modify the fracture toughness and more generally the mechanical properties. Because of the initial stable crack propagation, in the chevron-notched fracture test the critical fracture toughness is measured below the apex of the notch, along a crack front extending mostly across a region where the material is not affected by FIB-milling.

The principal drawback of the procedure consists in its operational complexity and, for some systems, in difficulty with crack nucleation. Indeed, as described above, the method involves a succession of different steps, which are not only complex, but also time consuming and expensive (as sample preparation involves usage of a FIB). The relatively low success rate in testing also requires that more samples be produced than will end up giving meaningful data.

In summary, the method is elegant and accurate, and it allows to measure the fracture toughness of different crystalline orientations, but it is not appropriate to test a large number of different compositions, as is the aim for this thesis. We thus use it as a yardstick by means of which we establish the fact that, in carbides of this work and despite its limitations, the indentation toughness measurement method yields reasonable data, and can thus be used as an exploratory tool to measure variations in the toughness of MC carbides with their composition.

6.3.3 Indentation toughness

The alternative to chevron-notched beam testing that we used here is to generate cracks via indents. In contrast to the chevron-notched microbeams, indentations are easy to perform on a large number of samples. On the other hand, the analysis of the cracks results in a less accurate

determination of the fracture toughness. We thus examine the crack system generated by an indentation, aiming in particular to define the sources of error in the measurement of toughness by the indentation method, keeping in mind that this measurement differs from traditional fracture toughness measurements and has been the subject of criticism.

There are three major practical concerns with indentation fracture: the complexity of the crack system that is generated by an indenter, the forces acting upon them and the use of an empirical calibration constant. Many equations have been proposed to determine the fracture toughness based on cracks produced after indentation; they have a common form:

$$K_C = \chi \cdot \frac{P}{c^{\frac{3}{2}}}$$

Eq. 6.7

where χ is an empirical function that depends both on the material properties and on the indenter geometry:

$$\chi = A \cdot \left(\frac{E}{H}\right)^n$$

Eq. 6.8

where A is a constant describing the effect of the tip geometry. Materials properties influence the fracture toughness via the ratio E/H; n is an exponent that varies with the model. These empirical factors have been selected as the best way to match traditional fracture toughness measurements on ceramics and glass; they exhibit however a large degree of uncertainty. $A = 0.016 \pm 0.04$ in the case of Augier's equation for a Berkovich indenter. The geometrical factor represents not only the tip geometry, but also the size and shape of the elastic-plastic zone around the indent; also, all brittle materials do not deform and fracture in a similar manner, as it is assumed by the model. That is one of the reasons explaining why so many models have been developed to treat this problem: they are only accurate for a single class of ceramic. A universal model suitable for the determination of the indentation-derived fracture toughness of all the brittle materials is apparently unrealistic.

A strong assumption has been made on the crack geometry in the above expressions. As explained in Chapter 2, one can consider four principal types of crack: radial, median, lateral and half-penny; however, in practice the generated cracks deviate most of the time from these idealized geometries. The method is furthermore based on observation of the sample surface only, and hence on its intersection with the cracks. Lateral and median cracks, however, propagate only beneath the surface and are therefore generally not accounted for because they are not visible under such observation. In that sense, indentation fracture measurements tend to overestimate the material's toughness by not considering the cracks that form below the surface. In practice, lateral cracks can deviate and propagate up to the surface, resulting in a very messy crack system (which is then considered as a failed test), and only the radial and half-penny cracks are analyzed.

Measuring the surface crack length can also be a complicated step, because the cracks are often not straight and are often not exactly initiated at an indent corner. The use of an optical microscope for the first measurement in the 70s and 80s was the source of a very important error in this regard; however, the accuracy of the modern SEM allows to measure the crack length with far higher, and seemingly sufficient, precision for meaningful data generation.

From the work of Evans and Lawn, a number of improvements have been proposed, mainly in the definition of the geometrical factor A and of the exponent n. Models have been developed for the two (radial and half-penny) surface-emerging crack geometries, for several different ceramics. Schiffmann[177] wrote in 2011 an interesting review of the different available models that can be used to determine the indentation toughness. He performed several indents with a cube corner indenter on different bulk ceramics: (100) silicon, fused silica and (0001) sapphire; as well as thin films: ZnO, SnO_2, DLC (diamond like carbon), amorphous carbon(a-C) and ITO (Indium Tin Oxide). The use of a cube corner indenter, with its smaller opening angle, reduces the fracture threshold. Schiffmann then evaluated the toughness with six different models (Fig. 6.17 & Fig. 6.18).

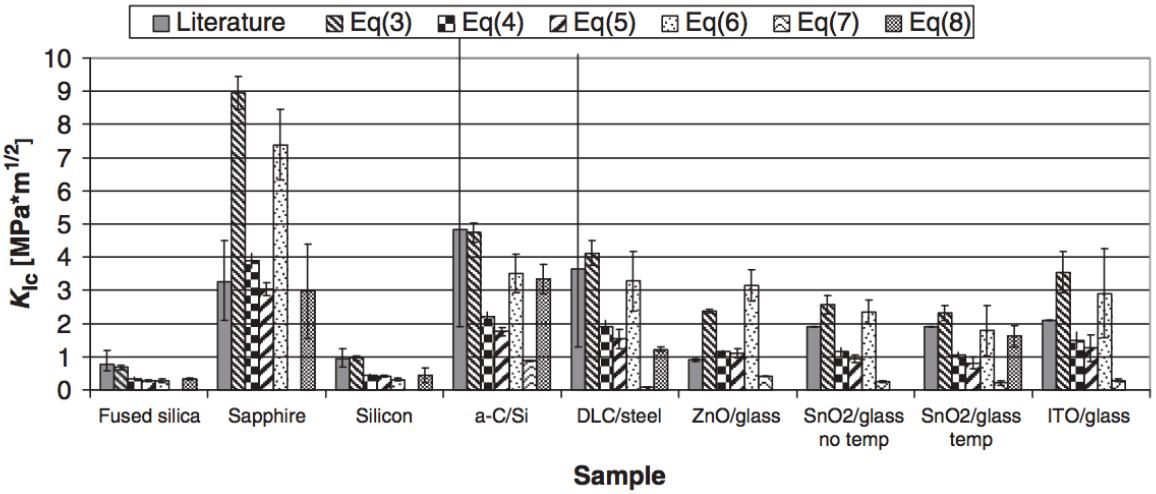

Fig. 6.17 – Fracture toughness evaluated with different models and comparison with literature; reproduced from Ref [177].

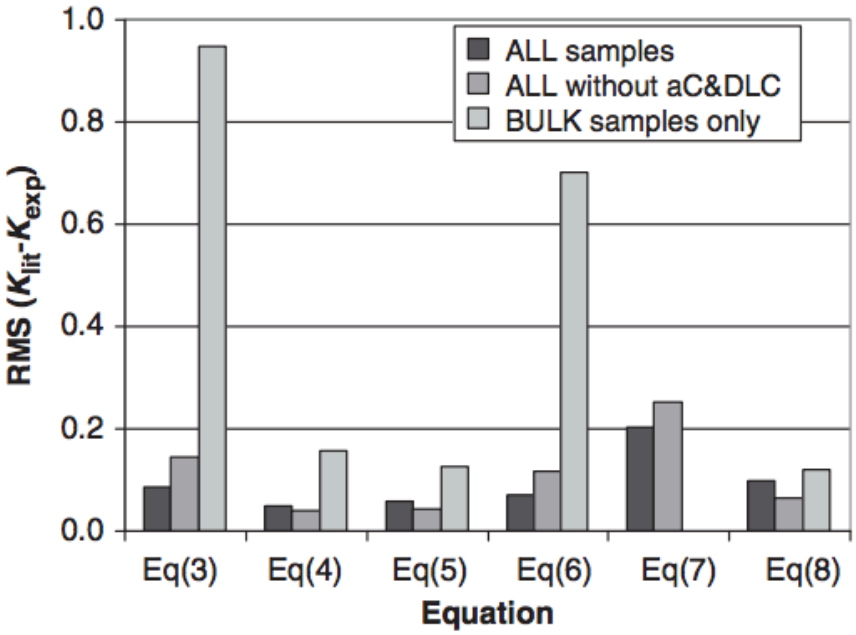

Fig. 6.18 – RMS deviation between literature and measurements for all equations and tested materials in Fig. 6.17 ; reproduced from Ref [177].

More details about the six compared models can be found in reference [177]; Eq(3) corresponds to the model of Jang and Pharr[179], based on the Evans and Lawn equation, but including an analytical expression for the geometrical factor that depends on the indenter opening angle. Both Eq(4) and Eq(5) are based on the Niihara[154,155] model; the first equation was modified for halfpenny cracks, the second for radial cracks. Eq(6) is an analysis developed by Laugier[180] and Ouchterlony[181], and Eq(7) is an adapted equation for thin films, proposed by Thurn and Cook[182]. The last equation, Eq(8), calculates the toughness by using energy-based considerations and was proposed by Li et al.[183].

The accuracy of these various methods is sensibly different. If we consider bulk sapphire, both Eq(3) and Eq(6) give completely unrealistic values for the fracture toughness; on the contrary, Eq(4-5) and Eq(8) are far more accurate if one compares results with literature values. For tin oxide SnO_2 or DLC thin films, the opposite is observed. Equations (4-5), given by Niihara's analysis, exhibit the smallest deviation from literature values and so we have consequently used those equations here for data analysis. Equation (8) could have been another option; however, the need for pop-in events to calculate the fracture toughness renders the method erratic in the present work.

Measuring fracture toughness of particles embedded in a steel matrix complicates the test. Indeed, the generated cracks must be restricted to the particle, not only along the surface, but also underneath. The interfaces act as a stopper for crack propagation, which obviously biases the measurement. For that reason, it was not possible to test all the compositions, and only sufficiently large particles have been indented.

In conclusion, the Niihara equations give, so far, the best agreement with literature values and are used here; however, the precision of the model can be as low as 40%, which is enough to determine the right magnitude of the result and compare different materials measured with the same method, but is insufficient to claim that one has measured with any precision the actual fracture toughness of a material.

6.3.4 Comparison between chevron-notched sample and indentation data

We now compare the measurements obtained with each of the two methods. Three materials were tested with the chevron-notched method: TiC, WC and $Ti_{81}W_{19}C$; for the two binary carbides, literature values are moreover available. The comparison is given in Fig. 6.19:

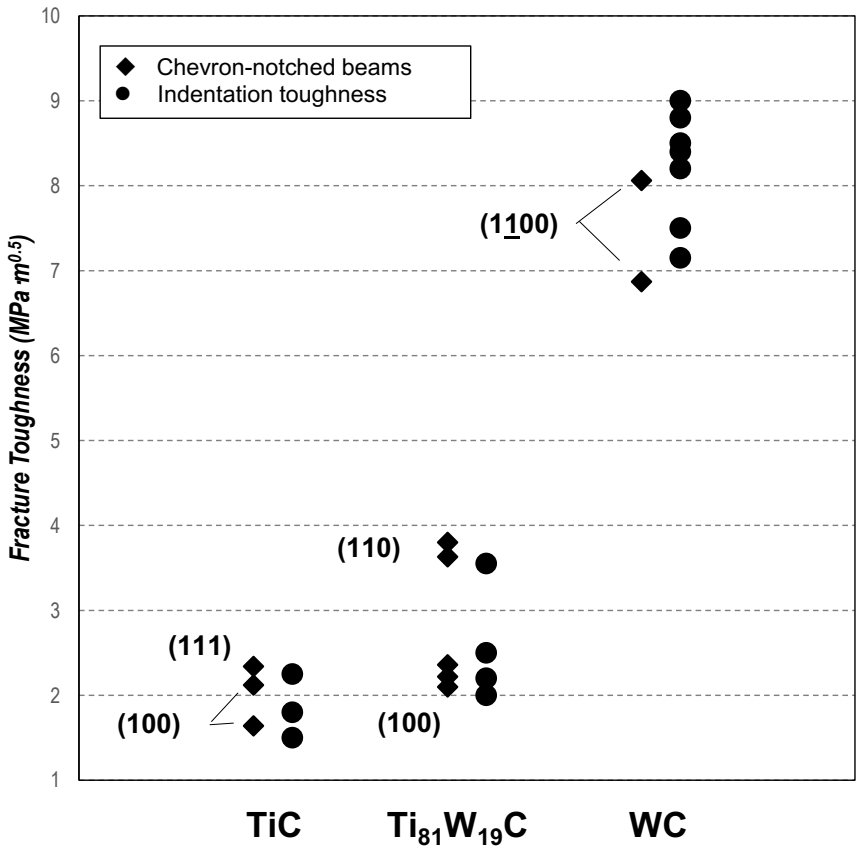

Fig. 6.19 – Comparison between indentation toughness and chevron-notched beams. CHANGED

As seen, for both TiC and $Ti_{81}W_{19}C$, the consistency between the chevron-notched beam data and the indentation-derived toughness values is very satisfactory. On Fig. 6.19, each point represents a single beam or a separate indent.

The consistency is slightly poorer for WC, where indentation toughness values tend on average to reach higher values than chevron-notched beam measurements. For that binary carbide, only two beams were tested, however, in which the crack plane was similar.

In some cases, the values of fracture toughness measured by nanoindentation can give meaningful results, while in other cases, the values can be significantly different from references. As discussed previously, the level of agreement depends mainly on the model and on the material behavior. The good consistency between the two methods for the three carbides of the (Ti,W)C system suggests that Niihara's model allows to characterize with sufficient accuracy the toughness measured on covalently-bonded cubic ceramics. That method was thus used to measure the indentation fracture toughness of the other ternary systems, whenever the dimensions of the particles allowed such a measurement.

6.3.5 Binary carbides: comparison with the literature

Comparatively few fracture toughness data are available for materials that are used mainly as reinforcements or as a coating, such as carbides. One main reason explaining such a lack of data is the difficulty that exists in the production of large samples, especially monocrystals, of sufficient quality to give meaningful measurements of the toughness via macro-mechanical tests (another is difficulty in precracking of test samples). Most of the data are thus measured using indentation-generated cracks.

TiC has been by far the most studied binary carbide. Maerky[6] published a thorough investigation of the fracture toughness anisotropy of $TiC_{0.96}$ in 1996 (see Chapter 2). Micro-indentation (2.94 N) measurements were performed, on three titanium carbide bulk single crystals with (001), (110) and (111) orientations. Both (001) and (110) crystals were indented with a Vickers pyramidal indenter, for symmetry reasons, while the (111) crystal was tested with a Berkovich triangular tip. Effects of anisotropy were not only investigated by indenting three different surfaces of different orientation, but also by rotating the indenter on the same surface. For the (001) crystal, angles from 0° to 90° were tested with increment of 15°; for the (110) crystal, angles from 0° to 180° with the same 15° increment; and for the (111) crystal, angles from 0° to 120° with 10° increments. The global measured fracture toughnesses range from 1.5 to 3.6 $MPa \cdot m^{0.5}$, the average error on each measurement being approximately ± 0.05. Another measurement series performed by A.J. Parry on polycrystalline TiC is reported by Maerky to give the same value of 3.6 $MPa \cdot m^{0.5}$, but without reference.

The fracture toughness of VC monocrystals was measured by Govila[8] in 1972, using fracture energy observations. The fracture energy was measured, based on Griffith's analysis of pre-cracked bulk specimens, for three carbon-to-metal ratios: $VC_{0.88}$, $VC_{0.84}$ and $VC_{0.76}$. The fracture energy only slightly exceeds the surface energy γ when almost no plastic deformation occurs at the crack front, which is the case for most of the covalent ceramics (slip steps are observed on WC). The fracture toughness can then be estimated as $K_c = \sqrt{2\gamma E}$; values for VC range thus from 1.3 to 1.9 $MPa \cdot m^{0.5}$. To our knowledge, there is no other reference value for the fracture toughness of vanadium carbide.

A reference value for TaC can be found in the paper of Nino[10]; sintered TaC bulk polycrystals were tested by indentation. The fracture toughness was estimated using the standard Evans equation, but few details are given in the paper about the methodology. The measured TaC fracture toughness values range from 3.5 to 4.5 $MPa \cdot m^{0.5}$, depending on the sintering temperature (and thus on the grain size). Other studies[9,184] have measured fracture toughness values for TaC, but for more porous sintered samples, finding nevertheless a coherent range from 3.5 to 5.1 $MPa \cdot m^{0.5}$. To our knowledge, no measurements have been done on single crystals of TaC.

The fracture toughness of sintered bulk NbC was measured by Kim et al.[13,185]. In these two papers, the authors compared sintered NbC made from powders that were milled from 0 to 10 hours; the relative density is 98%. They measured the indentation fracture toughness of their samples by performing Vickers indents, with a variation in data from 7.0 to 8.6 $MPa \cdot m^{0.5}$ depending on the milling time (smaller particles give a smaller toughness).

Warren[186] measured the fracture toughness of WC by Hertzian indentation, i.e. via the generation of conical cracks produced when indenting with a spherical indenter. The carbide was in the form

of sintered samples, with 1-4 μm grain size and negligible porosity. The fracture toughness was evaluated between 6.06 and 6.23 MPa·m$^{0.5}$. The NIST database for structural ceramics (NISTIR 6153) proposes, as a reference, measurements performed on pre-cracked sintered WC specimens (grain size = 6 μm, notched bend bars tested in flexion) by Chermant, Deschanvres and Osterstock[15]. The reported values for the fracture toughness range from 7.5 to 8.9 MPa·m$^{0.5}$.

Fig. 6.20 compares our measurements with these literature data. The data vary over a significant range; however, they are overall mutually consistent, showing that (i) our data make sense in the context of the literature and (ii) there are significant differences in the fracture toughness of these five binary carbides.

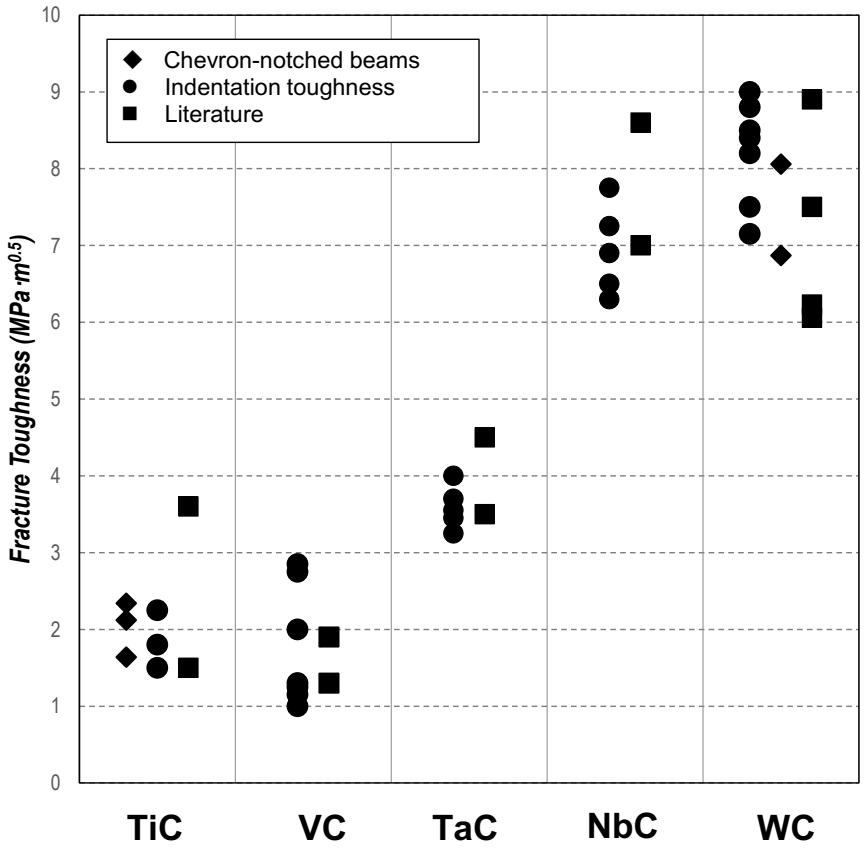

Fig. 6.20 – Comparison between indentation toughness measured on binary carbides and literature data. CHANGED

As a final note, it is important to consider these reference values carefully. Indeed, many data points are actually indentation toughness measurements, with the limitations discussed above. Many sample are also sintered materials, while our particle are dense single crystals. The values measured here can therefore be considered as good estimations of the fracture toughness but are not absolute values of that property. Many samples used in the literature were furthermore sintered materials, while our particle are dense single crystals.

6.3.6 Evolution of the toughness for ternary compositions

In contrast to hardness and elastic modulus, it is much harder to link the fracture toughness to the electronic structure of the crystals. Because fracture toughness is linked with crack propagation and thus the breaking of chemical bonds, parameters such as the bond strength and the bond density are obviously important and the change in composition should play a role; however, because of the anisotropy of fracture toughness and the often non-linear path of the crack, it is difficult to correlate that property with simplified interpretation schemes as were presented for E and H.

On the five graphs presented in Figs. 6.9-13, data points from each indent are plotted separately for all the tested compositions. As seen, for many compositions, the range of values is important and the difference between the maximal and the minimal values can reach 2 $MPa \cdot m^{0.5}$ in several cases. This to be expected for monocrystalline ceramics characterized by anisotropic fracture and cleavage planes. For several compositions, for example $Ti_{54}W_{46}C$ or $Ti_{43}Nb_{57}C$, the measured values seem to be separated into different sub-groups, suggesting indeed that differences between data points have an underlying physical cause, this being likely crystalline anisotropy. SEM observations have unfortunately not enable us to highlight a different orientation of the particles (based on their morphology or grey level) that would correlate with the measured indentation toughness data. For other compositions, however, e.g. $Ti_{75}V_{25}C$ or $Ta_{53}V_{47}C$, all the values are distributed relatively uniformly between the minimum and the maximum, suggesting rather an effect of experimental uncertainty. It is however difficult, if not impossible, to distinguish the error of the indentation method from the anisotropy of the material. A solution would be to mill many differently oriented chevron-notched samples, because such samples can measure accurately the anisotropy of toughness with crack plane and crack path: if we consider $Ti_{81}W_{19}C$, the good agreement coupled with data clustering in both sets around two separate values, indicates indeed that the differences in the indentation values are due to the anisotropy (Fig. 6.19).

In conclusion, the two methods used to measure the fracture toughness and discussed in this chapter present each their advantages and drawbacks. In terms of accuracy, only the chevron-notched beams are able to produce precise results that can be claimed to be unambiguous measurements of a material property; moreover, the method can distinguish the fracture toughness resulting from the fracture of different crystalline planes. By contrast, indentation fracture toughness measurements can only provide an estimation of the fracture toughness of the material; resulting values should not be used as a characteristic value for a given material, but can be useful as a means to compare different materials, or to provide a first approximation of the fracture toughness when no other data are available.

If we now turn to values measured across the spectrum of carbide systems explored here, one finds that this property varies quite differently than do the hardness and indentation modulus: alloying the carbides brings no visible improvement in this property (Table 6.3 and Figs. 6.9 to 6.13). Clearly, the best results are obtained with the two binary carbides WC and NbC, and exception made perhaps for the (Ti,V)C system, alloying does not produce toughness values that exceed those of the tougher among the two terminal carbides of the relevant ternary system (we thus did not explore quaternary carbides).

Figures 6.9 to 6.13 give (on the right-hand ordinate) a rapid comparison of trends observed here with the simple yet often used Pugh criterion, which proposes that brittleness should decrease with decreasing ratio of shear to bulk modulus. This is done here in very approximate fashion by translating this criterion into the ratio of indentation modulus M (a rough measure of variations in the bulk modulus) to the hardness H (a rough measure of shear modulus), which is plotted on the graphs over measured indentation toughness data for the five ternary systems: as seen variations in this parameter do not mimic the data with great accuracy and do not suggest either that great improvements are to be expected from carbide alloying. Rather, what the data show is that in alloyed carbides, the toughness tends to be raised if one alloys a less tough carbide with one that has a higher fracture toughness; notably, alloying TiC or VC with tantalum pulls the fracture toughness up, towards values higher than the rather low values (around 2 MPa$\sqrt{m}$) characteristic of those two carbides. Alloying MC carbides to produce hard and stiff phases is thus, a priori, not expected to be deleterious to their fracture toughness.

CHAPTER 7:

CONCLUSION

DESCRIPTION OF CORRECTIONS BROUGHT TO THE SUBMITTED THESIS VERSION:
Part of this last chapter has been corrected because the conclusion, mostly based on both the high elastic modulus and high hardness that were (erroneously) reported for quaternary carbides, is now only partially valid, given that the corrected hardness measurements proved to be lower.

I changed the hardness values according to the new measurements performed by Dr Léa Deillon; and I redrew the figures.

In this chapter, a summary of the results presented for the elastic modulus, the hardness and the fracture toughness is firstly given. We propose then a main conclusion to this thesis, in regard with the objectives exposed in Chapter 1. In a last part, we discuss potential perspectives for future work in the field of mechanical properties of multimetalllic carbides, as well as for testing small second phases embedded in a soft matrix.

7.1 Review of the results

Although mixed MC carbides constitute a major material in coatings or alloys for the machining industry, little is actually known about their properties. Only binary carbides have been widely investigated since the 60's and their mechanical properties have been measured by several authors, as well as by different methods. When reviewing carbides properties, a first obvious observation is that the mechanical properties are strongly dependent on many parameters, among which porosity and stoichiometry are the most important. Specifically, most of the measured carbide properties are gleaned on sintered samples, which can be produced to have macroscopic dimensions but can constitute poor approximations for monocrystalline carbide particles.

In this work, by generating small carbide particles *in situ* within steel and by using microtesting methods conducted on those particles, we were able to measure directly the mechanical properties, i.e. E, H and fracture toughness, of individual single crystal MC carbides across a wide spectrum of compositions. We applied methods developed in the literature (Oliver & Pharr analysis and indentation fracture toughness) or methods of our own (ultra-low load elastic indentation and triangular chevron-notched cantilever beams) to achieve this goal.

Overall, our data are consistent with literature data for binary carbides, for which the mechanical properties are known, particularly as concerns data gathered on single crystal carbides; this serves as a validation of the measurement methodologies that were used here. We have thus measured the mechanical properties of ternary compositions, with the aim of 1) characterizing the evolution of different mechanical properties with changes in the carbide composition and then filling gaps in mixed carbide knowledge, and 2) exploring whether there are optimal compositions for each system in terms of measured mechanical properties.

It is found in the five ternary systems explored here that the evolution of elastic modulus exhibits no discernable systematic behavior. The hardness evolution is characterized by the presence of a maximum for ternary systems, save for (Nb,Ti)C where values remained roughly constant across intermediate compositions (with a sudden dip at one of the end compositions). The toughness also varies in no systematic fashion while staying between the two binary carbide values at either end of the ternary composition spectrum. Table 7.1 summarizes the evolution of E from spherical indentation and H from the Oliver & Pharr analysis for the five investigated ternary systems.

Table 7.1 – Summary of E and H evolution with composition.
CHANGED

(M,M')C :	(Ti,W)C	(Ti,Nb)C	(Ti,V)C	(Ti,Ta)C	(Ta,V)C
E_{max} (GPa)	703	546	513	506	477
E_{MC} (GPa)	445	445	445	445	454
$E_{M'C}$ (GPa)	703	546	419	454	419
H_{max} (GPa)	36.4	32.1	33.2	33.4	36.1
H_{MC} (GPa)	30.9	30.9	30.9	30.9	31.6
$H_{M'C}$ (GPa)	31.1	25.7	30.4	31.6	30.4
Changes in:					
Lattice parameter	From fcc to hex	+3.5 %	-3.7 %	+3.0 %	-6.5 %
Bonding strength	+2.5 eV	+0.4 eV	-1.0 eV	+1.4 eV	-2.4 eV
VEC	8-10	8-9	8-9	8-9	9

We decided, at the end of the project, to investigate an additional quaternary system, with a goal to determine whether one can further improve the properties of MC carbides in terms of hardness and modulus. Data showed an increase in the elastic modulus but not in hardness. This is illustrated here by plotting the data on a Modulus-Hardness material selection chart for the systems that we investigated, including data for a few other reference materials[11].

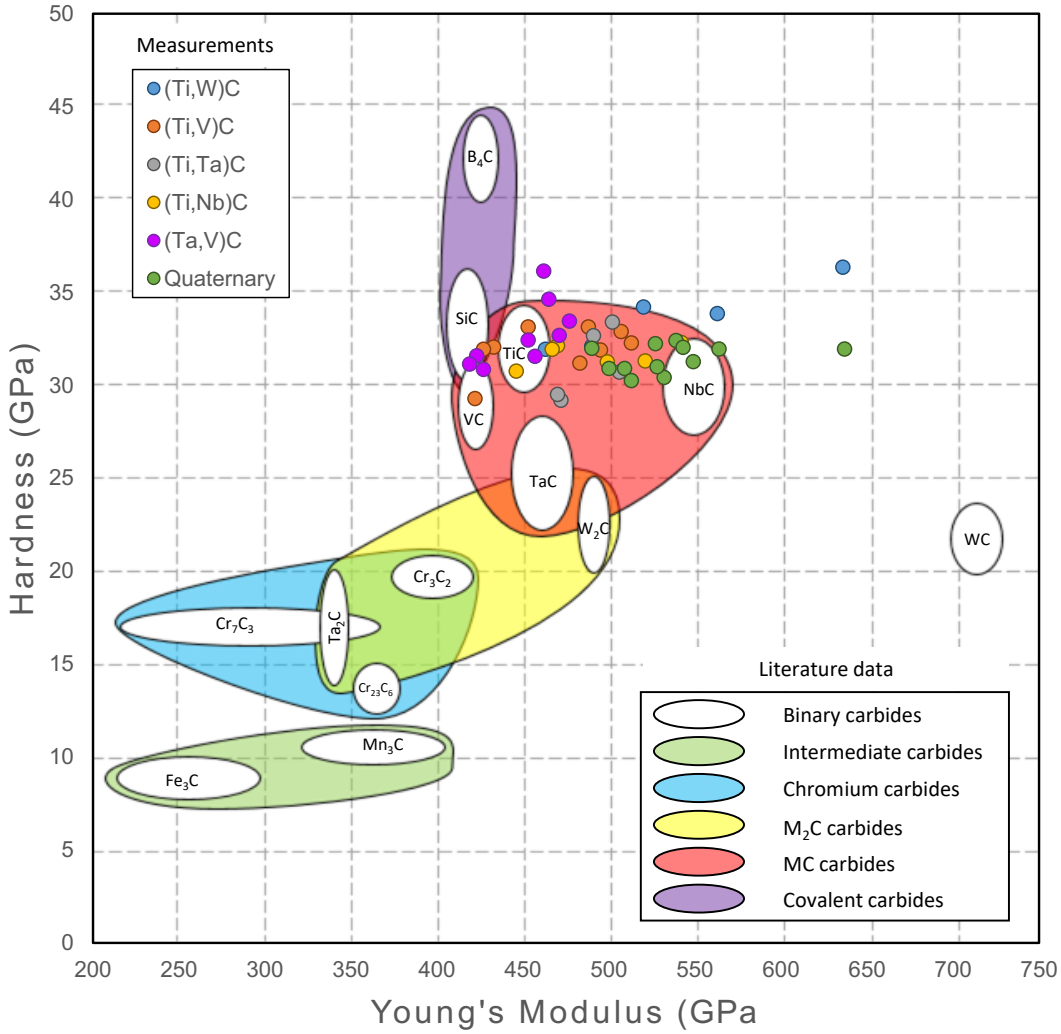

Fig. 7.1 – Hardness – Young's modulus material selection chart for our samples. Small circles denote values measured in this work CHANGED

As seen, compared with the mechanical properties of binary MC carbides, the ternary and quaternary compositions exhibit a significant improvement for the elastic modulus, while the hardness remains at a correct level around 30 GPa.

Fracture toughness measurements, performed both with chevron-notched cantilever beams and by nanoindentation, show that the fracture toughness of ternary compositions remains in the range defined by the values of the two binary carbides forming the bounds of a given system. Measurements vary significantly within the same carbide composition, however, betraying probably lack of precision of indentation toughness measurements, but also a strong influence of anisotropy on the resistance to cracking in those phases. From an engineering standpoint, it emerges that improvements in stiffness and hardness achieved by alloying in transition metal MC carbides do not come with a penalty as concerns their fracture toughness.

7.2 Thesis conclusions

The thesis objectives, described in Chapter 1, were subdivided in three parts:

1. The processing of binary, ternary and quaternary single crystal carbide particles in a steel matrix;
2. The development of testing methodologies to measure the elastic modulus, the hardness and the fracture toughness of those individual particles;
3. The use of those techniques to explore whether alloying of transition metal MC carbides has the potential to improve their mechanical properties.

With respect to these objectives, we can formulate the following general conclusions:

- Binary, ternary and quaternary carbide particles can be produced by reaction of Ti, Ta, V, Nb and/or W powders with cast iron in an arc-melting furnace;
- Both particle composition and morphology can be tuned by applying subsequent heat treatment;
- The Oliver & Pharr analysis for measurement of the elastic modulus derived from indentation is not valid for stiff particles embedded in a compliant matrix: added indenter displacement due to the matrix deformation leads to an underestimated value of the elastic modulus;
- The correction proposed by King for measuring the elastic modulus of thin films deposited on a flat substrate can be extended to ceramic particles embedded in metallic matrix; however, this requires a determination of the local thickness of the particle by a time-consuming FIB process;
- Spherical indentation at ultra-low load is an accurate modulus measurement method, as long as (i) the matrix is not too compliant, (ii) the particles are not too small, (iii) the contact area between the particle and the matrix is big and (iv) data treatment is conducted in a manner that derives appropriate constants over many measurements, so as to eliminate the influence of statistical sources of error;
- The Oliver & Pharr analysis allows to measure accurately the hardness of ceramics, as well as that of ceramic particles embedded in a metallic matrix;
- Chevron-notched triangular cantilever beams provide a novel micro-mechanical test by which one can measure the fracture toughness of brittle ceramic particles embedded in metal. Moreover, it is sensitive to the crystalline orientation of the crack plane and can thus be used to measure fracture toughness anisotropy (via a suitable choice of the notch plane and prior EBSD measurements);
- Indentation fracture toughness provides, with the present MC carbide particles, measurements that are consistent with data gleaned using other methods. The method

is not able to distinguish the effect of the crystal orientation but can provide an interval constituting an acceptable first estimation of the fracture toughness of these phases;

- Ternary carbide compositions explored here, namely (Ti,W)C, (Ti,Nb)C, (Ti,V)C, (Ti,Ta)C and (Ta,V)C show that alloying can bring significant improvements in their basic mechanical properties. Concerning the elastic (indentation and by extension Young's) modulus, the evolution with alloying can be either linear, as found with (Ti,W)C and (Ti,Nb)C, or exhibit a maximum (observed in the remaining three systems);
- With regard to the theory of Jhi et al., the present data show that other parameters than the valence electron concentration are equally important in governing the hardness and stiffness of carbides;
- Finally, quaternary (Ti,Ta,V)C compositions were produced and tested, leading to identify an optimal composition, $Ti_{53}Ta_{34}V_{13}C$, which exhibits a very high elastic modulus (637 GPa); the hardness of quaternary compositions is comparable to that of binary TiC, TaC or VC.

7.3 Perspective for future work

To conclude this thesis, we propose now a few perspectives for future work, in three distinct fields, namely processing, mechanical measurements and atomic bonding theory.

The main processing challenge we had to overcome was a precise control of the carbide composition. Indeed, as explained before, an arc melter is very convenient furnace, able to reach the very high temperatures required to form carbides, but its high cooling rate tends to produce fine and rather metastable microstructures. That feature was an advantage with the (Ti,W)C system, because the metastable compositions produced exhibited interesting mechanical properties; however, if a precise carbide composition must be produced, the technique becomes less attractive. The issue was solved by means of additional post-solidification heat treatments, designed to promote phase transformation progression up to the equilibrium microstructure. Although this method proved to be successful, the maximal weight of the produced samples could not exceed about 2 grams. Although not an intrinsic limitation (bigger arc melter furnaces exist, producing quantities such as 400 t in industrial steel production) sample production methods could be improved towards the production of larger quantities of carbide containing alloys.

The applications for such materials, mainly as cutting tools, suggest pieces with a rather small volume, such as drills or milling cutters, which are traditionally produced by powder metallurgy. In that sense, it could be an interesting challenge to apply new technologies, such as additive manufacturing processes, in particular SLM (selective laser melting), in order to develop alloys containing such carbide reinforcements. The high temperatures involved in the laser heating are sufficient to initiate the chemical reaction of carbide formation, and it could be possible to create such reinforcement *in situ*.

Up to now, WC is by far the most used carbide in cutting tools, mostly in WC-Co cermets. It is made by sintering tungsten and carbon powders at 2000°C, producing WC polycrystals. WC is characterized by a very high elastic modulus, around 700 GPa, but a "poor" hardness of ~20 GPa, in comparison with other carbides. Because hardness is the most important property for cutting

and abrasive applications, it could be very interesting to replace WC by a harder reinforcement, exhibiting an almost equal stiffness. We have shown here that the quaternary (Ti,Ta,V)C carbide system is a good candidate, able to produce compositions with an elastic modulus higher than 600 GPa and a hardness similar to WC. Moreover, the metallic elements involved, Ti, Ta and V are easier to work with, because of their lower melting point in comparison with W. The main limitation could come from the high price of Tantalum and Vanadium; however, given the small dimensions of cutting tools, and the impressive properties of quaternary carbides identified here, performance could by an attractive argument for the use of those carbides in producing extreme quality cutting tools.

The methods that we used in order to measure the mechanical properties of carbide reinforcements allowed us to determine with an acceptable accuracy the elastic modulus, the hardness and, to a lesser degree, the toughness of those phases; however, all the methods have important disadvantages and could be improved.

The nanoindentation method developed here for the measurement of indentation modulus proved to be accurate for MC carbides embedded in steel; however, the method has limitations and is not adapted to test all the combinations of reinforcements and matrices. In particular, it is not accurate for soft or compliant matrices (such as a polymer or even aluminium); in the first case, the matrix yield strength is not sufficient to avoid a plastic deformation of the matrix by the reinforcements (acting as an indenter), and in the second case the measurement error increases with the matrix compliance. Particle morphology plays also an important role; for example, we have never tested spherical reinforcements, which are characterized by a smaller interfacial area with the matrix, and then a higher stress for a given applied load. In summary, the method is not universal and would require improvement in order to measure Young's modulus for a larger variety of particles.

As discussed in Chapter 6, the two fracture toughness measurement methods used here, indentation toughness and chevron-notched beams, provide rather similar values, which are furthermore consistent with the literature. However, it had been proven that indentation toughness can provide erroneous values for several materials or material combinations, especially thin films. The chevron-notched bend beam method is, in that sense, a much better method, which furthermore is able to distinguish between different crystal orientations. The creation of a detailed fracture toughness database for ceramic materials, with data obtained by testing chevron-notched beam, would be a very useful endeavor.

Concerning the quaternary (Ti,Ta,V)C system, we focused on the Ti-Ta rich side of the pseudo-ternary TiC-TaC-VC phase diagram. Because VC has lower properties than TiC and TaC, it was an obvious choice also motivated by the data gleaned for the 3 ternary systems. However, it could be interesting to complete our measurements with V-rich quaternary compositions in order to have a better characterization of the evolution of properties.

The goal of this thesis was to measure three mechanical properties, namely the elastic modulus, the hardness and the fracture toughness. However, we have not determined the strength of such particle reinforcements. It could be an interesting additional measurement, because the main limitation of a composite is due to the fracture of the reinforcements or decohesion with the matrix, limiting then the maximal load that a piece can support before rupture. A very interesting method has been developed for silicon particles by Dr. Martin G. Mueller, a former member of our team, based on the 3-point bending of a trapezoid beam[165], or by breaking C-shape specimen[178]. He proved that silicon defect-free single crystal particles (as found in Al-Si alloys) can be very strong an support load as high as 12 GPa; he also identified which defects were responsible for the premature fracture of other particles. A similar approach would be very meaningful for carbide reinforcements.

The interpretation of both the hardness and the elastic modulus evolution with composition changes is a very interesting topic. On all our graphic representations, we used a polynomial fit as a visual guideline for the evolution with composition; however, it would be much more interesting to be able to predict such behavior. Several models have recently been developed to predict the hardness of covalent crystals[11,14]. For that reason, a more complete model, accounting for the d-orbital structure of MC transition carbides and filling the empty states according to the crystal symmetry as the VEC increases would be able, in theory, to predict the hardness evolution of mixed carbides. Such a work represents however a complex task, because the replacement of an atom of the element M by another atom M' changes simultaneously a large number of parameters, including the density of M-C, M'C, M-M, M'-M' and M-M' bonds, the crystal size and the d-orbital filling. Strong computational capabilities are then required in order to do all the calculations, and DFT could be useful in this situation.

Systematic DFT simulations for all the ternary and quaternary systems, could provide an interesting comparison with the measured data. The few simulations that have been run during the project were in good agreement with the mechanical tests (in the Ti-W-C system). Moreover, in order to understand better the presence of a maximum for all the hardness curves and for several of the elastic modulus evolution with composition, it would be necessary to quantify the effect of VEC, changes in bond strength (identified as the width of the pseudogap in DOS plots) or in crystal sizes, and the occupancy of antibonding states. Again, DFT could be a useful numerical tool to help us investigating deeper that field.

APPENDIX A:

THERMODYNAMICS DATA

In this appendix, we provide more detailed information about the thermodynamics of carbide formation reactions.

Table A.1 – Electronegativity difference of the various carbide forming elements in comparison with carbon.

	χ [-]	$\chi - \chi_C$ [-]	
C	2.55		
B	2.04	0.51	covalent
Si	1.90	0.65	covalent
Cr	1.66	0.89	intermediate
Mn	1.55	1.00	intermediate
Fe	1.83	0.72	intermediate
Co	1.88	0.67	intermediate
Ni	1.91	0.64	intermediate
Ti	1.54	1.01	interstitial
V	1.63	0.92	interstitial
Zr	1.33	1.22	interstitial
Nb	1.60	0.95	interstitial
Mo	1.80	0.75	interstitial
Hf	1.30	1.25	interstitial
Ta	1.50	1.05	interstitial
W	1.70	0.85	interstitial
Al	1.61	0.94	salt-like
Ca	1.00	1.55	salt-like

Table A.2– Gibbs free energy of carbide formation[xxv].

	Reaction	$\Delta G°$ [J·mol^{-1}·K^{-1}]	$T°$ range [K]
B_4C	$4B + C \rightarrow B_4C$	-56819 + 9.1T	298-1173
SiC	$Si + C \rightarrow SiC$	-53430 + 7.0T	298-1683
$Cr_{23}C_6$	$23Cr + 6C \rightarrow Cr_{23}C_6$	-53666 – 12.7T	1100-1250
Cr_7C_3	$7Cr + 3C \rightarrow Cr_7C_3$	-47976 – 12.7T	1100-1250
Cr_3C_2	$3Cr + 2C \rightarrow Cr_3C_2$	-46430 – 9.7T	973-1173
Mn_7C_3	$7Mn + 3C \rightarrow Mn_7C_3$	-11911 – 23.0T	893-990
Fe_3C	$3Fe + C \rightarrow Fe_3C$	-28714 – 27.7T	298-1048
TiC	$Ti + C \rightarrow TiC$	-183050 + 10.0T	298-1683
VC	$V + C \rightarrow VC$	-100834 + 6.3T	1150-1370
V_2C	$2V + C \rightarrow V_2C$	-147273 + 4.2T	1150-1370
NbC	$Nb + C \rightarrow NbC$	-130122 + 1.7T	1180-1370
Nb_2C	$2Nb + C \rightarrow Nb_2C$	-194138 + 4.2T	1180-1370
TaC	$Ta + C \rightarrow TaC$	-146022 + 2.1T	1250-1400
Ta_2C	$2Ta + C \rightarrow Ta_2C$	-196648 + 8.8T	1740-1900
WC	$W + C \rightarrow WC$	-37866 – 6.5T	878-1132
W_2C	$2W + C \rightarrow W_2C$	-30500 – 2.3T	1575-1600

Table A.3– Low temperature thermodynamical constants for transition carbides[xxvi].

	γ [mJ·mol^{-1}·K^{-2}]	T_D [K]
TiC	0.75	614
ZrC	0.75	491
HfC	0.75	436
VC	3.15	659
NbC	2.64	464
TaC	2.80	489
WC	0.79	493

[xxv] L. E. Toth, Transition Metal Carbides and Nitrides, 1971, Academic Press, New York

[xxvi] V.I. Ivashchenko et al., Met. and Mat. Trans., 37A, 2006, 12

Table A.4 – Thermodynamic values at room temperature for transition carbides[xxvii].

	$S^{\circ}_{298} - S^{\circ}_{0}$ [J·mol^{-1}·K^{-1}]	$H^{\circ}_{298} - H^{\circ}_{0}$ [J·mol^{-1}]	$c_{p,298}$ [J·mol^{-1}·K^{-1}]
$Cr_{23}C_6$	26.63	4565.4	27.42
Cr_7C_3	28.81	4930.8	29.99
Cr_3C_2	28.60	5069.4	32.93
TiC	24.32	4628.4	33.93
ZrC	33.30	5854.8	37.88
HfC	39.60	6396.6	37.63
VC	27.76	4951.8	32.42
NbC	35.53	5980.8	36.96
TaC	42.42	6543.6	36.79

Table A.5 – Enthalpies of formation for transition MC and M_2C carbides[xxvii].

	$-\Delta H^{\circ}_{f}$ [kJ·mol^{-1}]
Cr_3C_2	23.10
TiC	185.22
ZrC	197.40
HfC	210.33
VC	102.90
V_2C	69.30
NbC	141.12
Nb_2C	97.86
TaC	143.22
Ta_2C	104.58
WC	40.61
W_2C	26.46

[xxvii] E.K. Storms, "The Refractory Carbides", Academic Press, New York, 1967

Table A.6 – Thermodynamical data of titanium carbide[xxviii].

	T [K]	$H_T^\circ - H_{298}^\circ$ [kJ·mol^{-1}]	S_T° [J·mol^{-1}·K^{-1}]	c_p [J·mol^{-1}·K^{-1}]	ΔG_f [kJ·mol^{-1}]
SOLID	295.15	0.000	24.230	33.818	-180.844
	400	3.802	35.150	40.685	-179.605
	500	8.116	44.757	45.168	-178.441
	600	12.769	53.234	47.645	-177.336
	700	17.609	60.692	49.033	-176.272
	800	22.559	67.300	49.905	-175.226
	900	27.583	73.217	50.570	-174.179
	1000	32.671	78.577	51.179	-173.115
	1100	37.819	83.484	51.795	-172.021
	1200	43.031	88.018	52.446	-170.773
	1300	48.310	92.243	53.145	-169.281
	1400	53.662	96.209	53.894	-167.788
	1500	59.091	99.954	54.690	-166.292
	1600	64.601	103.510	55.529	-164.793
	1700	70.197	106.903	56.405	-163.288
	1800	75.883	110.152	57.316	-161.779
	1900	81.662	113.276	58.255	-160.263
	2000	87.535	116.289	59.221	-158.295
	2100	93.507	119.202	60.209	-156.039
	2200	99.578	122.026	61.216	-153.782
	2300	105.750	124.770	62.241	-151.530
	2400	112.026	127.441	63.282	-149.286
	2500	118.407	130.045	64.336	-147.053
	2600	124.894	132.589	65.402	-144.835
	2700	131.488	135.078	66.478	-142.636
	2800	138.190	137.515	67.564	-140.458
	2900	145.001	139.905	68.659	-138.304
	3000	151.922	142.251	69.761	-136.178
	3100	158.953	144.557	70.869	-134.080
	3200	166.096	146.824	71.983	-132.015
	3290	172.619	148.835	72.989	-130.185
LIQUID	3290	243.747	170.454	62.760	-130.185
	3400	250.651	172.518	62.760	-130.348
	3500	256.927	174.337	62.760	-130.501

[xxviii] Ihsan Barin, Thermochemical data of pure substances, Part II, VCH, 1993, New York, p.1528

Table A.7 – Thermodynamical data of vanadium carbide[xxix].

	T [K]	$H_T^\circ - H_{298}^\circ$ [kJ·mol^{-1}]	S_T° [J·mol^{-1}·K^{-1}]	c_p [J·mol^{-1}·K^{-1}]	ΔG_f [kJ·mol^{-1}]
SOLID	295.15	0.000	25.104	31.966	-99.030
	400	3.660	35.613	39.078	-98.138
	500	7.780	44.790	43.034	-97.317
	600	12.227	52.891	45.777	-96.558
	700	16.915	60.114	47.913	-95.857
	800	21.798	66.631	49.697	-95.207
	900	26.847	72.576	51.249	-94.601
	1000	32.042	78.049	52.635	-94.034
	1100	37.370	83.125	53.890	-93.498
	1200	42.817	87.864	55.037	-92.988
	1300	48.374	92.311	56.089	-92.498
	1400	54.032	96.504	57.055	-92.023
	1500	59.782	100.471	57.941	-91.556
	1600	65.617	104.237	58.751	-91.093
	1700	71.530	107.821	59.490	-90.629

[xxix] Ihsan Barin, Thermochemical data of pure substances, Part II, VCH, 1993, New York, p.1620

Table A.8 – Thermodynamical data of tantalum carbide[xxx].

	T [K]	$H_T^\circ - H_{298}^\circ$ [kJ·mol^{-1}]	S_T° [J·mol^{-1}·K^{-1}]	c_p [J·mol^{-1}·K^{-1}]	ΔG_f [kJ·mol^{-1}]
SOLID	295.15	0.000	42.384	36.789	-142.647
	400	4.018	53.943	41.665	-142.203
	500	8.339	63.572	44.529	-141.858
	600	12.893	71.870	46.449	-141.586
	700	17.613	79.143	47.888	-141.366
	800	22.462	85.617	49.075	-141.182
	900	27.423	91.458	50.105	-141.027
	1000	32.481	96.786	51.048	-140.896
	1100	37.630	101.694	51.939	-140.784
	1200	42.867	106.250	52.795	-140.691
	1300	48.189	110.509	53.627	-140.615
	1400	53.592	114.513	54.440	-140.555
	1500	59.076	118.296	55.240	-140.512
	1600	64.640	121.886	56.030	-140.485
	1700	70.282	125.307	56.812	-140.475
	1800	76.002	128.576	57.588	-140.482
	1900	81.799	131.710	58.359	-140.506
	2000	87.674	134.723	59.126	-140.548
	2100	93.624	137.626	59.890	-140.607
	2200	99.652	140.430	60.652	-140.683
	2300	105.755	143.143	61.411	-140.775
	2400	111.934	145.773	62.168	-140.883
	2500	118.188	148.326	62.924	-141.007
	2600	124.518	150.808	63.679	-141.145
	2700	130.924	153.226	64.432	-141.298
	2800	137.405	155.583	65.185	-141.463
	2900	143.961	157.883	65.936	-141.639
	3000	150.592	160.131	66.687	-141.823
	3100	157.298	162.330	67.438	-142.013
	3200	164.080	164.483	68.187	-142.205
	3300	170.936	166.593	68.937	-142.266
	3400	177.867	168.662	69.685	-141.488
	3500	184.873	170.693	70.434	-140.717

[xxx] Ihsan Barin, Thermochemical data of pure substances, Part II, VCH, 1993, New York, p.1447

Table A.9 – Thermodynamical data of niobium carbide[xxxi].

	T [K]	$H_T^\circ - H_{298}^\circ$ [kJ·mol^{-1}]	S_T° [J·mol^{-1}·K^{-1}]	c_p [J·mol^{-1}·K^{-1}]	ΔG_f [kJ·mol^{-1}]
SOLID	295.15	0.000	35.401	36.858	-136.890
	400	4.054	47.060	42.092	-136.269
	500	8.412	56.773	44.840	-135.777
	600	12.992	65.119	46.663	-135.371
	700	17.730	72.420	48.050	-135.024
	800	22.594	78.913	49.204	-134.718
	900	27.566	54.769	50.223	-134.440
	1000	32.636	90.109	51.158	-134.183
	1100	37.796	95.027	52.038	-133.943
	1200	43.042	99.591	52.880	-133.717
	1300	48.371	103.856	53.697	-133.502
	1400	53.781	107.865	54.494	-133.298
	1500	59.270	111.651	55.277	-133.103
	1600	64.836	115.243	56.049	-132.918
	1700	70.479	118.664	56.813	-132.743
	1800	76.198	121.933	57.570	-132.578

[xxxi] Ihsan Barin, Thermochemical data of pure substances, Part II, VCH, 1993, New York, p.1017

Table A.10 – Thermodynamical data of tungsten carbide[xxxii].

	T [K]	$H_T^\circ - H_{298}^\circ$ [kJ·mol^{-1}]	S_T° [J·mol^{-1}·K^{-1}]	c_p [J·mol^{-1}·K^{-1}]	ΔG_f [kJ·mol^{-1}]
SOLID	295.15	0.000	32.384	35.378	-38.372
	400	3.916	43.645	40.843	-37.810
	500	8.156	53.093	43.711	-37.355
	600	12.627	61.240	45.601	-36.975
	700	17.261	68.380	47.019	-36.644
	800	22.022	74.736	48.175	-36.346
	900	26.890	80.469	49.170	-36.068
	1000	31.852	85.696	50.059	-35.805
	1100	36.899	90.506	50.870	-35.551
	1200	42.024	94.965	51.621	-35.304
	1300	47.222	99.125	52.325	-35.060
	1400	52.488	103.027	52.989	-34.818
	1500	57.819	106.705	53.618	-34.578
	1600	63.211	110.184	54.215	-34.337
	1700	68.661	113.488	54.784	-34.096
	1800	74.167	116.635	55.325	-33.855
	1900	79.725	119.640	55.840	-33.612
	2000	85.334	122.517	56.331	-33.367
	2100	90.990	125.277	56.797	-33.120
	2200	96.692	127.929	57.241	-32.870
	2300	102.438	130.483	57.661	-32.616
	2400	108.224	132.946	58.059	-32.359
	2500	114.049	135.323	58.435	-32.098

[xxxii] Ihsan Barin, Thermochemical data of pure substances, Part II, VCH, 1993, New York, p.1642

APPENDIX B:

CONTACT MECHANICS

In this appendix, we give the equations for elastic indentation stress fields corresponding to various indenters. All the equations come from the book of A.C. Fischer-Cripps, "Contact Mechanics", second edition, Springer, 2007, New York.

B.1 Point contact

The stresses within a solid material loaded by a point contact have been calculated initially by Boussinesq; in cylindrical coordinates, they can be written as:

$$\sigma_r(r,\theta,z) = \frac{P}{2\pi}\left[(1-2\nu)\left[\frac{1}{r^2} - \frac{z}{r^2(r^2+z^2)^{\frac{1}{2}}}\right] - \frac{3r^2 z}{(r^2+z^2)^{\frac{5}{2}}}\right]$$

$$\sigma_\theta(r,\theta,z) = \frac{P}{2\pi}(1-2\nu)\left[-\frac{1}{r^2} - \frac{z}{r^2(r^2+z^2)^{\frac{1}{2}}} + \frac{z}{(r^2+z^2)^{\frac{3}{2}}}\right]$$

$$\sigma_z(r,\theta,z) = -\frac{3P}{2\pi}\frac{z^3}{(r^2+z^2)^{\frac{5}{2}}}$$

$$\tau_{rz}(r,\theta,z) = -\frac{3P}{2\pi}\frac{rz^2}{(r^2+z^2)^{\frac{5}{2}}}$$

Eq. B.1

The surface stresses (z = 0) are:

$$\sigma_r(r,\theta,z=0) = (1-2\nu)\frac{P}{2\pi r^2}$$

$$\sigma_\theta(r,\theta,z=0) = -(1-2\nu)\frac{P}{2\pi r^2}$$

$$\sigma_z(r,\theta,z=0) = 0$$

$$\tau_{rz}(r,\theta,z=0) = 0$$

Eq. B.2

Stress trajectories and isostress lines for Boussinesq "point load" are given in Fig. B.1:

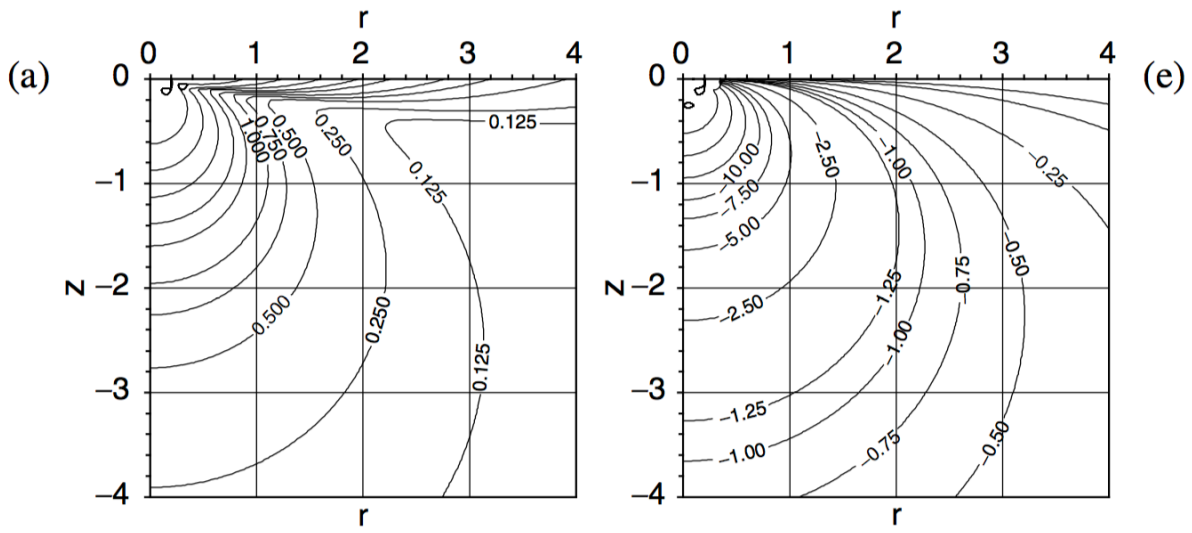

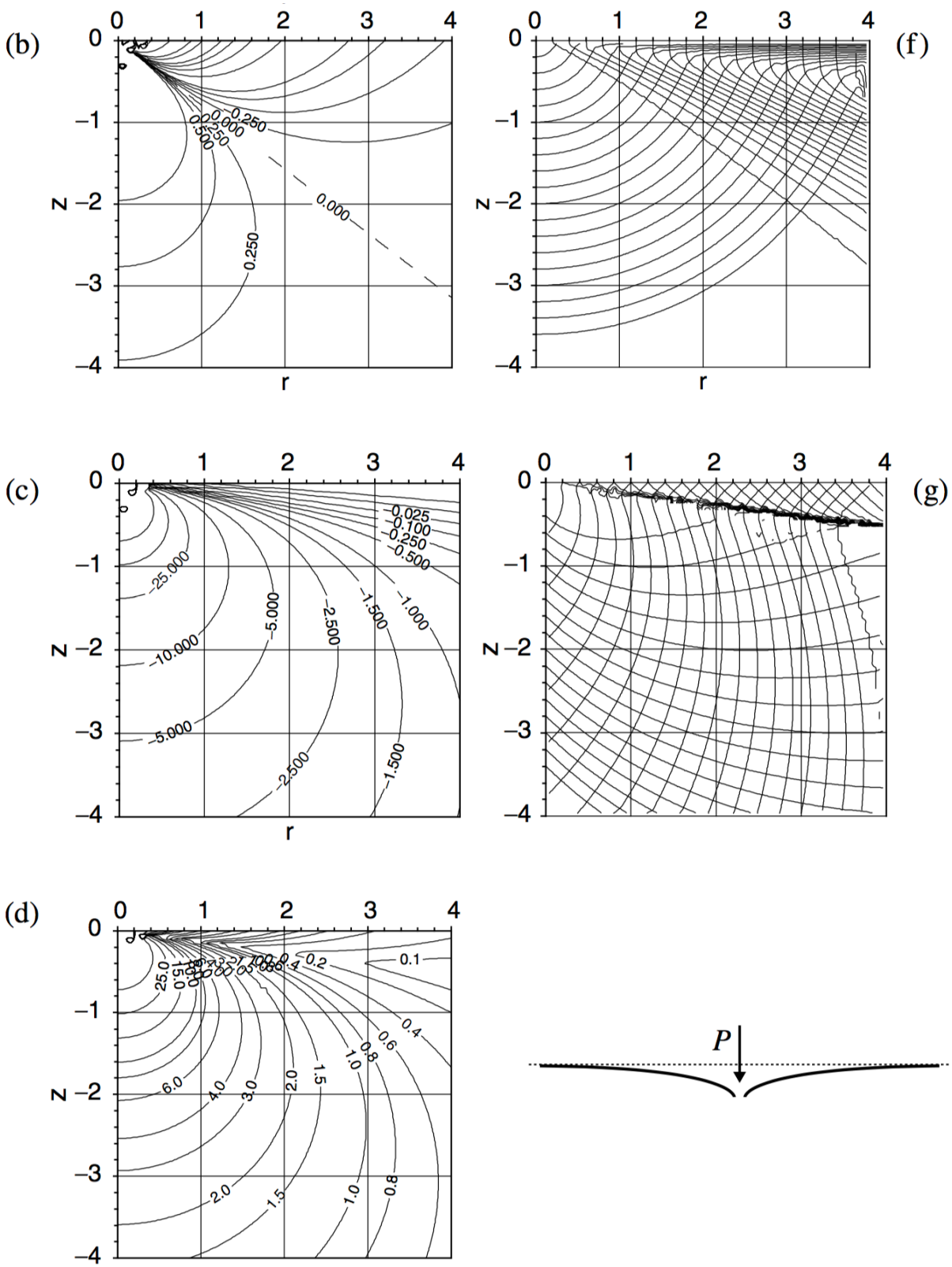

Fig. B.1 – Stress trajectories and iso-stress lines (in MPa) for Boussinesq "point load" configuration (P = 100 N and ν = 0.26); r and z in mm; a) σ_1; b) σ_2; c) σ_3; d) τ_{max}; e) hydrostatic stress; f) σ_1 and σ_3 trajectories; g) τ_{max} trajectories.

B.2 Spherical indenter

The stresses within a solid material loaded by a spherical indenter are:

$$\frac{\sigma_r(r,\theta,z)}{p_m} = \frac{3}{2}\left\{\frac{1-2\nu}{3}\frac{a^2}{r^2}\left[1-\left(\frac{z}{\sqrt{u}}\right)^3\right]+\left(\frac{z}{\sqrt{u}}\right)^3\frac{a^2u}{u^2+a^2z^2} + \frac{z}{\sqrt{u}}\left[u\frac{1-\nu}{a^2+u}+(1+\nu)\frac{\sqrt{u}}{a}arctan\left(\frac{a}{\sqrt{u}}\right)-2\right]\right\}$$

$$\frac{\sigma_\theta(r,\theta,z)}{p_m} = -\frac{3}{2}\left\{\frac{1-2\nu}{3}\frac{a^2}{r^2}\left[1-\left(\frac{z}{\sqrt{u}}\right)^3\right] + \frac{z}{\sqrt{u}}\left[2\nu+u\frac{1-\nu}{a^2+u}-(1+\nu)\frac{\sqrt{u}}{a}arctan\left(\frac{a}{\sqrt{u}}\right)\right]\right\}$$

$$\frac{\sigma_z(r,\theta,z)}{p_m} = -\frac{3}{2}\left(\frac{z}{\sqrt{u}}\right)^3\left(\frac{a^2u}{u^2+a^2z^2}\right)$$

$$\frac{\tau_{rz}(r,\theta,z)}{p_m} = -\frac{3}{2}\left(\frac{rz^2}{u^2+a^2z^2}\right)\left(\frac{a^2\sqrt{u}}{a^2+u}\right)$$

$$u = \frac{1}{2}\left[(r^2+z^2-a^2)+\sqrt{(r^2+z^2-a^2)^2+4a^2z^2}\right]$$

Eq. B.3

The surface stresses (z = 0) are:

$$\frac{\sigma_r(r,\theta,z=0)}{p_m} = \frac{1-2\nu}{2}\frac{a^2}{r^2}$$

$$\frac{\sigma_\theta(r,\theta,z=0)}{p_m} = -\frac{1-2\nu}{2}\frac{a^2}{r^2}$$

$$\frac{\sigma_z(r,\theta,z=0)}{p_m} = 0$$

$$\frac{\tau_{rz}(r,\theta,z=0)}{p_m} = 0$$

$$u_{z=0} = r^2 - a^2$$

Eq. B.4

Stress trajectories and isostress lines for spherical indentation are given in Fig. B.2:

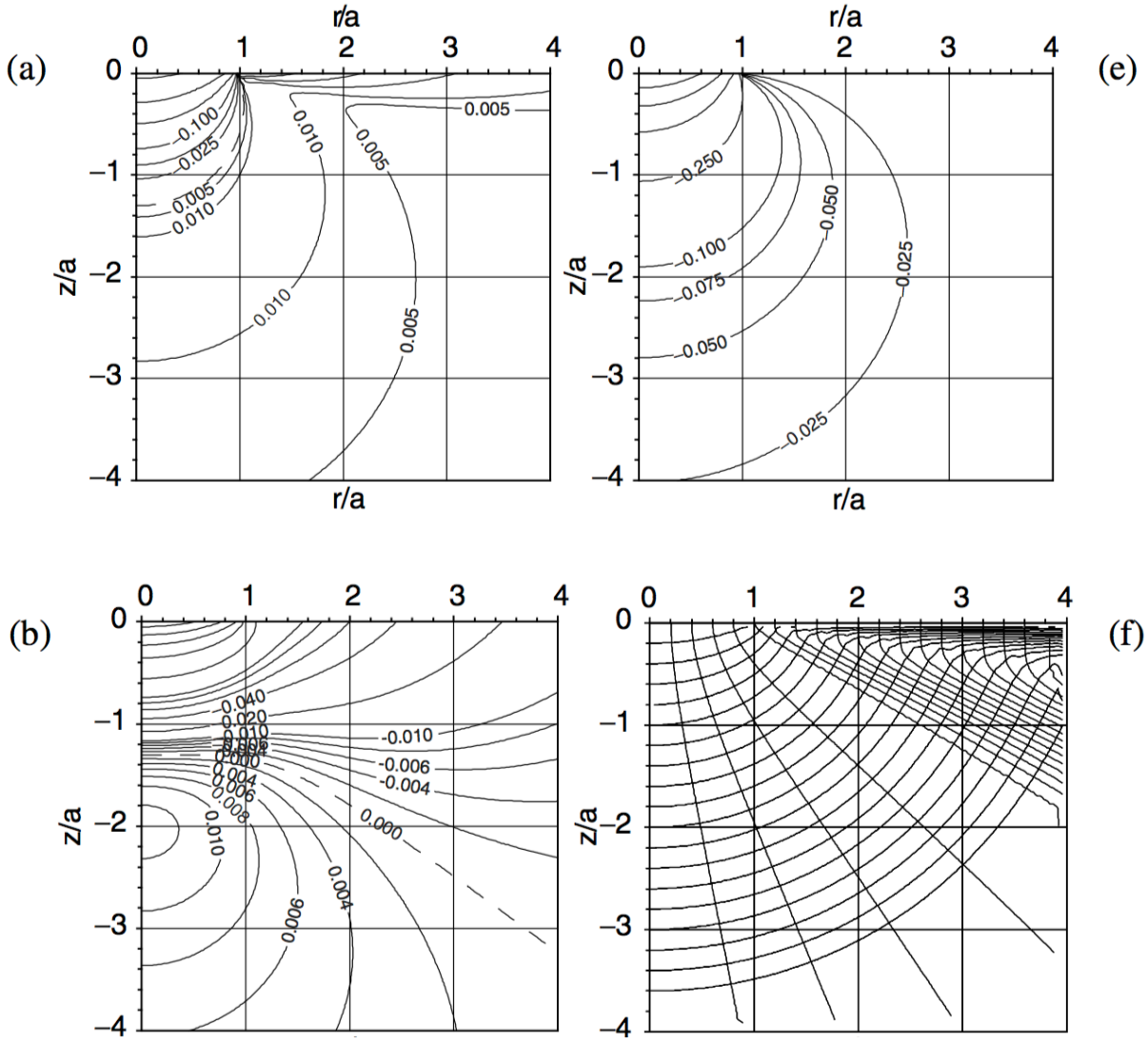

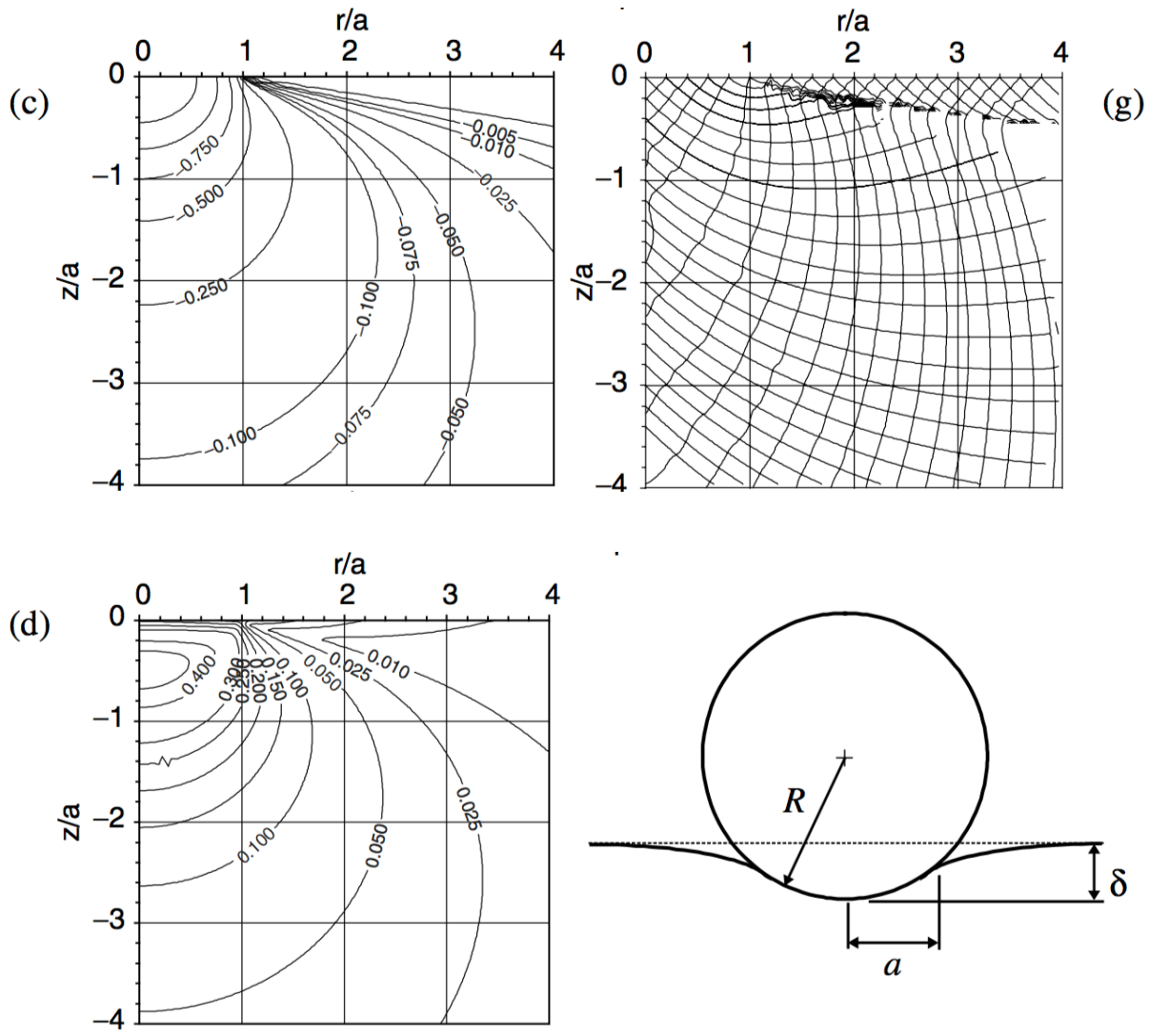

Fig. B.2 – Stress trajectories and iso-stress lines (in p_m) for spherical indentation configuration $\nu = 0.26$); r and z in mm; a) σ_1; b) σ_2; c) σ_3; d) τ_{max}; e) hydrostatic stress; f) σ_1 and σ_3 trajectories; g) τ_{max} trajectories.

B.3 Flat punch indenter

The stresses within a solid material loaded by a flat punch indenter are:

$$\frac{\sigma_r(r,\theta,z)}{p_m} = -\frac{1}{2}\left[J_{01} - \frac{z}{a}J_{02} - (1-2\nu)\frac{a}{r}J_{10} + \frac{z}{r}J_{11}\right]$$

$$\frac{\sigma_\theta(r,\theta,z)}{p_m} = -\frac{1}{2}\left[2\nu J_{01} + (1-2\nu)\frac{a}{r}J_{10} - \frac{z}{r}J_{11}\right]$$

$$\frac{\sigma_z(r,\theta,z)}{p_m} = -\frac{1}{2}\left[J_{01} + \frac{z}{a}J_{02}\right]$$

$$\frac{\tau_{rz}(r,\theta,z)}{p_m} = -\frac{1}{2}\frac{z}{a}J_{12}$$

$$J_{ii} = \begin{pmatrix} 0 & \sqrt{R}\,sin\left(\frac{\phi}{2}\right) & \sqrt{1+\frac{z^2}{a^2}}R^{-\frac{3}{2}}sin\left(\frac{3\phi}{2}-\theta\right) \\ \frac{a}{r}\left(1-\sqrt{R}\,sin\left(\frac{\phi}{2}\right)\right) & \sqrt{1+\frac{z^2}{a^2}}\frac{a}{r}R^{-\frac{1}{2}}sin\left(\theta-\frac{\phi}{2}\right) & \frac{r}{a}R^{-\frac{3}{2}}sin\left(\frac{3\phi}{2}\right) \end{pmatrix}$$

$$R = \sqrt{\left[\frac{r^2}{a^2}+\frac{z^2}{a^2}-1\right]^2 + 4\frac{z^2}{a^2}}$$

$$tan\,\phi = 2\frac{z}{a}\left[\frac{r^2}{a^2}+\frac{z^2}{a^2}-1\right]^{-1}$$

$$tan\,\theta = \frac{a}{z}$$

Eq. B.5

The surface stresses (z = 0) are:

$$\frac{\sigma_r(r,\theta,z=0)}{p_m} = -\frac{1}{2}\left[J_{01} - (1-2\nu)\frac{a}{r}J_{10}\right]$$

$$\frac{\sigma_\theta(r,\theta,z=0)}{p_m} == -\frac{1}{2}\left[2\nu J_{01} + (1-2\nu)\frac{a}{r}J_{10}\right]$$

$$\frac{\sigma_z(r,\theta,z=0)}{p_m} = -\frac{1}{2}J_{01}$$

$$\frac{\tau_{rz}(r,\theta,z=0)}{p_m} = 0$$

$$J_{ii,z=0} = \begin{pmatrix} 0 & \sqrt{R}\,sin\left(\frac{\phi}{2}\right) & R^{-\frac{3}{2}} sin\left(\frac{3\phi}{2} - \theta\right) \\ \frac{a}{r}\left(1 - \sqrt{R}\,sin\left(\frac{\phi}{2}\right)\right) & \frac{a}{r} R^{-\frac{1}{2}} sin\left(\theta - \frac{\phi}{2}\right) & \frac{r}{a} R^{-\frac{3}{2}} sin\left(\frac{3\phi}{2}\right) \end{pmatrix}$$

$$R_{z=0} = \frac{r^2}{a^2} - 1$$

Eq. B.6

Stress trajectories and isostress lines for flat punch indentation are given in Fig. B.3:

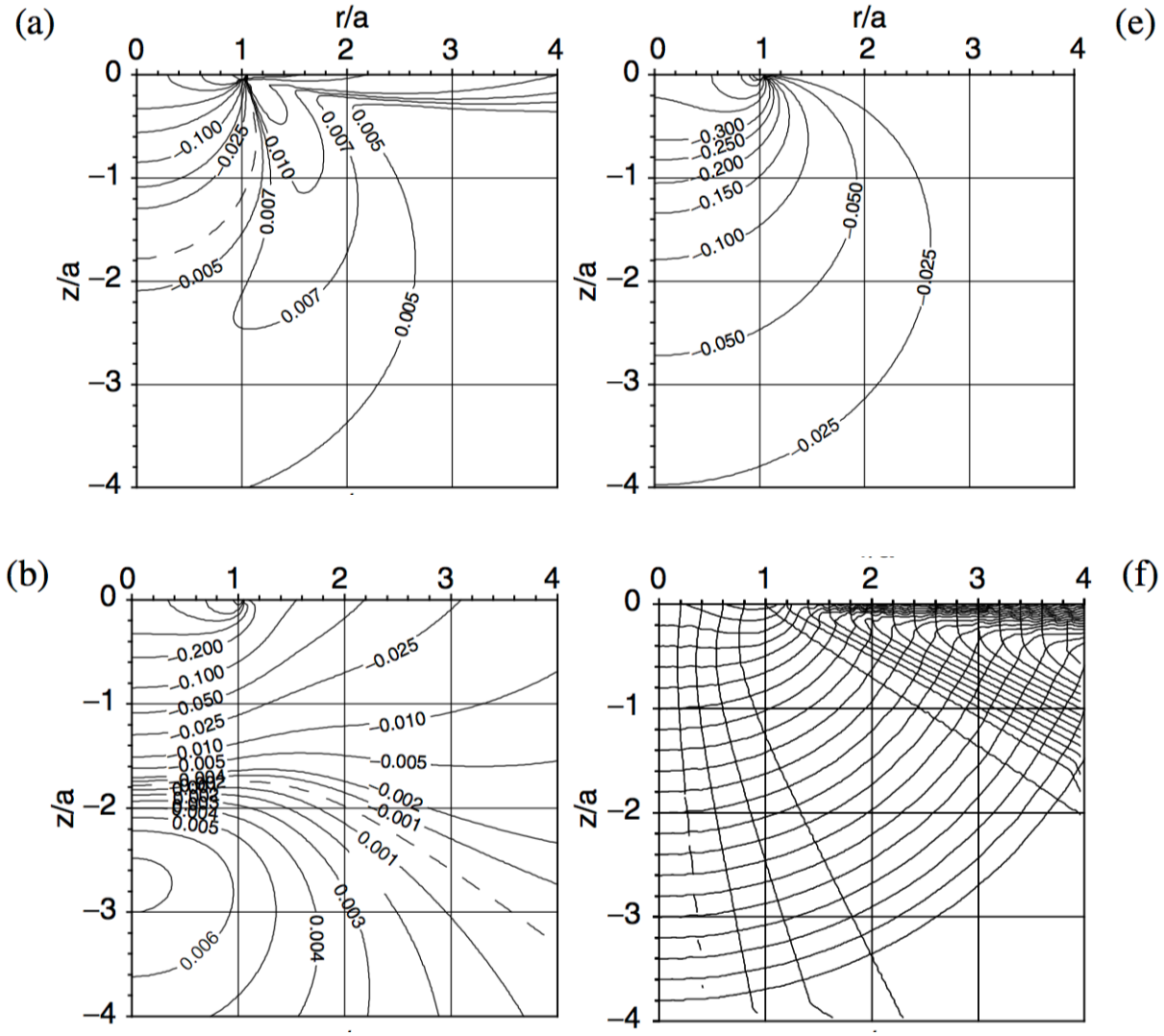

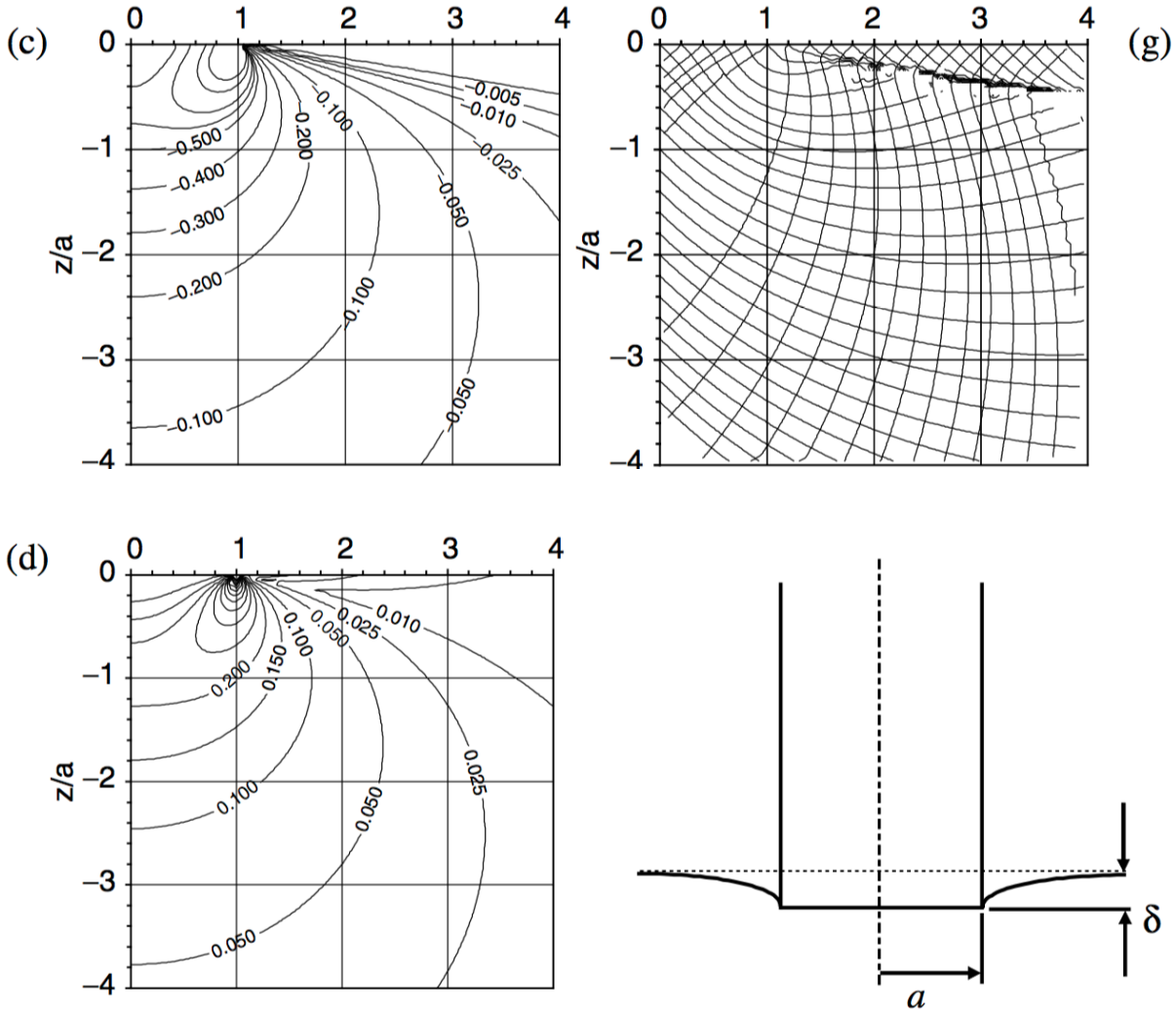

Fig. B.3 – Stress trajectories and iso-stress lines (in p_m) for flat punch indentation configuration $\nu = 0.26$); r and z in mm; a) σ_1; b) σ_2; c) σ_3; d) τ_{max}; e) hydrostatic stress; f) σ_1 and σ_3 trajectories; g) τ_{max} trajectories.

B.4 Conical indenter

The stresses within a solid material loaded by a conical indenter are:

$$\frac{\sigma_\theta(r,\theta,z)}{p_m} = -\left[2\nu J_{01} + (1-2\nu)\frac{a}{r}J_{10} - \frac{z}{a}J_{11}\right]$$

$$\frac{\sigma_z(r,\theta,z)}{p_m} = -\left[J_{01} + \frac{z}{a}J_{02}\right]$$

$$\frac{\sigma_r(r,\theta,z)}{p_m} = -2(1+\nu)J_{01} - \left(\frac{\sigma_z}{p_m} + \frac{\sigma_\theta}{p_m}\right)$$

$$\frac{\tau_{rz}(r,\theta,z)}{p_m} = -\frac{z}{a}J_{12}$$

$$J_{02} = \left(\frac{r^2}{a^2} + \frac{z^2}{a^2}\right)^{-\frac{1}{2}} - \frac{cos\,\phi}{R}$$

$$J_{11} = \frac{a}{r}\left[\sqrt{\frac{r^2}{a^2} + \frac{z^2}{a^2}} - R\,cos\,\phi\right]$$

$$J_{12} = \frac{a}{r}\left[\frac{\sqrt{1+\frac{z^2}{a^2}}}{R}cos(\theta-\phi) - \frac{z}{a}\sqrt{\frac{r^2}{a^2}+\frac{z^2}{a^2}}\right]$$

$$J_{01} = \frac{1}{2}ln\left[R^2 + 2R\sqrt{1+\frac{z^2}{a^2}}cos(\theta-\phi\,) + 1 + \frac{z^2}{a^2}\right]$$

$$J_{10} = \frac{1}{2}\left[\frac{r}{a}J_{01} + \frac{a}{r}(1 - R\,sin\,\phi) - \frac{z}{a}J_{11}\right]$$

$$R = \sqrt[4]{\left[\frac{r^2}{a^2} + \frac{z^2}{a^2} - 1\right]^2 + 4\frac{z^2}{a^2}}$$

$$tan\,2\phi = 2\frac{z}{a}\left[\frac{r^2}{a^2} + \frac{z^2}{a^2} - 1\right]^{-1}$$

$$tan\,\theta = \frac{a}{z}$$

Eq. B.7

The surface stresses (z = 0) are:

$$\frac{\sigma_\theta(r,\theta,z=0)}{p_m} = -\left[2\nu J_{01} + (1-2\nu)\frac{a}{r}J_{10}\right]$$

$$\frac{\sigma_z(r,\theta,z=0)}{p_m} = -J_{01}$$

$$\frac{\sigma_r(r,\theta,z=0)}{p_m} = -J_{01} + (1-2\nu)\frac{a}{r}J_{10}$$

$$\frac{\tau_{rz}(r,\theta,z=0)}{p_m} = 0$$

$$J_{02,z=0} = \frac{a}{r} - \frac{cos\,\phi}{R}$$

$$J_{11,z=0} = 1 - \frac{a}{r}R\,cos\,\phi$$

$$J_{12,z=0} = \frac{1}{R}\frac{a}{r}cos(\theta-\phi)$$

$$J_{01,z=0} = \frac{1}{2}ln[R^2 + 2R\,cos(\theta-\phi\,) + 1]$$

$$J_{10,z=0} = \frac{1}{2}\left[\frac{r}{a}J_{01} + \frac{a}{r}(1 - R\,sin\,\phi)\right]$$

$$R_{z=0} = \sqrt{\frac{r^2}{a^2} - 1}$$

Eq. B.8

Stress trajectories and isostress lines for conical indentation are given in Fig. B.4:

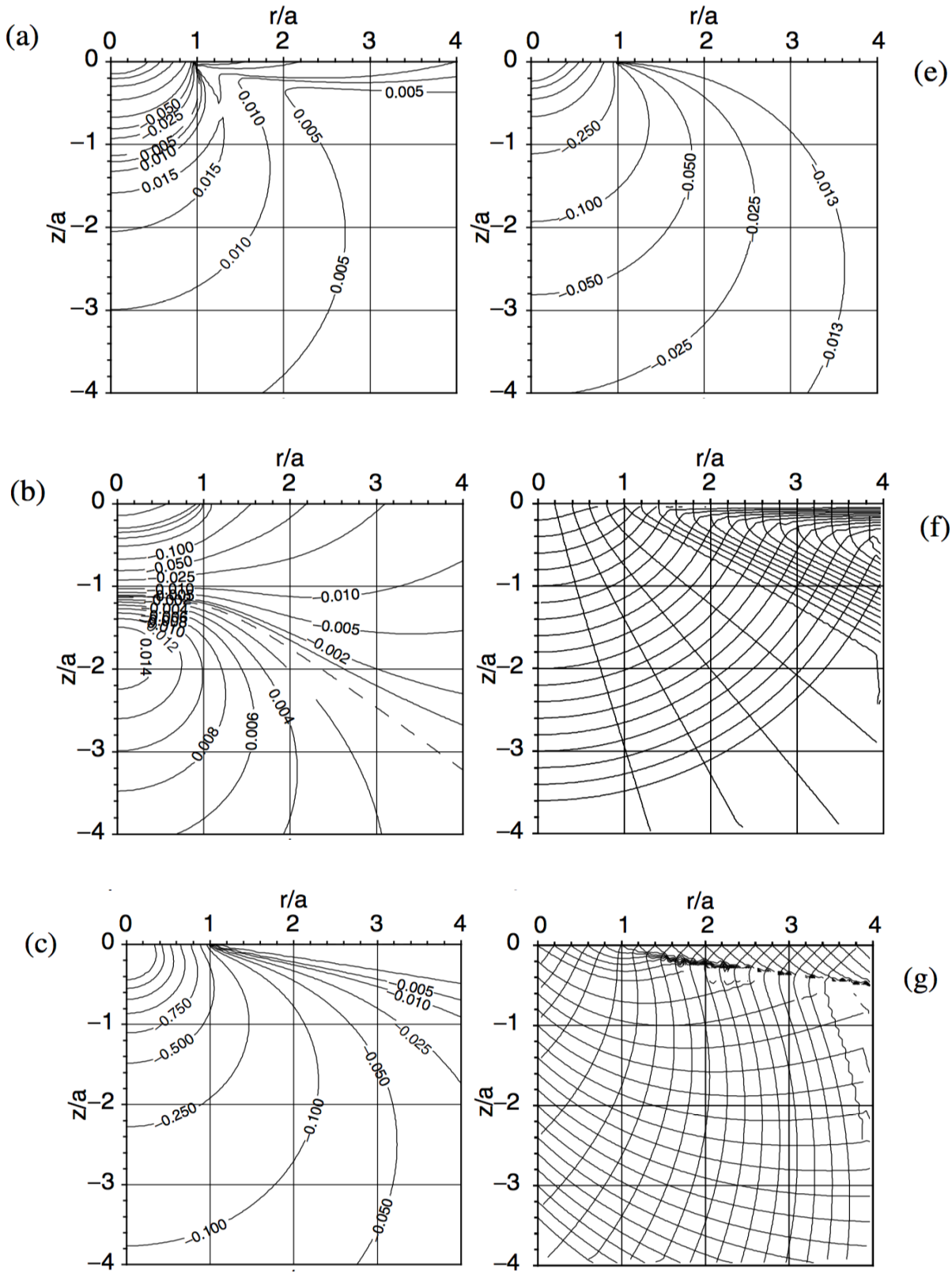
(a)
(b)
(c)
(e)
(f)
(g)
r/a
z/a
0
1
2
3
4
−1
−2
−3
−4
0.005
0.010
0.015
0.050
0.025
0.100
0.250
0.013
0.002
0.004
0.006
0.008
0.012
0.014
0.750
0.500

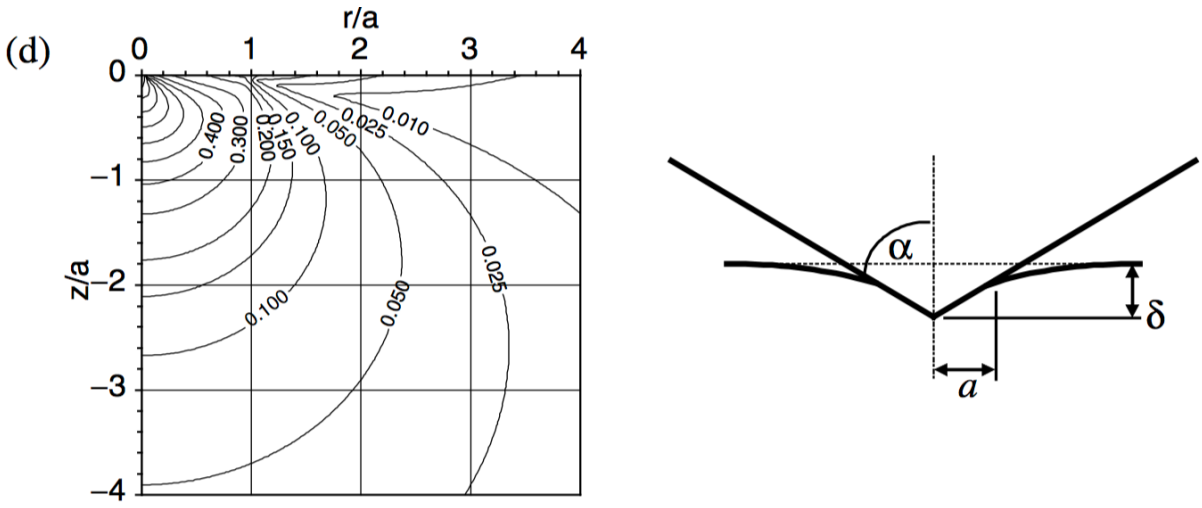

Fig. B.4 – Stress trajectories and iso-stress lines (in p_m) for conical indentation configuration $\nu = 0.26$); r and z in mm; a) σ_1; b) σ_2; c) σ_3; d) τ_{max}; e) hydrostatic stress; f) σ_1 and σ_3 trajectories; g) τ_{max} trajectories.

APPENDIX C:

EDX & XRD ANALYSES

In this appendix, we provide XRD and EDX spectra measured on binary and ternary carbide samples.

C.1 Binary MC carbides

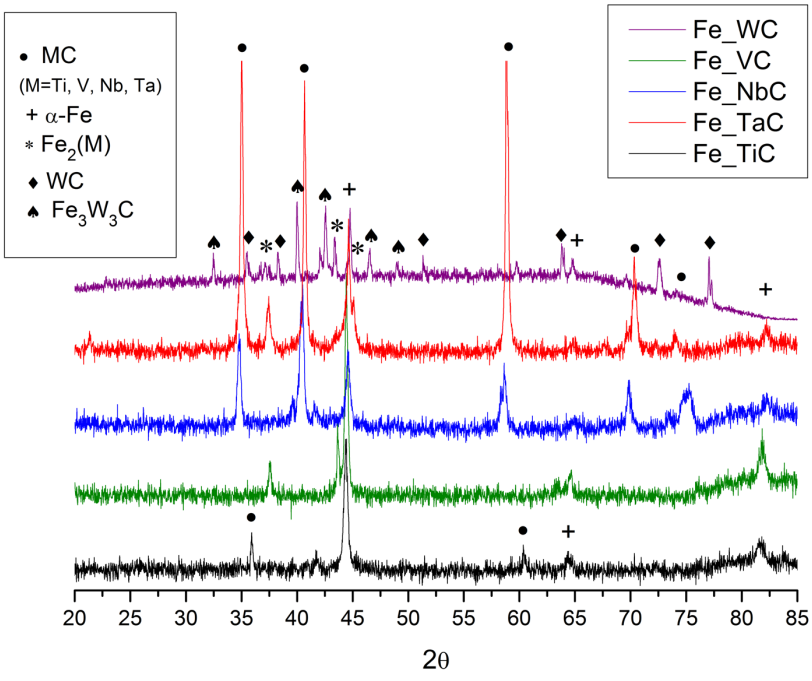

Fig. C.1 – XRD analysis of WC, VC, NbC, TaC and TiC binary carbides.

C.2 (Ti,W)C ternary system

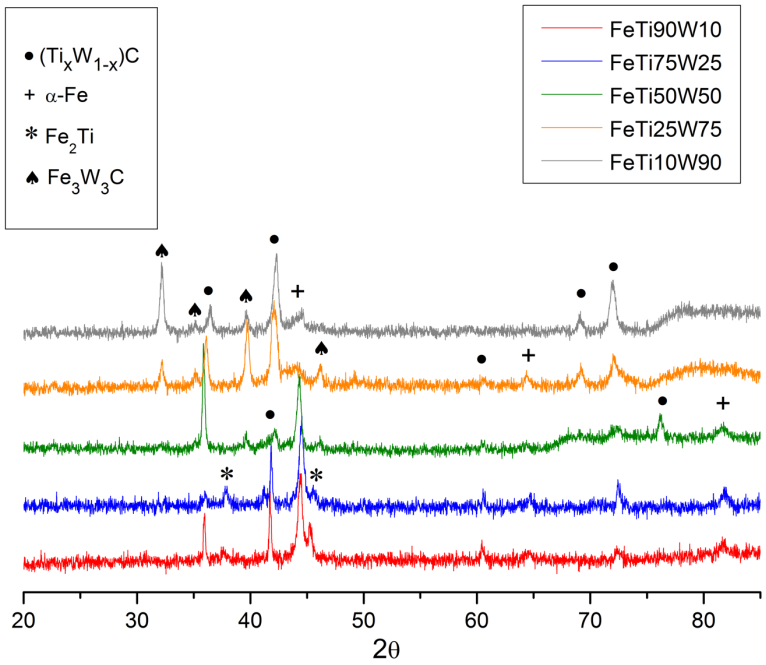

Fig. C.2 – XRD analysis of different ternary carbide of the (Ti,W)C ternary system.

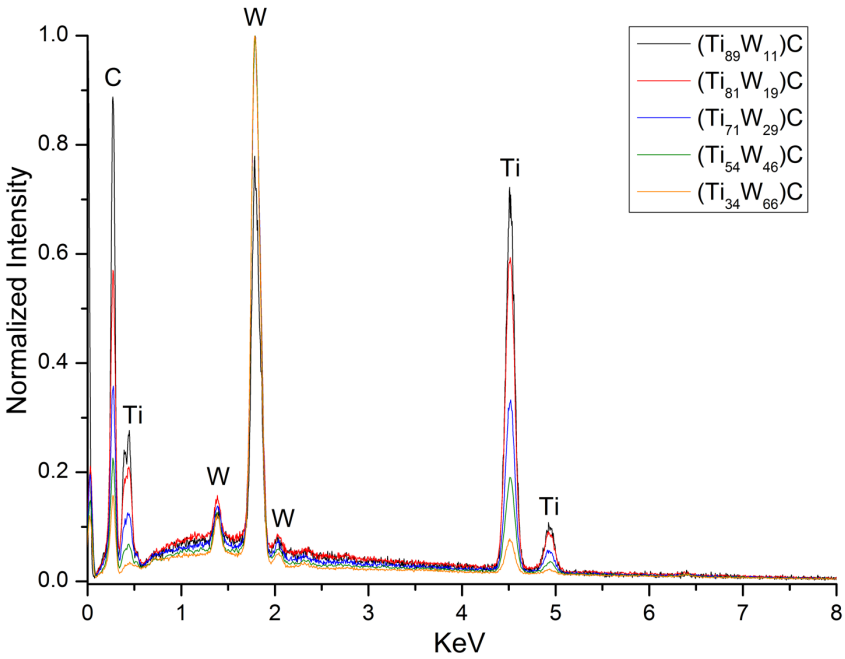

Fig. C.3 – EDX analysis of different ternary carbide of the (Ti,W)C ternary system.

C.3 (Ti,V)C ternary system

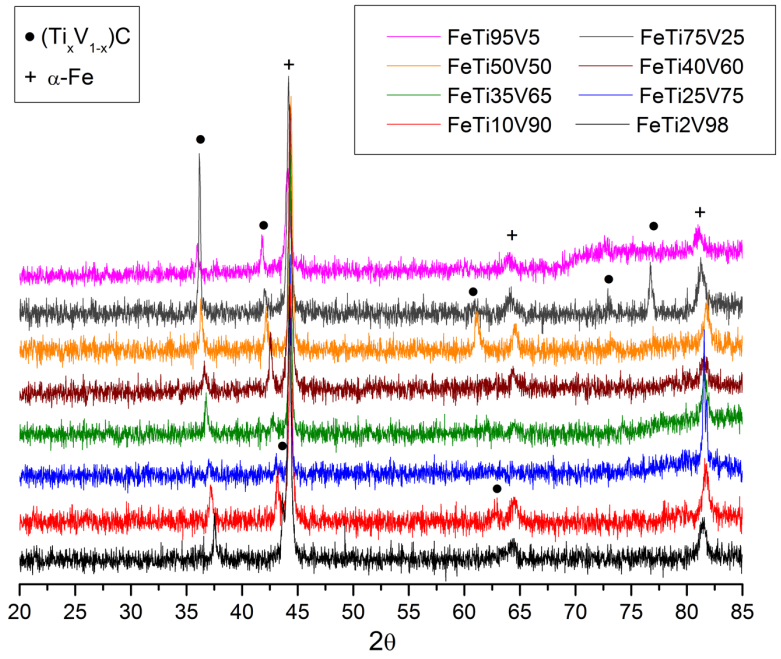

Fig. C.4 – XRD analysis of different ternary carbide of the (Ti,V)C ternary system.

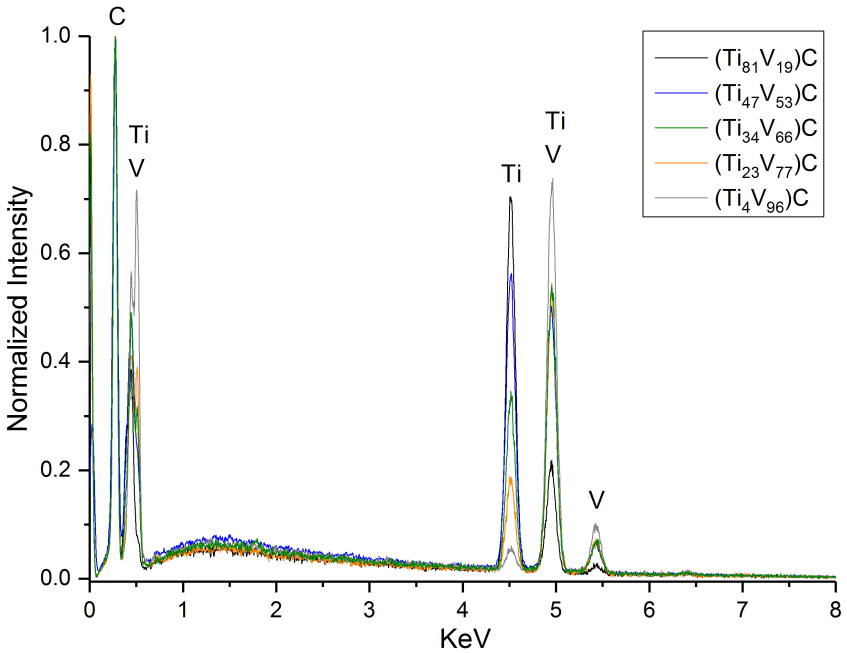

Fig. C.5 – EDX analysis of different ternary carbide of the (Ti,V)C ternary system.

C.4 (Ti,Ta)C ternary system

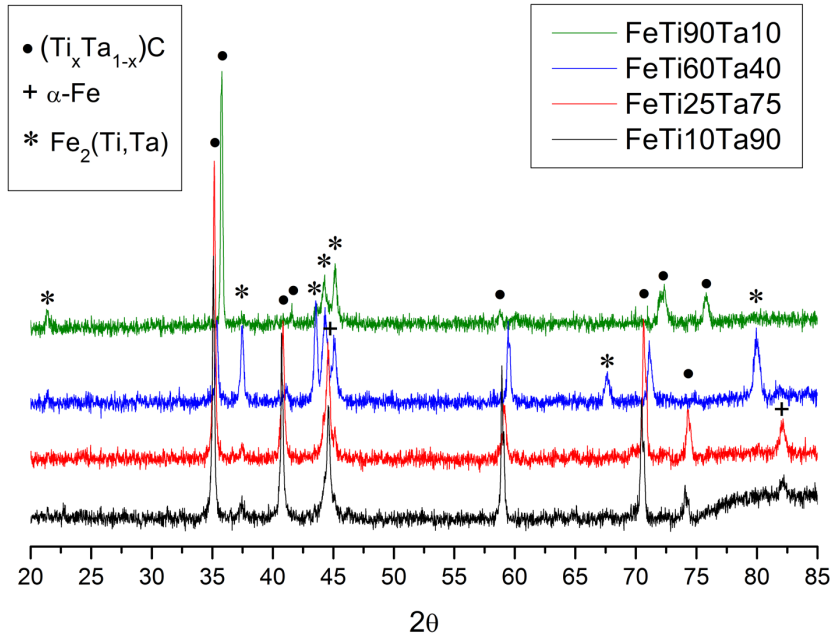

Fig. C.6 – XRD analysis of different ternary carbide of the (Ti,Ta)C ternary system.

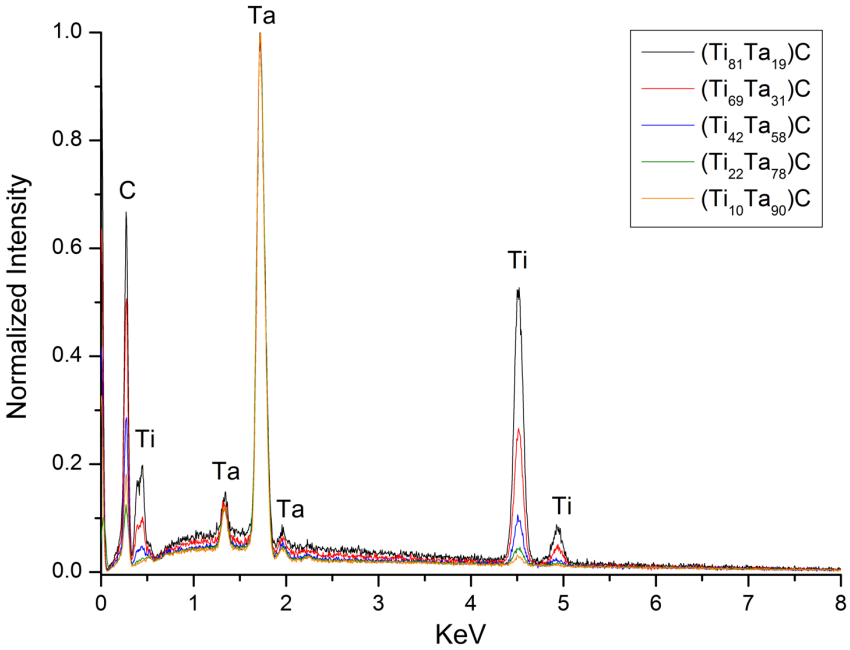

Fig. C.7 – EDX analysis of different ternary carbide of the (Ti,Ta)C ternary system.

C.5 (Ti,Nb)C ternary system

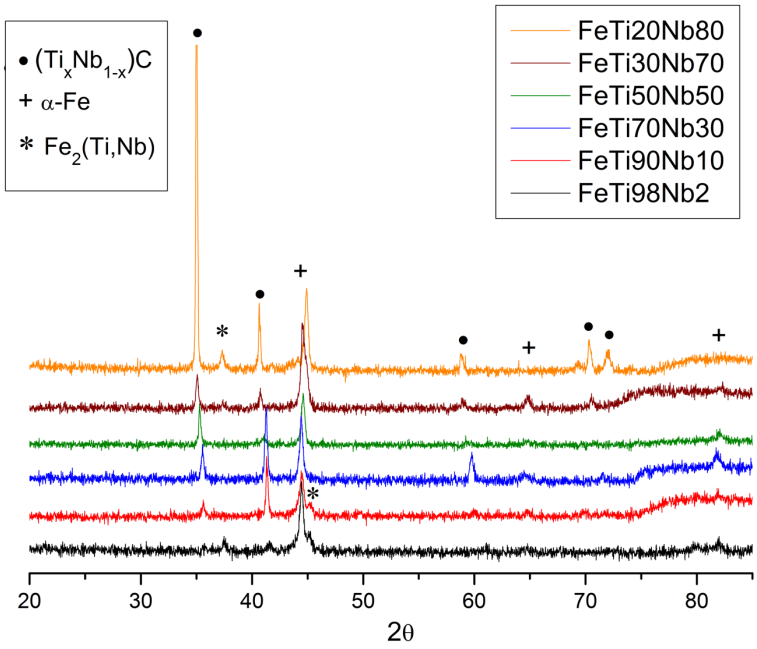

Fig. C.8 – XRD analysis of different ternary carbide of the (Ti,Nb)C ternary system.

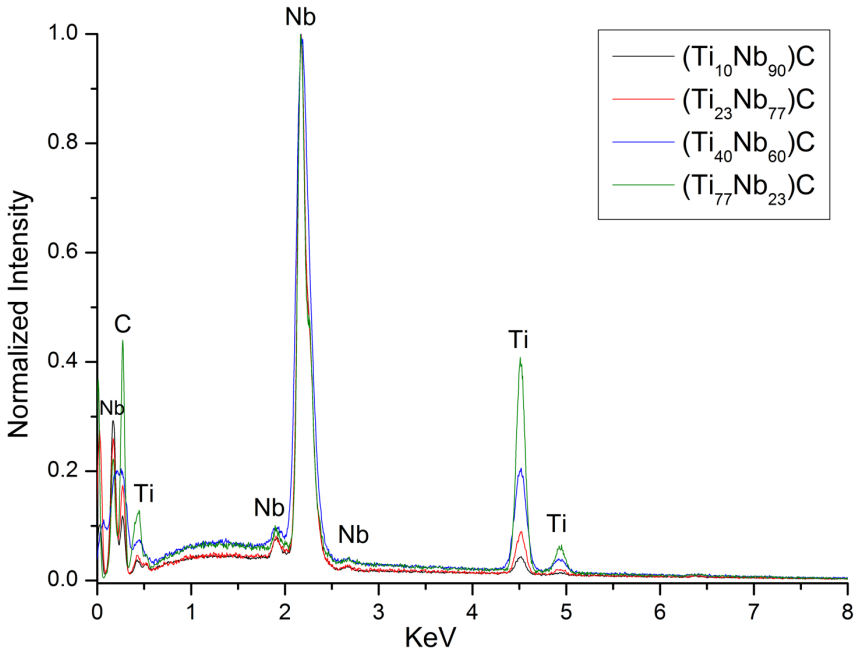

Fig. C.9 – EDX analysis of different ternary carbide of the (Ti,Nb)C ternary system.

C.6 (Ta,V)C ternary system

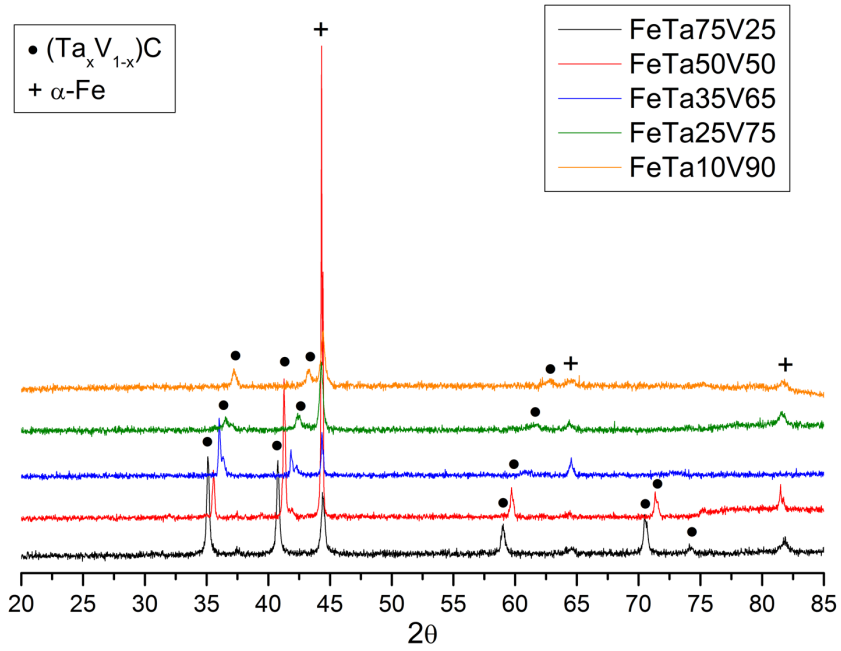

Fig. C.10 – XRD analysis of different ternary carbide of the (Ta,V)C ternary system.

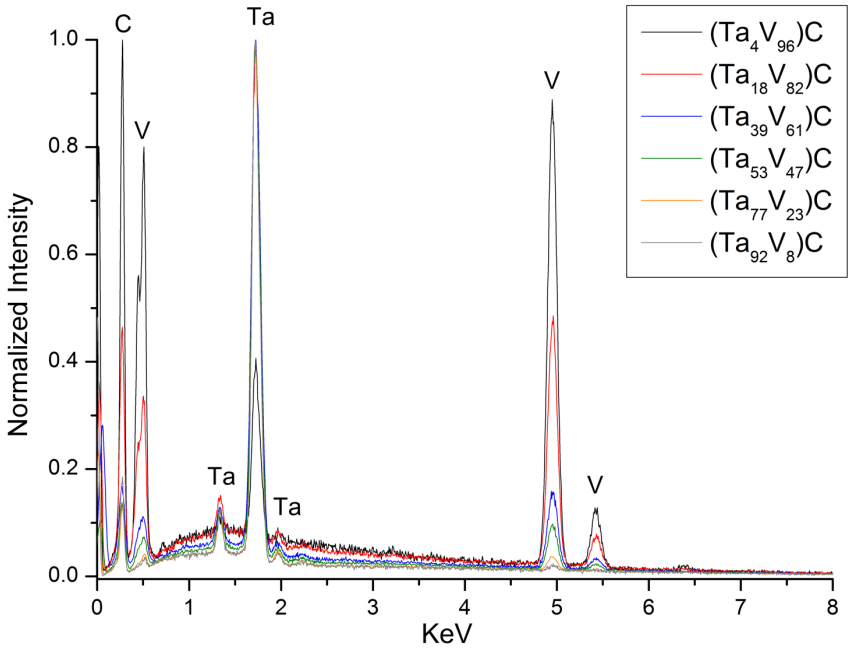

Fig. C.11 – EDX analysis of different ternary carbide of the (Ta,V)C ternary system.

APPENDIX D:

DENSITY OF STATES GRAPHS & DFT

In this last appendix section, we give the five DOS plots for the TiC, VC, TaC, NbC and WC binary carbides, as well as detail about DFT calculations performed on the (Ti,W)C system.

D.1 DOS graphs

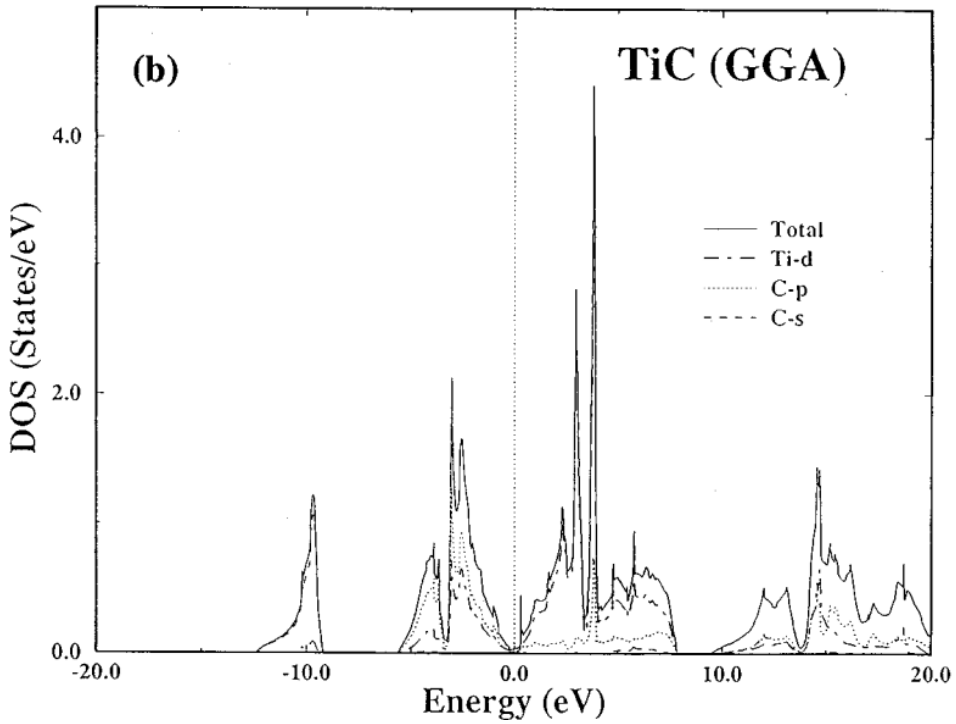

Fig. D.1 – DOS plot for TiC binary carbide; picture reproduced from Ref [187].

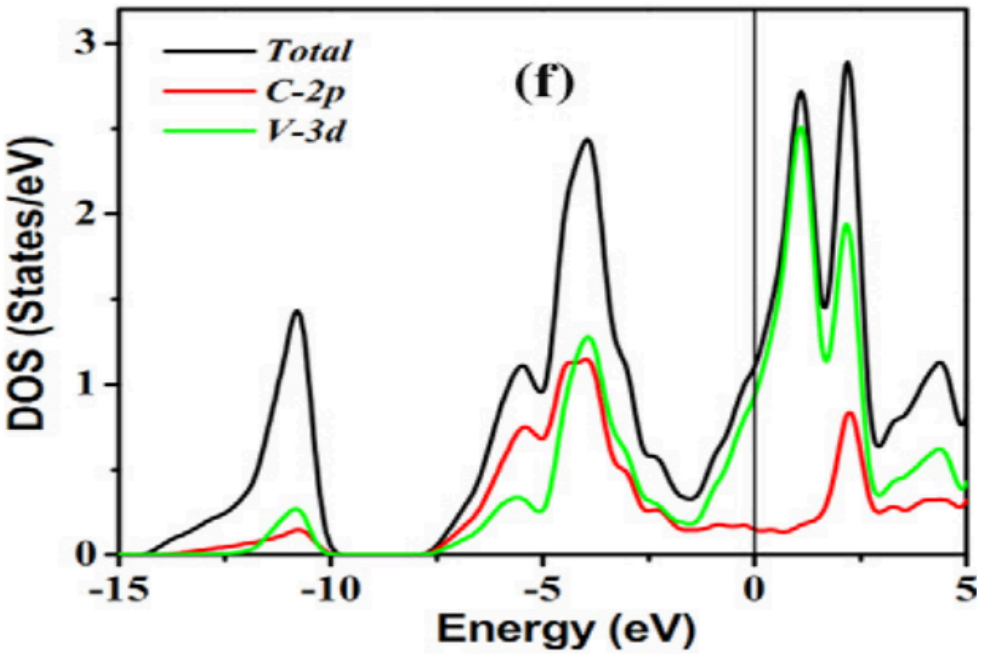

Fig. D.2 – DOS plot for VC binary carbide ; reproduced from Ref [188].

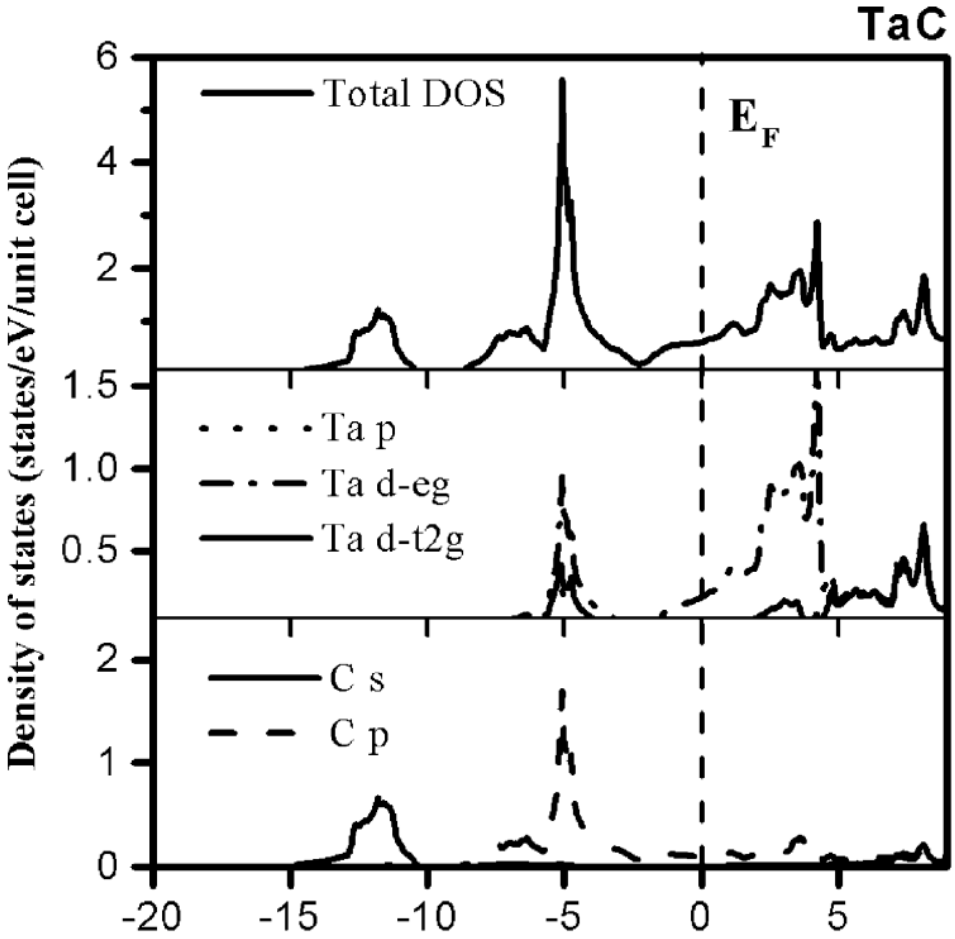

Fig. D.3 – DOS plot for TaC binary carbide ; reproduced from Ref [189].

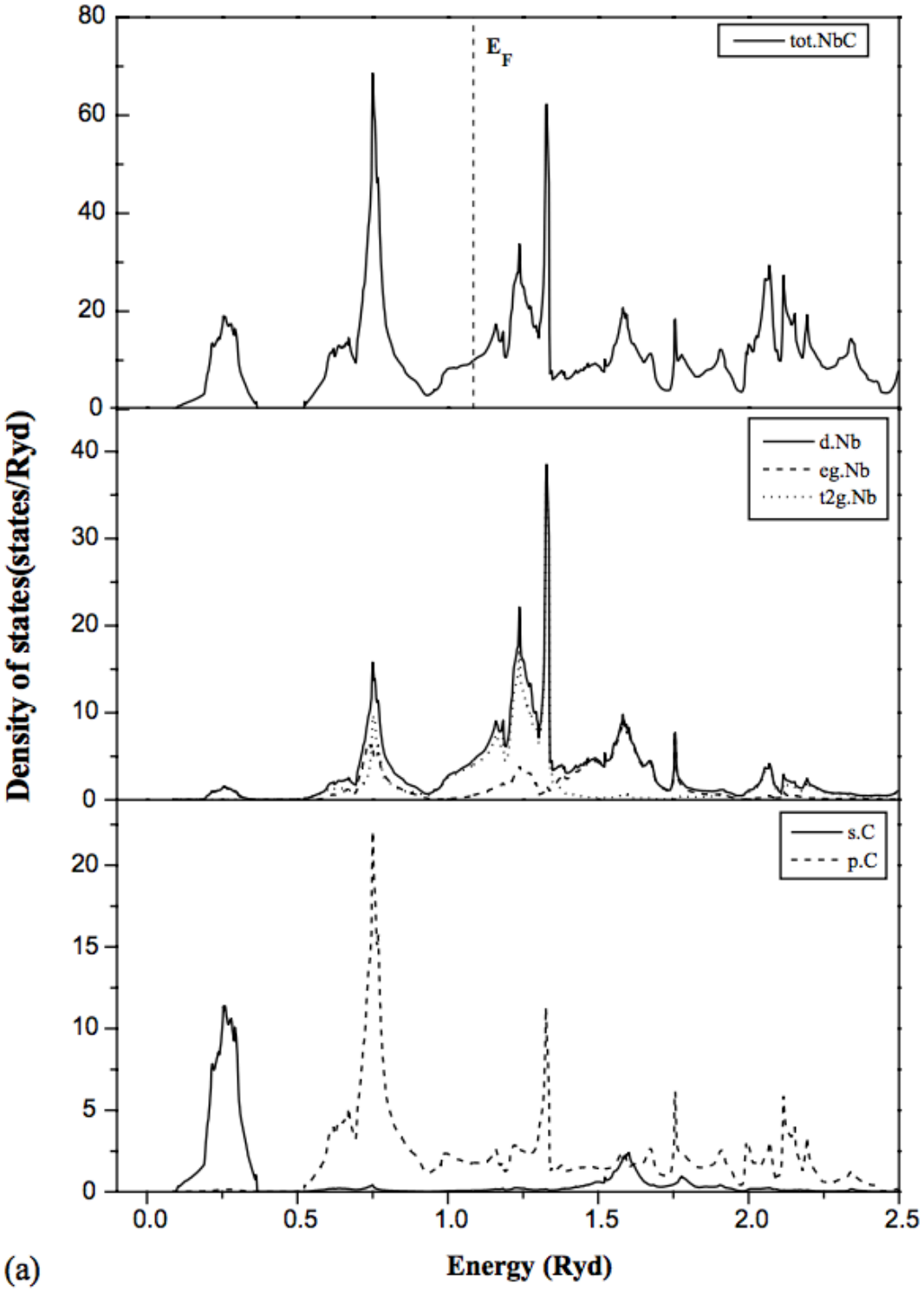

Fig. D.4 – DOS plot for NbC binary carbide ; figure reproduced from Ref [190].

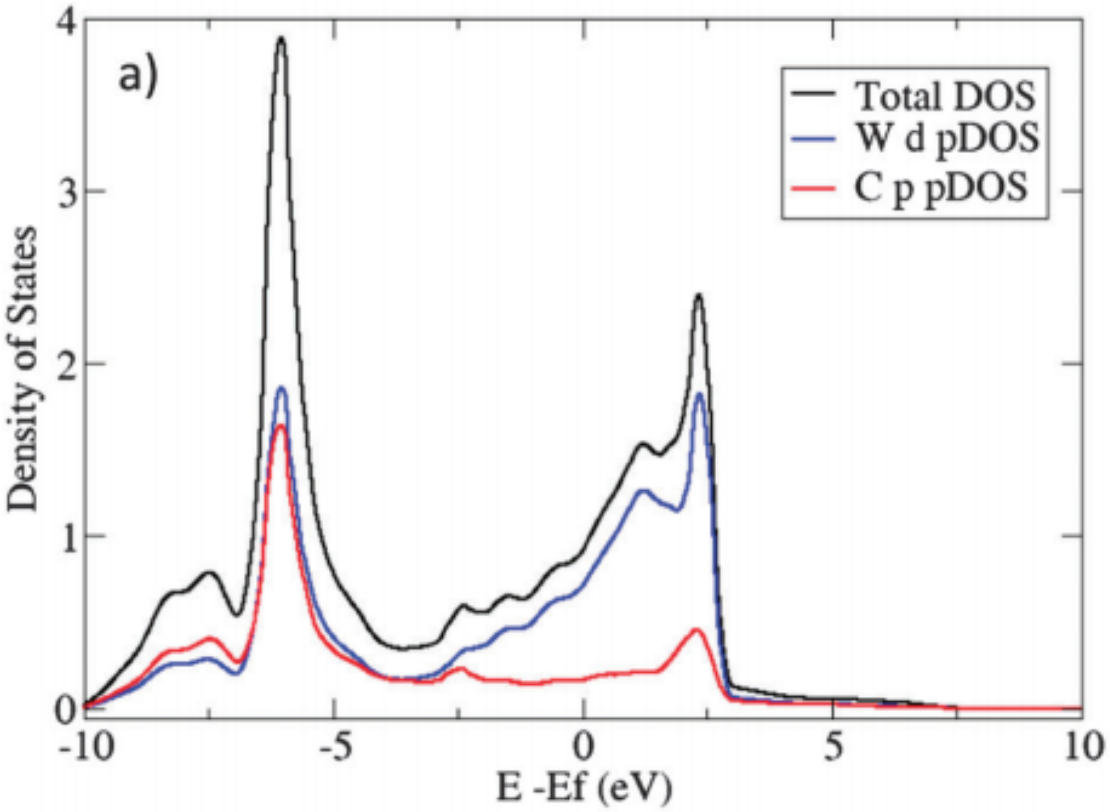

Fig. D.5 – DOS plot for WC binary carbide ; reproduced from Ref [191].

D.2 DFT calculations for the (Ti,W)C ternary system

The elastic constants of the mixed transition metal carbides, Ti-W-C, were predicted by using the first principle calculations based on the density functional theory (DFT). To this end, all DFT calculation were done by using the ABINIT code[192]. In DFT calculations, the interactions between valence electrons and the core ions of Ti, W and C atoms of the Ti-W-C mixed carbides were considered via the optimized norm-conserving Vanderbilt pseudo-potentials[193] (ONCVPSP v2) that were developed for the generalized gradient approximation (GGA) and Perdew-Burke-Ernzerhof (PBE)[194] exchange-correlation functional. The ONCVPSP v2 pseudo-potentials of Ti, W, and C atoms were obtained from the webpage of the ABINIT code. After performing the convergence studies for the rock-salt TiC and hexagonal close packed WC primitive unit cells, the self-consistent loop calculations for all mixed carbide structures were conducted with the plane wave kinetic energy cutoff set to 45 Ha, and the cold smearing with smearing parameter set to 0.02. Each considered structure of the mixed carbide in the rock-salt or hexagonal close packed lattice was first relaxed so that the inter-atomic forces in the structure do not exceed $1e^{-6}$ Ha / Bohr. The elastic constants of such relaxed structures were then calculated by exploiting the implementation of the density functional perturbation theory within the ABINIT code. The convergence of elastic constants with respect to the Brillouin zone sampling is checked by performing (repeating)

calculations using the discrete Monkhorst and Pack *k*-point sampling grids[195] of increasing density, i.e. starting from grid 6x6x6 via 8x8x8 up to grid 10x10x10 or higher if needed.

In order to search faster through the conformational space of possible ground state structures for mixed carbides of varying composition, we used the Alloy Theoretic Automated Toolkit (ATAT) code and therein implemented cluster expansion[196,197]. Based on the number of the exact total energies of different mixed carbide structures of different compositions obtained via the DFT calculations, the coefficients of the cluster expansion can be optimized so that the total energy of the new (any) mixed carbide structure is well approximated by evaluating its cluster expansion. By using such approach, we identified the mixed carbide structures at the bottom of the so called convex hull, i.e. the structures of the pseudo binary mixed carbide alloy at various compositions that have the lowest total energy. The computationally intensive DFT calculations ware then used to obtain the exact total energies and the elastic constant of in such a way predicted ground state mixed carbide structures.

CURRICULUM VITAE

Lionel Michelet

Ch. De la Venoge 05
1028 Préverenges

Phone number: +41 78 731 85 08
e-mail: lionel.michelet@alumni.epfl.ch

Education

Apr 2013 – Jun 2018	**PhD in Materials Science and Engineering** Ecole Polytechnique Fédérale de Lausanne (EPFL), Laboratory of Mechanical Metallurgy, Lausanne, Switzerland
Sep 2011 – Feb 2013	**Master in Materials Science and Engineering** Ecole Polytechnique Fédérale de Lausanne (EPFL), Institute of Materials, Lausanne, Switzerland
Sep 2008 – Jul 2011	**Bachelor in Materials Science and Engineering** Ecole Polytechnique Fédérale de Lausanne (EPFL), Institute of Materials, Lausanne, Switzerland
Sep 2003 – Jul 2007	**Secondary school** Lycée-Collège de l'Abbaye de St-Maurice, St-Maurice, Switzerland

Publications

L. Michelet, M. Fornabaio, L. Deillon, G. Zagar, A. Mortensen, Mechanical properties of quaternary (Ti,Ta,V)C carbide, *(to be submitted)*.

L. Michelet, M. Fornabaio, L. Deillon, G. Zagar, A. Mortensen, Mechanical properties of ternary (Ti,W)C carbide, *(to be submitted).*

L. Michelet, G. Zagar, A. Mortensen, Young's modulus measurement via ultra-low load spherical indentation on multimetallic transition carbides embedded in steel, *(to be submitted).*

M. Fornabaio, L. Deillon, L. Michelet, A. Mortensen, Microstructures of the ternary (Ti,W)C system, *(to be submitted).*

G. Zagar, V. Pejchal, M.G. Mueller, L. Michelet, A. Mortensen, Fracture toughness measurement in fused quartz using triangular chevron-notched micro-cantilevers, Scripta Materialia, 112, 2016, 132-135.

E. Russo-Averchi, M. Heiss, L. Michelet, P. Krogstrup, J. Nygard, C. Magen, J. Ramon Morante, E. Uccelli, J. Arbiol and A. Fontcuberta i Morral, Suppression of three dimensional twinning for a 100% yield of vertical GaAs nanowires on silicon, Nanoscale, 2012, 4, 1486-1490.

Professional Experience

Apr 2013 – Jun 2018	**PhD candidate** at **EPFL**, Lausanne, Switzerland
Sep 2012 – Feb 2013	**Master project** Ecole Polytechnique Fédérale de Lausanne (EPFL), collaboration with Constellium, Voreppe, France
Jun 2012 – Sep 2012	**R&D Internship** Holcim Granulats et Bétons, Eclépens, Switzerland
Jun 2011 – Jan 2012	**Accademic Internship** Laboratory of Semiconductors Materials (Prof. Ana Fontcuberta i Morral), EPFL, Switzerland
Jun 2010 – Sep 2010	**Accademic Internship** Laboratory for simulation of materials (Prof. Michel Rappaz), EPFL, Switzerland
Jun 2009 – Sep 2009	**R&D Internship** Holcim Granulats et Bétons, Eclépens, Switzerland

INDEX

H

I

K

L

M

N

O

P

Q

R

S

T

V

W

REFERENCES

1 Alfred Wilm, Verfahren zum Veredein von magnesiumhaltigen Aluminiumlegierungen, Kaiserliches Patentamt 244554 (Berlin, issued March 20, 1909).

2 M. H. Francombe et al., 'Thin Film and Bulk Structures of Phases in the System Gold-Aluminum', *Thin Solid Films* 1, no. 5 (March 1, 1968): 353–66, https://doi.org/10.1016/0040-6090(68)90025-4.

3 M. A. Weisser et al., 'On the Origin of Cementite Diffraction Peak Broadening during Tensile Deformation at Ambient Temperatures', *International Journal of Plasticity*, Plasticity of Textured Polycrystals In Honor of Prof. Paul Van Houtte, 66 (1 March 2015): 138–44

https://doi.org/10.1016/j.ijplas.2014.10.008.

4 A. Miserez et al., 'Fracture of Aluminium Reinforced with Densely Packed Ceramic Particles: Link between the Local and the Total Work of Fracture', *Acta Materialia*, 52, no. 5 (8 March 2004): 1337–51

https://doi.org/10.1016/j.actamat.2003.11.019.

5 M. Bauccio, ASM Engineered Materials Reference Book (Materials Park, OH: ASM International, 1994).

6 C. Maerky et al., 'Indentation Hardness and Fracture Toughness in Single Crystal TiC0.96', *Materials Science and Engineering: A*, Proceedings of the 5th International Conference on the Science of Hard Materials, 209, no. 1 (1 May 1996): 329–36

https://doi.org/10.1016/0921-5093(95)10152-7.

7 H. O. Pierson, Handbook of Refractory Carbides and Nitrides: Properties, Characteristics, Processing and Applications (William Andrew, 1996).

8 R. K. Govila, 'Further Observations on Fracture Energies in VC Monocrystals', *Scripta Metallurgica*, 6, no. 5 (1 May 1972): 353–55

https://doi.org/10.1016/0036-9748(72)90202-5.

9 X. Zhang et al., 'Densification and Mechanical Properties of TaC-Based Ceramics', *Materials Science and Engineering: A*, 501, no. 1 (15 February 2009): 37–43

https://doi.org/10.1016/j.msea.2008.09.024.

10 A. Nino et al., 'Preparation and Characterization of Tantalum Carbide (TaC) Ceramics', *International Journal of Refractory Metals and Hard Materials*, 52 (1 September 2015): 203–8

https://doi.org/10.1016/j.ijrmhm.2015.06.015.

11 F. Gao et al., 'Hardness of Covalent Crystals', *Physical Review Letters*, 91, no. 1 (2 July 2003): 015502

https://doi.org/10.1103/PhysRevLett.91.015502.

12 Y. Kumashiro and E. Sakuma, 'The Vickers Micro-Hardness of Non-Stoichiometric Niobium Carbide and Vanadium Carbide Single Crystals up to 1500° C', *Journal of Materials Science*, 15, no. 5 (1 May 1980): 1321–24

https://doi.org/10.1007/BF00551827.

13 B.-R. Kim et al., 'Mechanical Properties and Rapid Consolidation of Binderless Niobium Carbide', *Journal of Alloys and Compounds*, 481, no. 1 (29 July 2009): 573–76

https://doi.org/10.1016/j.jallcom.2009.03.036.

14 A. Šimůnek and J. Vackář, 'Hardness of Covalent and Ionic Crystals: First-Principle Calculations', *Physical Review Letters*, 96, no. 8 (3 March 2006): 085501

https://doi.org/10.1103/PhysRevLett.96.085501.

15 J. L. Chermant et al., 'Toughness and Fractography of TiC and WC', Fracture Mechanics of Ceramics, 1978, Volume 4.

16 H. Lammerman and G. Kienel, 'PVD Coatings for Aircraft Turbine Blades', Advanced Materials and Processes, 1991, Volume 140, Issue 6.

17 R. Diwakar, 'Silicon Carbide', Encylopedia of Chemical Technology (New York: Kirk-Othmer, 1990).

18 A. Savan et al., 'Increased Performance of Bearings Using TiC-Coated Balls', *Journal of Physics IV* Volume 3, no. C7 (November 1993): 943–48

https://doi.org/10.1051/jp4:19937145.

19 G. A. Roberts et al., Tool Steels, 5th Edition (ASM International, 1998).

20 H. Chandler, Heat Treater's Guide: Practices and Procedures for Irons and Steels, accessed 7 March 2018

http://www2.asminternational.org/content/ASM/StoreFiles/06400G_TOC.pdf.

21 R. Wilson, Metallurgy and Heat Treatment of Tool Steels (McGraw-Hill, 1975).

22 H. Mikado et al., 'On the Short Surface Fatigue Crack Growth Behavior in a Fine-Grained WC-Co Cemented Carbide', *Metals*, 7, no. 7 (6 July 2017): 254

https://doi.org/10.3390/met7070254.

23 P. Ettmayer, 'Hardmetals and Cermets', *Annual Review of Materials Science*, 19, no. 1 (1989): 145–64

https://doi.org/10.1146/annurev.ms.19.080189.001045.

24 J. Chipman, 'Thermodynamics and Phase Diagram of the Fe-C System', *Metallurgical and Materials Transactions B*, 3, no. 1 (1 January 1972): 55–64

https://doi.org/10.1007/BF02680585.

25 S. Ban-ya et al., 'Thermodynamics of Austenitic Fe-C Alloys', *Metallurgical and Materials Transactions B*, 1, no. 5 (1 May 1970): 1313

https://doi.org/10.1007/BF02900248.

26 R. Ruer and J. Biren, 'Über Die Löslichkeit Des Graphits in Geschmolzenem Eisen', *Zeitschrift Für Anorganische Und Allgemeine Chemie*, October 1920, Volume 113 edition, sec. Issue 1.

27 J. Chipman et al., *Transactions of American Society for Metals*, 1952, Volume 44.

28 J. A. Kitchener et al., 'Solutions on Liquid Iron. Part 2: The Influence of Sulphur on the Solubility and Activity Coefficient of Carbon', *Transactions of the Faraday Society*, 1952, Volume 48.

29 J. A. Cahill and A. A. Grosse, *Transactions of American Society for Metals*, 1964.

30 A. A. Vertman et al., 'An Investigation into the Transeutectic Region of the Iron-Carbon System (From 2.88 to 27 Wt% of C)', *Doklady Akademii Nauk SSSR*, 1964, Volume 159, Issue 1.

31 L. S. Darken and R. W. Gurry, 'Free Energy of Formation of Cementite and the Solubility of Cementite in Austenite', *JOM*, 3, no. 11 (1 November 1951): 1015–18

https://doi.org/10.1007/BF03397413.

32 E. Scheil, 'Ermittlung Der Gleichgewichte von Kohlenoxyd–Kohlensäure-Gemischen Mit Dem Γ-Mischkristall, Mit Zementit Und Mit Graphit', *Archiv Für Das Eisenhüttenwesen*, 32, no. 4 (1 April 1961): 251–60.

33 R.P. Smith, 'The Solubility of Cementite in Austenite', *Trans. AIME*, 215 (1959): 954–57.

34 A. Bergman et al., 'In-Situ Formation of Carbide Composites by Liquid/Solid Reactions', *Key Engineering Materials*, 79–80 (1993): 213–34

https://doi.org/10.4028/www.scientific.net/KEM.79-80.213.

35 H. Nowotny et al., 'Novel Complex Carbides and Nitrides and Their Relation to Phases of Hard Substances', *Planseeberichte Für Pulvermetallurgie*, 1964, Volume 12.

36 H. Nowotny and F. Benesovsky, 'Phase Stability in Metals and Alloys', (London: P. S. Rudman, J. Stringer and R. I. Jaffee, 1967).

37 H. L. Schick, Thermodynamics of Certain Refractory Compounds Vol. 1, accessed 7 March 2018

http://archive.org/details/in.ernet.dli.2015.459593.

38 H. L. Schick, Thermodynamics of Certain Refractory Compounds Vol. 2, accessed 7 March 2018

http://archive.org/details/in.ernet.dli.2015.459598.

39 Y. A. Chang, 'Thermodynamic Properties of Group 4, 5, and 6 Binary Transition Metal Carbides' (AFML-TR-65-2, 1965).

40 E. K. Storms, The Refractory Carbides (Elsevier, 2016).

41 G. V. Samsonov, ed., Refractory Carbides, Studies in Soviet Science (Springer US, 1974)

http://www.springer.com/in/book/9781468486001.

42 K.K. Kelley, 'Entropies of the Elements and Inorganic Compounds' (U.S. Printing Office, Washington, 1961).

43 D. R Stull and H. Prophet, and United States National Bureau of Standards, JANAF Thermochemical Tables, 2d edition (Washington, D.C. : U.S. Dept. of Commerce, National Bureau of Standards, 1971)

https://trove.nla.gov.au/work/21422031.

44 L. E. Toth, Transition Metal Carbides and Nitrides (Academic Press, 1971).

45 N. Pessall et al., Final Rep, Westinghouse Research Laboratories, AF 33 (615), 1967.

46 L. E. Toth and J. Zbasnik, 'Low Temperature Heat Capacities of Superconducting Molybdenum Carbides', *Acta Metallurgica*, 16, no. 9 (1 September 1968): 1177–82

https://doi.org/10.1016/0001-6160(68)90052-7.

47 R. Diwakar, 'Silicon Carbide', Encylopedia of Chemical Technology (New York: Kirk-Othmer, 1990).

48 I. Barin, Thermochemical Data of Pure Substances (VCH, 1993).

49 G. Hägg, 'Eigenschaften Der Phasen von Übergangselementen in Binären Systemen Mit Bor, Kohlenstoff Und Stickstoff', *Zeitschrift Für Physikalische Chemie*, 6B, no. 1 (2017): 221–232

https://doi.org/10.1515/zpch-1929-0122.

50 R. E. Rundle, 'A New Interpretation of Interstitial Compounds–metallic Carbides, Nitrides and Oxides of Composition MX', *Acta Crystallographica*, 1, no. 4 (2 September 1948): 180–87

https://doi.org/10.1107/S0365110X4800051X.

51 V. Ern and A. C. Switendick, 'Electronic Band Structure of TiC, TiN, and TiO', *Physical Review*, 137, no. 6A (15 March 1965): A1927–36

https://doi.org/10.1103/PhysRev.137.A1927.

52 M. J. Winter, D-Block Chemistry (Oxford ; New York: Oxford University Press, USA, 1995).

53 D.-B. Kang, 'Effect of Valence Electron Concentration on Elastic Properties of 4d Transition Metal Carbides MC (M = Y, Zr, Nb, and Rh)', *Bulletin of the Korean Chemical Society*, 34, no. 7 (2013): 2171–75

https://doi.org/10.5012/bkcs.2013.34.7.2171.

54 K. K. Korir et al., 'First-Principle Calculations of the Bulk Properties of 4d Transition Metal Carbides and Nitrides in the Rocksalt, Zincblende and Wurtzite Structures', *Diamond and Related Materials*, 20, no. 2 (1 February 2011): 157–64

https://doi.org/10.1016/j.diamond.2010.11.021.

55 S.-H. Jhi et al., 'Electronic Mechanism of Hardness Enhancement in Transition-Metal Carbonitrides', *Nature*, 399, no. 6732 (May 1999): 132–34

https://doi.org/10.1038/20148.

56 O. L. Anderson, 'Derivation of Wachtman's Equation for the Temperature Dependence of Elastic Moduli of Oxide Compounds', *Physical Review*, 144, no. 2 (15 April 1966): 553–57

https://doi.org/10.1103/PhysRev.144.553.

57 D.A. Speck and B.R. Micciolo, 'Advanced Ceramic Systems for Rocket Nozzle Applications' (Carborundum Company Report, October 1968).

58 H. Li et al., 'Structural, Elastic and Electronic Properties of Transition Metal Carbides TMC (TM=Ti, Zr, Hf and Ta) from First-Principles Calculations', *Solid State Communications*, 151, no. 8 (1 April 2011): 602–6

https://doi.org/10.1016/j.ssc.2011.02.005.

59 X.-G. Lu, Malin Selleby, and Bo Sundman, 'Calculations of Thermophysical Properties of Cubic Carbides and Nitrides Using the Debye–Grüneisen Model', *Acta Materialia*, 55, no. 4 (1 February 2007): 1215–26

https://doi.org/10.1016/j.actamat.2006.05.054.

60 F. W. Vahldiek, Anisotropy in Single-Crystal Refractory Compounds, vol. 1 (Springer US, 1968)

http://www.springer.com/gp/book/9781489953070.

61 F. W. Vahldiek and S. A. Mersol, Anisotropy in Single-Crystal Refractory Compounds: Proceedings (Plenum Press, 1968).

62 W. S. Williams, 'Influence of Temperature, Strain Rate, Surface Condition, and Composition on the Plasticity of Transition-Metal Carbide Crystals', *Journal of Applied Physics*, 35, no. 4 (1 April 1964): 1329–38

https://doi.org/10.1063/1.1713614.

63 G. E. Hollox and R. E. Smallman, 'Plastic Behavior of Titanium Carbide', *Journal of Applied Physics*, 37, no. 2 (1 February 1966): 818–23

https://doi.org/10.1063/1.1708264.

64 J. J. Gilman and B. W. Roberts, 'Elastic Constants of TiC and TiB_2', *Journal of Applied Physics*, 32, no. 7 (1 July 1961): 1405–1405

https://doi.org/10.1063/1.1736249.

65 G. Santoro, 'Variation of Some Properties of Tantalum Carbide with Carbon Content', *Transactions of the Metallurgical Society of AIME*, 227, no. 6 (1963): 1361.

66 R. Steinitz, 'Nuclear Applications of Non-Fissionable Ceramics', American Nuclear Society, Illinois, 1966, 75.

67 I.N. Frantsevich, Inorganic Materials 3 (1967).

68 V. Krasnenko and M. G. Brik, 'First-Principles Calculations of Hydrostatic Pressure Effects on the Structural, Elastic and Thermodynamic Properties of Cubic Monocarbides XC (X = Ti, V, Cr, Nb, Mo, Hf)', *Solid State Sciences*, 14, no. 10 (1 October 2012): 1431–44

https://doi.org/10.1016/j.solidstatesciences.2012.08.007.

69 Y. Z. Liu et al., 'First Principles Study the Stability and Mechanical Properties of MC (M=Ti, V, Zr, Nb, Hf and Ta) Compounds', *Journal of Alloys and Compounds*, 582 (5 January 2014): 500–504

https://doi.org/10.1016/j.jallcom.2013.08.045.

70 Y. Kumashiro et al., 'Micro-Vickers Hardness of TiC Single Crystals at High Temperature', *Bull. Electrotech. Lab.* , 41, no. 8 (1977): 600–609.

71 Y. Yang et al., 'First-Principles Calculations of Mechanical Properties of TiC and TiN', *Journal of Alloys and Compounds*, 485, no. 1 (19 October 2009): 542–47

https://doi.org/10.1016/j.jallcom.2009.06.023.

72 C. Kral et al., 'Critical Review on the Elastic Properties of Transition Metal Carbides, Nitrides and Carbonitrides', *Journal of Alloys and Compounds*, 265, no. 1 (30 January 1998): 215–33

https://doi.org/10.1016/S0925-8388(97)00297-1.

73 L. Wu et al., 'Understanding the Mechanical Properties of Vanadium Carbides: Nano-Indentation Measurement and First-Principles Calculations', *Journal of Alloys and Compounds*, 548 (25 January 2013): 60–64

https://doi.org/10.1016/j.jallcom.2012.09.014.

74 X.-X. Yu et al., 'Influence of Carbon Vacancy Formation on the Elastic Constants and Hardening Mechanisms in Transition Metal Carbides', *Journal of the European Ceramic Society*, 35, no. 1 (1 January 2015): 95–103

https://doi.org/10.1016/j.jeurceramsoc.2014.08.021.

75 L. López-de-la-Torre et al., 'Elastic Properties of Tantalum Carbide (TaC)', *Solid State Communications*, , 134, no. 4 (1 April 2005): 245–50

https://doi.org/10.1016/j.ssc.2005.01.036.

76 C. K. Jun and P. T. Shaffer, 'Elastic Moduli of Niobium Carbide and Tantalum Carbide at High Temperature', *Journal of the Less Common Metals*, 23, no. 4 (1 April 1971): 367–73

https://doi.org/10.1016/0022-5088(71)90046-4.

77 S. R. Bakshi et al., 'Spark Plasma Sintered Tantalum Carbide: Effect of Pressure and Nano-Boron Carbide Addition on Microstructure and Mechanical Properties', *Materials Science and Engineering: A*, 528, no. 3 (25 January 2011): 1287–95

https://doi.org/10.1016/j.msea.2010.10.009.

78 H. L. Brown et al., 'Elastic Properties of Some Polycrystalline Transition-Metal Monocarbides', *The Journal of Chemical Physics*, 45, no. 2 (15 July 1966): 547–49

https://doi.org/10.1063/1.1727602.

79 M. Lee and R. S. Gilmore, 'Single Crystal Elastic Constants of Tungsten Monocarbide', *Journal of Materials Science*, 17, no. 9 (1 September 1982): 2657–60

https://doi.org/10.1007/BF00543901.

80 D. R. Lide, CRC Handbook of Chemistry and Physics, 87th Edition, (Boca Raton, Fla.: CRC Press, 2006).

81 J. Haines et al., 'Synthesis and Design of Superhard Materials', *Annual Review of Materials Research*, 31, no. 1 (2001): 1–23

https://doi.org/10.1146/annurev.matsci.31.1.1.

82 J. H. Westbrook and H. Conrad, eds., The Science of Hardness Testing and Its Research Applications: Based on Papers Presented at a Symposium of the American Society for Metals, (American Society for Metals, 1973).

83 E. Rudy, Ternary Phase Equilibria in Transition Metal-Boron-Carbon-Silicon Systems. Part 5. Compendium of Phase Diagram Data, AFML-TR-65-2 (Ohio: PN, 1969).

84 E. Rudy, 'Constitution of Ternary Titanium-Tungsten-Carbon Alloys', *Journal of the Less Common Metals*, 33, no. 2 (1 November 1973): 245–73

https://doi.org/10.1016/0022-5088(73)90044-1.

85 A. G. Metcalfe, 'The Mutual Solid Solubility of Tungsten Carbide and Titanium Carbide', *Journal of the Institute of Metals*, 73, no. 8 (1947): 591.

86 W. H. Jiang, J Fei, and X. L Han, 'In Situ Synthesis of (TiW)C/Fe Composites', *Materials Letters*, 46, no. 4 (1 November 2000): 222–24

https://doi.org/10.1016/S0167-577X(00)00174-9.

87 W. Z. et al., 'A Thermodynamic Description of the C–Ti–V System over the Whole Composition and Temperature Ranges', *International Journal of Refractory Metals and Hard Materials*, 48 (1 January 2015): 346–54

https://doi.org/10.1016/j.ijrmhm.2014.10.002.

88 D. Bandyopadhyay et al., 'The Ti-N-C System (Titanium-Nitrogen-Carbon)', *Journal of Phase Equilibria*, 21, no. 2 (2000): 192.

89 K. Ono and J. Moriyama, 'The Phase Relationships in the Nb-Ti-C System', *Journal of the Less Common Metals*, 79, no. 2 (1 June 1981): 255–60

https://doi.org/10.1016/0022-5088(81)90074-6.

90 W. Q. Wei et al., 'Mechanical Properties of Nb Based Multiphase Alloy Studied by Nanoindentation and Atomic Force Microscopy', *Materials Science and Technology*, 27, no. 12 (1 December 2011): 1770–76

https://doi.org/10.1179/1743284711Y.0000000005.

91 G. V. Samsonov, Refractory Carbides, Springer, 1974, ISBN : 978-1-4684-8598-1

92 J. Jung and S. Kang, 'Sintered (Ti,W)C Carbides', *Scripta Materialia*, 56, no. 7 (1 April 2007): 561–64

https://doi.org/10.1016/j.scriptamat.2006.12.026.

93 L. A. Tret'yachenko and V. N. Eremenko, 'Structure and Certain Properties of Alloys of Sections TiC-$VC_{0.90}$, TiC-V_2C, TiC-V and in the Region TiC-$VC_{0.90}$-C of the Ternary System Ti-V-C', *Soviet Powder Metallurgy and Metal Ceramics*, 5, no. 7 (1 July 1966): 581–84

https://doi.org/10.1007/BF00780122.

94 E. A. Levashov et al., 'Characteristic Properties of Combustion and Structure Formation in the Ti-Ta-C System', *Russian Journal of Non-Ferrous Metals*, 49, no. 5 (1 October 2008): 404–13

https://doi.org/10.3103/S1067821208050179.

95 E. A. Levashov et al., 'Structure and Properties of Precipitation-Hardening Ceramic Ti-Zr-C and Ti-Ta-C Materials', *The Physics of Metals and Metallography*, 109, no. 1 (1 January 2010): 95–105

https://doi.org/10.1134/S0031918X10010102.

96 E. Chicardi et al., 'Effect of Sintering Time on the Microstructure and Mechanical Properties of (Ti,Ta)(C,N)-Based Cermets', *International Journal of Refractory Metals and Hard Materials*, 38 (1 May 2013): 73–80

https://doi.org/10.1016/j.ijrmhm.2013.01.001.

97 E. Chicardi et al., 'High Temperature Oxidation Resistance of (Ti,Ta)(C,N)-Based Cermets', *Corrosion Science*, 102 (1 January 2016): 125–36

https://doi.org/10.1016/j.corsci.2015.10.001.

98 P. Wu et al., 'Effect of TaC Addition on the Microstructures and Mechanical Properties of Ti(C,N)-Based Cermets', *Materials & Design*, 31, no. 7 (1 August 2010): 3537–41

https://doi.org/10.1016/j.matdes.2010.01.047.

99 H. Jiao et al., 'Microstructures and Mechanical Properties of Nb–Ti–C Alloys', *Materials Science and Engineering: A*, 485, no. 1 (25 June 2008): 359–66

https://doi.org/10.1016/j.msea.2007.08.035.

100 H. Holleck, 'Material Selection for Hard Coatings', *Journal of Vacuum Science & Technology A: Vacuum, Surfaces, and Films*, 4, no. 6 (1 November 1986): 2661–69

https://doi.org/10.1116/1.573700.

101 D. G. Sangiovanni et al., 'Supertoughening in B1 Transition Metal Nitride Alloys by Increased Valence Electron Concentration', *Acta Materialia*, 59, no. 5 (1 March 2011): 2121–34

https://doi.org/10.1016/j.actamat.2010.12.013.

102 S.-H. Jhi and J. Ihm, 'Electronic Structure and Structural Stability of TiC_xN_{1-x} Alloys', *Physical Review B*, 56, no. 21 (1 December 1997): 13826–29

https://doi.org/10.1103/PhysRevB.56.13826.

103 W. Feng et al., 'Electronic Structure and Elastic Constants of TiC_xN_{1-x}, $Zr_xNb_{1-x}C$ and HfC_xN_{1-x} Alloys: A First-Principles Study', *Physica B: Condensed Matter*, 406, no. 19 (1 October 2011): 3631–35

https://doi.org/10.1016/j.physb.2011.06.058.

104 A. Zaoui et al., 'First-Principles Calculations on the Electronic Structure of TiC_xN_{1-x}, $Zr_xNb_{1-x}C$ and HfC_xN_{1-x} Alloys', *Materials Chemistry and Physics*, 91, no. 1 (15 May 2005): 108–15

https://doi.org/10.1016/j.matchemphys.2004.10.056.

105 V. I. Ivashchenko et al., 'Electronic Origin of Elastic Properties of Titanium Carbonitride Alloys', *Metallurgical and Materials Transactions A*, 37, no. 12 (1 December 2006): 3391–96

https://doi.org/10.1007/s11661-006-1031-9.

106 R. Kieffer et al., 'Zur Entmischung von kubischen Mehrstoffcarbiden', *Monatshefte für Chemie / Chemical Monthly*, 99, no. 3 (1 May 1968): 1020–27

https://doi.org/10.1007/BF00913751.

107 T. Ma et al., 'Self-Organizing Nanostructured Lamellar (Ti,Zr)C — A Superhard Mixed Carbide', *International Journal of Refractory Metals and Hard Materials*, 51 (1 July 2015): 25–28

https://doi.org/10.1016/j.ijrmhm.2015.02.010.

108 Y. Li et al., 'Phase Decomposition of TiC−ZrC Solid Solution Prepared by Spark Plasma Sintering', *Ceramics International*, 41, no. 10, Part B (1 December 2015): 14258–62

https://doi.org/10.1016/j.ceramint.2015.07.055.

109 T. Ma et al., 'Microstructure Evolution during Phase Separation in Ti-Zr-C', *International Journal of Refractory Metals and Hard Materials*, 61 (1 December 2016): 238–48

https://doi.org/10.1016/j.ijrmhm.2016.09.019.

110 H. Hertz, 'On the Contact of Solid Elastic Bodies and on Hardness', *Journal of Math*, 92 (1881): 156–171.

111 H. Hertz, 'On Hardness', *Ver. Beförderung Gewerbe Fleisses*, 61 (1882): 410.

112 M. T. Huber, 'On the Theory of Contacting Solid Elastic Bodies', *Ann. Phys*, 14 (1904): 153–163.

113 S. Fuchs, 'Principal Stress Trajectories of a Sphere on Contact with a Plate', *Physikalische Zeitschrift*, U 1282 (1913).

114 M. T. Huber and S. Fuchs, 'Spannungsverteilung Bei Der Berührung Zweier Elastischer Zylinder', *Physikalische Zeitschrift*, 15 (1914): 298–303.

115 W. B. Morton and L. J. Close, 'XXX. Notes on Hertz's Theory of the Contact of Elastic Bodies', *Philosophical Magazine*, Series 6 43, no. 254 (1922): 320–329.

116 I. N. Sneddon, Fourier Transforms, International Series in Pure and Applied Mathematics (McGraw-Hill, 1951).

117 J. Boussinesq, 'Applications of Potentials for the Study of Equilibrium and Movement of Elastic Solids', Paris: Gautier-Villars, 1885.

118 S. P. Timoshenko and J. N. Goodier, Theory of Elasticity, 3rd Edition (Mcgraw Hill, 1970).

119 K. L. Johnson, Contact Mechanics (Cambridge University Press, 1987).

120 B. R. Lawn et al., 'A Computer Simulation Study of Hertzian Cone Crack Growth', *International Journal of Fracture*, 10, no. 1 (1 March 1974): 1–16

https://doi.org/10.1007/BF00955075.

121 I. N. Sneddon, 'Boussinesq's Problem for a Rigid Cone', *Mathematical Proceedings of the Cambridge Philosophical Society*, 44, no. 4 (October 1948): 492–507

https://doi.org/10.1017/S0305004100024518.

122 A. C. Fischer-Cripps, Introduction to Contact Mechanics, 2nd ed., Mechanical Engineering Series (Springer US, 2007)

http://www.springer.com/la/book/9780387681870.

123 W. C. Oliver and G. M. Pharr, 'An Improved Technique for Determining Hardness and Elastic Modulus Using Load and Displacement Sensing Indentation Experiments', J*ournal of Materials Research*, 7, no. 6 (June 1992): 1564–83

https://doi.org/10.1557/JMR.1992.1564.

124 A. C Fischer-Cripps, 'A Review of Analysis Methods for Sub-Micron Indentation Testing', *Vacuum*, 58, no. 4 (1 September 2000): 569–85

https://doi.org/10.1016/S0042-207X(00)00377-8.

125 A. C. Fischer-Cripps, 'Critical Review of Analysis and Interpretation of Nanoindentation Test Data', *Surface and Coatings Technology*, 200, no. 14 (10 April 2006): 4153–65

https://doi.org/10.1016/j.surfcoat.2005.03.018.

126 W. C. Oliver and G. M. Pharr, 'Measurement of Hardness and Elastic Modulus by Instrumented Indentation: Advances in Understanding and Refinements to Methodology', *Journal of Materials Research*, 19, no. 1 (January 2004): 3–20

https://doi.org/10.1557/jmr.2004.19.1.3.

127 M. F. Doerner and W. D. Nix, 'A Method for Interpreting the Data from Depth-Sensing Indentation Instruments', *Journal of Materials Research*, 1, no. 4 (August 1986): 601–9

https://doi.org/10.1557/JMR.1986.0601.

128 R. B. King, 'Elastic Analysis of Some Punch Problems for a Layered Medium', *International Journal of Solids and Structures*, 23, no. 12 (1 January 1987): 1657–64

https://doi.org/10.1016/0020-7683(87)90116-8.

129 R. Saha and W. D. Nix, 'Effects of the Substrate on the Determination of Thin Film Mechanical Properties by Nanoindentation', *Acta Materialia*, 50, no. 1 (8 January 2002): 23–38

https://doi.org/10.1016/S1359-6454(01)00328-7.

130 H. Li and J. J. Vlassak, 'Determining the Elastic Modulus and Hardness of an Ultra-Thin Film on a Substrate Using Nanoindentation', *Journal of Materials Research*, 24, no. 3 (March 2009): 1114–26

https://doi.org/10.1557/jmr.2009.0144.

131 H. Y. Yu et al., 'The Effect of Substrate on the Elastic Properties of Films Determined by the Indentation Test — Axisymmetric Boussinesq Problem', *Journal of the Mechanics and Physics of Solids*, 38, no. 6 (1 January 1990): 745–64,

https://doi.org/10.1016/0022-5096(90)90038-6.

132 E. G Herbert et al., 'On the Measurement of Stress–strain Curves by Spherical Indentation', *Thin Solid Films*, Proceedings of the 28th International Conference on Metallurgic Coatings and Thin Films, 398–399 (1 November 2001): 331–35

https://doi.org/10.1016/S0040-6090(01)01439-0.

133 H. Lee et al., 'A Numerical Approach to Spherical Indentation Techniques for Material Property Evaluation', *Journal of the Mechanics and Physics of Solids*, 53, no. 9 (1 September 2005): 2037–69

https://doi.org/10.1016/j.jmps.2005.04.007.

134 Y.-T. Cheng et al., 'Scaling Relationships for Indentation Measurements', *Philosophical Magazine A*, 82, no. 10 (1 July 2002): 1821–29

https://doi.org/10.1080/01418610208235693.

135 Y.-T. Cheng et al., 'Scaling, dimensional analysis, and indentation measurements', *Materials Science and Engineering Reports*, 44, no. 4-5 (August 2004): 91–149

https://doi.org/10.1016/j.mser.2004.05.001.

136 W. Ni et al., 'An Energy-Based Method for Analyzing Instrumented Spherical Indentation Experiments', *Journal of Materials Research*, 19, no. 1 (January 2004): 149–57

https://doi.org/10.1557/jmr.2004.19.1.149.

137 W. C. Oliver, 'Alternative Technique for Analyzing Instrumented Indentation Data', *Journal of Materials Research*, 16, no. 11 (November 2001): 3202–6

https://doi.org/10.1557/JMR.2001.0441.

138 J. Malzbender and G. de With, 'Indentation Load–displacement Curve, Plastic Deformation, and Energy', *Journal of Materials Research*, 17, no. 2 (February 2002): 502–11

https://doi.org/10.1557/JMR.2002.0070.

139 J. W. Leggoe, 'Determination of the Elastic Modulus of Microscale Ceramic Particles via Nanoindentation', *Journal of Materials Research*, 19, no. 8 (August 2004): 2437–47

https://doi.org/10.1557/JMR.2004.0300.

140 A. C. Fischer-Cripps, 'Elastic–plastic Behaviour in Materials Loaded with a Spherical Indenter', *Journal of Materials Science*, 32, no. 3 (1 February 1997): 727–36

https://doi.org/10.1023/A:1018552222072.

141 R. Hill et al., 'The Theory of Combined Plastic and Elastic Deformation with Particular Reference to a Thick Tube under Internal Pressure', *Proc. R. Soc. Lond. A*, 191, no. 1026 (18 November 1947): 278–303

https://doi.org/10.1098/rspa.1947.0116.

142 A. C. Fischer-Cripps, Nanoindentation, 3rd ed., Mechanical Engineering Series (New York: Springer-Verlag, 2011)

http://www.springer.com/la/book/9781441998712.

143 Y.-T. Cheng et al., 'Scaling Relationships for Indentation Measurements', *Philosophical Magazine A*, 82, no. 10 (1 July 2002): 1821–29

144 K. K. Tho et al., 'Uniqueness of Reverse Analysis from Conical Indentation Tests', *Journal of Materials Research*, 19, no. 8 (August 2004): 2498–2502

https://doi.org/10.1557/JMR.2004.0306.

145 W. Ni et al., 'An Energy-Based Method for Analyzing Instrumented Spherical Indentation Experiments', *Journal of Materials Research*, 19, no. 1 (January 2004): 149–57

https://doi.org/10.1557/jmr.2004.19.1.149.

146 S. V. Hainsworth et al., 'Analysis of Nanoindentation Load-Displacement Loading Curves', *Journal of Materials Research*, 11, no. 8 (August 1996): 1987–95

https://doi.org/10.1557/JMR.1996.0250.

147 T. F. Page et al., 'Nanoindentation Characterization of Coated Systems: P:S2 - A New Approach Using the Continuous Stiffness Technique', MRS Online Proceedings Library Archive 522 (ed 1998)

https://doi.org/10.1557/PROC-522-53.

148 S. Palmqvist, 'A Method to Determine the Toughness of Brittle Materials, Especially Hard Materials', *Jernkontorets Ann*, 141 (1957): 303–307.

149 B. R. Lawn et al., 'Elastic/Plastic Indentation Damage in Ceramics: The Median/Radial Crack System', *Journal of the American Ceramic Society*, 63, no. 9–10 (1 September 1980): 574–81

https://doi.org/10.1111/j.1151-2916.1980.tb10768.x.

150 R. Hill, The Mathematical Theory of Plasticity, Clarendon Press, 1998.

151 G. C. Sih, Handbook of Stress-Intensity Factors (Lehigh University, Institute of Fracture and Solid Mechanics, 1973).

152 A. S. Kobayashi, Experimental Techniques in Fracture Mechanics (Iowa State University Press, 1973).

153 M. T. Laugier, 'Palmqvist Crack Extension and the Center-Loaded Penny Crack Analogy', *Journal of the American Ceramic Society*, 68, no. 2 (1 February 1985): C–51

https://doi.org/10.1111/j.1151-2916.1985.tb15281.x.

154 K. Niihara et al., 'Evaluation of K_{IC} of Brittle Solids by the Indentation Method with Low Crack-to-Indent Ratios', *Journal of Materials Science Letters*, 1, no. 1 (1 January 1982): 13–16

https://doi.org/10.1007/BF00724706.

155 K. Niihara, 'A Fracture Mechanics Analysis of Indentation-Induced Palmqvist Crack in Ceramics', *Journal of Materials Science Letters*, 2, no. 5 (1 May 1983): 221–23

https://doi.org/10.1007/BF00725625.

156 J. S. Field et al., 'Determination of Fracture Toughness from the Extra Penetration Produced by Indentation-Induced Pop-In', *Journal of Materials Research*, 18, no. 6 (June 2003): 1412–19

https://doi.org/10.1557/JMR.2003.0194.

157 H. Tada et al., The Stress Analysis of Cracks Handbook, Third Edition (Three Park Avenue New York, NY 10016-5990: ASME, 2000)

https://doi.org/10.1115/1.801535.

158 T. Zhang et al., 'A Method to Determine Fracture Toughness Using Cube-Corner Indentation', *Scripta Materialia*, 62, no. 4 (1 February 2010): 199–201

https://doi.org/10.1016/j.scriptamat.2009.10.025.

159 A.-T. Akono et al., 'Experimental Determination of the Fracture Toughness via Microscratch Tests: Application to Polymers, Ceramics, and Metals', *Journal of Materials Research*, 27, no. 2 (January 2012): 485–93

https://doi.org/10.1557/jmr.2011.402.

160 M. Sebastiani et al., 'A Novel Pillar Indentation Splitting Test for Measuring Fracture Toughness of Thin Ceramic Coatings', *Philosophical Magazine*, 95, no. 16–18 (23 June 2015): 1928–44

https://doi.org/10.1080/14786435.2014.913110.

161 E. Frutos et al., 'Repetitive Nano-Impact Tests as a New Tool to Measure Fracture Toughness in Brittle Materials', *Journal of the European Ceramic Society*, 36, no. 13 (1 October 2016): 3235–43

https://doi.org/10.1016/j.jeurceramsoc.2016.04.026.

162 F. Iqbal et al., 'In Situ Micro-Cantilever Tests to Study Fracture Properties of NiAl Single Crystals', *Acta Materialia*, 60, no. 3 (1 February 2012): 1193–1200

https://doi.org/10.1016/j.actamat.2011.10.060.

163 D. Di Maio and S. G. Roberts, 'Measuring Fracture Toughness of Coatings Using Focused-Ion-Beam-Machined Microbeams', *Journal of Materials Research*, 20, no. 2 (February 2005): 299–302

https://doi.org/10.1557/JMR.2005.0048.

164 D. Kupka et al., 'A Combined Experimental-Numerical Approach for Elasto-Plastic Fracture of Individual Grain Boundaries', *Journal of the Mechanics and Physics of Solids*, 64 (1 March 2014): 455–67

https://doi.org/10.1016/j.jmps.2013.12.004.

165 M. G. Mueller et al., 'Fracture Toughness Testing of Nanocrystalline Alumina and Fused Quartz Using Chevron-Notched Microbeams', *Acta Materialia*, 86 (1 March 2015): 385–95

https://doi.org/10.1016/j.actamat.2014.12.016.

166 J. Schaufler et al., 'Determination of the Interfacial Strength and Fracture Toughness of A-C:H Coatings by in-Situ Microcantilever Bending', *Thin Solid Films*, EMRS 2011 symp Q, 522 (1 November 2012): 480–84

https://doi.org/10.1016/j.tsf.2012.08.031.

167 A. Riedl et al., 'A Novel Approach for Determining Fracture Toughness of Hard Coatings on the Micrometer Scale', *Scripta Materialia*, 67, no. 7 (1 October 2012): 708–11

https://doi.org/10.1016/j.scriptamat.2012.06.034.

168 K. Matoy et al., 'Interface Fracture Properties of Thin Films Studied by Using the Micro-Cantilever Deflection Technique', *Surface and Coatings Technology*, ICMCTF 2009, 204, no. 6 (25 December 2009): 878–81

https://doi.org/10.1016/j.surfcoat.2009.09.013.

169 B. N. Jaya and V. Jayaram, 'Crack Stability in Edge-Notched Clamped Beam Specimens: Modeling and Experiments', *International Journal of Fracture*, 188, no. 2 (1 August 2014): 213–28

https://doi.org/10.1007/s10704-014-9956-2.

170 F. Y. Cui and R. P. Vinci, 'A Chevron-Notched Bowtie Micro-Beam Bend Test for Fracture Toughness Measurement of Brittle Materials', *Scripta Materialia*, 132 (15 April 2017): 53–57

https://doi.org/10.1016/j.scriptamat.2017.01.031.

171 S. Liu et al., 'Measuring the Fracture Resistance of Hard Coatings', *Applied Physics Letters*, 102, no. 17 (29 April 2013): 171907

https://doi.org/10.1063/1.4803928.

172 B. Merle and M. Göken, 'Fracture Toughness of Silicon Nitride Thin Films of Different Thicknesses as Measured by Bulge Tests', *Acta Materialia 59*, no. 4 (1 February 2011): 1772–79

https://doi.org/10.1016/j.actamat.2010.11.043.

173 G. Boothroyd and C. Reynolds, 'Approximate Cost Estimates for Typical Turned Parts', *Journal of Manufacturing Systems*, 8, no. 3 (1 January 1989): 185–93

https://doi.org/10.1016/0278-6125(89)90040-X.

174 Z. Hashin and S. Shtrikman, 'A Variational Approach to the Theory of the Elastic Behaviour of Multiphase Materials', *Journal of the Mechanics and Physics of Solids*, 11, no. 2 (1 March 1963): 127–40

https://doi.org/10.1016/0022-5096(63)90060-7.

175 J. D. Lord and R. M. Morrell, 'Elastic Modulus Measurement—obtaining Reliable Data from the Tensile Test', *Metrologia*, 47, no. 2 (2010): S41.

176 A. C. Fischer-Cripps, Nanoindentation, 3rd ed., Mechanical Engineering Series (New York: Springer-Verlag, 2011)

http://www.springer.com/la/book/9781441998712.

177 K. I. Schiffmann, 'Determination of Fracture Toughness of Bulk Materials and Thin Films by Nanoindentation: Comparison of Different Models', *Philosophical Magazine*, 91, no. 7–9 (1 March 2011): 1163–78

https://doi.org/10.1080/14786435.2010.487984.

178 M. G. Mueller et al., 'Stable Room-Temperature Micron-Scale Crack Growth in Single-Crystalline Silicon', *Journal of Materials Research*, 32, no. 19 (October 2017): 3617–26

https://doi.org/10.1557/jmr.2017.238.

179 J.-I Jang and G. M. Pharr, 'Influence of Indenter Angle on Cracking in Si and Ge during Nanoindentation', *Acta Materialia*, 56, no. 16 (1 September 2008): 4458–69

https://doi.org/10.1016/j.actamat.2008.05.005.

180 M. T. Laugier, 'New Formula for Indentation Toughness in Ceramics', *Journal of Materials Science Letters*, 6, no. 3 (1 March 1987): 355–56

https://doi.org/10.1007/BF01729352.

181 F. Ouchterlony, 'Stress Intensity Factors for the Expansion Loaded Star Crack', *Engineering Fracture Mechanics*, 8, no. 2 (1976): 447–448.

182 J. Thurn and R. F. Cook, 'Mechanical and Thermal Properties of Physical Vapour Deposited Alumina Films Part II: Elastic, Plastic, Fracture, and Adhesive Behaviour', *Journal of Materials Science*, 39, no. 15 (1 August 2004): 4809–19

https://doi.org/10.1023/B:JMSC.0000035319.81486.62.

183 X. Li et al., 'Fracture Mechanisms of Thin Amorphous Carbon Films in Nanoindentation', *Acta Materialia*, 45, no. 11 (1 November 1997): 4453–61

https://doi.org/10.1016/S1359-6454(97)00143-2.

184 B.-R. Kim et al., 'Mechanical Properties and Rapid Consolidation of Binderless Nanostructured Tantalum Carbide', *Ceramics International*, 35, no. 8 (1 December 2009): 3395–3400

https://doi.org/10.1016/j.ceramint.2009.06.012.

185 B.-R. Kim et al., 'Properties and Rapid Consolidation of Binderless Nanostuctured NbC by Pulsed Current Activated Sintering', *Electronic Materials Letters*, 5, no. 3 (1 September 2009): 119–22

https://doi.org/10.3365/eml.2009.09.119.

186 R. Warren, 'Measurement of the Fracture Properties of Brittle Solids by Hertzian Indentation', *Acta Metallurgica*, 26, no. 11 (1 November 1978): 1759–69

https://doi.org/10.1016/0001-6160(78)90087-1.

187 R. Ahuja et al., 'Structural, Elastic, and High-Pressure Properties of Cubic TiC, TiN, and TiO', *Physical Review B*, 53, no. 6 (February 1, 1996): 3072–79

https://doi.org/10.1103/PhysRevB.53.3072.

188 X.-X. Yu et al., 'Influence of Carbon Vacancy Formation on the Elastic Constants and Hardening Mechanisms in Transition Metal Carbides', *Journal of the European Ceramic Society*, 35, no. 1 (January 1, 2015): 95–103

https://doi.org/10.1016/j.jeurceramsoc.2014.08.021.

189 M. Sahnoun et al., 'FP-LAPW Investigation of Electronic Structure of TaN and TaC Compounds', Computational Materials Science, Proceedings of the E-MRS 2004 Spring Meeting; Symposium H: Atomic Materials Design: Modelling and Characterization, 33, no. 1 (April 1, 2005): 175–83

https://doi.org/10.1016/j.commatsci.2004.12.010.

190 T Amriou et al., 'FP-LAPW Investigations of Electronic Structure and Bonding Mechanism of NbC and NbN Compounds', *Physica B: Condensed Matter*, 325 (January 1, 2003): 46–56

https://doi.org/10.1016/S0921-4526(02)01429-1.

191 J. L. Yates et al., 'Platinum–carbide Interactions: Core–shells for Catalytic Use', *Physical Chemistry Chemical Physics*, 17, no. 6 (2015): 4250–58

https://doi.org/10.1039/C4CP04974H.

192 X. Gonze et al., 'ABINIT: First-principles approach to material and nanosystem properties', *Comput. Phys. Commun.*, 180 (2009): 2582-2615

https://doi.org/10.1016/j.cpc.2009.07.007.

193 D. R. Hamann, 'Optimized norm-conserving Vanderbilt pseudopotentials', *Phys. Rev. B.*, 88 (2013)

https://doi.org/10.1103/PhysRevB.88.085117.

194 J. Perdew et al., 'Generalized Gradient Approximation Made Simple', *Phys. Rev. Lett.*, 77 (1996): 3865-3868

https://doi.org/10.1103/PhysRevLett.77.3865.

195 H. J. Monkhorst and J. D. Pack, 'Special points for Brillouin-zone integrations', *Phys. Rev. B.*, 13 (1976): 5188-5192

https://doi.org/10.1103/PhysRevB.13.5188.

196 A. Van de Walle et al., 'The Alloy Theoretic Automated Toolkit: A User Guide', *Calphad*, 26 (2002): 539-553

https://doi.org/10.1016/S0364-5916(02)80006-2.

197 A. Van de Walle and G. Ceder, 'Automating First-Principles Phase Diagram Calculations', *J. Phase Equilib.*, 23 (2002): 348–359

https://doi.org/10.1361/105497102770331596.